Autonomous Navigation: On Issues Concerning Measurement Uncertainty

John Stephen Mullane

School of Electrical and Electronic Engineering

A thesis submitted to the Nanyang Technological University
in partial fulfillment of the requirement for the degree of
Doctor of Philospohy

2009

Acknowledgements

First and foremost I would like to express my most heartfelt thanks to my immensely generous, always loving and ever supporting parents, without whom, nothing in my life would have been possible. Even though they may not understand a single word, I dedicate this work to them.

I would next like to thank my supervisors - Associate Professors Martin Adams and Sardha Wijesoma, as well as NTU, for providing me with the opportunity to pursue this research, supporting me throughout and most importantly, providing the necessary funding which allowed me to stave off homelessness and hunger in a foreign land, with even some fun thrown in along the way. I am indebted to Associate Professor Ba-Ngu Vo at the University of Melbourne for funding my visit to work with him in Australia, and his invaluable input into the work of this thesis. Also for his tireless effort during his visits to Singapore, spending many a late evening with me (along with the complimentary bottles of wine) working on algorithms, writing articles and accommodating my never ending questions. Thanks also to Professor Wang Dan Wei for (knowingly or unknowingly) allowing me to hijack his mobile platform and to 'Uncle' Teck Chew, Tan Chai Soon and Pham Minh Tuan in the ME Workshop for helping me pimp it up for my work. To Gerald, Agnes, Slim Jim and co. up in the RRC for tolerating my somewhat lax dress code (the infamous red knickers) for so many years, even during frequent visits to their world-renowned laboratory by the Singaporean Elite. I also wish to thank my brothers for their inputs on the process of pursuing such a degree, helping to keep me focussed and mucho coding help.

As for the other aspect of life, the more fun part, there are numerous people who helped make this a much less painful experience than it otherwise might have been. Thanks to Udang for the many cups of coffee and chats about anything and everything as long as its not robotics, Banath and Panda for getting me into diving (hanging out under the sea proved a very nice distraction from probabilities and x-hats), Sylvia for providing the most obscure stories and experiences, Lochana "something like that" Perera for his words of wisdom, Gringo for being the butt end of many a joke, as well as Giang and Lizie for putting up with me and my endless nonsense. Special thanks too to Hida, who also contributed her fair share of non-PhD related distractions, as well as (amongst other things) kitting my room out as a nice office from where much

of this thesis writing was performed.

For the non-specific acknowledgments, I'd like to express my gratitude to the collective mass of Singaporean taxi drivers, for giving me buckets of great laughs over the passed number of years as well as endless invaluable opinions on anything from the number of hercules aircraft required to airlift a HDB block to Indonesia, to the moral aspects of furthering autonomous robotics and threatening their very livelihood. To all the hawker center aunties and uncles who kept me well fed during my times of need, and indeed to my beloved holland village happy hours, always a students best friend. Also my flatmates down through the years, some of whom, when things got really bad and frustrating, so often reminded me that things could always be worse.

Now that this is over, I think I'll go sit on a beach somewhere, have a drink, a ponder, a few chortles and start planning how to take over the world. Its about time I did something.

Contents

Summary

Exteroceptive sensors provide absolute information from the surrounding environment and are a critical aspect of any autonomous navigation algorithm. These measurements are subject to many sources of uncertainty, namely detection and data association uncertainty, spurious measurements, biasses as well as measurement noise. To deal with such uncertainty, probabilistic methods are most widely adopted, especially metric based approaches. These probabilistic environmental representations, for autonomous navigation frameworks with uncertain measurements, can generally be subdivided into two main categories - grid based and feature based. Grid based approaches are popular for robotic exploration, obstacle avoidance and path planning, whereas feature based maps, with their reduced dimensionality, are primarily used for large scale localisation, i.e. SLAM. While researchers commonly distinguish both approaches based on their environmental representations, this thesis examines the fundamental theoretical aspects of estimation theoretic algorithms for both approaches, with emphasis on the measurement likelihoods used to incorporate measurement uncertainty, and their impact on the resulting stochastic problem.

Autonomous navigation involves both state estimation (localisation and map estimates) and decision making hypotheses (data association and loop closing). However, the hypothesis of landmark detection from noisy sensor data is less widely considered in the SLAM literature. Using a millimeter wave radar as the main sensor of choice, landmark detection methods are firstly introduced, developing insight as to the source of the detection uncertainty as well as spurious measurements present in the exteroceptive sensors. Adaptive detection methods are used to develop scan maps of outdoor environments and the resulting stochastic information that can be extracted is analysed. Theoretical implications measurement interpretation is also discussed focussing on vector and set based representations.

The thesis then focuses on grid based representations which primarily address detection uncertainty and spurious measurements, and do not maintain explicit densities on the landmark location estimates. Focussing on the standard range measurement used and the corresponding measurement likelihood, it is shown that such a measurement is in fact independent of the state of interest, and essentially provides an *a priori* assumed (as well as being noise free) measurement for the grid based filter.

By re-formulating the recursion with detection measurements, as opposed to range-bearing measurements, a statistically correct and state dependent filtering recursion can be derived. The new formulation thus unifies the landmark detection problem and grid-based occupancy approaches. As detection likelihoods are *a priori* unknown, a joint recursion is derived to solve for both the new measurement likelihoods and the grid map posterior. The proposed grid based filters are then analysed using the radar sensor for outdoor mapping experiments.

Feature based methods primarily address measurement noise (i.e the uncertainty in estimated feature locations) and sub-optimally, it is shown, address detection, spurious measurements and data association uncertainty. The standard measurement model is examined and it is shown that these measurement likelihoods fail to encapsulate the inherent uncertainty in the number of features within the sensor field of view, as well as measurement detection uncertainty and spurious measurements. It is shown that, in fact, the classical measurement equation only considers the measurement noise of a known number of features directly in the filter recursion. Consequently, only a (sub-optimal) density on the *assumed* number of features in the map is propagated. Using random set theory, the feature based framework is re-formulated for the more theoretically accurate set measurement likelihood and applied to the feature based mapping problem. The new approach jointly incorporates all the sources of measurement uncertainty (excluding biasses) into the feature-based filtering framework. The proposed formulation is then extended to the full Bayesian SLAM problem, which for the first time jointly considers the randomness in both feature number, their corresponding locations, as well as the noisy vehicle location estimate. Extensive experiments then validate the proposed filters.

The thesis argues that well established probabilistic autonomous navigation frameworks designed for handling exteroceptive measurement uncertainty, contain subtle oversights in their formulations, particularly in the measurement equations. These pitfalls are transferred to the corresponding measurement likelihoods used in the filter recursions, which compromise the optimality of the posterior density estimation. This work therefore aims to highlight such previous oversights and propose some possible solutions.

List of Figures

List of Tables

List of Notations and Glossary

The following details the symbols and notations used throughout the thesis.

Sensor Notations

c	speed of light in air
t_t	time of flight
d	true distance from sensor to landmark
Δ_f	beat frequency
B_s	signal bandwidth
T_s	signal sweep time
Ψ	an imaging sensor power spectrum
R	total number of range bins in a given spectrum
ψ_r	signal power in range bin $r \leq R$
T_r	signal power threshold value in range bin r
I	total number of bearing angles in a given scan
$p_{(x,y)}(\psi\|\cdot)$	pdf of ψ at map co-ordinates (x,y)
Ω_E	moments of the pdf of ψ given landmark absence
Ω_O	moments of the pdf of ψ given landmark presence
P_d	probability of detection
P_{fa}	probability of false alarm
P_{md}	probability of missed detection
P_n	probability of noise detection
$L(\psi_r)$	signal likelihood ratio in range bin r
μ	mean power of noise signal
σ	standard deviation of noise signal
$\Re$	signal to noise ratio
W	adaptive detector sliding window width
G	adaptive detector number of guard cells
τ	adaptive detector scale factor
k_{os}	adaptive detector k value

Ψ_{os}	ordered sliding window of power values
$\hat{\mu}$	estimated mean noise signal power

Filter Notations

k	time index
x_k	true vehicle x-coordinate at time k
y_k	true vehicle y-coordinate at time k
α_k	true vehicle heading at time k
X_k	true vehicle pose at time k
X^k	vector of vehicle trajectory
$\hat{X}_k$	estimated vehicle pose at time k
$\mathfrak{n}_X$	dimension of the vehicle state
u_k	vehicle control input at time k
u^k	vector of control input history
v_k	control input noise
Q_k	control input noise covariance
M	true map state
$\mathfrak{q}$	total number of elements in true map state
M_k	true observed map state at time k ($M_k \subseteq M$)
$\mathfrak{q}(k)$	true number of elements in observed map state at time k
$M_k = [\dots]$	observed map defined as a vector
$M_k = \{\dots\}$	observed map defined as a set
$\hat{M}_k$	estimated map state at time k
$\hat{\mathfrak{q}}(k)$	estimated number of elements in observed map state at time k
$m^i_{(x,y)}$	the i^{th} grid-based map element at coordinates (x, y)
m_i	the i^{th} feature-based map element
$\mathfrak{n}_m$	dimension of a map element
$Z_k = [\dots]$	vector of measurements at time k
$Z_k = \{\dots\}$	set of measurements at time k
Z^k	vector of measurement history
z^i_k	the i^{th} measurement at time k
$\mathfrak{z}_k$	the total number of measurements at time k
D	detection measurement
$\bar{D}$	non-detection measurement
w_k	measurement noise
R_k	measurement noise covariance matrix
ζ_k	joint vehicle-map state at time k

P_k	joint state covariance at time k
$\zeta_{k\|k}$	estimated joint vehicle-map state
$P_{k\|k}$	estimated state covariance at time k
$\nabla(\cdot)$	Jacobian function
K_k	Kalman gain at time k
S_k	innovation covariance at time k
$\mathcal{N}$	Gaussian distribution
$w_k^{(i)}$	i^{th} Gaussian weight at time k
N	total number of Gaussians (or particles)
$q(\cdot)$	proposal function
Π	Marlov transition matrix
$\Theta_k(\cdot)$	RFS of feature measurements at time k
$C_k(\cdot)$	RFS of clutter measurements at time k
$B_k(\cdot)$	RFS of new features at time k
v_k	intensity function at time k
c_k	intensity of clutter RFS
b_k	intensity of new feature RFS
λ_c	average number of clutter measurements
V	volume of surveillance region

Glossary

GB	grid-based
FB	feature-based
RM	robotic mapping
EKF	extended Kalman filter
SMC	sequential Monte Carlo
GM	Gaussian mixture
RFS	random finite set
PHD	probability hypothesis density
FMCW	frequency modulated continuous wave
MMWR	millimeter wave radar
CFAR	constant false alarm rate
OS	ordered statistics
CA	cell averaging
ROC	receiver operating characteristics
SNR	signal to noise ratio
FOV	field of view

Chapter 1

Introduction

This chapter outlines the motivation for the research undertaken in this work, as well as outlining the primary goals and objectives of the thesis. A chapter-by-chapter layout, introducing the work in more detail, is also presented.

1.1 Motivation

Autonomous Guided Vehicles (AGV) have been the focus of much research over the past few decades. As industrial and military interest in autonomous platforms increases year by year, the research community has been inspired to examine the theoretical challenges presented by such a system. The list of requirements for such a fully autonomous vehicle is extremely demanding, but the potential uses are enormous. Applications ranging from autonomous mining, underwater mapping and self-driving cars, to the robotic exploration of space all depend on having a fully stand alone platform. These are required to work without human intervention in any range of (potentially hazardous) situations, placing high demands on the on-board systems which must be robust enough to deal with all the various aspects of operating in real environments. To successfully operate in a given workspace, the autonomous vehicle must have an accurate understanding of its surroundings, in terms of where obstacles and hazards are, as well as places of interest to its mission goal. Furthermore, in order to maneuver in its environment, the vehicle must know where it is in relation to its working area. These two requirements are critical to autonomous navigation and have been shown to be fundamental research issues in the development of AGVs.

Major driving forces for the development of autonomous platforms come from the military and automotive industries. Early unmanned platforms that followed pre-installed wires to traverse their working environment have evolved into sophisticated vehicles which use a suite of on-board sensors and triangulation methods to determine their location and proceed with their task. The automotive industry is currently

pursuing multiple levels of autonomy to reduce accidents on the road and improve traffic flow. Fully unmanned cars are required to have an accurate description of their immediate surrounding to accomplish path planning and obstacle avoidance goals. In the military domain, attacks on transport vehicles are a major source of casualties in conflict zones, which resulted in the United States of America declaring its interest in automating its army ground vehicles. As a result, much funding has become available inspiring researchers to theoretically analyze the robotic navigation problem with impressive results demonstrated at both the off-road DARPA grand challenge in the mojave desert [1] and the urban challenge [2]. The off-road challenge demonstrated extensive autonomous navigation capabilities in rugged terrains whereas the urban challenge was more task-specific requiring the unmanned vehicle to safely perform numerous maneuvers, in the presence of typical urban obstacles.

Whilst the development of unmanned vehicles may require numerous application specific subsystems such as manipulator control, AI, or path planning, autonomous navigation is the focus of this thesis. Arguably the most critical sub-system of any autonomous platform, this involves acquiring knowledge of the platforms immediate environmental surroundings (typically through some exteroceptive sensors) in order to construct a spatial model representation. Using this information, it is then possible to derive knowledge of its location within this spatial model. With this powerful awareness, the platform can then proceed to make decisions required to achieve the mission goal. All of these requirements are generally categorised by three simple questions, namely (1) Where am I ? (2) Where am I going ? (3) How do I get there ?. The latter two questions are generally dealt with using target recognition and path planning algorithms. A prerequisite however to solving these two problems is the fundamental first question. If this is unknown, the vehicle is unable to plan its mission and its efficacy drastically reduces. To answer the question of location, the robot must first understand its surroundings (perception), and then determine its location with respect to these surroundings (localisation).

Perception-free methods of localisation are available through the use of proprioceptive sensors which only measure robot specific states and do not use any environmental information to determine their location. GPS or the more sophisticated DGPS systems use satellite triangulation methods to determine the location with respect to a global reference measure (longitude and latitude), however using such a stand-alone system makes the AGV prone to complete loss of localisation information due to signal outages. These are common in areas with dense tree coverage or tall buildings which interfere with the signals. On board Inertial Measurement Units (IMU) containing accelerometers and gyroscopes which examine the kinematic states of the robot can also used, but suffer from unbounded error accumulation over time. This error can only be bounded by using *absolute* information instead of incremental estimates that are returned by such systems.

While this absolute information may be available from *a priori* built maps, using such data is not the preferred approach adopted by the autonomous navigation community. Previously constructed maps can be erroneous, may be out of date and the environment may have changed, and would not be as accurate as maps built online by the platform itself at the time of deployment. Consequently, the research field of constructing a spatial representation of an environment (a map) using exteroceptive measurements from a known vehicle trajectory, due to the challenges of interpreting sensor data, has become known as Robotic Mapping (RM) [3]. However, as the vehicle trajectory is inherently unknown due to the previously mentioned unbounded errors researchers quickly sought to jointly solve both problems, eliminating the need for prior information and making the platforms' localisation and map building capability truly autonomous. As the construction of a map and the (tri-angulation based) localisation of the vehicle are co-dependant, online map building and active localisation *must* be jointly considered - a field generally referred to as SLAM (simultaneous localization and mapping) or CML (concurrent mapping and localization) [4]. Both the RM, and SLAM problems are studied in this thesis.

Due to the inherent uncertainty in the measurement process, probabilistic RM and SLAM approaches (the focus of this work) have gained the most popularity in recent years due to their ability to mathematically model and statistically propagate estimates subject to such uncertainty. Recursive estimation formulations are generally required to realize an online autonomous solution. The autonomous mapping and localisation system therefore constitutes a recursive filtering problem to propagate the joint estimates of the vehicle and the map (SLAM), or just the map (RM). The following section highlights the challenges associated with incorporating exteroceptive measurements into the stochastic framework.

1.1.1 Exteroceptive Sensing

Autonomous navigation is widely researched in a diverse range of environments, be it indoors [5], a general outdoor scene [6], in mines [7], and in the underwater [8] or even the planetary domains [9]. A given environment can contain a vast array of environmental landmarks (everyday physical objects), as well as requiring the deployment of various active and passive sensing methods operating at different ranges within the electromagnetic spectrum. As mentioned in the previous section, in order to obtain a truly autonomous system, *absolute* information from the surrounding environment, needs to be incorporated into the estimation theoretic algorithm. Such information however, is subject to numerous sources of uncertainty.

Figures 1.1 and 1.2, for example, show two sets of measurements of a typical roadside scene from a camera, laser, and frequency modulated continuous wave millimeter

wave radar (FMCW MMWR), which operate at three different electromagnetic frequencies. Raw laser measurement are projected into the camera image plane and plotted as yellow dots, while the same measurements are projected into the radar measurement plane and plotted as black dots. Figure 1.2, highlights one common source of sensor uncertainty - a missed detection - by the laser sensor, while reflections from the grass (difficult to use for localisation purposes) are evident in the radar data. Note the differing environmental representations and measurements reported by each sensor. The passive camera sensor interprets the scene through optical waves impinging on photodiodes, whose raw measurements are difficult to statistically quantify (in terms of landmark/non-landmark). The laser raw measurements comprise the relative range and bearing to hypothesised landmarks whereas the imaging MMWR sensor's raw measurements consist of reflected signal intensities at discrete relative range and bearing intervals. The magnitude of the reflected signal intensity is represented by a blue-red colour scale in the radar measurement plane.

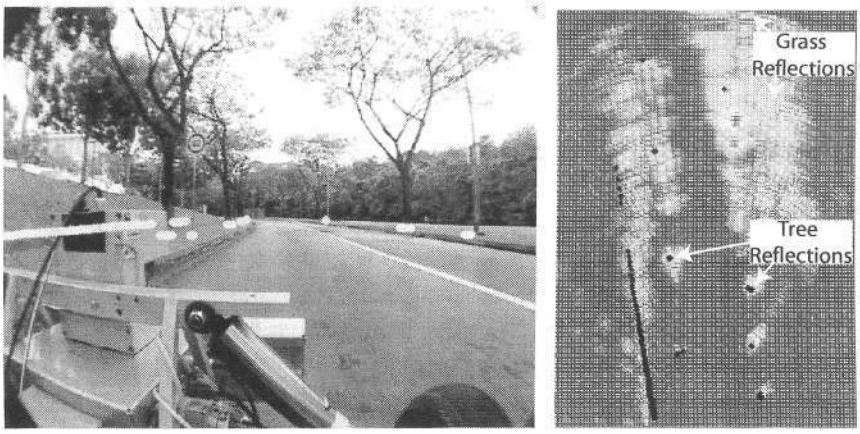

Figure 1.1: *An example of an outdoor roadside scene as captured from a monocular camera, laser and radar sensor. Yellow and black dots depict laser raw measurements, while the radar raw signal power measurements are represented in magnitude by the blue-red color scale.*

Due to the inherent randomness in any process, these raw sensor measurements are subject to measurement noise, be it in range and/or bearing readings or in the reflected intensities for the radar and camera sensors. The reported measurements may also be subject to, the less widely considered, internal and unknown sensor biasses which can corrupt the accuracy reported in the raw measurements[1]. Over successive frames, uncertainty also may be introduced (due to sensor noise or platform location

[1]This thesis does not address the sensor bias uncertainty. See [10] and [11] for excellent work related to this issue.

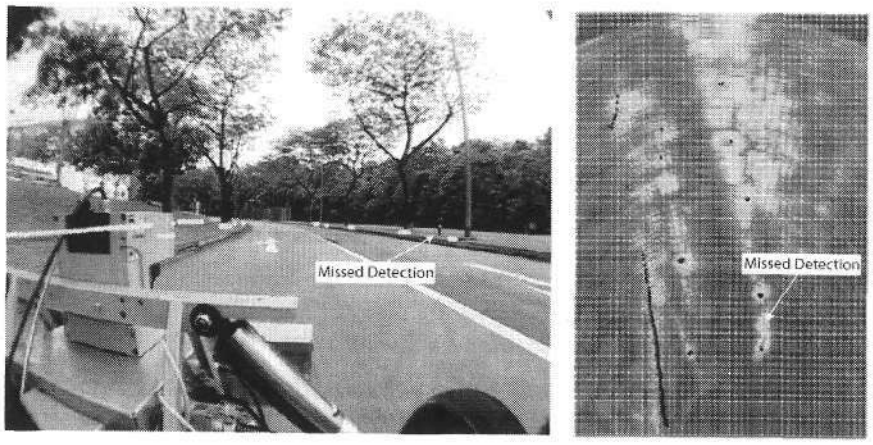

Figure 1.2: *An example of an outdoor roadside scene as captured from a monocular camera, laser and radar sensors, showing a missed landmark detection by the laser sensor.*

uncertainty) as to which landmark generated which measurement. This is commonly referred to as data association uncertainty [12], [13], [14]. Note that the raw measurements reported by the laser are in fact the output reported from an internal landmark detection algorithm, hypothesising the presence or absence of environmental objects in the noisy reflected laser beam. Due to the large dimensionality of the raw measurements from the camera and radar sensors, and resulting tractability problems in processing them, landmark detection [15], [16] and/or feature extraction methods [17], [18], [19], are typically adopted to condense the data for use in an autonomous navigation filter. Consequently, the total uncertainty associated with the measurement is expanded to include detection (or feature extraction) uncertainty, as in figure 1.2, as well as spurious measurements. Collectively, in this thesis, all these sources of 'randomness' are referred to as measurement uncertainty.

Such uncertainties have long been acknowledged by the autonomous navigation community, and numerous stochastic algorithms have been proposed over the years. Approaches generally stem from the two popular and widely used Bayesian frameworks for dealing with sensor uncertainty, the grid-based (GB) [20] and feature-based (FB) [21] metric spatial environmental representations. These well established frameworks were developed to handle and propagate the uncertain exteroceptive measurement information.

This thesis, however, exposes a subtle lack of proper treatment of sensor uncertainty in both frameworks. In GBRM approaches, state independent measurements compromise the accuracy of the resulting state estimation process and disregard explicit treatment of the detection uncertainty and spurious measurements. The

Bayesian FBRM and FB-SLAM frameworks for instance, only consider the measurement noise in the filter recursion, and thus require separate (from the filter recursion) data association and feature management methods to deal with the remaining sources of measurement uncertainty. Such approaches fail to encapsulate the entire uncertainty in the Bayesian filter recursion and consequently may compromise the Bayesian optimality of proposed FB solutions.

1.2 Objectives

Standard exteroceptive sensor measurements are subject to various uncertainties including measurement noise (in range and/or bearing), spurious measurements, detection and data association uncertainties as well as biasses. The widely adopted grid-based and feature-based frameworks address such problems in distinctly differing ways, and frequently adopt well established measurement likelihoods for the resulting estimation theoretic algorithms. The objective of this thesis is to investigate and analyze the applicability of these likelihoods to the given estimation state space, with the aim of highlighting the precise treatment of sensor uncertainty in each approach. By analysing the statistical nature of the measurement process, as well as scrutinising the methods of measurement interpretation, new insights can be obtained as to the structure of these estimation frameworks. Subtle theoretical oversights are exposed for the first time and as a result new rigorous formulations are derived. Consequently, by addressing the uncertainties under the newly proposed theoretically accurate frameworks, it is expected to improve the integrity and quality of autonomous navigation filters especially in outdoor cluttered and unstructured environments.

1.3 Contributions

The key contributions of the thesis can be summarized as:

- ✓ Analysis of the landmark detection problem for imaging range sensors in an autonomous navigation framework. The introduction of stochastically founded adaptive detectors and their applicability to autonomous navigation, whose efficacy is shown through statistical analysis in an outdoor environment.

- ✓ Highlighting the pitfalls of the standard measurement likelihood for the classical grid based robotic mapping problem. A re-formulation is then provided using state-dependent detection likelihoods as opposed to state-independent range likelihoods. The new discrete formulation provides a theoretically correct calculation of the occupancy random variable. Evidential and probabilistic discrete

filters are compared. A continuous joint filter is also proposed and implemented to deal with *a priori* unknown detection likelihoods.

- ✓ Development of *set-based* theoretic solutions to the feature-based robotic mapping problem, due to recognition of subtle oversights in the standard and widely adopted measurement equation. The new approach jointly considers the entire measurement uncertainty into the Bayesian filter recursion in an optimal manner.

- ✓ An optimal probabilistic set-based formulation for the feature based SLAM problem, with implementations provided. The new formulation inherits the attributes from the feature based mapping algorithm, while jointly incorporating an unknown vehicle trajectory.

1.4 Organisation

This chapter has outlined the motivations and objectives of this thesis, briefly highlighting the limitations of previous approaches and introducing the main contributions of this work. The rest of the thesis is organised as follows:

Chapter 2 describes and reviews the state of the art grid and feature based robotic mapping algorithms. Classical feature based SLAM approaches in outdoor environments are also detailed with emphasis placed on the oversights of the well-established measurement models and likelihoods adopted for both estimation theoretic frameworks.

Chapter 3 highlights the importance of the less well studied landmark detection hypothesis problem in autonomous navigation. Mainly applicable to imaging range sensors, the chapter discusses previous methods of landmark detection and introduced the adaptive stochastic constant false alarm rate detector (CFAR) for use in mobile robotics for the first time. The advantages of statistically founded detection algorithms are discussed, as is the theoretical significance of their interpretation, emphasising the diversity of measurements available apart from the standard range-bearing pair. Furthermore, the probabilistic significance of vector and set based measurements is presented, recognising for the first time that grid based frameworks use vector-based measurements whereas those for feature based frameworks are set-based. Experimental verification and statistical detection analysis is provided to show the efficacy of the CFAR detectors in real outdoor environments.

Chapter 4 examines the grid based mapping theoretic approach in detail, where the posterior of interest is the probability of occupancy at the discrete location indicated by an element (cell) in the map state vector. The chapter introduces subtle pitfalls in the standard measurement likelihood which is widely adopted by such

frameworks and proposes a more theoretically accurate discrete filtering framework. The significance of the re-formulation is the unification of the landmark detection and grid based mapping problems. This is as a result of highly non-linear state-dependant measurements of the occupancy state being derived from examination of the statistical signal processing that occurs in active exteroceptive sensors, specifically in this work, the FMCW MMWR. Furthermore, recognising that the required likelihoods of the new formulation are *a priori* unknown, a continuous version of the classically discrete grid based framework is introduced in which the likelihoods and occupancy random variables are jointly estimated. Using a particle approximation, implementations of the proposed filter are demonstrated using real radar data in various outdoor environments. The results show improvements in mapping capabilities in the presence of various landmark types (and detection probabilities) as is common to outdoor scenes.

Chapter 5 analyses the autonomous feature based mapping and navigation framework. Following the theme of the previous chapter, the commonly used measurement likelihood is again analysed and oversights are presented. The classical vector-based measurement likelihood is shown to inadequately deal with realistic outdoor sensing uncertainties such as missed detections, spurious measurements, varying feature numbers and data association uncertainty. These oversights consequently compromise the Bayes optimality of the estimated posterior and it is argued that previous solutions fail to encapsulate the entire uncertainty present. To this end, the feature based mapping problem is firstly re-formulated from a *set estimation* theoretic perspective. The new formulation incorporates the system uncertainty directly into the filter recursion, thus alleviating the needs for the independent (from the filter recursion) algorithms for feature management and data association that are adopted in previous approaches. Experimental verification proves the efficacy of the proposed mapping filter. The framework is then extended to the full Bayesian SLAM problem, where joint vehicle-map set based states are propagated to estimate the joint density. Thus, for the first time, an alternative set-based formulation of the SLAM problem is provided with Gaussian mixture and sequential monte carlo implementations tested on simulated and real data. The new formulation provides a theoretically optimal framework which allows for robust performance in high clutter environments.

Chapter 6 summarises and concludes the work presented in the thesis and provides directions for interesting further study.

Chapter 2

Related Work

An autonomous navigation system is assumed to consist of a mobile platform which receives command inputs to its motion controller and whose goal is to maneuver through a given environment whilst performing some useful task. A suite of on-board sensors are assumed available to the platform, consisting of both proprioceptive and exteroceptive units. Process models are used in conjunction with the proprioceptive measurements to generate an initial prediction of the vehicle's location. Exteroceptive measurements are then incorporated to reduce and place bounds on the location estimation error accuracy, whilst simultaneously creating a map of the working environment.

Such an autonomous system is subject to multiple sources of uncertainty. Errors in the vehicle process model as well as noise in both the motion controller inputs and proprioceptive measurements lead to an incremental localisation error. The exteroceptive measurements are subject to landmark detection or feature extraction uncertainty, spurious measurements, data association uncertainty as well as measurement (typically range-bearing) measurement noise. Furthermore, these errors are correlated due to the dependance between the map and localisation estimates.

To contend with the multiple sources of uncertainty, a multitude of probabilistic and non-probabilistic approaches have been proposed. Many researchers cast the problem into non-probabilistic theoretics such as Genetic Algorithms (GA) or Kinematic Link problems. D.F. Dong [22] and M. Begum [23] approach the problem from a GA perspective, with a kinematic approach being presented by J. Porta [24]. However, following the seminal paper by Smith, Self, and Cheeseman [21] which cast the autonomous navigation problem into the probabilistic domain of a joint Kalman filtering framework, stochastic approaches gained popularity. Probabilistic robotics has emerged as the most widely used framework as it statistically integrates both the imperfect process models and measurement models through well-established probabilistic laws.

As probabilistic approaches are also the focus of this thesis, in this chapter, the

classical probabilistic formulations of the problems under study are first outlined. A review of the most significant commonly adopted solutions is then presented, highlighting the pitfalls which are addressed in this thesis.

2.1 Bayesian SLAM - The Joint Problem

The vast majority of autonomous navigation algorithms developed recently are derived from approximations to the classical Bayesian SLAM recursion. The work in this thesis also focusses on Bayesian probabilistic solutions, therefore its derivation is briefly outlined here.

The SLAM scenario is a vehicle moving through an environment represented by an unknown number of landmarks[1]. At each time step, k, the vehicle is assumed to have received the noisy control inputs, u_{k-1}, to drive it to its next way point. Let the history of all vehicle control inputs, up to and including the input at time k–1, be denoted[2] $u^{k-1} = [u_0, \ldots, u_{k-1}]$. The vehicle state, X, is confined to exist on the state space $X \in \mathbb{R}^{\mathfrak{n}_X}$, where $\mathfrak{n}_X$ is the dimensionality of X. This is generally a three dimensional state consisting of an (x, y) Cartesian pair indicating the vehicles location on a global metric frame and the vehicle heading, α. The vehicle trajectory at time k is denoted, $X^k = [X_0, \ldots, X_k]$. The vehicle also receives a measurement at time k, Z_k, of the (assumed static) environment, denoted M, using exteroceptive measuring sensors located on the vehicle. The individual elements of Z_k are confined to exist on the state space $z \in \mathbb{R}^{\mathfrak{n}_m}$, with $\mathfrak{n}_m$ being the dimensionality of a map state. Also, let the vector $Z^k = [Z_0, \ldots, Z_k]$ denotes the history of all measurements, up to and including the measurement at time k. Note, that the formulation here is present for the general case of a map, M, and (assumed) state related measurement, Z. Later sections outline the mathematical structure and theoretical significance of the popular feature and grid map representations, as well as the associated measurements.

The SLAM problem requires a robot to begin in a known location, X_0, in an unknown environment, M, and use its suite of onboard sensors to both construct a map and localize itself within that map without the use of any *a priori* information. Thus the problem is to estimate robot pose, X, and the map, M. For a real world application, this should be performed online and incrementally as the robot maneuvers about the environment. Due to vehicle motion and a limited sensor field of view, at any given time, only a subset of the entire map, M, will be visible to the mobile vehicle. Therefore, let $M_k \subseteq M$, represent the portions of the map which has been observed, at least once, by the onboard exteroceptive sensor. Depending on the vehicle

[1]Terminology: A 'landmark' refers to any physical object in the given environment.

[2]Notation: '[ ]' denotes a vector, i.e. known number of elements (in this case, k) whose order is rigid and significant (indicating the order of sequential control inputs).

trajectory, it may therefore not be possible to determine an estimate of the entire map as $M_k \subset M$. As the robot motion introduces error, coupled with a landmark sensing error, both localisation and mapping must be performed simultaneously [4].

Probabilistic approaches model the system by a joint probability density function (pdf) on both the map and the vehicle location. Therefore at each time step k, the joint pdf (assuming that such a density exists) can be written as,

$$p_{k|k}(X_k, M_k|Z^k, u^{k-1}, X_0). \tag{2.1}$$

which, from an optimal Bayesian perspective, captures all relevant statistical information about the vehicle state and the map (which has been observed over the vehicle trajectoryX^k). Recursive probabilistic solutions generally take on a predictor/corrector form where the control inputs are used to predict the joint state, $p_{k|k-1}(X_k, M_k|Z^{k-1}, u^{k-1}, X_0)$, whilst the observations are used to provide some correction to the predicted state to get the posterior of (2.1). Using the total probability theorem and the Chapman-Kolmogorov equation, the predicted density (or time update) can be written as,

$$\begin{aligned} p_{k|k-1}(X_k, M_k|Z^{k-1}, u^{k-1}, X_0) &= \int p_{k|k-1}(X_k, X_{k-1}, M_k|Z^{k-1}, u^{k-1}, X_0)dX_{k-1} \\ &= \int p_{k|k-1}(X_k|X_{k-1}, M_k, Z^{k-1}, u^{k-1}, X_0) \\ &\quad \times p_{k-1|k-1}(X_{k-1}, M_{k-1}|Z^{k-1}, u^{k-2}, X_0)dX_{k-1}. \end{aligned}$$

Since the vehicle motion is independent from the observations, the map is assumed time-invariant, and vehicle inputs are temporally independent, the predicted joint density can be written as,

$$\begin{aligned} &p_{k|k-1}(X_k, M_k|Z^{k-1}, u^{k-1}, X_0) = \\ &\qquad \int p_{k|k-1}(X_k|X_{k-1}, u_{k-1})p_{k-1|k-1}(X_{k-1}, M_{k-1}|Z^{k-1}; u^{k-2}, X_0)dX_{k-1}. \end{aligned} \tag{2.2}$$

Eqn.(2.2) consists of the joint vehicle and map posterior density at time k–1, and the transition density, $p_{k|k-1}(X_k|X_{k-1}, u_{k-1})$ describing the predicted vehicle location given the control inputs at time k–1. The latter is assumed to obey a first-order Markov process, thus the predicted vehicle state at time k, depends solely on the previous state X_{k-1} and the input u_{k-1}. According to Bayes rule, the corrector (or

measurement update) is then written as,

$$p_{k|k}(X_k, M_k|Z^k, u^{k-1}, X_0) = \frac{g(Z_k|M_k, X_k)p_{k|k-1}(X_k, M_k|Z^{k-1}, u^{k-1}, X_0)}{\int g(Z_k|M_k, X_k)p_{k|k-1}(X_k, M_k|Z^{k-1}, u^{k-1}, X_0)dX_k dM_k} \quad (2.3)$$

where $g(Z_k|M_k, X_k)$ is the measurement likelihood function, i.e. given a state X_k and M_k at time k, the probability density of receiving the observation Z_k is given by $g(Z_k|M_k, X_k)$. Since the posterior joint density at time k, is a function of the measurement, Z_k, the vehicle control input, u_{k-1} and the previous joint density $p_{k-1|k-1}(X_{k-1}, M_{k-1}|Z^{k-1}, u^{k-2}, X_0)$ a recursive probabilistic framework for solving the SLAM problem has been established. This formulation assumes a single mobile vehicle and a single exteroceptive measurement sensor. As the SLAM problem requires the estimation of both the vehicle state and the map state. The following therefore discusses popular methods of modeling these states.

2.1.1 Vehicle State Representation

Representing the vehicle state, (X_k in the pdf of (2.1)), is relatively straight forward as most SLAM algorithms proposed in the literature are formulated for a single autonomous platform, which can maneuver around a continuous state space (the map) in response to its control inputs. The numbers of degrees-of-freedom (DOF) of the vehicle state thus depends on the dimensionality of an individual map element, $\mathfrak{n}_m$ (with $dim(M)$ representing the arbitrarily large dimensionality of the space represented by the map), as this defines the space about which the vehicle can maneuver. Generally,

$$\mathfrak{n}_X = 3 \text{ if } \mathfrak{n}_m = 2$$
$$\mathfrak{n}_X = 6 \text{ if } \mathfrak{n}_m = 3.$$

The majority of SLAM algorithms adopt a 3 DOF vehicle state which contains a Cartesian (x, y) pair with a heading angle α. This is due to most literature on SLAM assuming a planar, $\mathfrak{n}_m = 2$, navigation environment [4], [25], [26], [20], [27], [28], [13], [29], [3]. This is a common assumption for both indoor and outdoor landed autonomous vehicles.

However, for some applications such as airborne [30] or underwater autonomous vehicles [8], extensions to 6 DOF are necessary where the planar navigation environment assumption is no longer valid. Some researches have also examined 6 DOF algorithms for land vehicles [31] with the aim of constructing 3D maps whist maintaining accurate estimates of the vehicles 6 dimensional position. In this thesis, the

planar navigation case, $\mathfrak{n}_X = 3$, is assumed.

2.1.2 Map Representation

As the SLAM problem involves the estimation of the map state, (M_k in the pdf of (2.1)), a brief overview of the popular methods of modeling the map is given in this section. The map is assumed to consist of landmarks which can take on any physical form and comprise everyday objects that can be seen in any given environment. Furthermore, these landmarks are assumed static [4].

To handle the inherent difficulties in solving the map building problem due to sensor uncertainty, as well as possible vehicle location estimation error, two major probabilistic metric spatial map representations are commonly adopted in the autonomous navigation community. In a practical application, for a planar autonomous navigation application ($\mathfrak{n}_m = 2$) the mapping state space is regarded as a continuous region in which landmarks are free to exist anywhere with an *a priori* uniform probability.

2.1.2.1 Grid Based (GB) Maps

As the name implies, a grid-based map partitions the naturally continuous mapping state space into a grid of $\mathfrak{q}$ discrete cells at pre-defined Cartesian co-ordinates $m_{(x,y)}$ with reference to a global co-ordinate system [20], [32], [33], [34], [35], [36], [37], [38], [39], [40]. Each cell, $m_{(x,y)}$, contains a further dimension, commonly referred to as an 'occupancy', implying that even with a planar navigation plane, the dimensionality of a grid-based map state is in fact 3. The occupancy state is a binary random variable where,

$m_{(x,y)} = 0$, denotes complete certainty of no landmark occupying the cell at (x, y)
$m_{(x,y)} = 1$, denotes complete certainty of a landmark occupying the cell at (x, y)

and conversely, since the inverse, $\bar{m}_{(x,y)} = 1 - m_{(x,y)}$,

$\bar{m}_{(x,y)} = 0$, denotes complete certainty of a landmark occupying the cell at (x, y)
$\bar{m}_{(x,y)} = 1$, denotes complete certainty of no landmark occupying the cell at (x, y).

An example of an outdoor scene represented by a GB map can be seen in figure 2.1. A vehicle centric view in figure 2.2(a) shows the typical landmarks in this environment. Landmarks such as trees, lamp posts and fire hydrants, and embankments are all represented in the grid map as they all represent landmarks intersecting the assumed sensor's plane of navigation.

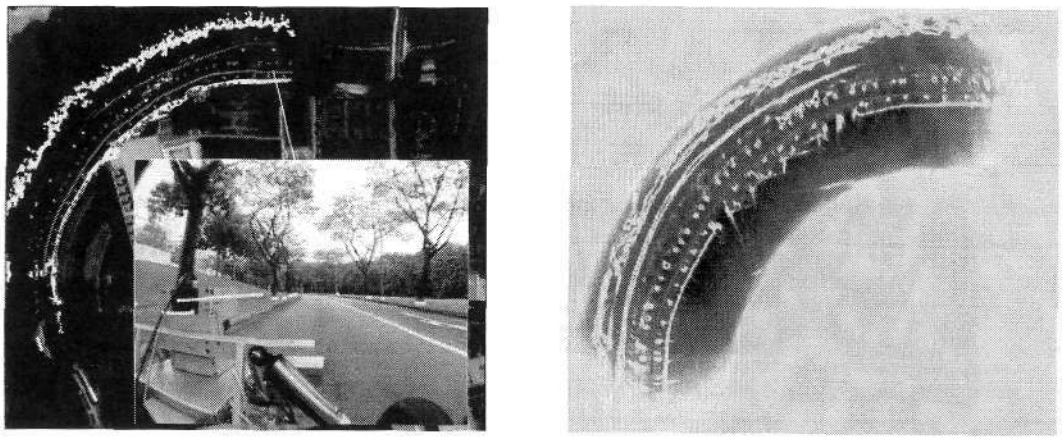

(a) Overview of Testing ground (b) Example of a grid map representation

Figure 2.1: Example of a grid-based map

For every cell, $m_{(x,y)}$ in the map M_k, that is scanned by the sensor, an estimate of the occupancy random variable is made. Successive fusion of sensor data can lead to a very informative map representations, however at the cost of increased memory requirements. Therefore, a GB map, $M = [m^1_{(x,y)}, \ldots, m^{\mathtt{q}}_{(x,y)}]$, is assumed to be comprised of $\mathtt{q}$ discrete cells each containing a value indicating the probability of occupancy by a landmark at the discrete location $m_{(x,y)}$ in the mapping space. Since discretisation is an *a priori* task, the total number of map elements (cells), $\mathtt{q}$, is a known constant. At any given time however, the observed map, M_k, will comprise $q \leq \mathtt{q}$ cells, $M_k = [m^1_{(x,y)}, \ldots, m^q_{(x,y)}]$, containing posterior occupancy estimates as a result of registering a sensor measurement. For the cells, $\overline{M_k \cap M}$, occupancy estimates are typically left at their *a priori* assumed value. Estimating a GB map, therefore involves estimating the occupancy random variable for each of the (known) q discrete cells from which sensor measurements have been received.

2.1.2.2 Feature Based (FB) Maps

Due to the vast diversity of landmarks which may appear in a vehicle's working environment, simplified representations of landmarks are commonly employed in SLAM algorithms. For instance, a tree may be parameterised by a single point [6], whereas a wall maybe represented by an Euler angle and a perpendicular distance [12]. Such simplified landmark representations are referred to as a features, with FB maps naturally referring to maps represented by a collection of features. An example of the same outdoor scene of figure 2.1, but represented by an FB map can be seen in figure 2.2. Here, a point feature model [6] is used to represent cylindrical landmarks such

as the trees, lamp posts and hydrants. Note that the embankment on the left of the figure 2.2(a) is a physical landmark in the environment, however as a consequence of its failure to fit the point feature model, it is not represented in the FB map of figure 2.2(b).

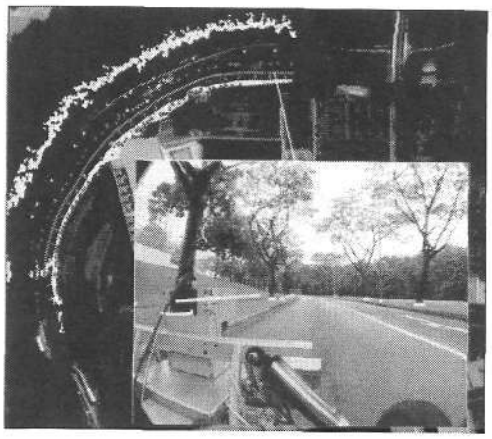

(a) Overview of Testing ground

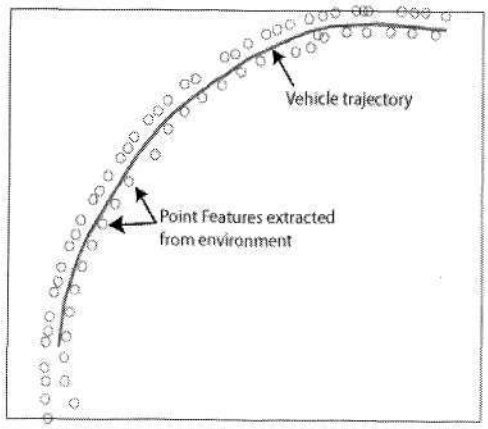

(b) Example of a feature map representation

Figure 2.2: Example of a feature-based map

FB maps are widely employed in the SLAM literature [28], [13], [30], [18], [26], [41], [5], [42], [12], [14], [43], [44]. Therefore, a feature-based map[3], $M = \{m_1, \ldots, m_{\mathfrak{q}}\}$, is assumed to be comprised of an unknown number of $\mathfrak{q}$ features[4] with $m_1, \ldots, m_{\mathfrak{q}}$ denoting their locations in $\mathbb{R}^2$ for planar maps. In a similar manner to the previous GB approach, let $M_k = \{m_1, \ldots, m_q\}$ denote the estimates of the (unknown) q features already observed, where $q \leq \mathfrak{q}$. Estimating a feature-based map, therefore involves estimating both the number of observed features, q, in M_k, and their corresponding locations.

2.2 Mapping Only Problems

The full SLAM recursion of eqn.(2.3) propagates the joint density on the vehicle state and map. Whilst not optimal in an autonomous navigation sense, much work has focussed on the individual problems, namely the problem of localisation, and that of mapping. These approaches propagate a density on either the vehicle state or the map, assuming the other to be known. In probabilistic approaches, which dominate

[3]Notation: '{ }' denotes a set, i.e. unknown number of elements whose order is insignificant.

[4]The symbol $\mathfrak{q}$ thus represents the number of 'elements' in the map. In the case of a GB map, its the number of cells, and in an FB map, it denotes the number of features.

current autonomous mapping and localisation research [3], the Bayesian formulations outlined here again form the basis for almost all proposed solutions.

2.2.1 Probabilistic Robotic Mapping

While some literature confuses probabilistic robotic mapping (RM), with the full SLAM problem [3], [45], in this work, probabilistic robotic mapping refers to stochastic methods of estimating the posterior density on the map (either FB or GB), when at each time instance, the vehicle trajectory, X^k, is assumed *a priori* known. The posterior density for the RM problem is therefore,

$$p_{k|k}(M_k|Z^k, X^k). \tag{2.4}$$

This posterior encapsulates all relevant statistical information of the map M_k. Measurements registered by the onboard exteroceptive sensor can be incorporated through the Bayesian update,

$$p_{k|k}(M_k|Z^k, X^k) = \frac{g(Z_k|M_k, X_k)p_{k|k-1}(M_k|Z^{k-1}, X_k)}{\int g(Z_k|M_k, X_k)p_{k|k-1}(M_k|Z^{k-1}, X_k)dM_k}. \tag{2.5}$$

Since a static map is commonly assumed [36],

$$p_{k|k-1}(M_k|Z^{k-1}, X_k) = p_{k-1|k-1}(M_{k-1}|Z^{k-1}, X^{k-1}) \tag{2.6}$$

that is, the time update density in the Bayes recursion is simply the posterior density at time $k-1$. Note that in general, a static map assumption does not necessarily imply that eqn.(2.6) is valid. This is due to occlusions which may result in corrupted segments of M_k, which consequently cannot be observed by the sensor, nor represented by the likelihood $g(Z_k|M_k, X_k)$. To model this added uncertainty, an extended formulation is required with vehicle state dependant Markov Transition matrices, or state dependant detection probabilities incorporated into the measurement likelihood. Although not explicitly formulated in this manner, this observation was considered in the seminal scan-matching paper of Lu and Milios [46].

2.3 Popular Robotic Mapping Solutions

This section focusses on popular solutions to the problems associated with autonomous navigation which are examined in this thesis.

2.3.1 GB Robotic Mapping

Since a grid map representation was first proposed in the seminal work performed by Moravec and Elfes [37], GBRM has been widely used and researched in the autonomous navigation community. The framework primarily address sensor detection uncertainty and spurious measurements, and does not explicitly deal with measurement noise. Data association uncertainty is typically approached using correlation based methods. As described previously in section 2.1.2.1, the map M_k is comprised of q cells, each indicating a probability of occupancy by a landmark at discrete locations in the mapping space. Since a trivial time update is typically employed [20], of critical importance to GB robotic mapping, is the form of the measurement likelihood, $g(Z_k|M_k, X_k)$, in eqn.(2.4). This is the likelihood of receiving a measurement, Z_k, given the grid map, M_k, and vehicle state, X_k.

The original formulation discussed in [32], [20], [47] assumed a zero order Markov random field model for the grid map, $M = [m^1_{(x,y)}, \ldots, m^{\mathfrak{q}}_{(x,y)}]$. Thus instead of jointly solving the full posterior over the entire map, $p_{k|k}(M|Z^k, X^k)$, the problem could be decomposed into $\mathfrak{q}$ independent filtering problems for each individual cell i.e.,

$$p_{k|k}(M|Z^k, X_k) = \prod_{i=1}^{i=\mathfrak{q}} p_{k|k}(m^i_{(x,y)}|Z^k, X^k).$$

which consequently implies,

$$p_{k|k}(M_k|Z^k, X_k) = \prod_{i=1}^{i=q} p_{k|k}(m^i_{(x,y)}|Z^k, X^k).$$

Furthermore, the recursion of eqn.(5.1) was written in the form of a likelihood ratio [47] of the density that the cell, $m^i_{(x,y)}$ is occupied by a landmark, or that it is empty, $\bar{m}^i_{(x,y)}$,

$$\frac{p_{k|k}(m^i_{(x,y)}|Z^k, X_k)}{p_{k|k}(\bar{m}^i_{(x,y)}|Z^k, X_k)} = \frac{p(m^i_{(x,y)}|Z_k, X_k)}{p(\bar{m}^i_{(x,y)}|Z_k, X_k)} \frac{p(\bar{m}^i_{(x,y)})}{p(m^i_{(x,y)})} \frac{p_{k-1|k-1}(m^i_{(x,y)}|Z^{k-1}, X_{k-1})}{p_{k-1|k-1}(\bar{m}^i_{(x,y)}|Z^{k-1}, X_{k-1})}. \quad (2.7)$$

Note that in this recursive formulation, the measurement likelihood, $g(Z_k|M_k, X_k)$ is obtained through Bayes rule, requiring the density on the map cell, $m^i_{(x,y)}$, given the measurement and vehicle location, $p(m^i_{(x,y)}|Z^k, X_k)$, to be known. The prior density on the occupancy random variable of a given cell is denoted $p(m^i_{(x,y)})$. From a theoretical perspective, the model, $p(m^i_{(x,y)}|Z^k, X_k)$, is directly inferring an estimate on the map, given the measurement and is contrary to the general form of the optimal

Bayesian recursion of eqn.(5.1). Furthermore, a deterministic measurement of the occupancy random variable is assumed which allows for the posterior likelihood ratio to be written in Odds form[5],

$$\frac{P_{k|k}(m^i_{(x,y)}|Z^k, X_k)}{P_{k|k}(\bar{m}^i_{(x,y)}|Z^k, X_k)} = \frac{P(m^i_{(x,y)}|Z_k, X_k)}{P(\bar{m}^i_{(x,y)}|Z_k, X_k)} \frac{P(\bar{m}^i_{(x,y)})}{P(m^i_{(x,y)})} \frac{P_{k-1|k-1}(m^i_{(x,y)}|Z^{k-1}, X_{k-1})}{P_{k-1|k-1}(\bar{m}^i_{(x,y)}|Z^{k-1}, X_{k-1})}. \quad (2.8)$$

or adopting the Odds notation (O),

$$O_{k|k}(m^i_{(x,y)}|Z^k, X_k) = O(m^i_{(x,y)}|Z_k, X_k) O_{k-1|k-1}(m^i_{(x,y)}|Z^{k-1}, X_{k-1}) O(m^i_{(x,y)})^{-1}. \quad (2.9)$$

Determining the probabilities, $P(m^i_{(x,y)}|Z_k, x_k)$, require extensive off-line prior training in the specific environment of deployment, thus making it unsuitable for general outdoor navigation applications. Furthermore, the lack of a statistical measurement likelihood, compromises the optimality of the result. Similar inferences from the sensor are made for evidential approaches, where a measurement likelihood is also not used. Whilst lacking statistical mathematical models and rules, such approaches produce some impressive results [38], [48].

In the work of Thrun, [39], the GBRM problem was approached from an optimisation perspective as opposed to a filtering and state estimation one. The pitfalls of modeling the sensor by the deterministic probability, $P(m^i_{(x,y)}|Z_k, X_k)$, were highlighted, namely potential conflicting inferences on a cell causing inconsistent maps. A discrete (with respect to the occupancy random variable) measurement likelihood, $G(Z_k|M, X_k)$ is established and an EM algorithm used to find the map, M, which maximizes the likelihood over all measurements, Z^k and known vehicle trajectory, X^k. While impressive results were produced for indoor environments, the method does not well suit autonomous deployments primarily due its lack of on online recursive formulation. Off-line batch processing is used to generate the (non-unique) maximum-likelihood map for a given sequence of measurements, Z^k. Furthermore, binary maps are produced and the desired posterior in the Bayesian formulation, $p_{k|k}(M|Z^k, X^k)$, is not estimated.

The problem of GB mapping in its original recursive filtering form was examined by Konolige [36], where a log-odds formulation of eqn.(5.1) was used,

$$\log\left(O_{k|k}(m_{(x,y)}|Z^k, X_k)\right) = \log\left(O(Z^k|m_{(x,y)}, X_k)\right) + \log\left(O_{k-1|k-1}(m_{(x,y)}|Z^{k-1}, X_{k-1})\right) \quad (2.10)$$

[5]Note that $p(\cdot)$ denotes a probability density function, whereas $P(\cdot)$ denotes a discrete probability.

where the Odds is given by,

$$O_{k|k}(m_{(x,y)}|\cdot) = \frac{P_{k|k}(m_{(x,y)}|\cdot)}{P_{k|k}(\bar{m}_{(x,y)}|\cdot)}.$$

An intuitive measurement likelihood for $G(Z_k|m_{(x,y)}, X_k)$ was derived based on Gaussian profiles of the range measurement noise, whereas the converse likelihood $G(Z_k|\bar{m}_{(x,y)}, X_k)$ was modeled by a uniform constant due to an implicit assumption that there is at least one occupied cell within range. Thus the possibility of a spurious measurement, i.e. a range reading when *all* cells are empty, is not considered. A recursive log-odds mapping approach was also adopted by Foessel [33] for occupancy grid mapping with a millimeter wave radar sensor. The measurement odds was a deterministic function based on the signal to noise ratio of a reflection from a target. While intuitively appealing, the adopted model lacks theoretical and statistical justification and the results were poorly quantified.

GB mapping is also popular in the scan-based SLAM [46], [35], [40] community, where successive raw (usually laser) measurements are aligned to estimate the vehicle pose. As the maps from scan based approaches lack the formal statistical representation of their feature-based counterparts, the outlined GB mapping methods here are employed to fuse scans into a meaningful probabilistic map. Extensive mapping of indoor and semi-structured outdoor environments were presented.

In all of these approaches however, the uncertainty caused by measurement noise is not explicitly maintained (in the statistical sense), instead 2D Gaussian spread functions are used to 'smear' the occupancy posterior of a given cell, $P_{k|k}(m_{(x,y)}|\cdot)$, into neighbouring cells according to the range/bearing measurement noise magnitude. Furthermore, a discrete version of eqn.(5.1) is used to propagate estimates of the occupancy random variable. This is because the likelihood of a range measurement, corrupted by Gaussian noise, is used as the occupancy measurement. The evaluation of the cumulative distribution of the Gaussian in the cell, $m_{(x,y)}$, is then used as the likelihood of occupancy. While a range measurement can be used as a likelihood of a hypothesised landmarks location, this thesis argues that *it should not be used as a likelihood of cell occupancy.* For the first time this thesis shows that, from a theoretical perspective, only the detection statistics can infer any meaningful (and state related) measurement of the occupancy random variable. Range measurements are generally achieved by thresholding a received signal power, whose statistics can be incorporated in a theoretically concise manner, into the GB robotic mapping problem.

2.3.2 FB Robotic Mapping

While less widely researched, but no less important, FB robotic mapping addresses the FB map estimate from a robotic feature mapping algorithm. FBRM can also

include the map produced by any FB-SLAM algorithm, where both the vehicle model is assumed correct and the vehicle control input noises are zero. Even with a known vehicle trajectory, the interpretation of sensor data and consequent generation of a map estimate is far from trivial. Detection decisions or feature extraction routines [5], [17] from raw sensor measurements can be highly uncertain, resulting in frequent missed detections or numerous spurious readings. In areas of dense features, even with a known vehicle trajectory or high measurement noise, data association decisions can be challenging. Sensor biasses [11] can also have detrimental affects on the estimate feature map, even from known vehicle locations.

As highlighted previously in section 2.1.2.2, a FB map is assumed to consist of an unknown number, $\mathfrak{q}$, features. At any given time, a random number, $q \leq \mathfrak{q}$ of these features can be present within the sensors field of view, thus for an *a priori* map, q is a random number while $\mathfrak{q}$ is a fixed but unknown quantity. This is not a new observation and was acknowledged many years ago in [49]: "*...the simultaneous localisation and mapping problem,..., which phrased (the problem) as a state estimation problem involving a variable number of dimensions*".

Assuming an infinite sensor field of view, the measurement likelihood used in FB algorithms, $g(Z_k|M, X_k)$, represents the likelihood of receiving a measurement from each of the $\mathfrak{q}$ features assumed to exist in the map. That is,

$$Z_k = H(M, X_k) + \boldsymbol{w}_k \tag{2.11}$$

where $H(\cdot)$ is generally a non-linear function mapping the landmark and vehicle locations into the relative range and bearing measurement, with $\boldsymbol{w}_k$ being the additive (usually assumed Gaussian) noise component. As written in the seminal work of Smith, Self and Chessman [21], "*the sensor function is a function of all the variables in the state vector*". However, an intuitive observation immediately exposes that this equation contains no accommodation of spurious measurements, or detection and data association uncertainty, and therefore a real sensor measurement is *not* simply a function of all the variables in the state vector. The likelihood from the sensor function in eqn.(2.11) only represents the likelihood of measurements from each of the features in the map state and when used in the FB Bayes recursion of eqn.(5.1), can *only* result in the posterior, $p_{k|k}(m_1, \cdots, m_{\mathfrak{q}}|Z^k, X_k)$. It cannot jointly consider the problem of estimating the *a priori* unknown number of features, $\mathfrak{q}$. Furthermore, the standard measurement model of eqn.(2.11) assumes that all features have a unity probability of detection/extraction. Thus it is argued in this thesis, that this FB measurement model adopted by a multitude of FB mapping (and FB SLAM algorithms) [44], [43], [21], [5], [28], [50], [13], [5] fails to encapsulate all the uncertainty in a practical measuring sensor. Even though it is recognised that a FB approach has variable number of dimensions, as well as measurements being subject

to numerous sources of uncertainty, the FB representation and resulting estimation theoretic algorithms, primarily address only the sensor uncertainty as a result of measurement noise.

Due to the variable dimensionality of the FB map, it's estimation involves jointly solving for both the random number of features within the field of view at each time instant, q (and consequently the total number of features $\mathfrak{q}$), as well as their corresponding locations in a 2D Cartesian state space (in the case of planar, $\mathfrak{n}_m = 2$, mapping). Due to the subtle oversight of the measurement equation in eqn.(2.11), to estimate q, FBRM algorithms typically incorporate intuitive feature management routines which exploit the static map assumption. Extracted features are stored in a tentative list and a 'feature quality' criterion is calculated over multiple time instances. When the quality measure exceeds a pre-defined threshold, features are considered non-spurious and included in the map. If the 'quality' of a feature in the map drops below the threshold, the feature is removed from the map. Some approaches simply use the number of successful associations as the metric [13], while others evaluate a 'feature quality' density function [12], [28] or adopt discrete occupancy estimation routines from GB mapping [44]. Approaches using exponential decay functions have also been proposed [51]. These are usually performed as a post-processing step on the estimated map posterior, $p_{k|k}(M_k|Z^k, X_k)$, after a data association decision has been made [14], [12].

Separate data association algorithms are required as a direct consequence of modeling the map state, M_k, as a *vector*[6] [21], [4], [50], [26], [18], [52]. Consequently the measurement (function of the map and vehicle state) is a vector. Since the order of elements in a vector is rigid, modeling in such a manner assumes that both the measurement and state vectors are perfectly aligned, i.e. z_1 is from m_1, z_2 is from m_2, and so on, with $z \in Z_k$ and $m \in M_k$. Clearly, when a mobile platform is considered, this is not the case. Therefore, data association routines are required to solve the measurement-map relationship prior to the Bayesian map update.

While in SLAM approaches it has been long acknowledged [21], that the problems of localisation and map building must be jointly considered, no approach jointly solves the FB robotic mapping problem in its optimal Bayesian structure, i.e. the joint estimation of *the number of features* and their corresponding locations. The FB framework, in its current form, is unable to optimally deal with detection and data association uncertainty as well as spurious measurements in an optimal manner, an issue which is addressed in this thesis.

[6] Recall from section 2.1 the implications of vector modeling.

2.4 Popular Bayesian FB-SLAM Solutions

The Bayesian SLAM formulation outlined in section 2.1 forms the basis of most probabilistic autonomous navigation algorithms proposed over the passed 20 years. Direct implementations of the recursions are typically computationally intractable thus approximations are used. Gaussian and particle approximations remain the dominant methods amongst the autonomous navigation research community [4].

2.4.1 Bayesian FB-SLAM - Approximate Gaussian Solutions

This section reviews proposed Gaussian based solutions to the Bayesian FB-SLAM problem. As the optimal solution requires the joint estimation of both the vehicle pose and the map let,

$$\zeta_k = [X_k \;\; M_k]^T \tag{2.12}$$

be the *true* joint state on the vehicle and map, at time k. The most popular approximation of the recursion of eqn.(2.3) is to assume that the SLAM posterior density at time k is Gaussian distributed, $p_{k|k}(\zeta_k|Z^k, u^{k-1}, X_0) \approx \mathcal{N}\big(\zeta_k; \zeta_{k|k}, P_{k|k}\big)$, with estimated mean, $\zeta_{k|k}$ and covariance, $P_{k|k}$, given all the information up to and including time k. The observation, Z_k is modeled as in eqn.(2.11). The measurement variance, $R_k = E[w_k w_k^T]$. Assuming the joint state transition equation, $F(\cdot)$, to be a non-linear discrete time function of the control inputs corrupted by white Gaussian noise v_k, and the previous state (first order Markov),

$$\zeta_k = F(\zeta_{k-1}, u_{k-1} + v_{k-1}) \tag{2.13}$$

it can be shown that the predicted density can also be approximated by a Gaussian distribution,

$$p_{k|k-1}(\zeta_k|Z^{k-1}, u^{k-1}, X_0) \approx \mathcal{N}\big(\zeta_k; \zeta_{k|k-1}, P_{k|k-1}\big)$$

through appropriate linearisation methods, with $\zeta_{k|k-1}$ and $P_{k|k-1}$ being the predicted mean and covariance respectively. Assuming a Gaussian distributed measurement likelihood, it can be shown through algebraic methods that the first two moments of the Gaussian state can be propagated through the Bayesian recursion to produce a Gaussian distributed posterior $p_{k|k}(\zeta_k|Z^k, u^{k-1}, X_0) \approx \mathcal{N}\big(\zeta_k; \zeta_{k|k}, P_{k|k}\big)$ where,

$$\zeta_{k|k} = \zeta_{k|k-1} + K_k(Z_k - H\zeta_{k|k-1}) \tag{2.14}$$

$$P_{k|k} = [I - K_k \nabla H_{(X)}] P_{k|k-1}. \tag{2.15}$$

and $\zeta_{k|k}$, $P_{k|k}$, are the estimated mean and covariance of the true joint state ζ_k. The components required to evaluate the above are given by,

$$K_k = P_{k|k-1}\nabla H_{(X)}^T S_k^{-1} \tag{2.16}$$

$$S_k = R_k + \nabla H_{(X)} P_{k|k-1} \nabla H_{(X)}^T \tag{2.17}$$

$$P_{k|k-1} = \nabla F_{(X)} P_{k-1|k-1} \nabla F_{(X)} + \nabla F_{(u)} Q_{k-1} \nabla F_{(u)} \tag{2.18}$$

with $Q_{k-1} = E[v_{k-1} v_{k-1}^T]$ and ∇ indicating a Jacobian function. Thus, $\nabla H_{(X)}$ is the Jacobian of the measurement equation with respect to the estimated vehicle state, $\nabla F_{(X)}$ is the Jacobian of the transition equation with respect to the vehicle state and $\nabla F_{(u)}$ is its Jacobian with respect to the control inputs. These equations are those commonly found in Kalman (or Extended Kalman) filtering literature [53], [54], [55], [56].

This joint state Kalman solution to the SLAM problem, with the non-linear Gaussian measurement model, was first outlined in the seminal paper by Smith, Self and Chessman [21]. This work focussed on propagating the joint vehicle map estimate in the presence of the interfering Gaussian noise from the vehicle process model and the range-bearing exteroceptive sensor measurements. Moutarlier [57] then implemented the framework on a land robot. The SLAM solution presented in [21] can be viewed as a special case (Gaussian noise and a joint vehicle-map state) of the Bayesian FB-SLAM filter recursion, and thus one of the first proposed approximate Gaussian solutions to the Bayesian FB-SLAM problem. Under Gaussian noise assumptions, the Kalman filter produces the *optimal minimum-variance Bayesian estimate* of the joint-vehicle map state. The example discussed in [21] had a map with features of unity detection probability, assumed that the measurement-map association was known, the sensor had no biasses and there were no spurious measurements. Emphasis was on highlighting that the consistent maintenance of the correlations between the vehicle and map feature estimates was critical to the structure of the problem. With these strict assumptions on the measurement, the Kalman based SLAM estimate is indeed Bayes optimal. This structure has received much attention and convergence properties of the map estimates were analyzed by Dissanayake *et al.* [28]. First-order linearisation errors introduced in the extended Kalman framework were addressed by using higher-order Hessian functions [54] or the Unscented Kalman Filter of Julier and Uhlmann [58].

These approximate Gaussian implementations of the formulation, presented in section 2.1, assuming a FB map, inherits the very same measurement uncertainty oversights as presented in the case of the FBRM problem in section 2.3.2. Again, there is a failure to encapsulate the entire measurement uncertainty. However, researchers began to include data association and feature management routines in SLAM algorithm,

along with a conditional measurement independence assumption, with some impressive results being demonstrated with a variety of sensor types. Laser based SLAM was demonstrated by Guivant *et. al* [6], MMWR based SLAM by Clark [59], [26], Sonar based SLAM by Leonard [5] and underwater SLAM by Smith [60]. With an ideal sensor, and known landmark number, an implementation of the Bayes recursion can be individually optimal given the correct data association decision for each landmark, however this does not imply joint optimality over the whole map and vehicle estimate. Furthermore, as outlined previously in section 2.3.2, the dimensionality of the map (number of features) is not jointly considered.

In [61], [62], a Gaussian Mixture (GM) implementation of the Bayesian SLAM recursion was described. The joint posterior was assumed a Gaussian Mixture density, $p_{k|k}(\zeta_k|Z^k, u^{k-1}, X_0) \approx \sum_{i=1}^{N} w_k^{(i)} \mathcal{N}\big(\zeta_k; \zeta_{k|k}^{(i)}, P_{k|k}^{(i)}\big)$, as was the measurement likelihood, $g(Z_k|\zeta_k)$. The work emphasised the fact that explicit data association decisions were not required in the implementation as the measurement was incorporated by the convolution with the predicted density $p_{k|k-1}(\zeta_k|Z^{k-1}, u^k, X_0)$. However, this work was essentially assuming the same standard measurement model of eqn.(2.11) in that detection uncertainty and/or biasses were not considered in the formulation. Using a GM density for the measurement likelihood can only describe the uncertainty in location of a single feature. The condition of $\sum_{i=1}^{N} w_k^{(i)} = 1$ assumes that the feature lies somewhere within the measurement, Z_k, i.e. spurious detections are not considered. Furthermore, the Bayes posterior distribution $p_{k|k}(\zeta_k|Z^k, u^{k-1}, X_0)$ is not useful unless information about the state can be extracted. For the GM approach to the Bayesian FB-SLAM problem, such extraction was not clearly outlined and no error plots were produced. Furthermore, as highlighted in [63], when applied to an underwater sonar sensor [61], the measurement can contain either multiple point features, or multiple readings from the surface of the same (extended) feature. Thus the convolution with the predicted density would result in the divergence of the filter. However, the work was significant in the fact that convolution, instead of explicit data association decisions, was used to calculate the posterior density.

2.4.2 Bayesian FB-SLAM - Approximate Particle Solutions

Although never fully implemented, the Bayesian SLAM recursion of eqn.(2.3) can, in principle, be directly approximated by particle methods. In the SLAM context, each particle consists of a vehicle state and a map. Thus the particles themselves may have varying dimensions, due to the potential dimensionality differences of the map estimates.

Assume at time $k-1$, a set of weighted particles $\{w_{k-1}^{(i)}, \zeta_{k-1|k-1}^{(i)}\}_{i=1}^{N}$ representing

the posterior, $p_{k-1|k-1}(\zeta_{k-1}|Z^{k-1}, u^{k-2}, X_0)$ is available, i.e.

$$p_{k-1|k-1}(\zeta_{k-1}|Z^{k-1}, u^{k-2}, X_0) \approx \sum_{i=1}^{N} w_{k-1}^{(i)} \delta\big(\zeta_{k-1} - \zeta_{k-1|k-1}^{(i)}\big).$$

The particle filter proceeds to approximate the posterior at time k by a new set of weighted particles $\{w_k^{(i)}, \zeta_{k|k}^{(i)}\}_{i=1}^N$ as follows

---

Particle FB-SLAM Filter

At time $k \geq 1$,

Step 1: *Sampling Step*

- For $i = 1, ..., N$, sample $\widetilde{\zeta}_{k|k-1}^{(i)} \sim q(\cdot|\zeta_{k-1|k-1}^{(i)}, Z_k)$ and set

$$\widetilde{w}_k^{(i)} = \frac{g(Z_k|\widetilde{\zeta}_{k|k-1}^{(i)}) p(\widetilde{\zeta}_{k|k-1}^{(i)}|\zeta_{k-1|k-1}^{(i)}, u_{k-1})}{q(\widetilde{\zeta}_{k|k}^{(i)}|\zeta_{k-1|k-1}^{(i)}, Z_k)} w_{k-1}^{(i)}. \tag{2.19}$$

- Normalise weights: $\sum_{i=1}^N \widetilde{w}_k^{(i)} = 1$.

Step 2: *Resampling Step*

- Resample $\left\{\widetilde{w}_k^{(i)}, \widetilde{\zeta}_{k|k}^{(i)}\right\}_{i=1}^N$ to get $\left\{w_k^{(i)}, \zeta_{k|k}^{(i)}\right\}_{i=1}^N$.

The importance sampling density $q\left(\cdot|\zeta_{k-1|k-1}^{(i)}, Z_k\right)$ is a joint density of the vehicle state and the map. After the resampling step, an optional Markov Chain Monte Carlo (MCMC) step can also be applied to increase particle diversity. Since the particles belong in spaces of different dimensions (each particle represents a different map), the proposal and target densities may belong to a space of different dimensions, therefore a reversible jump MCMC step [64] may be required. Joint MAP or EAP estimates of the vehicle and map can then be obtained from the particle approximation of the posterior, $\left\{w_k^{(i)}, \zeta_{k|k}^{(i)}\right\}_{i=1}^N$.

The main practical problem with the particle FB-SLAM filter presented here is the need to perform importance sampling in very high dimensional spaces if the number of features is large. Moreover, it can be difficult to find an efficient importance density. A naive proposal density will typically lead to an algorithm whose efficiency decreases

exponentially with the number of landmarks for a fixed number of particles. Approximation of the optimal proposal, i.e. $\propto g(Z_k|\widetilde{\zeta}^{(i)}_{k|k-1})p(\widetilde{\zeta}^{(i)}_{k|k-1}|\zeta^{(i)}_{k-1|k-1}, u_{k-1})$, such as outlined in [65] can be adopted to mitigate this problem, but this requires intensive computations and is still inefficient with large number of landmarks. Also, the weight update can be expensive due to the combinatorial nature of the measurement likelihood, collectively resulting extremely expensive solution for the Bayesian FB-SLAM solution.

Despite this, insightful Rao-Blackwellisation strategies can be applied by exploiting the structure of the problem to reduce the computational cost. Such a strategy was introduced by Montemerlo [66], [44] where the posterior of (5.21) was modified to model the entire trajectory of the vehicle, X^k, as opposed just its most recent state, X_k, and factorised as,

$$p_{k|k}(\zeta^k|Z^k, u^{k-1}, X_0) = p_{k|k}(X^k|Z^k, u^{k-1}, X_0) \prod_{q=1}^{\mathfrak{q}} p_{k|k}(m_q|X^k, Z^k, u^{k-1}, X_0). \quad (2.20)$$

This allowed for the FB-SLAM problem to be decomposed into $\mathfrak{q}$ independent state estimators for each feature in the map, $m \in M$, when the vehicle trajectory, X^k, is given. A Rao-Blackwellisation strategy thus allowed for a particle approximation of the density $p_{k|k}(X^k|Z^k, u^{k-1}, X_0)$,

$$p_{k|k}(X^k|Z^k, u^{k-1}, X_0) \approx \sum_{i=1}^{N} w_k^{(i)} \delta\big(X^k - X^{k|k,(i)}\big).$$

with, $X^{k|k,(i)}$, representing a hypothesised vehicle trajectory, while independent extended (due to non-linear measurement model) Kalman filters were used to estimate each feature density, $p_{k|k}(m_q|X^{k,(i)}, Z^k, u^{k-1}, X_0)$ [67].

Again, in this widely popular FB-SLAM approach [42], [68] subtle theoretical pitfalls exist in the treatment of the exteroceptive measurement uncertainty. A similar vector-based measurement equation (2.11) is adopted which fails to encapsulate detection uncertainty and spurious measurement. The data association uncertainty is dealt with in a multi-hypotesis approach sampled vehicle trajectory, $X^{k,(i)}$, maintains its own corresponding map estimate, $M_k^{(i)}$. However, further incorporation of sub-optimal feature management methods are required and the problem of map dimensionality is not addressed in an optimal manner.

2.5 Algorithm Performance Metrics

This section reviews popular methods of evaluating a SLAM algorithm. Performance metrics are critical to any stochastic theoretic problem such as SLAM. SLAM involves the joint estimation of both the vehicle location *and* the map. Thus the results from *both* estimates must be extensively analyzed to prove the performance of any proposed solution. The review however, shows that while most proposed SLAM algorithm rigorously analyze the performance of the localisation estimate, statistical evaluation of the resulting map is less widely performed and in many cases, not performed at all.

2.5.1 Vehicle State Estimate Evaluation

For a single vehicle system (as is the case for most SLAM algorithms), estimation error metrics are well established in the tracking literature and are frequently adopted to analyze the localisation estimate of a SLAM algorithm. When available, GPS signals are commonly used as the ground truth reading for the vehicle location. For Gaussian based solutions (section 2.4.1), common vehicle estimation error metrics examine the absolute difference between the ground truth and estimated vehicle locations [6]. Estimated error covariances can also be used to check the consistency of the filter's vehicle location estimate [28] (note this gives no information of the consistency of the corresponding map estimate). In [13], the square innovation of the 3-DOF pose is used as the error metric, with the chi-square (due to the Gaussian assumption) confidence limit used to show the consistency of the location estimate. Some algorithms [69], [70] simply use visual comparison of the GPS data with the estimated path, whilst some work (assuming GPS signal is not available) visually compares the path with a satellite image [52].

For particle based solutions (section 2.4.2), the root mean square error (RMSE) of the particle representation of $p_{k|k}(X^k|Z^k, u^{k-1}, X_0)$, is evaluated at each time instant [43], [44], [42], [68]. As the particle representation models a non-Gaussian density, stochastic bounds on the estimation error are difficult to obtain. For indoor deployments where there is no GPS signal available, in some cases there is no explicit quantitative evaluation of the localisation results, [40], [35], although in other extensive analysis was performed [71].

2.5.2 Map Estimate Evaluation

While error metrics are well established in the case of the localisation estimation aspect of a SLAM algorithm, methods of map estimation are less well studied. Since the goal of a SLAM algorithm is to also estimate the map, it's estimation error is

equally as important as that of localisation. The primary difficulty with obtaining a map error estimate is obtaining the ground truth. For feature based mapping, the GPS co-ordinates of a certain number of features can be manually obtained [6], [28] whose estimation errors are examined in a similar fashion to that of the vehicle. However, since a map is inherently a joint multiple-feature state, individual feature error evaluation does not imply or evaluate the estimate of the joint state, specifically for the case of either falsely declared or missed features. Even in simulated tests, where ground truth is available, adequate map estimate quantification is rare. In [72], [68], where simulated tests are performed for FB-SLAM, the map estimate is typically evaluated through sub-optimal methods of plotting the estimated features mean location along with the ground truth. With multiple features there is no method of evaluation which jointly considers the entire map estimate in a mathematically concise manner. Other FB mapping algorithms, provide no quantification of the map estimate whatsoever, [43], [44]. Indoor SLAM experiments, generally rely on visual inspection and intuitions of a structured (walls, corners etc.) environment [34], [40] with no map (or localisation) error metric shown.

From the literature, it can therefore be seen that most research assumes that a "good" vehicle estimate, inherently implies a "good" map estimate, with no explicit evaluation of the map estimate resulting from the SLAM or RM algorithm. In the presence of large sensor discrepancy such as detection/feature extraction uncertainty, spurious measurements, biasses and data association uncertainty, this assumption overlooks a major aspect of a SLAM algorithm.

2.6 Conclusions

This chapter highlighted how exteroceptive measurement uncertainty is handled by the most popular SLAM and RM research contributions. A general formulation of the SLAM problem was shown, with the popular grid-based (GB) and feature-based (FB) methods of map representation introduced. While many seemingly successful implementations have been reported in the literature, this chapter highlighted some subtle theoretical oversights in modeling the sensor's measurement uncertainty in both frameworks.

Emphasis was initially placed on the mapping aspect of autonomous navigation algorithms which is equally as important as the localisation aspect. The structure of the estimation theoretic RM algorithms are dependant on the form of the measurement likelihood, and furthermore limit what can be represented by the resulting posterior density. These was discussed for both the GBRM and FBRM approaches. The analysis was then extended to the full Bayesian FB-SLAM problem, whose optimality was questioned as a result of the subtle assumptions in the standard measurement equations. It was shown that general filtering approaches do not encapsulate the entire

uncertainty directly into the filter recursion, thus compromising filter performance.

Evaluation of (specifically feature-based) map estimates are also not very well addressed in most SLAM algorithms. As the algorithm jointly considers the map estimate and the vehicle location estimate, this thesis argues that both are equally as important. It was shown that even for simulated environments where ground truth can be evaluated, errors are not treated in a joint optimal manner.

Based on this discussion and the analysis of the related work, the importance of the study of theoretically rigorous measurement equations and corresponding likelihoods is well established. This thesis therefore further analyses the applicability of the well-established measurements equations to the estimation theoretic GBRM, FBRM, and FB-SLAM problems, as well as exposing their oversights in encapsulating the entire sensor uncertainty. The rigorous formulations presented here also serve as building blocks for the subsequent contributions of the proceeding chapters. The review highlights the necessity of developing new measurement equations to better incorporate the inherent sensor uncertainty, as well as proposing the necessary estimation theoretic filtering frameworks, and performance evaluation methods.

Chapter 3

Measurement Modeling

The previous chapter highlighted the importance of accurate interpretation of sensor measurement data, as well as incorporating all the sources of uncertainty into the estimation theoretic framework. This chapter further explores the sources of measurement uncertainty, namely the spurious measurements and detection uncertainty. The stochastic significance of measurement interpretation, specifically the importance of the *number* of measurements at a given time instant is highlighted for the first time. Through analysis of general range-bearing measuring sensors, it is shown that for both the GB and FB navigation frameworks, previous measurement models overlook some theoretical aspects of the measuring process which consequently are not incorporated into the resulting filtering frameworks. Note that in this context, the measuring process refers to the application of a threshold to the received signal to determine a range reading. In sensors such as laser or sonar this is typically performed in the internal circuitry of the sensor. However for sensors such as the millimeter wave radar, the raw signal is available to the user and allows for custom detection algorithms to be applied.

3.1 Introduction

Autonomous navigation systems depend on exteroceptive sensory information in order to provide them with true autonomous capabilities. Such sensors are used to provide a spatial estimate of the vehicles surroundings to facilitate in both its active localisation, and task completion. Exteroceptive sensors such as Laser Measurement Systems (LMS) [6], [7], polaroid sonar [5], [73], vision systems [18], [74], as well as imaging sensors such as millimeter wave radar (MMWR) [28] and [75], and scanned imaging sonars (SIS) [61], [19] have been often been used in FB SLAM (and FBRM) algorithms. For GB methods, LMS have been used in [40], [35], polaroid sonar in [39], [32], vision systems in [76], [77] and MMWR in [33], [27]. To the authors knowledge,

there are no publications where the GB estimation framework has been implemented using SIS sensors.

For both GB and FB autonomous algorithms, and any estimation framework, a critical aspect of the estimation process is that measurements are state related. Furthermore, measurements are typically treated as being 'noisy' in nature. That is, they are measurements of the true state, corrupted by (usually assumed Gaussian) noise. Such measurements can then be readily incorporated into an estimation theoretic filter and used in the process of state estimation. This chapter investigates the causes for detection uncertainty and spurious measurements, focussing specifically on the statistical aspects of detection algorithms which can be exploited for use in autonomous navigation filtering frameworks. The rarely addressed issue of the *number* of the detections is also introduced, as are the stochastic consequences for resulting filtering frameworks.

3.2 Operating Principles

This section provides a brief overview of the operating principles of the commonly used sensors in autonomous navigation platforms. This serves as a basis to understanding the probabilistic form of measurements available from such sensors.

3.2.1 Bearing Only Measurements

Bearing only measurements generally refer to those captured by a monocular camera. This passive sensor uses an array of photodiodes to capture photons of light reflected from the robots surroundings, which are focussed through a lens. Figure 3.1 shows a standard camera model where the landmark's pixel co-ordinates can be translated into bearing measurements through appropriate equations. As a single camera cannot measure the range from a fixed vehicle position, a bearing only measurement can be obtained.

A monocular camera sensor, can then be interpreted as having a discrete bearing (and elevation) measuring state space, as defined by the photodiode array and camera transformations. At each discrete bearing angle, a typically 3x8bit RGB colour measurement is reported. These are the raw measurements reported by the sensor and comprise of the colour of the light reflected from the scene. In order to extract a bearing measurement of the environmental landmark in the scene (if any), landmark detection (or feature extraction) methods must be used to distinguish the background colours from the landmarks of interest. This is made difficult however as the theoretical relationship between the reported colour and the presence or absence of environmental landmarks is extremely vague, given the vast possibilities of colours returned from natural landmarks.

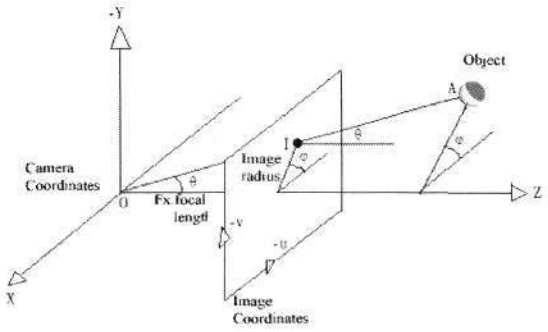

Figure 3.1: *Diagram of a typical monocular camera model showing the generation of a bearing measurement from an environmental landmark.*

3.2.2 Range and Bearing Measurements

Active range sensors are also commonly used in autonomous navigation systems for gaining environmental information. Such sensors emit an electromagnetic wave which, when reflected by environmental landmark and registered by the sensor, can generate a reading related to the range of the landmark. By rotating a mirror such systems can be used to register both range and bearing readings. The information available depends on the modulation method used.

3.2.2.1 Pulsed Sensing

The majority of state-of-the-art autonomous mapping and localisation algorithms use range measuring sensors which contain time-of-flight (TOF), or phase correlation TOF range detection modules. Sensors such as the SICK laser measurement unit [78] and ultrasonic sonar [79] frequently adopt such methods for determining the range to a landmark. This method simply measures the time taken for the emitted light pulse (of fixed frequency) to return to the receiver, the distance then being trivially calculated form,

$$d = \frac{ct_t}{2} \tag{3.1}$$

where c is the speed of light and t_t is the time interval between emitting and receiving the pulse. Prior to calculating the t_t however, the returned pulse must be detected to estimate the exact time of flight. This is far from trivial as the emitted signal has become corrupted with both system and environmental noise, as well as the likely attenuation of the signal and deterioration of the signal-to-noise ratio. Detection is usually achieved by thresholding the amplitude (or power) of the received signal. The time of flight, t_t, is then estimated from the times at which transmitted and received signals exceed the threshold. A significant body of work exists on using

TOF sensors to perform outdoor SLAM, [25], [6], [80]. The use of polaroid sonars is usually restricted to indoor environments [5], [12]. These use geometric feature extraction or scan correlation techniques to provide localisation and map building.

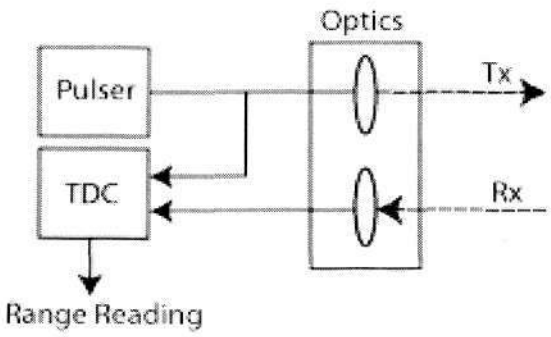

Figure 3.2: *The front end block diagram of a pulsed TOF range sensing unit.*

The only information available from such a measurement, is the range and bearing (corrupted by measurement noise) to a detected point. This detected point may or may not correspond to a physical landmark intersecting the navigation plane, due to detection uncertainty or spurious measurements.

3.2.2.2 Frequency Modulated Continuous Wave Sensing

Imaging sensors such as millimeter wave radar [81] and imaging sonars [62], emit a continuous wave which has been frequency modulated (FMCW) in order to determine an 'echo-image' of the surrounding terrain. By transmitting a chirp and applying FFT signal processing methods, profiles of the echo amplitude in discrete range bins along the axis of projection can be obtained. Such sensors are capable of providing much more information than their fixed frequency counterparts and are the major sensor type under study in this work.

In an FMCW system, a signal of linearly varying frequency with time is transmitted, and mixed upon its return with its modulating component to generate an output spectrum. This spectrum is then passed through a Fast Fourier Transform (FFT) to convert it to the spatial domain and give echo amplitude information relative to the distance from the radar. A basic block diagram of the homodyne system can be seen in figure 3.3 [27].

As can be seen from figure 3.3, the returned signal is mixed with a portion of the transmitted one to generate the output. The input to the system is a linearly increasing voltage with time which is applied to the voltage controlled oscillator (VCO). This in turn produces a signal whose frequency is (ideally) linearly increasing with time, with a bandwidth, B_S. The sweep time is denoted, T_S, as seen in figure 3.4. The

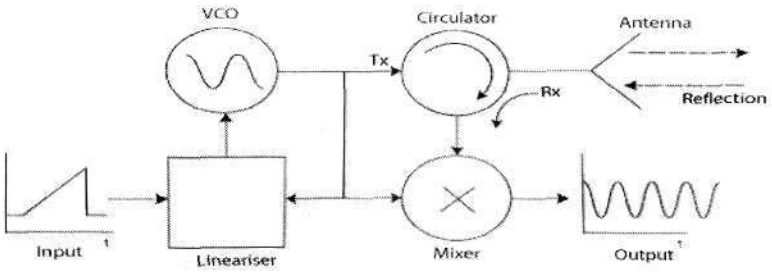

Figure 3.3: *The front end block diagram of the FMCW sensing unit.*

frequency modulated wave is then transmitted at each bearing angle of the swash plate. When the wave strikes a landmark, a portion will be reflected back to the transceiver, t_t seconds later, a time which is proportional to its distance, in a manner similar to TOF techniques. Therefore at a given time instant, and beat frequency,

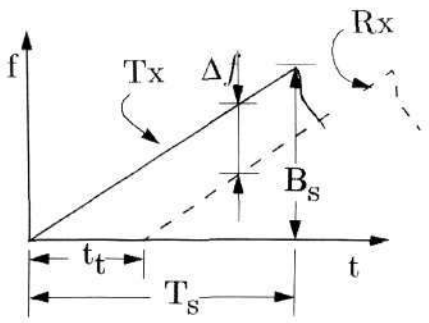

Figure 3.4: *The transmitted, Tx and Received Rx, waves. For a single landmark, there will be a constant Δf between the Tx and Rx waves.*

Δf (commonly referred to as a beat frequency), will exist between the transmitted and received waves. An intuitive analysis, by using the laws of similar triangles and the previous eqn.(3.1), shows that the distance formula can be derived in terms of the constants c, B_s, T_s and beat frequency Δf:

$$\begin{aligned} \frac{\Delta f}{t_t} &= \frac{B_s}{T_s} \\ d &= \frac{ct_t}{2} \\ d &= \frac{cT_s}{2B_s}\Delta f \end{aligned} \tag{3.2}$$

Since T_S and B_s are constants for a given sensor, therefore the range to an environmental landmark is proportional to frequency difference between the transmitted and reflected waves. In the frequency domain, after being passed through an FFT, the output of the mixer is a signal containing a peak power at frequency, Δf. As the wave propagates, its footprint increases with distance from the sensor, and consequently may propagate passed objects that are present within its footprint. Some portions of the wave will then be scattered and reflected, and a portion will continue to propagate out. Each landmark may reflect a portion of the wave, which arrives at the transceiver with a beat frequency, Δf_n, proportional to the distance, d_n where n is the number landmarks per line of sight of the sensor. Herein lies the advantage of FMCW over standard fixed frequency techniques. By mixing the received signal and examining its spectrum, it will be seen to exhibit peaks at different values representing the different beat frequencies, Δf_n of the different landmarks.

By mixing the transmitted and received signal (if any) at discrete time increments, the raw FMCW measurement is thus a power spectrum giving an indication or the presence or absence of a landmark at each discrete time (and distance) increment. If, at a given sample time, there is no received signal, the output would be just a noise signal. A more rigorous mathematical derivation of this process can be seen in [82], [83]. From eqn.(3.2) it can be seen that the maximum range resolution is determined by the smallest measurable increment in Δf, furthermore the maximum range is a function of the chirp bandwidth, B_s. Following the application of an FFT, a single power spectrum therefore be interpreted as containing R discrete 'range bins', each containing an echo intensity measurement at a discrete range from the sensor. A mechanically scanned sensor, can then obtain such spectrum measurements at arbitrary bearing angles.

3.2.3 Raw Measurement Analysis

Figure 3.5 shows a comparison of the raw data (rendered onto a planar cartesian grid) acquired from both an imaging radar and a pulsed SICK laser sensor, superimposed on a section of a satellite image of the university campus. Due to the beam propagating passed environmental landmarks, multiple returns can be registered at a given bearing angle. Figure 3.6 shows a single power range spectrum extracted from the raw measurement scan. The corresponding reading for a laser sensor at the same bearing angle is also shown, verifying the radars range measuring capabilities. Due to a discretised range measuring space (the range bins), naturally some accuracy is sacrificed, adding to the range measurement noise. The intensity of the echo received is generally a function of the landmark's size, material as well as angle of impingement.

The advantage of an imaging sensor, as illustrated in this section, compared to the commonly used LMS sensors, is its ability to propagate downrange and receive

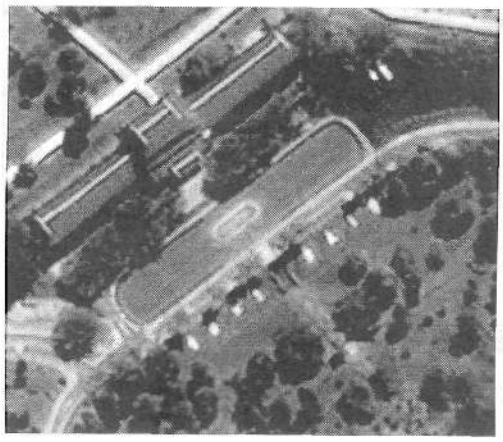

(a) Aerial view of Campus Dataset Segment

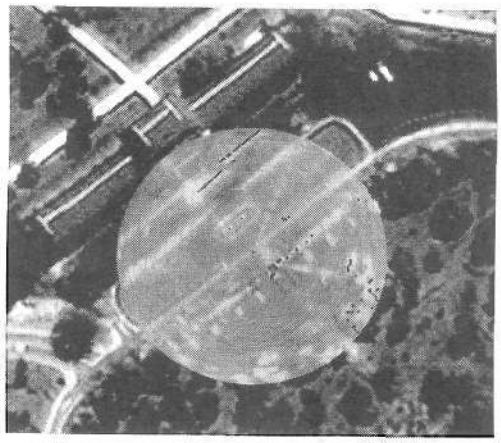

(b) Aerial view with superimposed radar scan.

Figure 3.5: Plan-view example showing raw power measurements from discrete range bins as returned from the output FFT for a 360^o scan. A raw laser measurement is also shown.

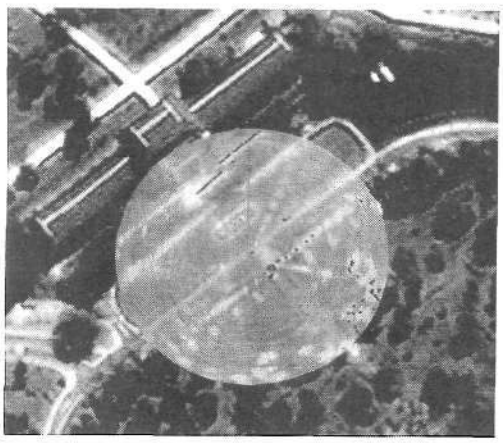

(a) Aerial view with selected radar spectrum

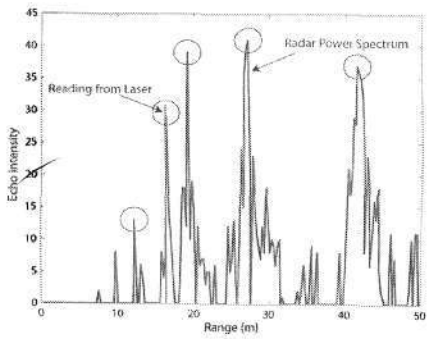

(b) The corresponding power spectrum. Circles indicate reflections from valid landmarks in the scene as verified by the satellite image.

Figure 3.6: Example of the multi-landmark imaging capability of an FMCW Radar. Note that due to its fixed frequency emitted wave, the laser sensor can only return a single range value, at the same bearing angle.

measurements from multiple landmarks at a single bearing angle, as in figure 3.5. As the beam propagates downrange its footprint area increases with distance, (as does the bearing measurement uncertainty of any detection). With a narrow beam width, $\sim 1.8^o$, it has the ability to provide high resolution environmental images, however this resolution is reduced at large range. This provides numerous advantages in outdoor navigation applications, increasing the mapping capabilities as well as providing an increased number of landmarks/features to potentially reduce the localisation uncertainty of the mobile vehicle.

This sensor is however not without its drawbacks. Although the theoretical resolution and range are as stated, in practise they are much reduced. Major sources of uncertainty are in the linearity of the modulating signal applied to the VCO, phase noise from the VCO as well as signal leakage (measurement noise and detection uncertainty), harmonics and multi-path (detection uncertainty and spurious measurements) [82]. Signal attenuation can also increase landmark detection uncertainty [84]. Corrupting noise signals, clutter reflections and the cumulative effects of the measurement uncertainty make detection of the landmark signals, while simultaneously suppressing the noise signals, a challenging research issue that must be addressed in such imaging sensors.

The MMWR is robust and applicable to outdoor robotic navigation due to its relative immunity to the effects of dust, fog, or light rain which can drastically affect other sensors [85], [28], [86], [33]. The imaging sonar is widely deployed for underwater robotic applications [62], [16], [19]. The majority of the work in this thesis uses the MMWR as its primary exteroceptive sensor. As can be seen from figure 3.6(b), multiple peaks are present in the power spectrum, only some of which are from valid landmarks. The following section deals with detecting landmark reflections from a noisy power spectrum.

3.3 The Landmark Detection Problem

Landmark detection concerns the detection of landmark signals from noisy sensor measurement data such as that in figure 3.6(b). Feature extraction [17], [6], [12] then concerns the reduction of the dimensionality of the hypothesised landmark detections, into feature models. Commonly used LMS and polariod sonars [73] internally perform the landmark detection and the sensor output is the range and bearing measurement of each *single* hypothesised detection at each bearing angle. However, as mentioned in the previous section, imaging sensors like MMWR [15] and some scanning sonars [16], return raw power measurements without any landmark detection algorithm applied. A similar analogy can, in principle, be made about the raw measurements from a camera [18].

3.3.1 Non-Adaptive Detection

Landmark detection problems are not new to the field of autonomous mapping however they but are generally treated in a simplified manner. Previous works which adopt imaging sensors, [28], [86], [19], [16], generally use *a priori* fixed thresholding[1] methods or heuristics to hypothesise the presence of a landmark in the data. Single landmark presence is assumed and generally only one landmark is extracted at each bearing angle. Figure 3.7 shows the previous spectrum with a non-adaptive threshold used to perform landmark detection. While computationally simple to apply, a non-adaptive detection method requires an *a priori* setting of the threshold power, T, which is non-intuitive.

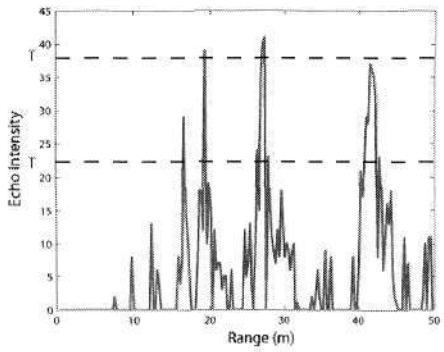

Figure 3.7: *A single radar power spectrum being processed by a constant threshold landmark detector.*

Since the power reflected from a landmark fluctuates with respect to vehicle position, an *a priori* constant threshold can be prone to missed detections. Furthermore, extracting a single detection per bearing angle, discards much useful information in terms of map building and localisation capability. Most importantly however, there is no statistical information which can be extracted from landmark detections using an *a priori* threshold.

3.3.2 Hypothesis Free Modeling

To overcome the fallacies of constant thresholding methods, some researchers attempt to model the power spectrum by a Gaussian mixture model [61]. Figure 3.8 shows a Gaussian mixture fitted to the power spectrum. The Gaussian number can be *a priori* set, or based on a function of the number of peaks detected in the spectrum.

[1]Fixed threshold detection is indeed the optimal detector in the case of spatially uncorrelated and homogenous noise distributions of known moments.

While this approach seemingly reduces the dimensionality of the data (reduced to N Gaussians), it possess some fundamental probabilistic flaws.

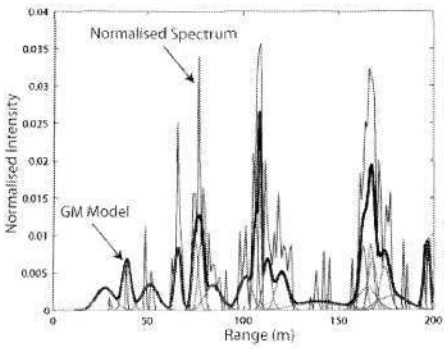

Figure 3.8: *A Gaussian mixture approximation of a single power-range spectrum from an imaging radar sensor.*

This approach attempts to transform directly from the power spectrum to a measurement likelihood,

$$g(z|M, X_k) = \sum_{i=1}^{N} w^{(i)} \mathcal{N}\left(z; \mu^{(i)}, R^{(i)}\right). \tag{3.3}$$

A fundamental property of a probability density function requires that the total integral of $g(\cdot)$ is unity. A mixture model can thus only model a normalised power spectrum. This consequently assumes (with complete certainty) that there is a *single* landmark present the spectrum. As seen previously in figure 3.6(b), this is clearly not always the case for imaging sensors. Furthermore, the power spectrum cannot be interpreted as modeling the positional noise of a single landmark estimation, and is in fact simply the power received in each discrete incremental range bin. Range and bearing measurement noise are a property of the sensor, and not a property of the power received in each range bin.

It can therefore be seen that the processing of imaging sensors in not adequately dealt with in the realm of autonomous navigation. This chapter thus proceeds to analyze the theoretical properties of imaging sensor's power spectra in order to maximise the information content of the measurement and improve mapping and localisation capabilities.

3.4 Stochastic Signal Model

While not considered in the robotics community, imaging sensors generally have well founded statistical principles which can be exploited to increase the information content of a measurement. From an imaging sensors perspective, the environment can be considered to consist of a random number of density functions of signal power, which are spatially distributed about the given environment. These model the power which *may* be reflected to the radar sensor at a given location. In an *a priori* unknown environment, the power pdfs are unknown both in distribution and moments. If, $\Omega_{(x,y)}$, denotes the moments of the power density function at global cartesian co-ordinates, (x, y), let the corresponding environmental density be,

$$p_{(x,y)}(\psi|\Omega_{(x,y)}). \tag{3.4}$$

where, ψ, denotes the raw power measurement registered by the imaging sensor. The density, $p_{(x,y)}(\cdot)$, may take on a number of forms including Exponential, Rayleigh, Ricean, Gaussian, Chi-Square etc. depending on the environment at location (x, y). Let the measurement from the imaging sensor, at time k, be denoted, $Z_k = [z_{k,1}, ..., z_{k,IR}]$, and consists of $I \times R$ (considered independent) samples, $z \sim p_{(x,y)}(\psi|\Omega_{(x,y)})$, where (x, y) is a function of the vehicles location and the polar co-ordinates of the given range bin. R is the total number of range bins in a single power spectrum, and I is the total number of bearing angles sampled for a given measurement. Note that due to a fixed sensor range, $I \times R$, is generally a constant for all scans, i.e. there is always a fixed number of raw measurements. Z_k is usually segmented into rows for each of the individual power spectra (figure 3.6(b)), in a complete scan. Let $Z_k^{(i)} = [z_{k,Ri+1}, ..., z_{k,Ri+R}]$, where the measurement index $(Ri + 1), \ldots, (Ri + R)$ corresponds to the measurements contained in power spectrum $i \leq I$.

The random environmental densities are considered *strictly* stationary, as the moments are considered constant with time and ergodic, however, from a sensor perspective the ergodicity is violated, as the vehicle moves resulting in Z_{k+1} sampling potentially different environmental pdfs than those sampled in Z_k. Typically for an autonomous platform, an ensemble of a particular pdf cannot be obtained as only a single realization (single scan) is taken, before the platform moves to sample a (potentially) different distribution. Deriving probabilistic landmark detectors for such data is clearly a challenging task, as both the distribution types and associated moments are unknown. Therefore most work has been developed based on some distribution (for both regions containing landmarks and empty space) assumptions.

3.4.1 Adaptive Detection and Ranging

This section introduces the stochastic detection theory used to generate a range reading from a given raw sensor measurement using a statistically founded adaptive threshold. Signal detection is typically formulated as a likelihood of landmark signal presence versus noise signal presence, which is then compared to a threshold value. As previously outlined, the measurement data contained in a single power spectrum, $Z_k^{(i)}$, contains R samples from an unknown number of (potentially correlated) pdfs, such as (3.4), at time k. The distribution of a given environmental pdf at a given location is a function of many factors including the terrain profile, landmark presence/absence, viewing aspect and landmark radar-cross section (RCS) fluctuation properties.

Due to the vast diversity of potential distribution types, coupled with the unknown moments, for tractable solutions some simplifying assumptions are generally made. Exteroceptive sensing typically requires a solution to the binary classification problem of landmark presence or landmark absence. Distribution assumptions are therefore commonly segmented into those indicating empty space, and those indicating a landmark is present [87]. A null hypothesis, denoted $\mathcal{H}_E$ in this work, indicates landmark absence (i.e. empty region), with the alternate, denoted $\mathcal{H}_O$, indicating landmark presence (i.e. occupied region). Let the corresponding distributions be denoted, $p_{(x,y)}(\psi|\mathcal{H}_E, \Omega_E)$ and $p_{(x,y)}(\psi|\mathcal{H}_O, \Omega_O)$ respectively, where the corresponding distribution moments, Ω_E and Ω_O, remain *a priori* unknown.

Landmark detectors are typically formulated as a likelihood ratio of the pdf under landmark presence over the pdf under landmark absence and compared to a threshold. If the likelihood (or test statistic) exceeds the threshold, a landmark is declared present. In the simplest case, both the landmark and noise pdfs are known completely. Clearly, in the case of an imaging sensor, neither of these pdfs are known, and assumptions *must* be made. Two detection errors are possible in this case. Declare a landmark when no landmark is present (known as a type I error, or *false alarm*), and declaring no landmark when a landmark is present (known as a type II error, or *missed detection*). These can be denoted as P_{fa} which is the false alarm probability and P_{md} being the missed detection probability. Note $P_{md} = 1 - P_d$, where P_d is the probability of detection. Given 2 known pdf's the Neyman Person test aims to maximise P_d subject to a constant P_{fa} (a Lagrangian optimization situation). P_{fa} and P_d can be calculated from,

$$P_{fa} = \int_S p(\psi|\mathcal{H}_E)d\psi$$

$$P_d = \int_S p(\psi|\mathcal{H}_O)d\psi$$

where S is the region of integration (bounded by the threshold and infinity), $p(\psi|\mathcal{H}_E)$

and $p(\psi|\mathcal{H}_O)$ are the *known* pdfs of the noise and landmark power fluctuations.

The next degree of complexity is where one (or both) of the distributions are known, but their moments are not. A common example is assuming the noise to be exponentially distributed with an unknown mean. In this case the Neyman Pearson detector will become,

$$L(\psi) = \frac{p(\psi|\mathcal{H}_O)}{p(\psi|\mathcal{H}_E)} = \frac{\int p(\psi|\mathcal{H}_O, \Omega_O)p(\Omega_O)\delta\Omega_O}{\int p(\psi|\mathcal{H}_E, \Omega_E)p(\Omega_E)\delta\Omega_E}$$

where Ω_O and Ω_E are the unknown parameters of the known (or assumed) distributions given landmark present and absent hypotheses. In a general likelihood ratio test, an estimate (usually unbiased and of minimum variance) is made of the distribution moments. If, under $\mathcal{H}_E$ hypothesis, an expression for P_{fa} can be derived which does not depend on any unknown moments, Ω_E, the detector is known as a constant false alarm rate (CFAR) detector. CFAR detectors are useful due to the extent of the probabilistic information which can be extracted from a given detection (or non-detection).

A detector with the CFAR property, can therefore generate an adaptive threshold at such a level, that the probability of a noise signal exceeding the threshold in each range bin (and consequently registering a false alarm) is constant and known. Thus, the threshold can be set such that probability of accepting an *incorrect* signal can be determined. Note however, that there is no information about the converse, i.e. the probability of accepting a valid signal from a landmark. This is analogous to the commonly used *normalised innovation squared* data association gating threshold [55], which according to its χ^2 distribution and threshold choice, indicates the probability of accepting a *correct* measurement, whilst giving no information as to the probability of accepting an incorrect measurement. Furthermore, autonomous navigation algorithms that do consider the false alarm probability [13], [12], [39], [36], inherently assume that the landmark detector being used has the CFAR property, as P_{fa} is assumed constant through out the entire experiment.

3.4.2 Single Spectrum CFAR Detector

A CFAR detector for a given measurement spectrum, $Z_k^{(i)}$, is outlined here. The likelihood ratio test for each range bin, $r \in \{1, \ldots, R\}$, is written as,

$$L(\psi_{Ri+r}) = \frac{p(\psi_{Ri+r}|\mathcal{H}_O)}{p(\psi_{Ri+r}|\mathcal{H}_E)} = \frac{\int p(\psi_{Ri+r}|\mathcal{H}_O, \Omega_O)p(\Omega_O)\delta\Omega_O}{\int p(\psi_{Ri+r}|\mathcal{H}_E, \Omega_E)p(\Omega_E)\delta\Omega_E} > T_{Ri+r} \qquad (3.5)$$

where Ω_O and Ω_E are the unknown parameters of the known (or assumed) distributions given landmark presence and absence hypotheses. $L(\psi_{Ri+r})$ is then compared to

a decision threshold, T_{Ri+r}, to chose the corresponding hypothesis. If the noise in each bin is assumed to be exponentially distributed, with an independent and identically distributed (IID) assumption, we can write,

$$p(\psi|\mathcal{H}_E, \Omega_E = \mu) = \begin{cases} \frac{1}{\mu}\exp^{-\psi/\mu} & \text{if } \psi > 0 \\ 0 & \text{Otherwise} \end{cases} \tag{3.6}$$

In the case of landmark presence, the resulting power pdf may be assumed to be [88],

$$p(\psi|\mathcal{H}_O, \Omega_O = \{\mu, \Re\}) = \frac{1}{\mu}\exp^{\left((-\psi/\mu)+\Re\right)} .I_0\left(2\sqrt{\frac{\Re\psi}{\mu}}\right) \tag{3.7}$$

where I_0 is the modified Bessel function of order zero, and $\Re$ is the signal to noise ratio (SNR) sampled from the Swerling I model with mean SNR $\bar{\Re}$,

$$p(\Re|\bar{\Re}) = \begin{cases} \frac{2\Re}{\bar{\Re}}\exp^{-\Re^2/\bar{\Re}} & \text{if } \Re > 0 \\ 0 & \text{Otherwise.} \end{cases} \tag{3.8}$$

A graphical representation of the resulting detection problem in a single range bin is shown in figure 3.9.

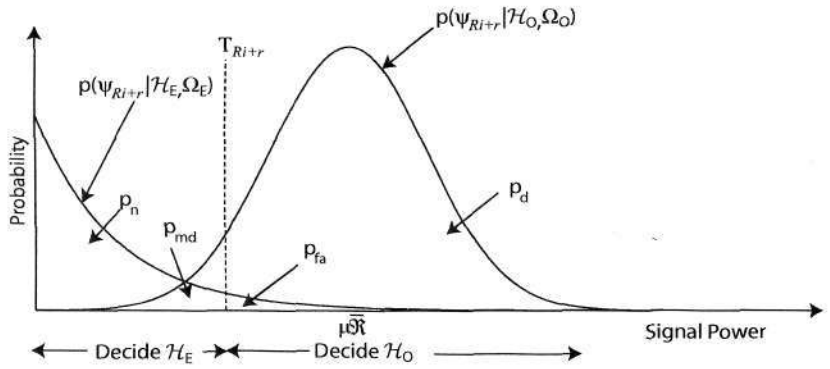

Figure 3.9: *Signal classification in range bin Ri+r. Here 4 probabilities are present giving the probability of correct detection of noise signal P_n, landmark signal P_d, and both type I (false alarm), P_{fa} and type II (missed detection), P_{md} errors.*

The mean noise power μ is assumed unknown and must be locally estimated from the data in the spectrum, $Z_k^{(i)}$, using a sliding window with a width of W range bins[2].

[2]Typically, to account for spectral spreading, guard cells (denoted G) are included on each side

Given the assumed power density statistics in the presence of noise and landmark signals, as shown in figure 3.9, the 4 following probabilities for any CFAR process can be determined for each range bin k,

$$P_d = \int_0^\infty P[\psi_{Ri+r} \geq T_{Ri+r}|\mathcal{H}_O] f_\mu(\mu) d\mu \tag{3.9}$$

$$P_n = \int_0^\infty P[\psi_{Ri+r} < T_{Ri+r}|\mathcal{H}_E] f_\mu(\mu) d\mu \tag{3.10}$$

$$P_{md} = \int_0^\infty P[\psi_{Ri+r} < T_{Ri+r}|\mathcal{H}_O] f_\mu(\mu) d\mu \tag{3.11}$$

$$P_{fa} = \int_0^\infty P[\psi_{Ri+r} \geq T_{Ri+r}|\mathcal{H}_E] f_\mu(\mu) d\mu \tag{3.12}$$

Clearly for a given landmark signal, P_d and P_{md} will be a function of the mean SNR, $\bar{\Re}$. It can be shown that in the case of exponentially distributed noise, various detectors with the CFAR property can be derived [89], [90]. An ordered-statistics (OS) approach has been shown to be most robust in situations of high clutter, as is commonly encountered in a field robotics environment, and is therefore adopted in this work. The decision threshold for each range bin is set as,

$$T_{Ri+r} = \tau \hat{\mu}_{Ri+r} \tag{3.13}$$

where, $\hat{\mu}_{Ri+r}$ is a local estimate of the average noise power μ and τ is a scaling factor to achieve a desired false alarm probability, P_{fa}, given by

$$P_{fa} = \int_0^\infty P[\psi_{Ri+r} \geq \tau \hat{\mu}_{Ri+r}|\mathcal{H}_0] f_{\hat{\mu}}(\hat{\mu}) d\hat{\mu}. \tag{3.14}$$

This is evaluated as,

$$P_{fa} = k_{os} \binom{2W}{k_{os}} \frac{(k_{os}-1)!(\tau + 2W - k_{os})!}{(\tau + 2W)!} \tag{3.15}$$

where $f_{\hat{\mu}}(\hat{\mu})$ is the pdf of the noise estimate $\hat{\mu}_{Ri+r}$. For an ordered statistic noise estimate, $\hat{\mu}_{Ri+r} = \psi_{k_{os}}$, the k_{os}^{th} element of the 2W ordered (according to power) samples $[\psi_1, \ldots, \psi_W]$ in the sliding window. Since the false alarm probability in eqn.(3.15) is independent of any unknown moments, such a detector maintains a CFAR property. A full derivation of the OS-CFAR adaptive detector is outlined in Appendix B.1. The output of an Ordered Statistics-CFAR detector with parameters

of the cell under test and so the window is split into a lead and lag section.

W = 20, $P_{fa} = 1\text{x}10^{-6}$, G = 2, and $k_{os} = 3\text{W}/2$ on the MMWR data can be seen in figure 3.10. The adaptive threshold can be seen to detect 4 landmark signals in the data, without reporting any false alarms. The local maximum of each peak which exceeds the threshold, can then be used to generate a range estimate at the given bearing angle.

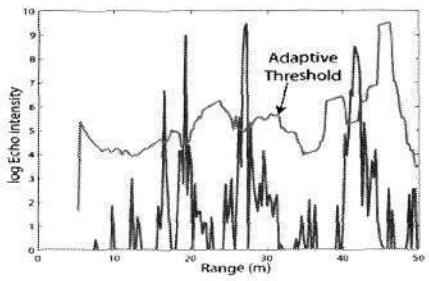

Figure 3.10: *OS-CFAR detector output on a single power spectrum. The adaptive threshold resulted in the correct detection of 4 out of the 5 landmark signals present in the data.*

3.4.3 Measurement Analysis

Assuming that the assumption on the signal distribution in the absence of a landmark is met, as well as being IID[3] through out the environment, the probability of a non-landmark, registering a detection is given by, P_{fa}. For a direct CFAR detector implementation, there is no information as to the validity (from a real environmental landmark) of a given detection. Previous methods of detection [28], [16] do not consider the underlying statistics of the signal, and thus no statistical information can be extracted from a given detection. In the case of IID noise signal distributions with known moments, an *a priori* threshold may be used to guarantee a given false alarm probability. Clearly, the probability of the power of a noise signal, not exceeding the threshold, is given by $1 - P_{fa}$.

Various measurements can thus be extracted from such frequency modulated sensors including the output of the adaptive detector, the range-bearing pair of each range bin, and the power of the reflection. The output of a given CFAR detection given the input power spectrum measurements, $Z_k^{(i)} = [z_{k,Ri+1} = \psi_{Ri+1}, ..., z_{k,Ri+R} = \psi_{Ri+R}]$, is a series of R detection, D, or non-detection, $\bar{D}$, measurements based on the power measurements, $z_{k,Ri+1}, ..., z_{k,Ri+R}$, and corresponding statistical threshold values, $T_{k,Ri+1}, ..., T_{k,Ri+R}$. That is, the measurement becomes, $Z_k^{(i)} = [z_{k,Ri+1} \in$

[3]The IID assumption is frequently assumed when approaches consider false alarms to be uniformly distributed through out the environment.

$\{D, \bar{D}\}, ..., z_{k,Ri+R} \in \{D, \bar{D}\}]$. Also, the non-detections can be disregarded to obtain a random number, $n_k^{(i)}$, $(n_k^{(i)} \leq R)$) of detection measurements. Generally, the range and bearing to each detection is then used as the measurement for a given navigation filter, $Z_k^{(i)} = [z_1 = [r_1; \theta_1], ..., z_{n^{(i)}(k)} = [r_{n_k^{(i)}}; \theta_{n_k^{(i)}}]]$. Depending on the form of measurement adopted, a different estimation theoretic framework is required to propagate the measurement, as highlighted in the following sections.

3.4.3.1 Probabilistic vector measurements

Autonomous navigation platforms using exteroceptive measuring sensors, generally adopt the measurement equation at time k,

$$Z_k = H(X_k, M_k) + w_k \tag{3.16}$$

where $H(\cdot)$ is generally a non-linear function transforming the map elements, M_k, and vehicle location, X_k, into relative range and bearing measurements, with w being a Gaussian distributed random variable which encapsulates the additive measurement noise. Examination of this common measurement equation, highlights that the *number* of measurements equals the *number* of elements in the map, M_k. Therefore, in order to apply this equation, the number of elements of the map M_k (within sensor range), must be *a priori* known. When GB methods are adopted, the map grid size and resolution are *a priori* assigned. Consequently, the dimensionality of, M_k, is known. Taking the spectrum measurement example from section 3.4.2, where the measurement, $Z_k^{(i)} = [z_{k,Ri+1} \in \{D, \bar{D}\}, ..., z_{k,Ri+R} \in \{D, \bar{D}\}]$, comprises detection and non-detection hypothesis for *every* range bin, the number of measurements equals the length of M_k and the equation is valid. A measurement equation which satisfies this requirement is referred to, in this work, as a vector measurement.

A common function, $H(\cdot)$, for FB approaches models the relationship between the i^{th} map element and the vehicle location, $X_k = [x_k, y_k, \alpha_k]$ to generate the range and bearing measurements as,

$$r_i = \sqrt{(m_{(x)}^i - x_k)^2 + (m_{(y)}^i - y_k)^2} \tag{3.17}$$

$$\theta_i = \arctan \frac{m_{(y)}^i - y_k}{m_{(x)}^i - x_k} - \alpha_k. \tag{3.18}$$

In the case of well understood measurements as described by eqn.(3.17) and eqn.(3.18), where the measurements are related through well founded equations, but corrupted by (Gaussian) measurement noise, such measurements can be referred to as probabilistic. Thus, a measurement equation which jointly satisfies both requirements is referred to as being a probabilistic vector measurement.

3.4.3.2 Evidential vector measurements

The case of the number of measurements equalling the number of elements of the map, M, but the measurement equation is poorly understood, the measurement is referred to as an evidential vector measurement, in this thesis. In the case of M consisting of the Euclidean coordinates of hypothesised features, (FB deployments) the measurement model relating the state to the measurement is straight forward. However, in the case of GB deployments where the state is 'existence' or 'occupancy', the measurement model relating the state to measurement can be less certain. For instance, if a detection implies that the occupancy in the given cell, $m_{(x,y)}$, should be assigned the value $\emptyset$,

$$p(m_{(x,y)}|z_{k,Ri+r}) = \emptyset \tag{3.19}$$

general probabilistic approaches assume that $p(\bar{m}_{(x,y)}|z_{k,Ri+1}) = 1 - \emptyset$. However, in the presence of no measurement indicating a belief of 'emptiness', evidential vector measurements assume $p(\bar{m}_{(x,y)}|z_{k,Ri+1}) = 0$. Thus the remaining 'ignorance' is encapsulated in an 'unknown' term, $p(\tilde{m}_{(x,y)}|z_{k,Ri+1}) = 1 - \emptyset$. In this case, the number of measurements equals the number of elements in the map, but the measurement model is treated in an evidential framework as opposed to a probabilistic one.

3.4.3.3 Probabilistic set measurements

Probabilistic set measurements refer to those in which the function, $H(\cdot)$, is well understood, however the number of measurements, does not equal the number of elements in the map, M. In the case where measurements, $z_{k,1}$, comprise detections only with non-detections being disregarded (such as in most FB implementations), the number of measurements in a given scan at time k, becomes a random number. Since with a finite P_{fa}, coupled with non unity landmark signal detection, given a map, M, the number of measurements may differ from the number of elements of M which are within sensor range. In this case, the measurement equation becomes,

$$Z_k = \bigcup_{m \in M} \Theta_k(m, x_k) \cup C_k(x_k) \tag{3.20}$$

where $\Theta_k(m, x_k)$ models the measurements generated by the elements in M (if any) and $C_k(x_k)$ models the spurious measurements received at time k. Therefore Z_k consists of a random number of measurements. The relationship between landmarks and measurements is well understood, (equivalent to eqn.(3.17) and eqn.(3.18)), the measurement is thus referred to as a probabilistic set measurement. Chapter 5 examines the case of autonomous navigation with these measurements.

3.4.3.4 The Filtering Frameworks

Identifying the stochastic attributes of a measurement is of paramount importance to the estimation theoretic being adopted to attempt to solve the state estimation process. Probabilistic vector measurements must be incorporated to the recursive estimation process through probabilistic vector-based likelihoods. Evidential vector measurements require evidential likelihoods and consequently a different estimation theoretic. Probabilistic set measurements require set-based likelihoods and a set-based estimation theoretic which differs fundamentally to its vector-based counterpart due to the uncertainty in the measurement number. These issues are highlighted for the first time in the thesis in relation to the autonomous navigation problem.

3.5 Experiments

In this section, the outlined landmark detection methods are implemented in an outdoor scene using both a laser and radar exteroceptive sensor. Extensive statistical analysis shows the advantages of the statistically founded approaches over the commonly used *a priori* landmark detection routines. Emphasis is on the statistical information which can be extracted from a given detection.

3.5.1 The Carpark Dataset

An overview of the testing environment is shown in figure 3.11 showing the roads and environmental landmarks present in the scene. For data verification and comparison with the laser sensor, a static radar scan rendered onto a 2D planar grid is also shown. 2D Gaussian spread functions [91] are used to 'smear' the received power according to the range and bearing measurement noise, as well as the beam width. The corresponding colour is an indication of the magnitude of the reflected power. The mobile platform (see appendix A for further details) was then driven in loops as (approximately) shown in the image. Note that at the time of data acquisition, there was only a single car in the carpark. Approximately 300 radar scans are registered per 100m loop.

Note that the radar measurement receives power reflections from the low lying bush in front of the marked trees, as well as from the trees themselves. Due to the occluding car and single landmark/bearing angle assumption, the laser sensor fails to detect two out of the four trees, as well as completely missing the bush. The vehicle was then driven around the carpark collecting radar scans. At a velocity of 1m/s and a radar scanning rate of 2.5Hz, inflated measurement noise due to doppler distortion was considered negligible and not addressed in this work. Due to the unavailability of GPS signals in the semi-structured environment (tall buildings result in frequent

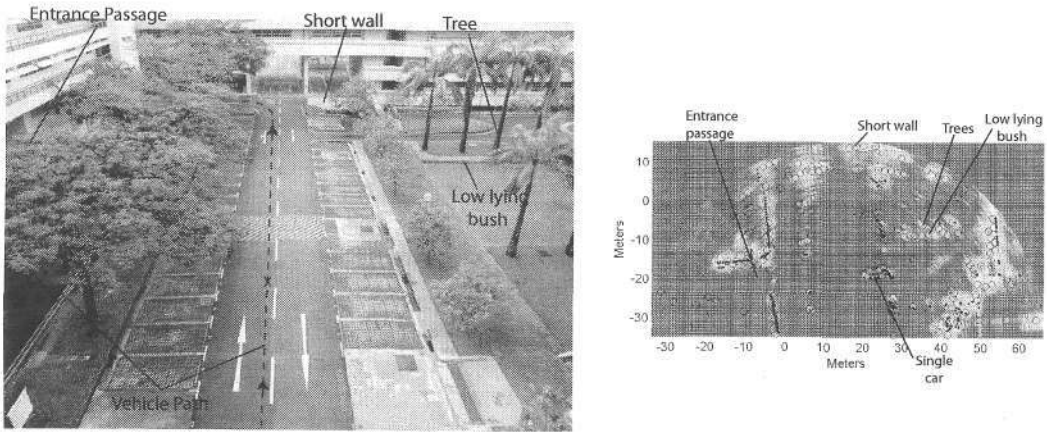

Figure 3.11: *A photographic overview of the carpark testing ground within university campus. The approximate vehicle path is shown along with the static location, 'X'. A sample scan from a radar and laser sensor are also shown.*

outages), ground truth location was obtained by manually aligning successive laser scans.

3.5.2 Scan Maps

Scan maps refer to maps produced by plotting successive range-bearing measurements over the course of an experiment, and are frequently adopted by the laser scan matching community [80], [7]. Figures 3.12(a) and 3.12(b) show the laser scan map of the carpark and estimated vehicle trajectory from the proprioceptive measurements, and that from the proposed ground truth location. Alignment of the environmental landmarks proves the accuracy of the proposed ground truth vehicle trajectory. As mentioned in the previous chapter, scan maps contain no statistical knowledge of the map and are simply a display of the detections registered by the sensor over the course of the loop. Due to some slight roll of the vehicle, some ground reflections are evident along the center of the map. Reflections from the grassy median can also be seen.

Using this trajectory, corresponding radar scan maps are thus created from the various detection methods. Figures 3.13(a) and 3.13(b) show a scan map using detections registered from non-adaptive constant thresholds at $30dB$ and $50dB$ respectively. The resulting carpark scan map produced from using the points of maximum signal intensity above the threshold is shown in figure 3.14. Figures 3.15(a) and 3.15(b) show the resulting scan maps produced from the radar sensor using an OS-CFAR adaptive threshold. P_{fa} was set at 1×10^{-6} and 1×10^{-24} respectively. From visual inspection of

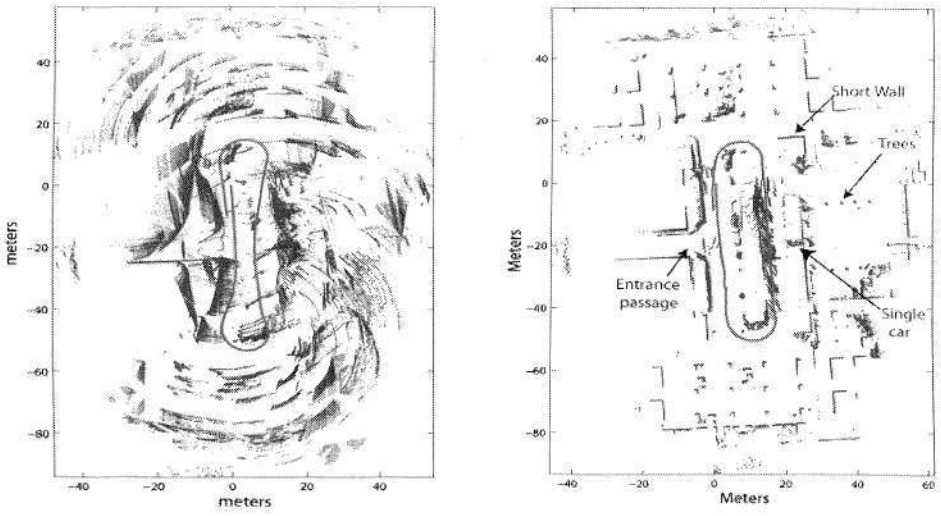

(a) (b)

Figure 3.12: *This figure shows the laser scan map produced from a vehicle driving a single loop around the carpark. The image on the left shows that from the raw odometry readings, whilst that on the right shows laser scan map from the manually matched ground truth location.*

the resulting scan maps, it can be seen that at $30dB$, there are a large number of false alarms, which are significantly reduced with the threshold placed at $50dB$. However, this naturally comes at the cost of detection probability, where the chain across the entrance passage for instance, is not detected with a threshold of $50dM$. Using the maximum intensity approach can improve the result however there is no guarantee that over successive scans, the same landmark will return the maximum power in a given power spectrum due to considerable fluctuations. The scan map produced by the the adaptive threshold with theoretical false alarm probability $1{\times}10^{-6}$, reports an actual false alarm at a rate similar to the constant threshold of $30dB$. At a theoretical rate of $1{\times}10^{-24}$, the false alarm rate is reduced with a detection performance superior to that of either the constant thresholding or maximum intensity approaches. Visual inspection of the resulting maps, as is typically performed, provides an overview of algorithm performance however it fails to adequately analyze the statistics of the detector.

3.5.3 Statistical Detector Analysis

In order to obtain a meaningful performance evaluation of a given detection algorithm, the ground truth map must be known. For the outlined carpark dataset,

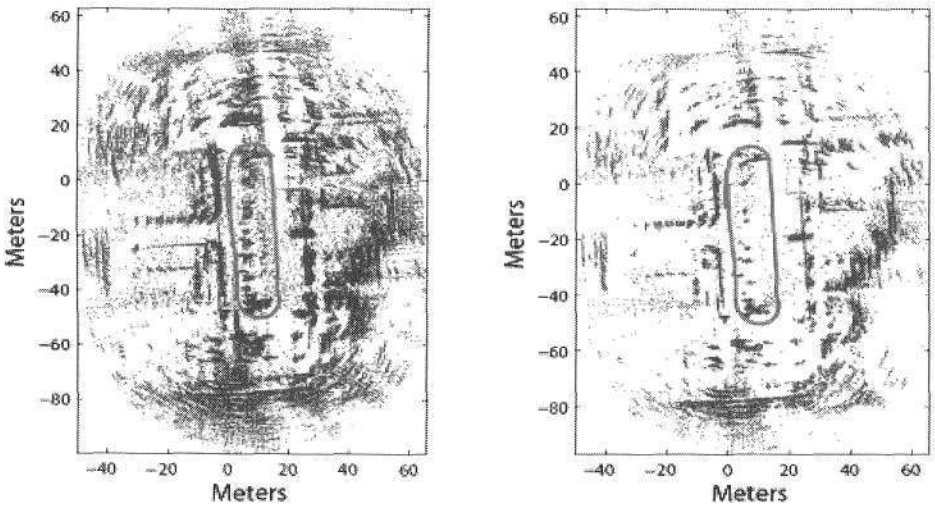

(a) (b)

Figure 3.13: *This figure shows the radar scan maps produced from constant threshold detectors. The figures on the left and right show the results from a constant detector with T set at $30dB$ and $50dB$ respectively.*

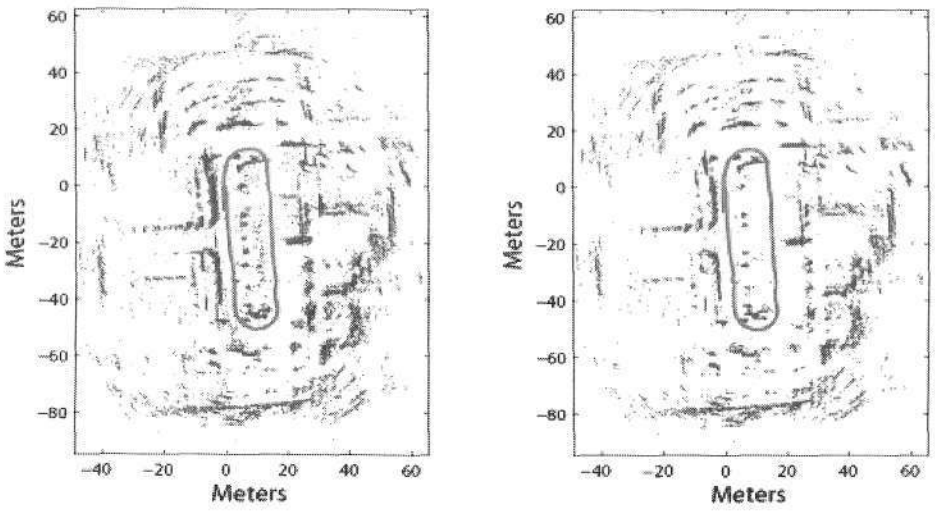

(a) (b)

Figure 3.14: *This figure shows the resulting scan maps produced from a maximum intensity detector, with a threshold of $30dB$ and $50dB$ respectively.*

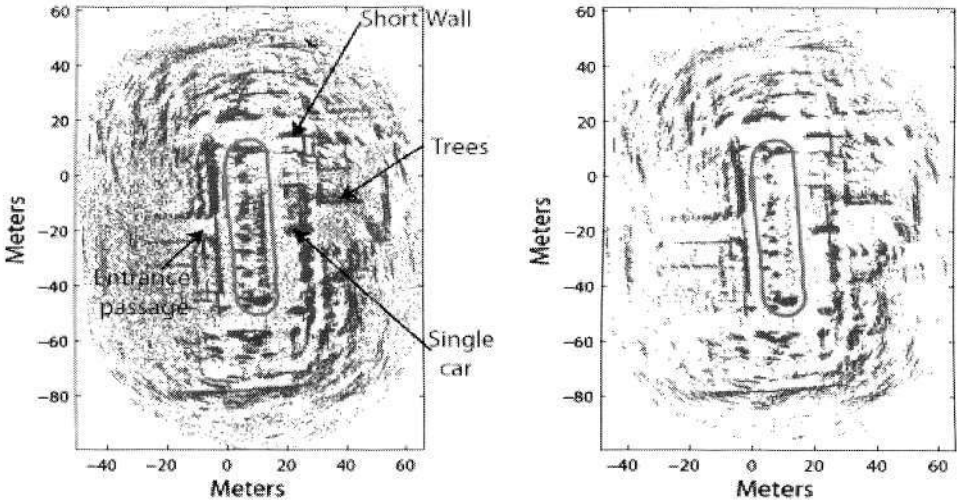

(a) (b)

Figure 3.15: *This figure shows radar scan maps produced from a vehicle driving a single loop around the carpark. The results are from an OS-CFAR detector with* P_{fa} *set at* 1×10^{-6} *and* 1×10^{-24} *respectively.*

ground truth maps were obtained from the manual observation of the physical ground truth, as well as observing the sensor data. Due to different operating principles, the ground truth map for the laser, figure 3.16(a) differs from that of the radar, figure 3.16(b). These ground truth maps are consequently used in the analysis of the detection methods discussed in this chapter. Using the proposed ground truth, the actual statistics of various outlined detectors can be examined. This provides a more rigorous analysis of the detectors and is the first time such statistics have been examined for exteroceptive perception in the autonomous navigation community.

Figure 3.17 shows the actual rate of false alarm for the *a priori* thresholding and the maximum signal intensity detection methods. Since the detectors do not consider the signal statistics, false alarm and detection statistics are arbitrary. The intuitive result shows that with an increasing constant threshold, the number of false alarms reduces significantly as expected. When the maximum intensity detection approach is used (figure 3.17(b)), naturally the false alarm rate drops drastically as there is a reduced number of measurements, however this comes at the cost of frequency missed detections.

For the case of the statistically motivated CFAR detector, the tuning parameters are statistically motivated as opposed to the ad-hoc threshold methods which are commonly used. Generally, the input parameter is the desired rate of false alarm, P_{fa}. Figure 3.18 then shows the effect of varying the desired P_{fa} for the OS-CFAR detector

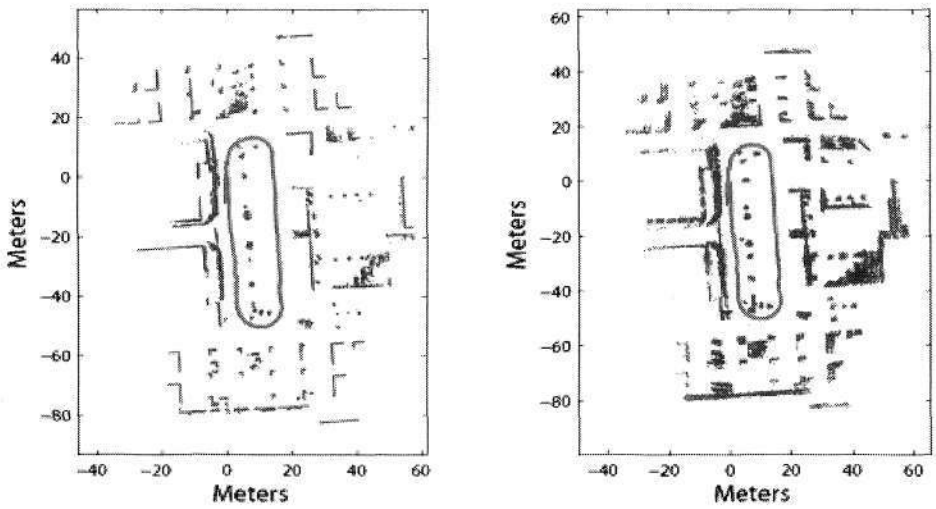

(a) (b)

Figure 3.16: *Figures (a) and (b) show the hypothesised ground truth map for both the laser and radar sensor respectively. Some landmarks do not appear to the laser due to a narrower beam width, and single frequency wave transmission.*

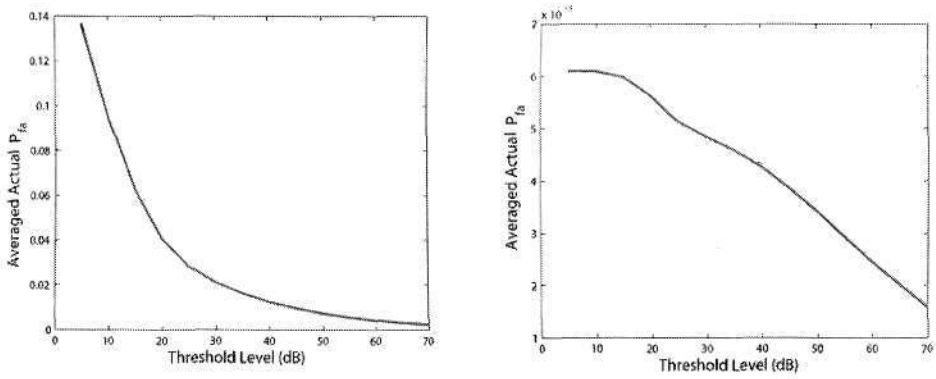

(a) (b)

Figure 3.17: *Figures (a) and (b) show the averaged actual false alarm rate over the course of the loop for constant threshold (a) and maximum intensity (b) detectors.*

described earlier, while comparing it to the actual false alarm rate as confirmed from the ground truth of figure 3.16(b).

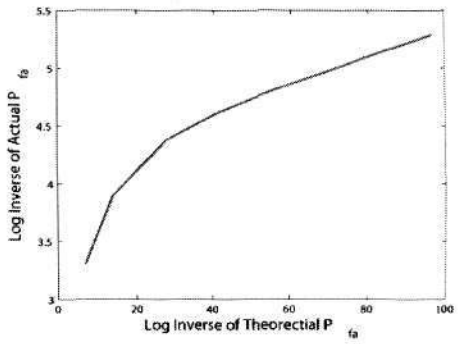

Figure 3.18: *This figure shows the actual P_{fa} vs the theoretical one for the OS-CFAR detector over the course of the carpark experiment.*

The OS-CFAR detector was derived based on a number of assumptions, namely a known noise signal distribution (assumed exponential), and an intra range-bin measurement independence assumption. Only when these assumptions are valid, will the actual P_{fa} meet the theoretically desired one. The result of figure 3.18 therefore shows large discrepancies between the theoretical and actual rate of false alarms for the carpark test. For land based autonomous navigation with radar, frequent reflections from the ground can corrupt the noise signal distributions and result in increased false alarm rates. Furthermore, when landmarks are present some correlation is introduced between successive range bins which may result in the biasses within the moment estimation.

Other parameters in the CFAR thresholding algorithm are the window width, W, and the k-value. The effects on the false alarm rate while varying the window width, W, and k, are shown in figure 3.19. Increasing the window size, W, can improve the moment estimation when no landmark signals enter the sliding window. However, at ground level for land based autonomous navigation, high landmark density can bias the estimation for larger windowing widths. For an ordered statistics approach, the $k-value$ k_{os} is used as the estimate for the moments of the noise distribution. The window width was fixed at $W = 20$ (for both the leading and lagging sliding windows), and k_{os} was altered.

As is common in the detection literature, to analyse the performance of a given detector, the Receiver-Operating-Characteristics (ROC) curve is adopted to plot the detection probability versus the false alarm probability. An ideal detector is determined as one that has a unity detection probability while simultaneously maintaining

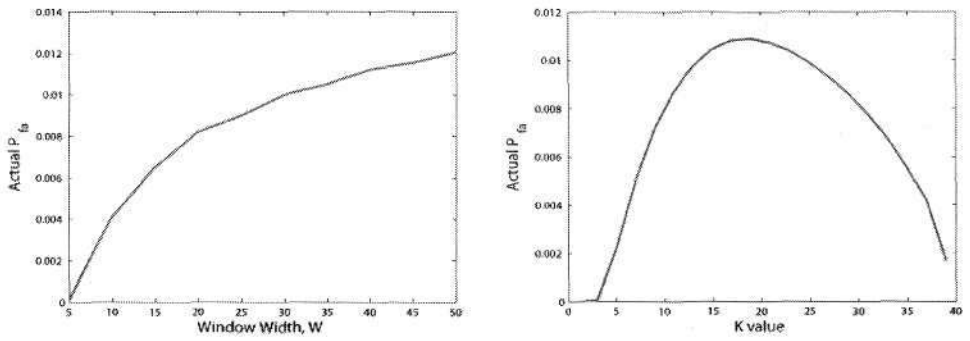

(a) (b)

Figure 3.19: *Actual false alarm rate for varying OS-CFAR detector parameters, with the theoretical P_{fa} set at 1×10^{-24}.*

a zero false alarm probability. In the detection literature, where ROC curves are generally applied, the surveillance region is fixed and a single target is maneuvering. The detection probability of that given target can then readily be plotted as a function of the false alarms reported. For autonomous mapping however, the surveillance region as well as the landmark number and type changes with time as the vehicle maneuvers. Standard detection ROC curves and mapping ROC curves therefore cannot be interpreted in the same manner.

In this analysis, the average detection probability over the course of the carpark test is used. This is obtained by taking the number of detections in each scan and comparing with the number of true landmarks within the senors field of view. Since individual landmarks have varying detection probabilities, performing individual ROC tests for each landmark is infeasible. Therefore, for detector comparison, an averaged detection probability for all landmarks was chosen, and hence the reported detection probabilities, do not indicated those of the individual landmarks present the in scene. Furthermore, the average number of false alarms over the entire trial is used. While this compromises the interpretation of the actual values plotted, it serves as a common basis of comparison between each detection algorithm presented in this chapter.

Taking this into consideration, for the three detectors discussed, the corresponding ROC curves are shown in figure 3.20. The figure thus shows the improved performance of the OS-CFAR routine over the previously used landmark detection methods in autonomous navigation literature. Also included is the inferior Cell Averaging (CA) processor (see appendix B). The maximum intensity approach, limits the number of measurements to one per bearing angle, and therefore has a large number of missed detections indicated by the lower detection probability. The constant threshold ROC

is also shown to have a reduced average detection probability for the same false alarm rate when compared to the OS-CFAR ROC. Consequently, the result highlight that for a given false alarm probability, the CFAR detector displays the maximum average landmark detection probability, and thus verifies its advantages over traditional detection methods.

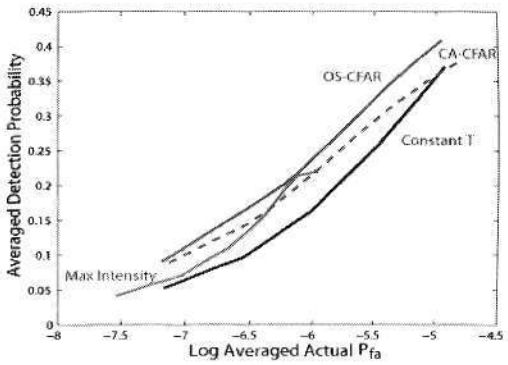

Figure 3.20: *ROC for the various landmark detection algorithms in the carpark environment.*

3.6 Conclusions

This chapter concerned itself with the interpretation of measurements from popular exteroceptive sensors, for the purpose of autonomous navigation. It was shown that, through various methods of modulation, the information available from a measurement varies with sensor type. It was shown how laser and polaroid sonar sensors can be regarded as returning pre-processed information as the landmark detection algorithms are typically internally performed. For imaging sensors such as MMWRs, underwater imaging sonars and cameras however, the measurement can be considered as containing raw signal intensity measurements without any landmark detection pre-processing. It was also shown how imaging sensors can contain information from multiple down-range landmarks in a single power spectrum, consequently highlighting the fallacies of standard detection and modeling methods in the literature. The adaptive threshold method with CFAR properties was introduced for performing landmark detection with an imaging sensor. This detector assumes some statistics on the signal and exploits them to attempt to obtain a statistical threshold, analogous to the normalised innovation square threshold used for data association.

From the carpark analysis however, it can be seen that the actual resulting statistics of the detector differ drastically from the theoretical ones. This is primarily due to violation of the idealistic assumptions made in the detectors derivation. However,

in terms of maximising the detection probability while minimizing the false alarm probability, the CFAR approach was demonstrated to out perform standard methods of landmark detection used in previous autonomous navigation applications with imaging sensors. Thus this chapter showed that an adaptive CFAR approach, is superior to previously used detection methods for autonomous navigation with imaging sensors.

Chapter 4

Measurement Uncertainty in Grid Based Frameworks

The previous chapter developed methods of producing scan maps of a given environment from the landmark detections registered by a detection algorithm. Scan maps themselves, contain no statistical information and are simply plots of scans registered over the history of the vehicle trajectory. Such maps fail to encapsulate the two major sources of uncertainty in a map, namely the uncertainty in the location of a landmark due to measurement noise, and the uncertainty in its very existence given a measurement. As a result of their binary representations (detection or no detection), they are of limited use to the probabilistic autonomous navigation community.

To encapsulate the inherent uncertainty in the map, as outlined previously in section 2.1.2, Grid-Based (GB) and Feature-Based (FB) methods have emerged as the most popular approaches. This chapter concerns itself with the stochastic formulation as well as the measurement models commonly used in previous GB mapping solutions. GB approaches infer a probabilistic representation of the map through a tessellation of the continuous mapping state space and recursively propagate a probability of landmark presence (or Occupancy) in each grid cell over the history of measurements, and known vehicle poses. This chapter highlights for the first time, that current measurement likelihoods implementable in a GBRM framework fail to adequately incorporate a major aspect of measurement uncertainty - namely the landmark detection uncertainty and that caused by spurious measurements. As a result, the measurement input to the framework is adjusted from a range measurement to a detection measurement, with corresponding approximate solutions being proposed and analysed. The remaining structure of this mathematically consistent and popular framework remains unaltered and the standard intra-cell independence assumption is maintained throughout the chapter.

4.1 Introduction

At its most crude level, a map can simply infer a unity occupancy probability for cells in which a detection is registered, and zero (indicating a cell free of landmarks) elsewhere. Such an approach however clearly disregards the realistic situations of missed detections and spurious measurements and can result in erroneous maps. For example, if the probabilistic map built by the robot from the laser sensor measurements in the carpark environment was a binary representation of the scan map in figure 4.1(a), autonomous navigation would be seriously compromised. A probabilistic representation of the same data, in the form of an occupancy map using the 'forward mapping' algorithm [39], can be seen in figure 4.1(b). The stochastic modeling of the sensor measurements can be used to recursively propagate occupancy random variables and handle the randomness of real sensor data. Probabilistic map representations are therefore critical to produce consistent spatial representations of the surrounding environmental landmarks.

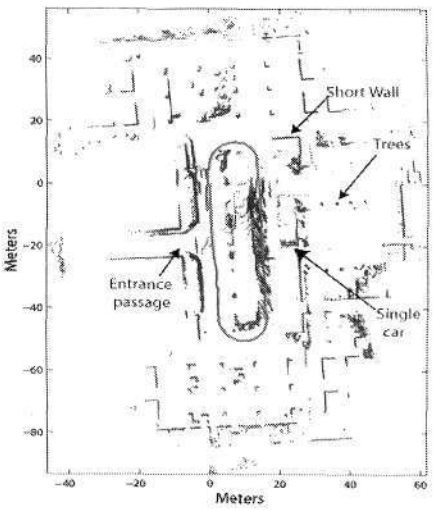

(a) Carpark Environment: Laser Scan Map

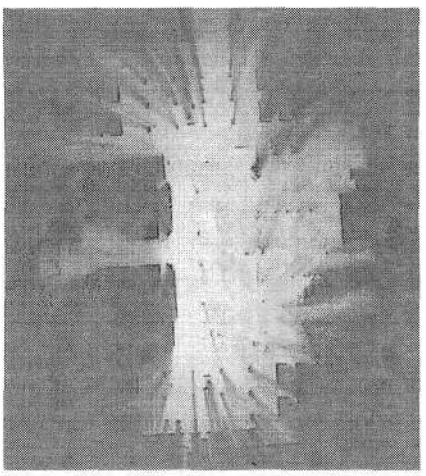

(b) Carpark Environment: Laser Occupancy Map

Figure 4.1: *This figure shows the scan map of the carpark environment using laser measurements and an occupancy map representation of the same measurement data. The occupancy of a given map cell is represented by a white-black colour scale, with white denoting emptiness and black denote occupied.*

As discussed in the previous chapter, there are number of various measurements available from a given exteroceptive sensor, especially from imaging exteroceptive sensors. For a planar autonomous navigation application, the most commonly used

measurements are relative range and bearing, (r, θ) readings to hypothesised features (or landmarks) in the environment. Some approaches consider the collection of (r, θ) measurements as conditionally independent [6], [13], [12], while some consider them jointly as a single 'scan' [14], [40], [46]. However, a measurement can come in other forms. Imaging sensors, for example, can have measurements comprising signal intensity samples from the surrounding environment, or can consider the measurement as a binary random variable indicating a detection (or non-detection) as reported from the landmark detection algorithm, without considering the range and bearing of the detection. The suitability of certain measurements (and their corresponding likelihoods) to the given state estimation problem is initially examined in this chapter. The classical probabilistic GBRM formulation is then shown to require the use of a priori known measurement likelihoods whose values are typically either assumed, or learned from training data [37]. Furthermore the likelihoods used to propagate the occupancy map variables are shown to be independent of the state of interest and are instead derived from the spatial uncertainty of the detected point. This consequently allows for the use of a discrete Bayes filter as a solution to the problem, as discrete occupancy measurement likelihoods are used.

In this chapter, it is shown for the first time, that once the measurement space is re-defined, theoretically accurate and state dependant measurement likelihoods can be obtained and used in the propagation of the occupancy random variable. The required measurement likelihoods for occupancy filtering are in fact those commonly encountered in both the landmark detection and data association hypotheses decisions. However, the required likelihoods are generally *a priori* unknown as they are typically a highly non-linear function of the landmark's signal-to-noise ratio and the surrounding environment. The probabilistic GBRM problem is therefore reformulated as a continuous joint estimation problem where the measurement likelihoods are treated as continuous random states which must be jointly estimated with the map. In particular, this work explicitly considers the sensors detection and false alarm probabilities in the occupancy mapping formulation. A particle solution is then proposed which recursively estimates both the posterior on the map and the measurement likelihoods.

4.2 Estimation Theoretic Problem Formulation

As previously outlined in section 2.2.1, probabilistic GBRM requires the recursive evaluation of the density on the map,

$$p_{k|k}(M_k|Z^k, X^k) \tag{4.1}$$

which encapsulates the complete uncertainty of the map at time k, M_k, given the history of sensor measurements, Z^k, and the vehicle trajectory, X^k. This can be propagated in time via the Bayes recursion,

$$p_{k|k}(M_k|Z^k, X^k) = \frac{g(Z_k|M_k, X_k)p_{k|k-1}(M_k|Z^{k-1}, M_{k-1}X^k)}{\int g(Z_k|M_k, X_k)p_{k|k-1}(M_k|Z^{k-1}, M_{k-1}, X^k)dM_k}. \tag{4.2}$$

For the GBRM problem, the entire map, $M = [m^1_{(x,y)}, \ldots, m^{\mathfrak{q}}_{(x,y)}]$, which can be considered a vector of $\mathfrak{q}$ variables, each containing the true landmark occupancy in the cell centered at global cartesian coordinate (x, y) in the continuous mapping state space. For GB approaches, the map is *a priori* discretised, implying that the number of elements in the map vector state, M, is *known*, i.e. $\mathfrak{q}$ is a known constant for GB approaches, and $\hat{\mathfrak{q}}(k) = \mathfrak{q}\ \forall\ k$. As described previously in section 3.4.3, the measurement is also considered a *vector* measurement where, $Z_k = [z^1_k, ..., z^{\mathfrak{z}(k)}_k]$, contains $\mathfrak{z}(k)$ measurements at time k, which are incorporated in the Bayes recursion of eqn.(4.2). With a sensor of fixed range, the *number* of measurements at each time instant, $\mathfrak{z}(k)$, is also a fixed known constant. Furthermore, each vector, Z_k, comprises measurements from a subset of the entire grid map, M. If $FOV(X^k)$ contains the indices of the grid cells that have entered the field-of-view of the sensor over the trajectory, X^k, then let,

$$M_k = FOV(X^k) \cap M$$

and thus measurement likelihood in eqn.(4.2) is written as, $g(Z_k|M_k, X_k)$. The significance of this is that the *number* of measurements at any given time k, $\mathfrak{z}(k)$, then equals the *number* of map cells within the sensor field of view (and represented by the vector M_k), i.e. each measurement, z^n_k, in Z_k, originates from a discrete cell in the map subset M_k, and whose likelihood is represented by, $g(Z_k|M_k, X_k)$. Thus the measurement for the GBRM problem is a vector. This implies that the standard vector-based measurement equation used for autonomous navigation algorithms,

$$Z_k = h(M_k, X_k) + w_k \tag{4.3}$$

with $h(\cdot)$ typically being a non-linear measurement model, and w_k representing the additive measurement noise, is valid since all measurements in Z_k are a function of M_k and X_k. Note this is not a trivial observation and validates, for the first time, the application of all subsequent vector based estimation theoretic algorithms. The following chapter highlights that FBRM (and FB-SLAM) approaches violate this condition, discusses the consequences, and presents possible solutions to the resulting problems.

4.2.1 The Filtering State Space

In FBRM approaches, if a feature is extracted from the raw measurement data, it is assumed to exist. This assumption is explicit in that the probabilistic sum under the distribution of its spatial co-ordinates is unity, i.e. the feature *definitely* exists somewhere within the region modeled by the density function. Therefore, only the continuous spatial co-ordinates are filtered. In GBRM, since the continuous spatial state space of the surveillance region is tesselated into discrete cells, filtering does not occur in the spatial state space. Instead, each discrete spatial cell is assigned a map state, $m_{k,(x,y)}$, denoting the probability, at time k, of a landmark occupying the cell centered at the discrete spatial co-ordinates (x, y). In this work, this is referred to as the *occupancy state space* as opposed to the *spatial state space* typically considered FB maps. The state variable, $m_{k,(x,y)}$, assigned to each cell is a discrete binary random variable which typically has two states - Occupied (O, or $m_{k,(x,y)} = 1$) and Empty (E, or $m_{k,(x,y)} = 0$), indicating the presence of a landmark or empty space. The estimate of $m_{k,(x,y)}$ is confined to exist on the bounded region $[0, 1]$ and thus,

$$P_k(m_{k,(x,y)} = O) = P_k[m_{k,(x,y)} \geq 0.5] \tag{4.4}$$

$$P_k(m_{k,(x,y)} = E) = P_k[m_{k,(x,y)} \leq 0.5] \tag{4.5}$$

and these two states being exclusive and exhaustive implies,

$$P_k(m_{k,(x,y)} = O) + P_k(m_{k,(x,y)} = E) = 1. \tag{4.6}$$

Note that the grid based approach allows for cells to be empty as the total probabilistic sum in each cell is always unity, therefore satisfying the discrete probability density function unity sum property. In this case the measurement likelihood $g(Z_k|M_k, X_k)$ denotes the probability of the on-board range finding devices receiving a measurement vector, Z_k, at time k, given the occupancy probability of the map cells within the sensor FOV, M_k and the vehicle pose X_k.

4.2.2 Hybrid Solutions

The optimal solution to the probabilistic mapping problem should encapsulate the merits of both the feature and grid based map approach. Fusing the filtering state space of both complimentary approaches, would provide the optimal solution in terms of jointly filtering both the estimates on the spatial parameters of the landmark and its occupancy estimate. To date, a theoretically sound approach which unifies the feature based and grid based mapping algorithms remains elusive. Approaches have been used in the past [44], which invoke an independence assumption to allow for separate filters to propagate the spatial parameter estimates and the occupancy

estimate. That is, a GBRM filter is applied to the region (x, y) in which a feature has been declared according to the feature based mapping algorithm. While such an approach may work reasonably well in practise, and is intuitively appealing, this section shows that by doing so theoretically nullifies the spatial filtering element of the algorithm as the spatial and occupancy estimates are highly dependant on each other.

As stated previously, in feature based approaches, when a feature is declared present, its spatial co-ordinates are initialised in the filter in the form of a *probability density function* $p_{k|k}(m_k|Z^k, X_k)$[1]. Whilst this density function describes the posterior estimate of the landmarks spatial state, it is also providing an estimate of the occupancy state since the integral of the density function under a region, $S \in \mathbb{R}^{n_m}$, equates to the probability of the feature existing in that region S. Bayesian probabilistic based filtering approaches, which now dominate modern robotics algorithms [3] require the system variables to be modeled by such density functions. However, a fundamental property of the probability density function is that at any time k,

$$\int_S p_{k|k}(m_k|Z^k, X_k) = 1 \tag{4.7}$$

i.e. when integrated over the entire surveillance region. In the hybrid approach, where the grid based filtering over the occupancy state space provides an estimate of the cells' occupancy, eqn.(4.7) becomes,

$$\int_S p_{k|k}(m_k|Z^k, X_k) = \sum_{(x,y)\subseteq S} P_{k|k}(m_{k,(x,y)} = O|Z^k, X_k) \tag{4.8}$$

which intuitively states that the probability of a landmark being present within the entire region of the continuous spatial state space $\mathbb{R}^{n_m}$ (regardless of the form of the density function, $p_{k|k}(m_k|\cdot)$) is given by the sum of the posterior occupancy estimate $P_{k|k}(m_{k,(x,y)} = O)$ in each tesselated discrete cell within region S. However, these posterior occupancy estimates may exist anywhere within the bounds $[0, 1]$, the estimate of which is determined from the GBRM filter being adopted. Therefore not only are the spatial and occupancy states dependent but, more critically, when they are jointly considered, the unity volume property of the probability density function may be violated. In the case when the posterior occupancy estimate is not unity, the posterior density function modeling the estimate of the spatial state, $p_{k|k}(m_k|Z^k, X^k)$, is *not* a pdf, which compromises all the stochastic filtering techniques used to propagate it as well as methods of extracting estimates from it. Herein lays the difficulty

[1]Note the notation change, m_k implies a spatial estimate of a feature at time k whereas $m_{k,(x,y)}$ implies an occupancy estimate in the cell at (x, y) at time k.

of the optimal mapping solution, as the propagation of system variables modeled by such functions remains a tough research challenge. The remainder of this chapter examines the theoretical modeling of a measurement for the GB mapping framework.

4.3 The Discrete GBRM Filter: Range Measurements

This section describes the mathematical frameworks used in evaluating the GBRM recursion of eqn.(4.2) where the measurements are provided by an active range finding sensor. For clarity of exposition, a one-dimensional system shall be adhered to where the on board sensor provides range-only measurements. The framework can be readily expanded to include the more common two-dimensional measurement which typically includes a bearing reading. Thus for the recursions, in individual measurement at time k, $z_k \in Z_k$, comprises range readings reported by the sensor. The range measurement based mapping framework is well established in the autonomous navigation community since the seminal work performed by A. Elfes during the development of the Occupancy Grid Framework [20], [39], [37], [34].

In GBRM problems, the map state M_k can consist of an arbitrary number of hypotheses but usually contains $\{O, E\}$ in the case of a Bayesian approach [39] and $\{O, E, U\}$ in the case of a Dempster-Shafer approach [38], with U denoting the 'unknown' state. Thus, $P_{k|k}(m_{k,(x)} = O)$ contains an estimate on the occupancy state space, at the discrete one-dimensional coordinate x. Since the Bayesian grid mapping framework is a binary discrete estimation problem, probability distribution functions are used as opposed to probability density functions. Therefore the grid based recursion is written,

$$P_{k|k}(m_{k,(x)}|z^k, X^k) = \frac{G(z_k|m_{k,(x)}, X_k)P_{k|k-1}(m_{k,(x)}|z^{k-1}, X^k)}{\sum_{m_{k,(x)}} G(z_k|m_{k,(x)}, X_k)P_{k|k-1}(m_{k,(x)}|z^{k-1}, X^k)}. \tag{4.9}$$

Since the true state of $m_{k,(x)}$ is binary, the recursion can have a separate form for each of the occupancy states $m_{k,(x)} = O$ and $m_{k,(x)} = E$. In the case of $m_{k,(x)} = O$, as before, assume at time $k-1$ that the prior probability $P_{k|k-1}(m_{k,(x)}|z^{k-1}, X^k)$ is available. If the covariance of the range measurement is denoted, Σ_z, the range based GBRM filter proceeds to calculate the posterior $P_{k|k}(m_{k,(x)}|z^k, X^k)$ at time k as follows,

---

The Range based GBRM Filter

At time $k \geq 1$,

Step 1: *Time Update Step*

- $P_{k|k-1}(m_{k,(x)} = O|z^{k-1}, X^k) = P_{k-1|k-1}(m_{k-1,(x)} = O|z^{k-1}, X^{k-1})$

Step 2: *Measurement Likelihood Calculation Step*

- For $m_{k,(x)} = O$, $G(z_k|m_{k,(x)} = O, X_k) = \frac{1}{\sqrt{2\pi\Sigma_z}} \exp \frac{-(z_k - d)^2}{2\Sigma_z}$
- For $m_{k,(x)} = E$, $G(z_k|m_{k,(x)} = E, X_k) = 1 - G(z_k = r|m_{k,(x)} = O, X_k)$ where $d = x - x_k$ is the range to the landmark.

Step 3: *Measurement Update Step*

- $P_{k|k}(m_{k,(x)} = O|z^k, X^k) =$

$$\frac{G(z_k|m_{k,(x)} = O, X_k) P_{k|k-1}(m_{k,(x)} = O|z^{k-1}, X^k)}{P_{k|k}(z_k|m_{k,(x)}, X^k)}$$

---

where in the update step, according to Kolmogorov's total probability theorem,

$$P_{k|k}(z_k|m_{k,(x)}, X^k) = \sum_{m_{k,(x)} \in \{E,O\}} G(z_k|m_{k,(x)}, X_k) P_{k|k-1}(m_{k,(x)}|z^{k-1}, X^k) \tag{4.10}$$

with,

$$P_{k|k-1}(m_{k,(x)} = E|z^{k-1}, X^k) = 1 - P_{k|k-1}(m_{k,(x)} = O|z^{k-1}, X^k)$$

according to the unity probabilistic sum constraint. MAP estimates are then commonly used to extract an optimal estimate of the map (in terms of which cells are occupied) such that,

$$\hat{m}_k = \underset{m_k}{argmax}\, P_{k|k}(m_k = O|z^k, X^k). \tag{4.11}$$

From this it can be seen that the range reading is used to distribute the measurement likelihood according to the sensor noise model, in this case being Gaussian. z_k and d are discretised range values according to the dimensions of the surveillance region tessellation. The likelihood generally has its maximum at the range reported by the sensor. In some grid mapping approaches [36], the empty measurement likelihood, $G(z_k|m_{k,(x)} = E, X_k)$ has been modified to model a uniform distribution since

'the landmark has an equal chance of being detected anywhere along the beam'. Using this framework, along with modeling the tessellated space as a zero order Markov Random Field to allow for independent cell updates, has become the standard in grid based autonomous mapping algorithms.

4.3.1 Range Measurement Likelihood

Whilst the previous range based GBRM filter is extremely popular in the literature, this section highlights some of the pitfalls with the formulation, specifically the measurement likelihoods used. A fundamental property of any tracking algorithm, requires the system to have state dependant measurements (i.e. eqn.(4.3)). For the FB case, if m_k describes the 2D spatial estimate of a hypothesised feature, then let $m_k^{(x)}$ correspond to its individual x state estimate. The range measurement is then trivially obtained through,

$$z_k = x_k - m_k^{(x)} \tag{4.12}$$

Thus when the filtering state space contains a single dimension spatial estimate of the map feature, the measurement, being a range reading, is state dependent. This can be seen from the examination of the standard measurement equation for FB methods,

$$z_k = h(m_k, X_k) + w_k \tag{4.13}$$

where $h(\cdot)$ relates the state to the measurement through eqn.(4.12) and w_k is the additive Gaussian noise.

In the case of the GBRM problem, the state space is not the spatial parameter, $m_k^{(x)}$, but the occupancy state at the discrete (x) coordinate, $m_{k,(x)}$. That is, the space of the landmark existing or not existing. Thus the measurement equation becomes,

$$z_k = h(m_{k,(x)}, x_k) + w_k. \tag{4.14}$$

Assuming that $m_{k,(x)} \in \{E, O\}$, this chapter poses the question:

> what is the function $h(\cdot)$ that relates $m_{k,(x)}$ and x_k to z_k, where z_k is range reading ?

From examination of the classical GBRM recursion in section 4.3, it can be seen that with respect to the *spatial state space* from eqn.(4.13), that the measurement likelihood becomes,

$$G(z_k | m_k^{(x)}, X_k) = \frac{1}{\sqrt{2\pi\Sigma_z}} \exp \frac{-(z_k - d)^2}{2\Sigma_z} \tag{4.15}$$

where the Gaussian measurement noise component, w_k, is white with covariance Σ_z. Previous GBRM formulations consequently adopt the same likelihood (Step 2),

however when considered with respect to the *occupancy state space*, (i.e. the space under consideration in GBRM approaches), taking the discrete range reading to be, $z_k = d_{-2}$, the corresponding *occupancy* measurement in the cell centered at, d_{-2}, becomes,

$$\frac{1}{\sqrt{2\pi\sigma^2}} e^{\frac{(d_{-2}-d)^2}{2\sigma^2}} + 0$$

$$\text{i.e. } h(\cdot) = \frac{1}{\sqrt{2\pi\Sigma_z}}.$$

This process is depicted in figure 4.2, outlining the generation of occupancy state measurements given a range reading.

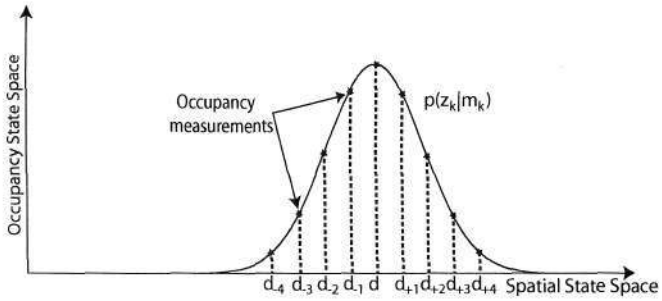

Figure 4.2: *This figure shows the indirect generation of occupancy measurements from standard range-based algorithms. The evaluation of the Gaussian range likelihood in the surrounding discrete cells with spatial states, $d_{-4}, \ldots, d_{+4}$, are used as occupancy measurements.*

From this observation, it can be seen that when the range measurement likelihood is considered with respect to the occupancy state space, (*a*) a noise free measurement is used and (*b*) the measurement is independent of the state of interest (the occupancy random variable). Furthermore, the occupancy and the spatial distribution of the location estimate are merged in such approaches. For instance, in the case of a spurious detection, the occupancy probability at that location is related to the sensors probability of false alarm. This is completely independent from that detections spatial uncertainty (which is commonly uniform within the surveillance region). This measurement is a function of the range reading, d_{-2}, and the range measurement noise, σ^z. However, with respect to the filtering state of interest, m_k, it can be seen that such a measurement has no dependance on the occupancy state. Therefore, this shows that range-based approaches adopt a *state-independent* measurement for propagation of the occupancy state estimate. Furthermore, the occupancy measurement is discrete, which allows for the subsequent discrete Bayes filter implementation proposed in the literature [36], [39], [37].

Using such a measurement likelihood compromises the independence between a landmarks existence probability, and its spatial uncertainty distribution (assuming that it exists). Furthermore, the measurements are deterministic (there is no associated stochastic measurement noise) which allows for the discrete Bayes solution that is common in the literature. In this thesis, it is therefore proposed that the range at which the sensor reports the presence of a landmark can be used in the filtering of a features spatial state estimate. However, while this may be correlated with the sensor's ability to correctly detect the landmark[2], the reported range at which the feature is hypothesised to exist does not provide a measurement of its occupancy state, since the occupancy state and the range measurement are independent. Thus for the GBRM problem, the measurement z_k as a range reading is not a state dependent measurement.

To the authors knowledge, this observation has never before been acknowledged in the literature, and GBRM algorithms frequently adopt range-based measurements in the filter recursion. Due to the high detection reliability of commonly used sensors such as the SICK LMS, seemingly impressive results are still achievable through the use of intuitive, as opposed to theoretically accurate, measurement models. However for the case of imaging sensors for outdoor or underwater domains, detection reliability deteriorates greatly both in missed detections and spurious measurement count. Consequently, the practical implications of the state independent range measurements for the GBRM problem become evident, as shown later in sections 4.7 and 4.8.

4.3.2 Redefining the Measurement Space

This chapter proposes that to have a truly state dependant measurement, let the measurement space be redefined as binary with $z_k \in \{Detection\ (D), No\ Detection\ (\bar{D})\}$ as opposed to a range reading. Doing so allows for $h(\cdot)$ to be a function of the state of interest and therefore validates the measurement for the GBRM problem. The GBRM measurement likelihood then becomes,

$$G(z_k = D|m_{k,(x)}, X_k)$$

which is also referred to a the probability of detection (if $m_{k,(x)} = O$) and the probability of false alarm (if $m_{k,(x)} = E$). Furthermore, when the measurement space is altered as such, the measurement equation, $h(\cdot)$, becomes a non-linear function of the occupancy state. Therefore, previous occupancy sensor models are in fact subtly assuming complete knowledge of the sensors' detection characteristics (probabilities of detection and false alarm), as the likelihoods are calculated according to a Gaussian function evaluated at the discrete cell locations surrounding the range

[2]If, for example, the detection probability deteriorates with range from the sensor.

reading. That is, the detection measurement likelihood, $p(z_k = D|m_{k,(x)} = O)$ (and $p(z_k = D|m_{k,(x)} = E)$), are assumed completely known. Note this is typically the case most for likelihood calculations including data association [13] and particle filter SLAM solutions [40]. This will be outlined in more detail in the following section which outlines the reformulation of the grid based mapping filter using the detection measurement space.

4.4 The Discrete GBRM Filter: Detection Measurements

This section proposed a new mathematical framework for the GBRM problem, where the measurement exists in detection space, rather than the spatial state space as is normally the case. When the measurement space becomes the detection space, the measurement likelihoods (for both detection and non-detection) become real signal processing parameters. Consider again the one dimensional problem of estimating the posterior given a history of measurements and the vehicle location,

$$P_{k|k}(m_{k,(x)} = O|z^k, X^k).$$

The measurement history z^k can now be considered as a set of hypothesis decisions on the presence or absence of a landmark (derived through some function of the measured signal intensity) given by the occupancy measurement model. Thus each measurement, z_k, is the output of a likelihood ratio test and can be denoted D if a detection was made, or $\bar{D}$ if no detection was made.

Detection Based GBRM Filter

At time $k \geq 1$,

Step 1: *Time Update Step*

- $P_{k|k-1}(m_{k,(x)} = O|z^{k-1}, X^k) = P_{k-1|k-1}(m_{k-1,(x)} = O|z^{k-1}, X^{k-1})$

Step 2: *Measurement Likelihood Calculation Step*

- For $m_{k,(x)} = O$: $G(z_k = D|m_{k,(x)} = O, X_k) = \int_0^\infty P[\psi_r \geq T_r|\mathcal{H}_1] f_\mu(\mu) d\mu$
- For $m_{k,(x)} = E$, $G(z_k = D|m_{k,(x)} = E, X_k) = \int_0^\infty P[\psi_r \geq T_r|\mathcal{H}_0] f_\mu(\mu) d\mu$

Step 3: *Measurement Update Step*

- $P_{k|k}(m_{k,(x)} = O|z^k, X^k) =$

$$\frac{G(z_k|m_{k,(x)} = O, X_k)P_{k|k-1}(m_{k,(x)} = O|z^{k-1}, X^k)}{P_{k|k}(z_k|m_{k,(x)}, X^k)} \tag{4.16}$$

---

where the measurement likelihoods are those detection probabilities discussed in the previous chapter (section 3.4.2). Note that the reported range of the detection, r, is simply an indicator function for the range bin in which the likelihood should be evaluated. This proposed filter propagates a statistically correct posterior of the occupancy random variable, where the measurement likelihoods are state dependant. This is in contrast to the classical algorithms where functions of the range measurements are used to propagate the occupancy state. Furthermore, when reformulated in this manner, the occupancy measurement likelihoods are identical to those encountered in the signal detection theory which is inherent to active range sensing devices. Thus for the first time, the theoretical dependance between the GBRM problem and the landmark detection problem is highlighted in this thesis. A graphical comparison of the influence of this filter can be seen in figure 4.3, which compares classical approaches (shown previously in section 4.3.1 and figure 4.2), to the newly proposed state-dependent approach. Note again that the range reading, $r = d$, is simply an indicator to specify the location of the Gaussian profile (set as a function of the range noise). In this case, the measurements in the occupancy state space are state-dependent, theoretically derived from the detection statistics and propagated through the filter.

Therefore, to correctly evaluate the posterior estimate on the occupancy state requires both P_d and P_{fa}. In the previous range based GBRM filter, the likelihoods evaluated at the range reported by the sensor are,

$$P_d = \frac{1}{\sqrt{2\pi\Sigma_z}}$$
$$P_{fa} = 1 - \frac{1}{\sqrt{2\pi\Sigma_z}}.$$

which are a function of the range measurement noise. These likelihoods are thus evaluated without any consideration of the true statistics of the detection problem. The signal processing methods and measurement intensity information that may be available, are disregarded. Note that such complimentary likelihoods are only possible under Gaussian noise and landmark signal distributions, as well as a unique decision threshold value, T_{Ri+r}, as depicted in figure 4.4.

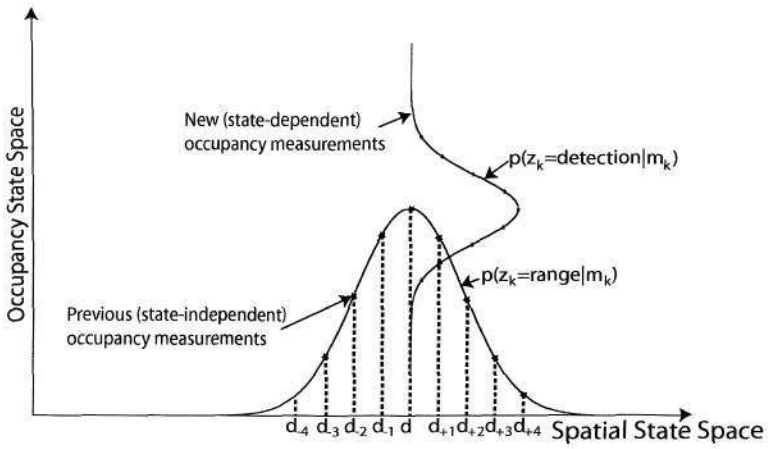

Figure 4.3: *A graphical comparison of the classical occupancy profile with state-independent measurements, and that from the proposed approach with state-dependent measurements. Note that the uncertainty in measurement space is now shifted to the filtering state-space, i.e. occupancy.*

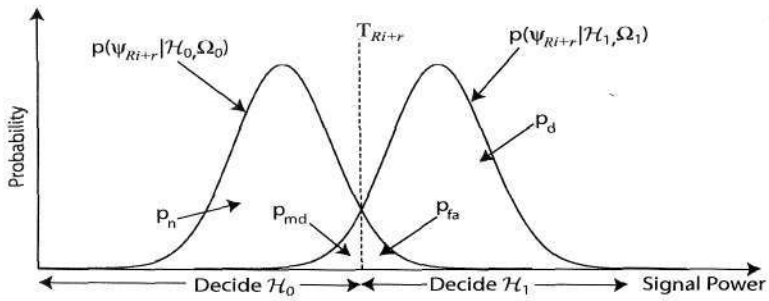

Figure 4.4: *A graphical representation of the received signal classification problem required to ensure* $G(x_k = D|m_{k,(x)} = O, X_k) = 1 - G(z_k = D|m_{k,(x)} = E, X_k)$

As a result of this subtlety, previous occupancy sensor models typically assume complete knowledge of the sensors' detection characteristics (probabilities of detection and false alarm), and the occupancy measurements become discrete and deterministic. Consequently, this assumption allows for each cell to contain a discrete occupancy measurement which can be updated using the discrete log-odds equation (or Dempsters equation in the case of evidential measurements). This is in contrast to spatial estimates which use continuous measurement likelihoods and are propagated in a Kalman or particle filter framework.

In order to ensure deterministic measurement likelihoods in this newly proposed detection based framework, (and consequently validating the applicability of the discrete Bayesian recursion), a number of *a priori* parameters need to be known. Parameters such as distribution type as well as their corresponding moments (see section 3.4.2) for both the noise signal and the landmark signals is required to be fully known. Only under such strict assumptions, do the occupancy measurement likelihoods become deterministic and the discrete Bayes recursion valid.

4.4.1 Filter Comparison using Ideal Measurements Likelihoods

As an example, In this section, the occupancy posterior is propagated for a set of simulated data, illustrating that optimal performance (in terms of estimating the correct number of landmarks) can be achieved when the proposed detection measurement likelihoods are used, as opposed to the commonly adopted range based likelihoods. The signal amplitude in empty cells fluctuates according to an assumed noise model, $p(\psi_{r=1,\ldots,21}|m_{k,(x)} = E, \Omega_E)$ as in figure 4.4. A landmark exists in range bin 11, with other cells empty. The landmark fluctuating signal, $p(\psi_{r=11}|m_{k,(x)} = O, \Omega_O)$, therefore models the change in signal amplitude from a landmark with changing vehicle pose [92]. That is,

$$\psi_{k,r} \sim p(\psi|m_{k,(x=r)} = E, \Omega_E) \; \forall r \; \forall k \tag{4.17}$$

$$\psi_{k,r=11} = \sim p(\psi_{r=11}|m_{k,(x=11)} = O, \Omega_O) + \psi_{k,r=11} \tag{4.18}$$

with k being the time index, r being the range bin index and ψ being the signal amplitude. Ω_O and Ω_E represent the moments of the signal distribution under both hypothesis. Since the moments, Ω_O and Ω_E are known in this example, a threshold, T_r, can be set to achieve any user defined values for P_{fa} [93]. Due to the IID assumption, $T_r = T \; \forall r$, i.e the threshold is a constant value. The corresponding P_d values can then be derived as a function of T. As is evident from figure 4.4, an increase in T has the effect of reducing P_{fa}, whilst simultaneously reducing P_d, given the presence of a landmark.

Figure 4.5 shows an example of sampled measurement data according to eqns

(4.17) and (4.18) where both the noise signal and the landmark signal are Gaussian distributions of known moments. This idealistic case makes the evaluation of the threshold, T relatively easy to perform. Generally, in detection algorithms, the user defined parameter is the probability of false alarm. This is because in typical detection systems, the distribution (but not necessarily the moments) of the noise signal is assumed to be known, and IID in the environment, which allows for a threshold to be set as a function of the desired false alarm probability. As there is no a priori knowledge of the landmarks and their corresponding distribution moments, P_d cannot be a user defined parameter (although in most hypothesis decision algorithms such as data association, it is assumed *a priori* known). Here, since both the moments and the distribution of the noise are known, T_{Ri+r} can be obtained $\forall$ r using the error function, Φ as,

$$T = \arg\min_{T} \left(1 - \Phi\left(\frac{T-\mu}{\sigma}\right) - P_{fa}\right) \tag{4.19}$$

with μ and σ being the mean and standard deviation of the signal noise amplitude within the active range finding sensor. (Note that in the case of unknown moments, if the noise signal is Gaussian distributed, a detector cannot attain CFAR properties, see Appendix B.3). The right hand plot of figure 4.5 therefore shows the corresponding detection measurements obtained from the sampled data, using the outlined Gaussian based detector. Where in this idealistic case of known moments we simply have,

$$z_{k,r} = \begin{cases} D & \text{if } \psi_{k,r} > T \\ \bar{D} & \text{Otherwise.} \end{cases}$$

In this example, the false alarm likelihood is set high at 0.1, due to the small sample window (21x20 cells) to ensure some false alarms fall within the surveillance region.

Assuming measurement independence between each range bin, the occupancy posterior, $P_{k|k}(M_k|Z^k, X^k)$ at each time step, k, is evaluated, where the vector map, $M_k = [m_{k,1}, \ldots, m_{k,21}]$. As a result of the grid based map, and using both detection and non-detections, the measurement is also a vector (section 4.2), $Z_k = [z_{k,1}, \ldots, z_{k,21}]$ and is of equal dimension to the map, M_k. Using the detection threshold determined by eqn.(4.19), a binary detection sequence is obtained, for a given P_{fa}. From this input data, both the range based (section 4.3) and detection based (section 4.4) GBRM filters are compared. For the range-based approach, the reported range of a detection is used in the likelihood, whereas the detection-based approach considers the statistics of the signal. As outlined in section 4.4, using the range-based approaches [39] [36], detection measurement likelihoods are inherently *a priori* assumed and the actual statistics of the detection algorithm are ignored. To thoroughly analyise the algorithms, the occupancy posterior was obtained from the scene after 20 updates, with

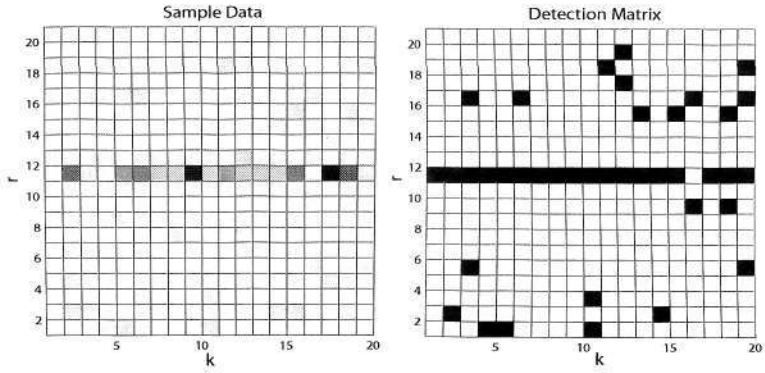

Figure 4.5: *Sample data and the resulting detection matrix. Note numerous false alarms within the surveillance region as the false alarm likelihood is set to 0.1. For the signal data, the darker the shade of gray, the higher the measured power intensity in that range bin. The detection matrix output shows black for* $z_{k,r} = D$ *in that cell and white for* $z_{k,r} = \bar{D}$.

100 Monte Carlo runs being performed for each simulated landmark of varying mean SNR (and consequently varying P_d). Cells in which the posterior occupancy probability, $P_{k|k}(M_k|Z^k, X^k)$, is greater than 0.51 are deemed occupied, whereas cells with values less than 0.49 are deemed empty. Figures 4.6, 4.7, 4.8, and 4.9 then show the estimated number of occupancy cells from both the range based GBRM, and the proposed detection based GBRM. The false alarm rates for each test are $P_{fa} = 5 \times 10^{-2}$, $P_{fa} = 1 \times 10^{-1}$, $P_{fa} = 3 \times 10^{-1}$ and $P_{fa} = 5 \times 10^{-1}$ respectively. The range variance for the range based GBRM, is set at the commonly used value of 0.5. The figures then plot the average estimated number of landmarks, over each Monte Carlo test, for each landmark of varying detection probability. The detection sequence plotted is a sampled Monte Carlo sequence, where the detection probability of the landmark in range bin 11, $P_d \approx 0.65$. Given the resulting threshold value, T, and the moments of the landmark signal, the detection probability can be empirically obtained using the error function.

The results from the posterior of the proposed Detection-GBRM filter with ideal measurements likelihoods verifies the performance with respect to estimating the correct number of landmarks present in the data. In all tests, the proposed method outperforms the standard approaches, with the improvements becoming more evident at higher false alarm rates. For all tests, the proposed filter reports far less 'ghost' landmarks of low detection probability, which may be common to rugged outdoor terrains. As the false alarm rates increase, the range likelihood based GBRM consistently over estimates the true number of landmarks present in the dataset. This error is drastically reduced by the proposed filter as the true statistics of the detection

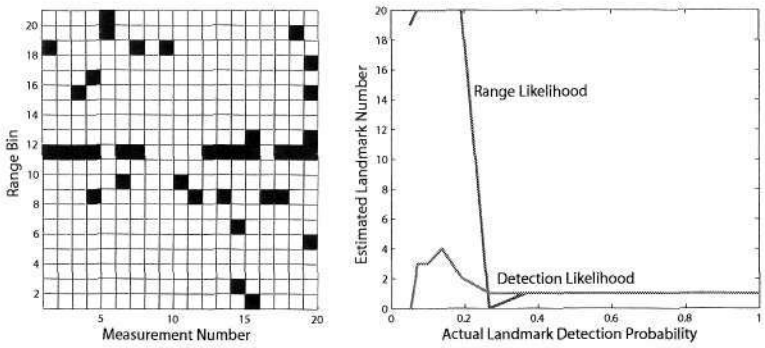

Figure 4.6: *Comparison of the proposed Detection-GBRM filter with ideal measurements, and that of the range-GBRM, with* $P_{fa} = 5\times10^{-2}$.

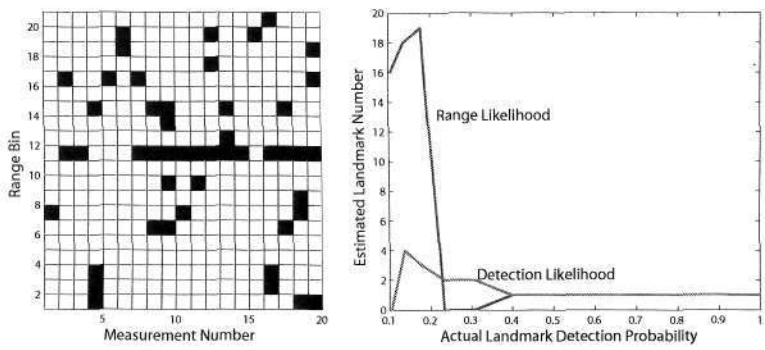

Figure 4.7: *Comparison of the proposed Detection-GBRM filter with ideal measurements, and that of the range-GBRM, with* $P_{fa} = 1\times10^{-1}$.

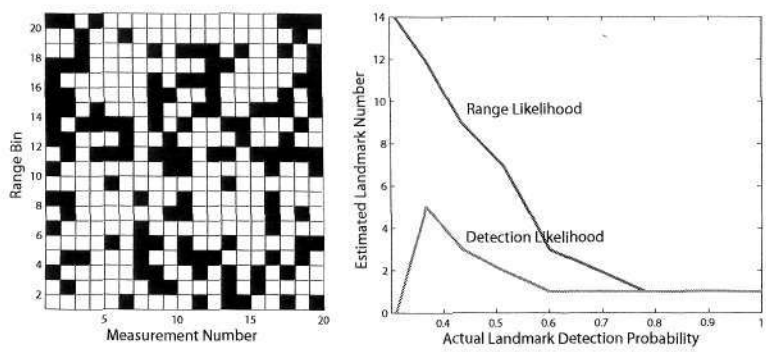

Figure 4.8: *Comparison of the proposed Detection-GBRM filter with ideal measurements, and that of the range-GBRM, with* $P_{fa} = 3\times10^{-1}$.

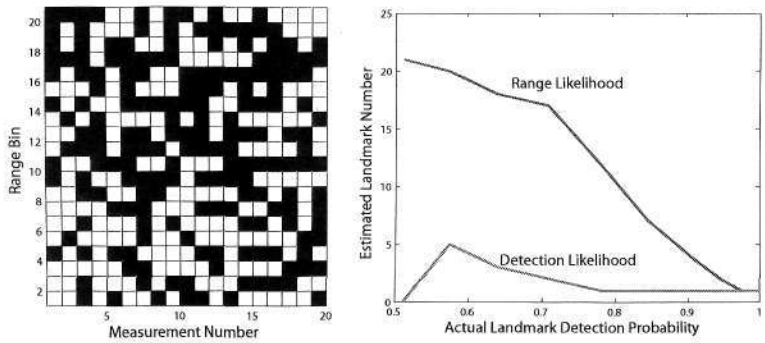

Figure 4.9: *Comparison of the proposed Detection-GBRM filter with ideal measurements, and that of the range-GBRM, with* $P_{fa} = 5\times10^{-1}$.

measurement process are directly incorporated into the GBRM filter. This theoretically accurate approach therefore presents and improved solution to the GBRM problem, especially in situations of high spurious measurements and high detection uncertainty. By examining the theoretical sources of this measurement uncertainty, and formulating it directly into the filter recursion, an improve approach has been proposed.

While this section highlights the improvements of the proposed filter, the likelihoods used in the filter recursion here were *a priori* known. In practise, naturally such likelihoods for a given landmark are unknown and must be estimated from the measurement data. Furthermore, the likelihoods are dependant on the detection algorithm adopted. Following from the detection algorithms introduced and analysed in the previous chapter, the following section outlines the measurement equations for a MMWR sensor.

4.4.2 Measurement Equation for Imaging Radar

If the true grid map is the vector, $M = [m_{(1)}, \ldots, m_{(R)}]$, an imaging radar sensor will produce a raw measurement, $Z_k^{(i)} = [\psi_1, ..., \psi_R]$, which is a function of M, and the landmark signal distribution, $p(\psi_r|m_{(r)} = O, \Omega_O)$, corrupted by the measurement noise, $p(\psi_r|m_{(r)} = E, \Omega_E)$. Assuming *a priori* knowledge on the signal distributions under landmark absence and presence, let the raw measurement equation for the radar sensor be written as,

$$\Psi = f(M, \Omega_O) + v(\Omega_E). \tag{4.20}$$

Note that, while the distribution of the noise is assumed to be known, unlike most filtering formulations[3], the moments remain *unknown* and must be estimated from the data. In eqn.(4.20), v is an IID random variable sampled from the noise signal distribution $p(\psi_r|m_{(r)} = E, \Omega_E)$ and the signal model,

$$f(M, \Omega_O) = \begin{cases} 0, & \text{if } m_{(r)} = E \\ \sim p(\psi_r|m_{(r)} = O, \Omega_O), & \text{if } m_{(r)} = O \end{cases} \tag{4.21}$$

which is then a function of the map vector and the signal distribution moments. A sample spectrum can be seen in figure 4.10, in which v is assumed exponentially distributed.

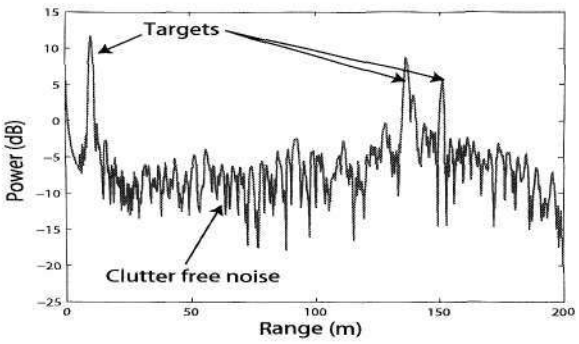

Figure 4.10: *A sample power-range spectrum measurement, $\Psi(M, \Omega_O)$, which is a function of the true state, M, corrupted by exponentially distributed noise.*

For an imaging sensor, that uses a likelihood ratio test, $L(\Psi) \geq T$, to hypothesise the presence or absence of a landmark, the detection measurement likelihood, P_d, is a non-linear function, $h(\cdot)$, of the intensity samples in the power-range spectrum, Ψ, and the decision threshold, T,

$$Z_{P_d} = h_{det}(\Psi, \Omega_{det}) + w \tag{4.22}$$

with w, being the additive measurement noise. The measurement model, h_{det}, depends on the landmark detection algorithm adopted, with Ω_{det} denoting the parameters associated with that algorithm (such as window width, desired false alarm probability, etc., see section 3.4.1).

Assuming an OS-CFAR detection algorithm, $\Omega_{det} = \{W, k_{os}, P_{fa}\}$ where W is the length of a leading and lagging sliding window, P_{fa} is the desired false alarm

[3]White Gaussian noise, for example, assumes known moments. Kalman or particle filter based SLAM and RM algorithms, also assume known noise moments.

probability, and k_{os} is the k-value used to estimate the noise distribution moments. A priori signal distribution assumptions are made on both $p(\psi_r|m_{(r)} = E, \Omega_E)$ and $p(\psi_r|m_{(r)} = O, \Omega_O)$, where the distribution moments Ω_E and Ω_O are generally assumed unknown and must be estimated using the signal intensity information. The measurement model in a given range bin, r, is then derived as [88],

$$h_{det}(\psi_r, W, k_{os}, P_{fa}) = \left(1 + \frac{T_r}{1 + \bar{\Re}_r}\right)^{-2W} \tag{4.23}$$

where,

$$T_r = \tau \hat{\mu}_r \tag{4.24}$$

$$\tau = \arg\min_{\tau} \left(k_{os} \binom{2W}{k_{os}} \frac{(k_{os} - 1)!(\tau + 2W - k_{os})!}{(\tau + 2W)!} - P_{fa} \right) \tag{4.25}$$

$$\hat{\mu}_r = \Psi_{os,k_{os}} \tag{4.26}$$

$$\Psi_{os} = \text{sort}([\psi_{r-G-W}, \ldots, \psi_{r-G}] \cup [\psi_{r+G+1}, \ldots, \psi_{r+G+W}]) \tag{4.27}$$

$$\bar{\Re}_r = \frac{\psi_r - \hat{\mu}_r}{\hat{\mu}_r}. \tag{4.28}$$

Note that in general, radar detection analysis assumes *known* landmark distribution moments [88], [94], [95], [87], [92]. Classical approaches consider only the detection performance of a given algorithm. This work differs however in that filtering problem is the posterior probabilities of occupancy *given* a detection (or non-detection) measurement. Furthermore, in an *a priori* map, the landmark distribution moments are *a priori* unknown, thus the measurement equation is necessary to estimate the likelihoods for the proposed detection-GBRM filter. From these equations it can be seen that to make an estimate of P_d, the mean landmark SNR, $\bar{\Re}$, must initially be estimated in a given range bin. Taking the measured intensity in r, ψ_r, as the raw signal + noise measurement (assuming the existence of a landmark, according to eqn.(4.20)), a local (for a given range bin) estimate of the noise intensity is made through *any* CFAR process [94]. An ordered-statistics approach [90], which is adopted in this work, has been shown to be most robust in situations of high clutter and multi-landmark situations, as is commonly encountered in a field robotics environment. The improved detection vs. false alarm characteristics of this detector were also highlighted in the previous chapter. This detector estimates local noise signal, $\hat{\mu}_r$, as the, k_{os}^{th} element of the sorted (in order of ascending signal magnitude) sliding window, Ψ_{os}. The sliding window, Ψ_{os}, is comprised of the union of the leading, $[\psi_{r+G+1}, \ldots, \psi_{r+G+W}]$, and lagging, $[\psi_{r-G-W}, \ldots, \psi_{r-G}]$ sliding windows of width, W, range bins. The local threshold value, T_r, can then be seen to be a function of the noise estimate, and the scale factor τ. The noise and landmark signal distribution

assumptions required to validate the given measurement equations are,

$$p(\psi_r|m_r = E, \Omega_E = \{\mu\}) = \frac{1}{\mu}\exp(-\psi_r/\mu)$$

$$p(\psi_r|m_r = O, \Omega_O = \{\mu, \Re\}) = \frac{1}{\mu}\exp\left((-\psi_r/\mu) + \Re\right)I_0\left(2\sqrt{\frac{\Re\psi_r}{\mu}}\right)$$

$$p(\Re|\bar{\Re}) = \frac{2\Re}{\bar{\Re}}\exp(-\Re^2/\bar{\Re}).$$

which are common signal distribution assumptions in the radar signal processing literature [94], [90], [88]. Assuming the actual signal statistics are represented by these assumed models, the true rate of false alarm, P_{fa}, is then equal to the desired rate as given as an input parameter to the detector, i.e. $Z_{P_{fa}} = P_{fa}$.

4.5 Discrete GBRM Filter Implementations

The previous section developed the theoretical framework of the proposed detection-GBRM filter, highlighting that state dependant measurements can be obtained by adjusting the measurement space. The improvements of the proposed methods were demonstrated in a simulated environment, using a priori known measurement likelihoods. As these likelihoods are in fact a priori unknown, the measurement equations required were outlined for an MMWR sensor. This section outlines a probabilistic and evidential implementation of the detection-GBRM filter, where the measurements, Z_{P_d} and $Z_{P_{fa}}$ are discrete. Consequently a discrete Bayes and Dempster-Shafer recursion are used to propagate the measurements and estimate the posterior occupancy.

4.5.1 Probabilistic Vector Measurements

Recall from section 3.4.3.1 that probabilistic measurements require a well-understood measurement model. This was outlined for the commonly considered range and bearing measurements from an environmental feature. In the case of the detection-GBRM filter, probabilistic measurements require the signal statistics outlined previously in section 4.4.2 to be valid. Under the assumption that any given landmarks signal will instantaneously disturb the noise signal, the local maxima in a given spectrum are considered to be from potential landmark.

Using the detection measurement space, the filter can then be written as,

$$\begin{aligned} P_{k|k}(M_k = O|z_{k,(r)} = D) &= \frac{Z_{P_d}\mathbf{1}(\psi_{(r)})}{Z_{P_d}\mathbf{1}(\psi_{(r)}) + Z_{P_{fa}}} \\ P_{k|k}(M_k = O|z_{k,(r)} = \bar{D}) &= \frac{Z_{P_{md}}\mathbf{1}(\psi_{(r)})}{Z_{P_{md}}\mathbf{1}(\psi_{(r)}) + Z_{P_n}}. \end{aligned} \tag{4.29}$$

where,

$$\mathbf{1}(\psi_{(r)}) = \begin{cases} 1 & \text{if } \psi_{(r-1)} < \psi_{(r)} > \psi_{(r+1)} \\ 0 & \text{otherwise} \end{cases}$$

and,

$$Z_{P_{md}} = 1 - Z_{P_d}. \tag{4.30}$$

The discrete implementation of the proposed detection-based filter thus requires the use of instantaneous measurements of the detection and false alarm likelihoods. The derivation of the measurement for the detection likelihood was outlined previously in eqn.(4.22). Assuming the distribution assumptions to be valid, the false alarm likelihood measurement, $Z_{P_{fa}}$, is simply the *a priori* probability of false alarm used in the detection likelihood measurement equation. A discrete implementation, therefore uses discrete measurements of the detection likelihoods. A block diagram of the proposed discrete probabilistic filter is provided in figure 4.11.

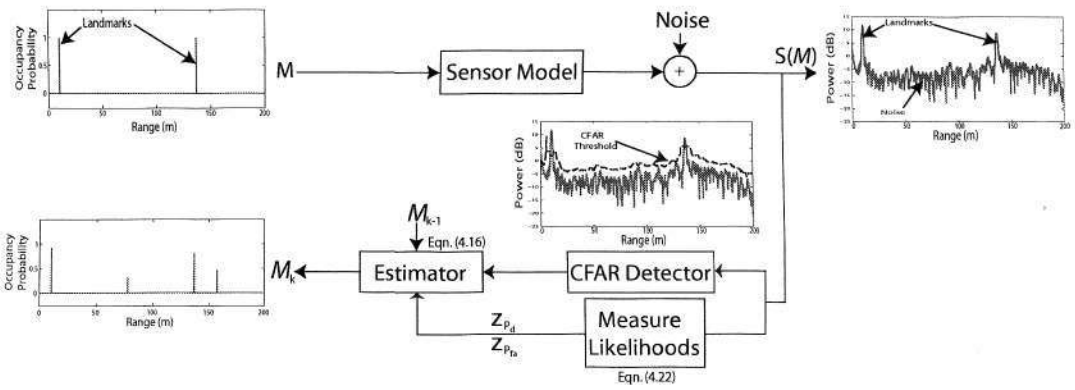

Figure 4.11: *An overview of the proposed discrete probabilistic GBRM filter. Also shown are the associated equations which each block represents.*

However, in order for the measurement equations of section 4.4.2 to be valid, it is essential that the noise signal distribution assumption, $p(\psi|m = E, \Omega_E)$ be accurate. In an outdoor deployment, a typical autonomous platform may encounter clutter

signals, whose amplitude distribution may violate the noise signal distribution assumption. The consequence of this in an added uncertainty in the measurement. Taking a discrete approach, a Bayesian implementation cannot encapsulate measurement uncertainty (measurement not modeled as a continuous density). The following section therefore outlines an evidential approach to dealing with discrete measurement uncertainty.

4.5.2 Evidential Vector Measurements

The GBRM implementation with probabilistic vector measurements can be prone to measurement noise in the case of clutter measurements violating the noise distribution assumption. To deal with this added uncertainty in a discrete framework, this section adopts evidential vector measurements of the detection likelihoods and propagates the posterior belief on the map, through an evidential filtering framework. This section deviates temporarily from the Bayesian probabilistic methods examined through out this thesis.

An evidential framework requires the definition of a *frame of discernment*,

$$\Theta = \{m_k^F, m_k^E\} \tag{4.31}$$

contain fullness and emptiness beliefs, where the subsets, denoted 2^Θ, are known as the *power set*,

$$2^\Theta = \{m^\emptyset, m^F, m^E, m^{F \cup E}\}.$$

with $\emptyset$, F, E, and $F \cup E$ representing the null, full, empty and unknown sets respectively. Thus, when the observation z_k is made at time k in an arbitrary range bin the beliefs are assigned as,

$$\left.\begin{aligned}
\mathfrak{m}_z(m_k^F|z_k = D) &= \frac{Z_{P_d}\mathbf{1}(\psi)}{Z_{P_d}\mathbf{1}(\psi) + Z_{P_{fa}} + Z_{P_u}} \\
\mathfrak{m}_z(m_k^E|z_k = D) &= \frac{Z_{P_{fa}}}{Z_{P_d}\mathbf{1}(\psi) + Z_{P_{fa}} + Z_{P_u}} \\
\mathfrak{m}_z(m_k^U|z_k = D) &= \frac{Z_{P_u}}{Z_{P_d}\mathbf{1}(\psi) + Z_{P_{fa}} + Z_{P_u}}
\end{aligned}\right\} \text{for } \mathcal{H}_1 \tag{4.32}$$

$$\left.\begin{aligned}
\mathfrak{m}_z(m_k^F|z_k=\bar{D}) &= \frac{Z_{P_{md}}\mathbf{1}(\psi)}{Z_{P_{md}}\mathbf{1}(\psi)+Z_{P_n}+Z_{P_u}}\\
\mathfrak{m}_z(m_k^E|z_k=\bar{D}) &= \frac{Z_{P_n}}{Z_{P_{md}}\mathbf{1}(\psi)+Z_{P_n}+Z_{P_u}}\\
\mathfrak{m}_z(m_k^U|z_k=\bar{D}) &= \frac{Z_{P_u}}{Z_{P_{md}}\mathbf{1}(\psi)+Z_{P_n}+Z_{P_u}}
\end{aligned}\right\} \text{for } \mathcal{H}_0 \qquad (4.33)$$

$$\mathfrak{m}_z(m_k^{\emptyset}|z_k)=0 \qquad \text{for } \mathcal{H}_0,\mathcal{H}_1.$$

where $\mathfrak{m}(A|B)$ is the *mass distribution* on A given B. Here, $\mathfrak{m}(m_k^U|z_k)$ represents the unknown or 'ignorance' evidence given sensor data at time k. It can consequently be seen the normalizing constraint is still satisfied as,

$$\sum_{A\subset 2^{\Theta}} \mathfrak{m}_z(A|z_k)=1. \qquad (4.34)$$

The resulting triplet $\{\mathfrak{m}_z(m_k^F|z_k),\mathfrak{m}_z(m_k^E|z_k),\mathfrak{m}_z(m_k^U|z_k)\}$ is known as the *body of evidence*, from a given measurement. However, with the above unity constraint, clearly only $\mathfrak{m}_z(m_k^F|z_k)$ and $\mathfrak{m}_z(m_k^E|z_k)$ need to be stored to maintain a full description of the map.

4.5.2.1 Unknown Measurement

In typical signal detectors, neighbouring (in time or range) signal samples are used to make a local estimate of the mean noise power, through the use of a sliding window. If leading and lagging windows of width W are used, then a 2*W particle approximation is made of the assumed noise signal pdf, $p(\psi|m=E,\Omega_E)$. As outlined previously, measurement uncertainty can be introduced when the assumed distributions are violated. The method adopted in this section, is to quantify the degree by which the 2*W neighboring signal samples deviate from the assumed distribution. This measure is then used to weight the probabilistic measurement through the 'ignorance' measurement, Z_{P_u}.

As it is assumed that the distribution moments are unknown, non-parametric goodness of fit algorithms [96] allow for a probability of null hypothesis (samples are from the assumed density) rejection to be obtained. In what is referred to as the Lilliefors Test, a test statistic is derived from the difference between the cumulative exponential distribution function and the empirical distribution function evaluated at intervals proportional to the 2*W signal samples. Probabilities of rejection can then be obtained from look-up tables. That is, the probability that the power samples used in the measurement eqn.(4.22) are from the assumed noise distribution. The consequence being that, $Z_{P_{fa}} \neq P_{fa}$. Note under ideal noise conditions, as $W\rightarrow\infty$,

$Z_{P_u} \rightarrow 0$ and the model returns to the Bayesian form, with probabilistic measurements.

4.5.2.2 The Filter Recursion

A discrete filter for use with evidential vector measurements was developed by Dempster [97]. It is stated that given two mutually independent *bodies of evidence*, i.e. a sensor reading and a map, $\mathfrak{m}_z(A)$ and $\mathfrak{m}_m(B)$ respectively, then for any possibility C (equivalent to a posterior) the combined evidence provided by the 2 sources is given by,

$$\mathfrak{m}_m(C) = \frac{\sum\limits_{A \cap B = C} \mathfrak{m}_z(A)\mathfrak{m}_m(B)}{1 - \sum\limits_{A \cap B = \emptyset} \mathfrak{m}_z(A)\mathfrak{m}_m(B)} \tag{4.35}$$

where A, B, C $\subset 2^{\Theta}$. The numerator represents the aspects of the sensor data that confirms the map data and can be separated into the 'fullness confirmation' and 'emptiness confirmation', denoted $\mathfrak{m}(\beta_k^F|z^k)$ and $\mathfrak{m}(\beta_k^E|z^k)$ respectively. The denominator is a measure of the conflict between the new sensor data and the map data, and will be denoted $\mathfrak{m}(\kappa_k|z^k)$. Thus, as with the Bayesian update, Dempsters rule of combination can fuse independent *bodies of evidence*, to recursively update the state of the grid map. Expanding the equation to determine the posteriors for map 'fullness', $\mathfrak{m}_m(m_k^F|z^k)$ and 'emptiness', $\mathfrak{m}_m(m_k^E|z^k)$,

$$\mathfrak{m}_m(m_k^F|z^k) = \frac{\mathfrak{m}(\beta_k^F|z^k)}{\mathfrak{m}(\kappa_k|z^k)}$$
$$\mathfrak{m}_m(m_k^E|z^k) = \frac{\mathfrak{m}(\beta_k^E|z^k)}{\mathfrak{m}(\kappa_k|z^k)}$$

where,

$$\mathfrak{m}(\beta_k^F|z^k) = \mathfrak{m}_m(m_k^F|z^{k-1})\mathfrak{m}_z(m_k^F|z_k) + \mathfrak{m}_m(m_k^U|z^{k-1})\mathfrak{m}_z(m_k^F|z_k) + \mathfrak{m}_m(m_k^F|z^{k-1})\mathfrak{m}_z(m_k^U|z_k)$$

$$\mathfrak{m}(\beta_k^E|z^k) = \mathfrak{m}_m(m_k^E|z^{k-1})\mathfrak{m}_z(m_k^E|z_k) + \mathfrak{m}_m(m_k^U|z^{k-1})\mathfrak{m}_z(m_k^E|z_k) + \mathfrak{m}_m(m_k^E|z^{k-1})\mathfrak{m}_z(m_k^U|z_k)$$

$$\mathfrak{m}(\kappa_k|z^k) = 1 - \mathfrak{m}_m(m_k^E|z^{k-1})\mathfrak{m}_z(m_k^F|z_k) - \mathfrak{m}_m(m_k^F|z^{k-1})\mathfrak{m}_z(m_k^E|z_k).$$

For clarity, an overview of the evidential implementation is provided in the form of a block diagram in figure 4.12. Results from the examination of the posterior

stochastic map estimate from both these discrete approaches are analysed in section 4.7.

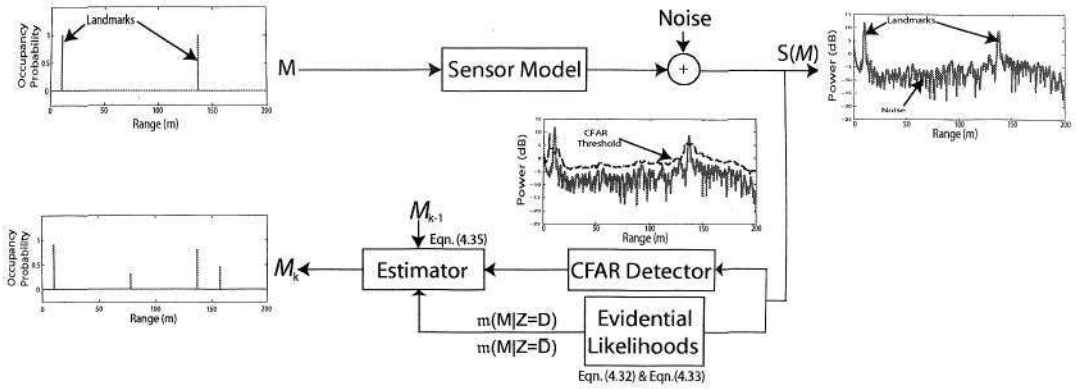

Figure 4.12: *An overview of the proposed discrete evidential GBRM filter. The associated equations for each block are also shown.*

4.6 The Continuous GBRM Filter

Section 4.4 outlined the proposed detection-based GBRM filter, with the previous section outlining probabilistic and evidential discrete implementations. It was highlighted that the state-dependant likelihoods required for a grid-based RM filter, are those encountered in detection theory, and remain *a priori* unknown. Discrete approaches are common, but fail to encapsulate the inherent measurement uncertainty (w term in eqn.4.22) in a consistent manner. The approach proposed in this section, adopts a continuous measurement space as opposed to a discrete one, and re-formulates the GBRM problem, as a joint estimation problem in which the likelihoods as well as the occupancy posterior have to be estimated, as both are *a priori* unknown.

4.6.1 Problem Formulation

Let the true grid map be denoted, $M = [m_{(1)}, \ldots, m_{(R)}]$, which is a vector of R binary numbers indicating the presence, $m_{(r)} = 1$, or absence, $m_{(r)} = 0$, of a landmark in each range bin. In order to evaluate the posterior on the map, the measurement likelihoods need to be evaluated (as opposed to *a priori* assumed). The estimation

problem is therefore to evaluate the joint likelihood on the occupancy and measurement likelihood random variables at each time k,

$$p_{k|k}(M_k, \Lambda_k | Z^k) \tag{4.36}$$

where the measurement, Z^k consists a history of all raw measurements, Λ_k, contains the measurement likelihoods (detection and non-detection). Assuming measurement independence between successive range bins,

$$p_{k|k}(M_k, \Lambda_k | Z^k) = \prod_{r=1}^{R} p_{k|k}(m_{k,(r)}, \lambda_{k,(r)} | z^k_{(r)}). \tag{4.37}$$

The independent terms can then be expanded to,

$$p_{k|k}(m_{k,(r)}, \lambda_{k,(r)} | z^k_{(r)}) = p_{k|k}(m_{k,(r)} | \lambda_{k,(r)}, z^k_{(r)}) p_{k|k}(\lambda_{k,(r)} | z^k_{(r)}) \tag{4.38}$$

and since occupancy is a discrete binary random variable,

$$p_{k|k}(m_{(r)} = 0 | \lambda_{(r)}, z^k_{(r)}) = 1 - p_{k|k}(m_{(r)} = 1 | \lambda_{(r)}, z^k_{(r)}). \tag{4.39}$$

As previously stated, $\lambda_{(r)}$ contains estimates of both the detection and non-detection likelihoods, however,

$$\begin{aligned}
p(\lambda_{(r)} = D | m_{(r)} = 1, z^k_{(r)}) &= P_d \\
p(\lambda_{(r)} = D | m_{(r)} = 0, z^k_{(r)}) &= P_{fa} \\
p(\lambda_{(r)} = \bar{D} | m_{(r)} = 1, z^k_{(r)}) &= 1 - P_d \\
p(\lambda_{(r)} = \bar{D} | m_{(r)} = 0, z^k_{(r)}) &= 1 - P_{fa}
\end{aligned}$$

representing a complimentary set of measurement likelihoods. Thus, for a given range bin r, we only need maintain an estimate of $p(\lambda_{(r)} = D | z^k_{(r)})$ which will be denoted $p(\lambda_{(r)} | z^k_{(r)})$ unless explicitly stated otherwise, and whose true value is $p(\lambda_{(r)} | z^k_{(r)}) \in [0, \ldots, 1]$.

As the vehicle traverses the environment, landmarks may randomly appear/disappear in the data due to occlusions as well as falling in and out of the senors' perception field. Contrary to standard occupancy grip mapping algorithms, a *non-static* time update is used here (i.e. $p(m_{k,(r)} | m_{k-1,(r)}, z^{k-1}_{(r)}) \neq p(m_{k-1,(r)} | z^{k-1}_{(r)})$. That is, cells can randomly change from occupied to empty or vice-versa during vehicle motion. Thus the process is modeled as a Hidden Markov Model (HMM) where the transition

matrix is given by,

$$\Pi = \begin{bmatrix} P_{oo} & P_{eo} \\ P_{oe} & P_{ee} \end{bmatrix}$$

with, P_{oo} being the probability of an occupied remaining occupied (a stationary landmark remaining within the sensors field of view), P_{eo} being the probability of an empty cell becoming occupied (possibly due to occlusion effects) with P_{oe} being the opposite. P_{ee} then being the probability of an empty cell remaining empty. Using Bayes rule on the first term of eqn.(4.38) we get,

$$p_{k|k}(m_{k,(r)}|\lambda_{k,(r)}, z^k_{(r)}) \propto p(\lambda_{k,(r)}, z_{k,(r)}|m_{k|k-1,(r)})p_{k|k-1}(m_{k|k-1,(r)}|z^{k-1}_{(r)}) \tag{4.40}$$

As $\lambda_{(r)}$ is not dependant the occupancy variable,

$$p(m_{k,(r)}|\lambda_{(r)}, z^k_{(r)}) \propto \lambda_{(r)}p(z_{k,(r)}|m_{k|k-1,(r)})p(m_{k|k-1,(r)}|z^{k-1}_{(r)}). \tag{4.41}$$

The second term of eqn.(4.38) is a sensor specific representation of the detection likelihood density where a detection may mean range readings in terms of laser, sonar and radar sensors, or feature detections if feature extraction methods are applied to the raw sensor data, as outlined previously in section 4.4.2. An overview of this proposed filter is shown in figure 4.13. A detailed description of the implementation of this filter is provided later in section 4.8.1.

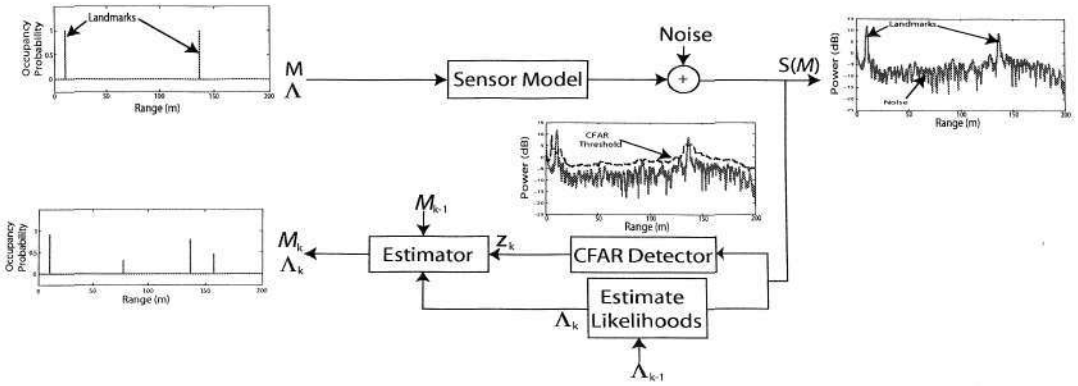

Figure 4.13: *An overview of the proposed continuous probabilistic GBRM filter. The associated equations for each block are also shown. Note that in this filter, the likelihoods are also being recursively estimated along with the map state.*

4.6.2 Particle Filter Implementation

The objective of this filter is to propagate the posterior density of the joint density, $p_{k|k}(m_{k,(r)}, \lambda_{k,(r)}|Z^k_{(r)})$, in a given grid cell, r. Assume the prior, $p_{k-1|k-1}(m_{k-1,(r)}, \lambda_{k-1,(r)}|z^{k-1}_{(r)})$ can be represented by a set of weighted particles $\{o^{(i)}_{k-1,(r)}, w^{(i)}_{k-1,(r)}\}_{i=1}^N$ such that,

$$p_{k-1|k-1}(o_{k-1,(r)}|z^{k-1}_{(r)}) \approx \sum_{i=1}^{N} w^{(i)}_{k-1,(r)} \delta_{o^{(i)}_{k-1,(r)}}(o_{k-1,(r)})$$

where,

$$o_{t-1,(r)} = \begin{bmatrix} m_{k-1,(r)} \\ \lambda_{k-1,(r)} \end{bmatrix}$$

is the joint state containing the estimate on the map and the corresponding measurement likelihoods. Note that the measurement likelihood λ exists for both $m_{(r)} = 1$ (where it will be the landmark detection likelihood) and $m_{(r)} = 0$ (where it will be the false alarm likelihood).

To propagate the densities the standard particle filter recursion with resampling is followed,

$$o^{(i)}_{k,(r)} \sim q(o_{k,(r)}|o^{(i)}_{k-1,(r)}, z_{k,(r)}) \tag{4.42}$$

$$w^{(i)}_{k,(r)} = w^{(i)}_{k-1,(r)} \frac{p(z_{k,(r)}|o^{(i)}_{k,(r)}) p(o^{(i)}_{k,(r)}|o^{(i)}_{k-1,(r)})}{q(o^{(i)}_{k,(r)}|o^{(i)}_{k-1,(r)}, z_{k,(r)})} \tag{4.43}$$

The transition likelihood $p(o^{(i)}_{k,(r)}|o^{(i)}_{k-1,(r)})$ describes the predicted state values and consists of the Markov time update to propagate the occupancy random variable. This is a random particle set sampled from the previous posterior $p(o_{k-1,(r)}|z^{k-1}_{(r)})$ where the binary value of the $m_{(r)}$ component is changed or remains fixed according to the probabilities set by the transition matrix, Π. A static time update for the measurement likelihood estimate (as it is assumed constant for each landmark) is used.

$$p(m_{k-1,(r)}|z^{k-1}_{(r)}) \sim p(m_{k-1,(r)} = 1|z^{k-1}_{(r)}, \Pi) \tag{4.44}$$

$$p_{k|k-1}(\lambda_{k,(r)}|z^{k-1}_{(r)}) = p_{k-1|k-1}(\lambda_{k-1,(r)}|z^{k-1}_{(r)}) \tag{4.45}$$

The proposal likelihood $q(o_{k,(r)}|o^{(i)}_{k-1,(r)}, z_{k,(r)})$ depends on whether the cell continues in its same state, i.e. during the Markov transition the cell value remains unchanged, or whether it changes state. In the case of the state remaining the same,

$$q(o^{(i)}_{k,(r)}|o^{(i)}_{k-1,(r)}, z_{k,(r)}) = p(o^{(i)}_{k,(r)}|o^{(i)}_{k-1,(r)}). \tag{4.46}$$

In the case of the state changing or a new detection, the data at time k is used to initialize the estimate on λ according to the measurement likelihood estimate algorithm outlined in the previous section 4.6.1. That is, the proposed detection likelihood is taken to be the estimated likelihood at that location using measurement data $z_{k,(r)}$. Finally the likelihood used to weigh the particles is obtained from the likelihood of a landmark being present in the cell which is also the same likelihood used by the detection algorithm and is given by,

$$p(z_{k,(r)}|o^{(i)}_{k,(r)}) = \frac{p(\psi_r|m_{(r)} = 1, \Omega_O)}{p(\psi_r|m_{(r)} = 0, \Omega_E)} \tag{4.47}$$

where ψ_r is the signal intensity at particle location $x^{(i)}$. The weighted particle set is then re-sampled. Estimates of the posterior occupancy and measurement likelihood can be extracted using the expected *a posteriori*,

$$\hat{o}_{k,(r)} = \sum_{i=1}^{N} w^{(i)}_{k,(r)} o^{(i)}_{k,(r)}. \tag{4.48}$$

4.7 Discrete Implementation Experiments

This section analyses the performance of the discrete implementations of the proposed GBRM filter with unknown measurement likelihoods. The performance of both probabilistic and evidential approaches are examined in an outdoor carpark environment. Synthetic analysis was performed previously in section 4.4.1, where discrete and idealistic likelihoods were compared with standard range measurement based approaches. The advantages of integrating the detection statistics into the mapping estimate problem were demonstrated. This section applies the outlined discrete implementations to real data acquired by a MMWR sensor in an outdoor carpark environment, as introduced in the previous chapter in section 3.5.1.

As shown in figure 4.14, the environment contains numerous objects of varying dimensions with differing probabilities of detection. Radar sensor detections registered by an OS detection method are used for both the detection based and range based approaches, with the range of a given detection being used in the range-based occupancy likelihood. The detector parameters chosen for the radar detection results shown in figure 4.14, are W=20, K=30, P_{fa}=1×10^{-6}. These represent the measurements for the GBRM filters outlined in this chapter. For comparison purposes, a laser scan map created from the detections registered by a laser sensor is also shown. The range/bearing of a given detection, along with the range/bearing noise variance, set at $0.5m$ and 2^o respectively, are used in the classical range-based likelihood approach, where as the detection statistics are incorporated in the proposed

detection-based likelihood approach. Grid maps produced from the various discrete approaches outlined in this chapter are compared and contrasted.

Figure 4.15 shows the ideal GBRM result from the given environment, which has been manually constructed. The grid map comprises cells containing binary indices indicating a cell being occupied by a landmark or being empty. Classical error metrics for GBRM filter quantification are based on the sum of squared error [98], [99], [47] between the estimated map posterior, $\hat{M}$, and the ground truth map, M. This metric however, equally treats all cells, whether they are occupied or empty. When the map comprises of similar numbers of empty and occupied cells (perhaps in an indoor environment), this metric works well to quantify algorithm performance. However, in the case of vastly more empty cells than occupied, the metric can be less susceptible to missed landmark declarations, which can be catastrophic for an outdoor autonomous platform. Therefore in this section a new metric, referred to as the normalised average sum of the squared error (NASSE), is adopted as,

$$NASSE = 0.5\left(\frac{1}{\mathfrak{q}_O}\sum_{i=0}^{\mathfrak{q}_O}\left(P(m_k^i|z^{i,k}, m^i{=}1) - 1\right)^2 + \frac{1}{(\mathfrak{q} - \mathfrak{q}_O)}\sum_{i=\mathfrak{q}_O+1}^{\mathfrak{q}}\left(P(m_k^i|z^{i,k}, m^i{=}0) - 0\right)^2\right) \quad (4.49)$$

where $\mathfrak{q}_O$ is the total number of occupied cells. This metric equally weights the effects of a false landmark declaration and a missed landmark. Figure 4.16, for example, plots the NASSE and standard SSE metrics over the course of a carpark loop, where noise has been injected into the vehicle trajectory, X^k. The NASSE metric clearly shows map divergence, as the metric increases due to multiple missed landmarks as a result of the pose error. The SSE metric however, shows monotonic error reduction indicating an accurate map estimate, due to the majority of empty cells in the ideal map of figure 4.15. The NASSE is therefore adopted for algorithm analysis. The following sections examine the performance of discrete implementations proposed in this chapter, with comparison to classical range-based likelihood approaches.

As mentioned in the previous chapter, laser data typically returns the range to the *first* landmark detected along the beam. For the case of the radar, a single beam can in fact contain information from multiple landmarks mainly due to the wider beamwidth (wave can propagate passed narrow landmarks) and the ability of the radar beam to penetrate some light foliage. In this work, the most 'optimistic' approach therefore assumed which implies that *every* measurement (detection and non-detection) along the entire beam is valid. That is, for each time step k, each peak in the data (under both the null and alternate detection hypotheses), is treated as a potential landmark, and no model of the sensor beam propagation properties is

assumed.

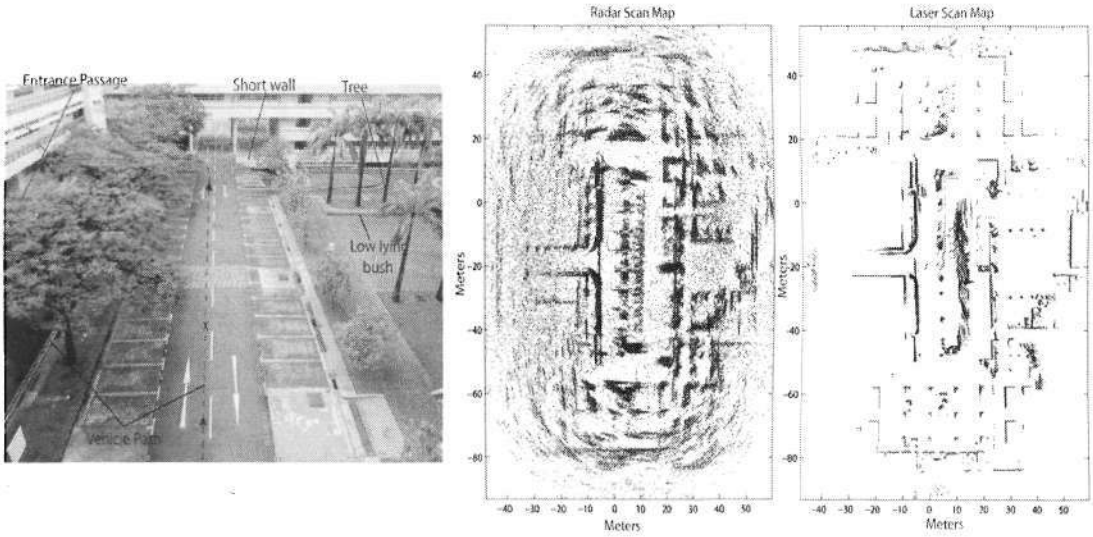

Figure 4.14: *The figure shows an overview of the testing ground with the corresponding measurement set (output of stochastic detector) for the radar sensor. Laser sensor detections are shown for comparison. The resulting detection (and non-detection) measurements are used as the inputs for the GBRM filters.*

4.7.1 The Probabilistic Implementation

This section applies the discrete probabilistic GBRM filter to real MMWR data, and the merits of incorporating the detection statistics into the filter recursion are highlighted for the GBRM problem in the carpark environment. The detection sequence depicted previously in figure 4.14, provides the measurements for the filters, along with the associated detection likelihood measurements, Z_{P_d} and $Z_{P_{fa}}$. Figure 4.17 shows a comparison of the posterior map estimates from the proposed detection-based GBRM filter, and that from the classical range-based approaches. Visual inspection shows a reduction in false landmark declarations and an improved posterior map estimate. However, using the manually constructed ground truth map of the environment in figure 4.15, quantitative comparisons with previous approaches can be generated which highlight the advantages of the proposed method.

Figure 4.18 plots the NASSE metric for the GBRM filter's posterior map estimate over the course of the experiment. It can be seen that the rate of monotonic error reduction of the proposed approach exceeds that of standard methods, with a reduced mapping error achieved in the final posterior map estimate. This confirms the results

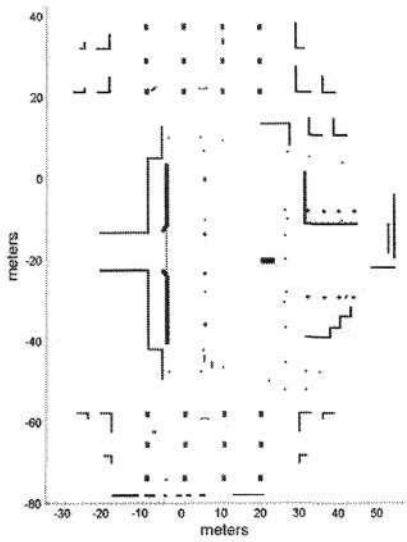

Figure 4.15: *The binary ground truth GB map of the carpark environment. This was manually constructed from observation of the testing environment and is used for algorithm evaluation.*

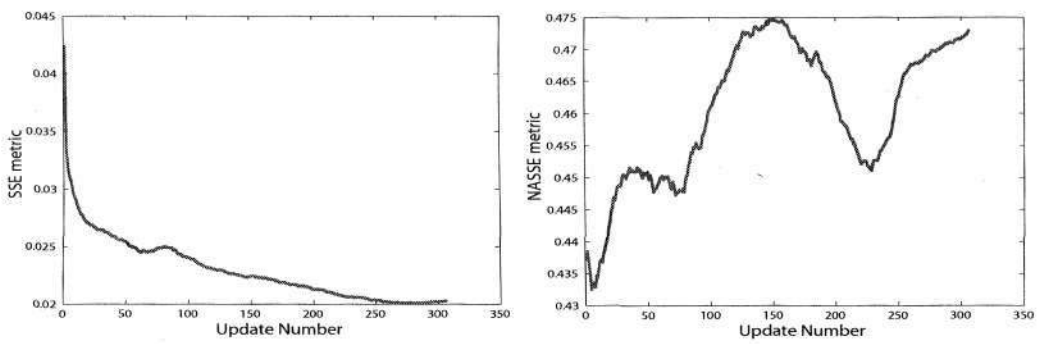

Figure 4.16: *Comparison of the error metrics for a loop with noise injected into the location estimates. This figure shows the susceptibility of the classical sum of squared error (SSE) metric, to maps containing unequal number of occupancy and empty cells. The NASSE error metric clearly indicates a non-converging map due to multiple missed landmarks, whereas the standard metric shows a monotonically decreasing error.*

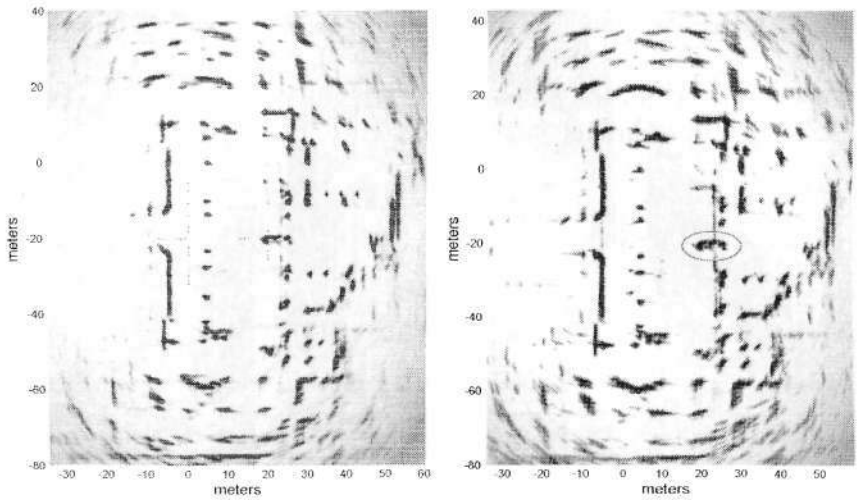

Figure 4.17: *Comparison of simulated mapping results using discrete detection likelihoods and the classical occupancy models where the likelihood is effectively assumed, through a range-based likelihood.*

from the simulations, where the incorporation of detection statistics into the filter recursion leads to improved accuracy in mapping capability. While the discrete probabilistic implementation directly used the discrete measurements Z_{P_d} and $Z_{P_{fa}}$, as opposed to recursively estimating the true likelihoods P_d and P_{fa} as is carried out by the continuous implementation, the results still show a dramatic improvement over previous approaches. This is due to the majority of environmental landmarks in the carpark having very high (close to unity) detection probabilities, with P_{fa}=1×10^{-6}. To synthesise an environment consisting primarily of landmarks with low detection probability, the P_{fa} parameter of the detection algorithm can be set arbitrarily low. Equally, an environment of excessively high clutter can be synthesised by setting the P_{fa} parameter high. To examine the filter performance under these different conditions, the adaptive detector P_{fa} parameter was set at $P_{fa}=1\times10^{-30}$ and $P_{fa}=1\times10^{-1}$ respectively. Thus creating and environment of very low detection probability landmarks, and one of very high clutter. The NASSE error plots for these excessively low and high P_{fa} values are also shown in figure 4.18. At extremely low P_{fa}, further advantages of the proposed detection-based algorithm are evident, since it explicitly considers the detection statistics, specifically the missed detection likelihoods, in the mapping recursion. For range-based methods, no range reading (as a result of a missed-detection), results in no range likelihood existing. Standard approaches therefore typically assign intuitive occupancy measurements in regions of no range reading [39], [20], [33], [36]. At high rates of false alarm, an increased rate of error

reduction is evident with the proposed approach due to the formulation incorporating the detectors false alarm probability. This demonstrates the advantages of the proposed approach in the presence of both landmarks with low detection probability, and high rates of spurious detections.

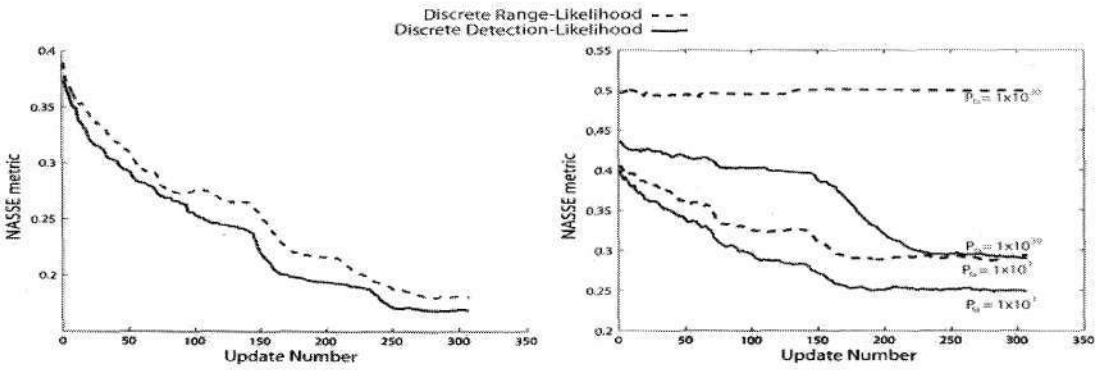

Figure 4.18: *The left hand figure shows the comparison of the NASSE metric for the discrete implementation of the range and detection based likelihood filters, with the nominal value* P_{fa}=1×10^{-6}. *The right hand figure shows the comparison of the NASSE metric in the carpark environment for very low detection probability,* P_{fa}=1×10^{-30}, *and very high false alarm rate,* P_{fa}=1×10^{-1}.

While the adaptive detector parameters may influence the detections registered by the imaging radar, this is common to any application adopting such a sensor. The results presented here highlight that given *any* set of detector parameters, the proposed stochastic mapping approach outperforms that of classical approaches, as it theoretically incorporates the resulting statistics, as a result of a given parameter choice, into the mapping recursion.

4.7.2 The Evidential Implementation

The proposed evidential solution to the discrete GBRM problem, outlined in section 4.5.2 is examined here. As discussed previously, ambiguity in the measurement process is quantified through a goodness of fit test, and propagated through an evidential filter recursion as an 'ignorance' measurement. A sample discrete evidential measurement triplet, $\mathfrak{m}_z(m_k^F|z_k)$, $\mathfrak{m}_z(m_k^E|z_k)$ and $\mathfrak{m}_z(m_k^U|z_k)$ from the carpark environment is shown in figure 4.19 with the hypothesised ground truth superimposed. The framework presents a method of addressing the measurement uncertainty which is overlooked by the discrete probabilistic approach. As the distribution in the sliding window, Ψ_{os}, deviates from the exponential assumption, 'unknown' beliefs $\mathfrak{m}_z(m_k^U|z_k)$ are generated.

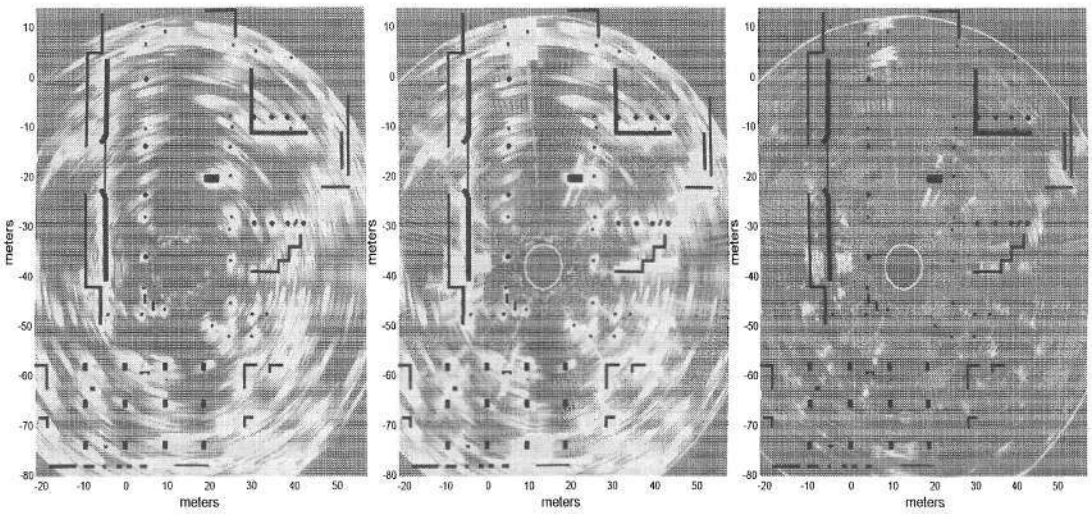

Figure 4.19: *Occupied (left), empty (center) and unknown (right) mass distributions on the carpark map given a single sensor scan (blue to red magnitude colour scale). The unknown scan shows increased uncertainty in areas in which high power returns are present in the sliding window, Ψ_{os}. A minimum operating sensor range of 5m is also evident.*

The posterior grid map estimate obtained from the evidential recursive framework outlined in section 4.5.2, is compared with the range likelihood method in figure 4.20. Taking a simplistic interpretation of evidence as being directly analogous to probability, the NASSE metric for the evidential filter can be evaluated and is illustrated in figure 4.21. The results show while the evidential framework performs well at suppressing spurious landmarks when compared with the probabilistic range-likelihood approaches, it may also be susceptible to missed landmarks as a result of insufficient evidence gathered to hypothesise an occupied cell. The NASSE shows that at the beginning of the mapping experiment, the mapping accuracy is in fact less than that of classical approaches, as the unknown evidence delays the filters belief of occupancy for some landmarks.

Note that for the evidential implementation, the 'unknown' measurements is independent of the detector parameters and is only a function of the sliding window, Ψ_{os}, and as such, is not affected by changing detector parameters.

4.8 Continuous Implementation Experiments

This section analyses the performance of the continuous implementation of the proposed GBRM framework, outlined in section 4.6, on both simulated and actual datasets.

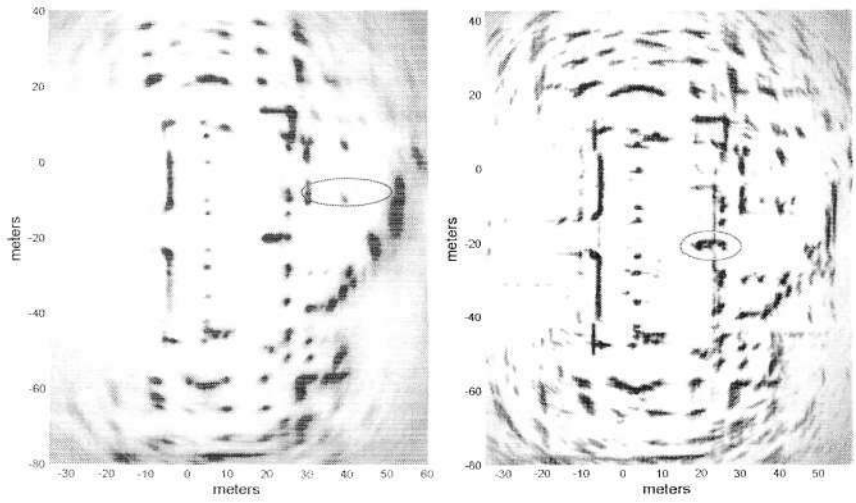

Figure 4.20: *Comparison of estimated map using the proposed evidential framework to handle uncertainty in the measurement model. The results shows reduced false landmark declarations when compared with the range-likelihood method, however some landmarks (such as the trees) are poorly classified.*

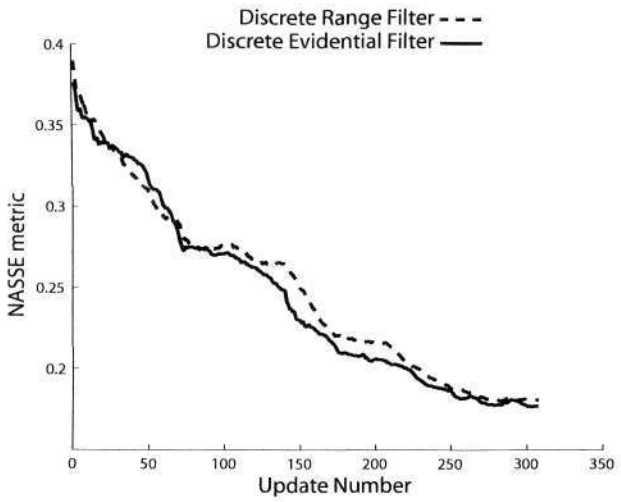

Figure 4.21: *The NASSE trajectory over the course of the experiment for the evidential filter, compared to that of the range-likelihood based filter.*

4.8.1 Synthetic Data

This experiment uses the same synthetic data from section 4.4.1, and is used to evaluate the performance of the probabilistic GBRM filter with unknown measurement likelihoods. In contrast to the analysis in section 4.4.1, in this section the likelihoods are assumed *a priori* unknown and must be jointly estimated along with the map. One hundred Monte Carlo trials were performed in which the occupancy posterior of each cell was propagated using the proposed algorithm with online likelihood estimation, and the standard occupancy algorithm where the likelihoods are *a priori* assumed. Trials at varying false alarm probabilities are carried out for landmarks of all possible detection probabilities $[0, 1]$. As described previously in section 4.6.1, the continuous implementation recursively estimates the measurement likelihood at a given location, and propagates it through the occupancy filter. The detection sequence acts as an indicator function, choosing which likelihood to use to update the posterior.

Figure 4.22 shows an excerpt of the the simulated Monte Carlo raw data for a landmark (present in range bin 11) with a theoretical detection probability of $\sim$0.63, as well as the corresponding detection sequence for a false alarm probability of 0.3. The figure also shows the empirical detection likelihoods obtained from the the sample sequence, which resemble the theoretical values. As depicted in the block diagram of figure 4.13, the data is initially processed by a statistical detector (chapter 3), which forms the detection sequence. Figure 4.23 presents the recursive estimate of the measurement likelihood, $p(z_{k,(r)}|o^{(i)}_{k,(r)})$ term in eqn.(4.43), which is used to update the occupancy posterior estimate. As confirmed from the ideal measurement likelihood trials of section 4.4.1 this improves the reliability of the occupancy estimate.

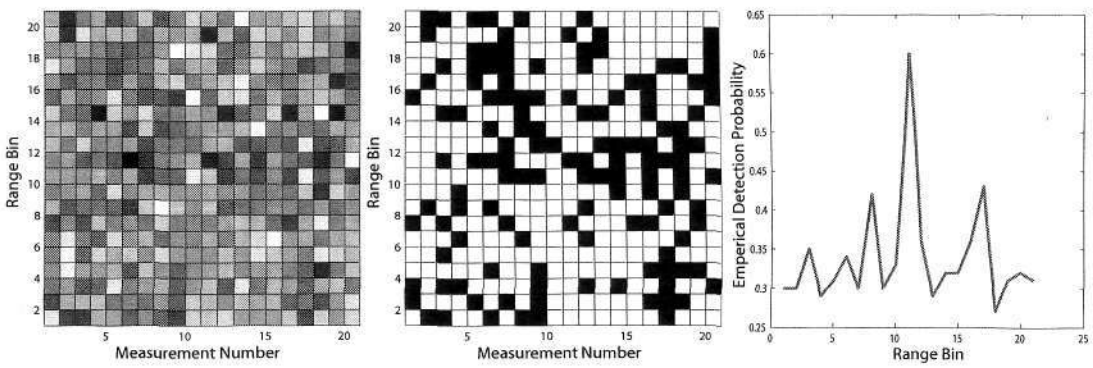

Figure 4.22: *Simulated raw sensor data (left), the detection sequence (middle) and the empirical detection probabilities (right).*

Extensive trials are carried out using data sequences such as that in figure 4.22, and the averaged posterior occupancy estimates are plotted. As before, cells in which

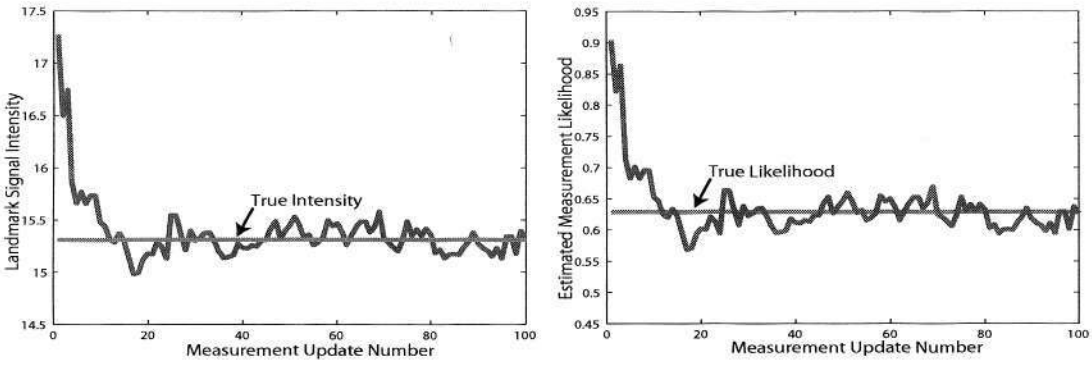

Figure 4.23: *Estimated mean landmark intensity and measurement likelihood using the proposed framework of section 4.6.1.*

the posterior occupancy estimate is greater than 0.51 are declared occupied, and those less than 0.49 are declared empty. Figures 4.24 and 4.25 show the average estimated number of landmarks for situations of low and high rate of spurious measurement (P_{fa}). The results confirmed the ideal results prevented previously, and confirm the reliability of the proposed continuous implementation of the detection-based framework. While for a given rate of false alarm, previous ad-hoc approaches are capable of producing accurate estimates, the proposed framework is more robust to low detection landmarks as well as increased false alarm rates due to its recursive measurement likelihood estimation.

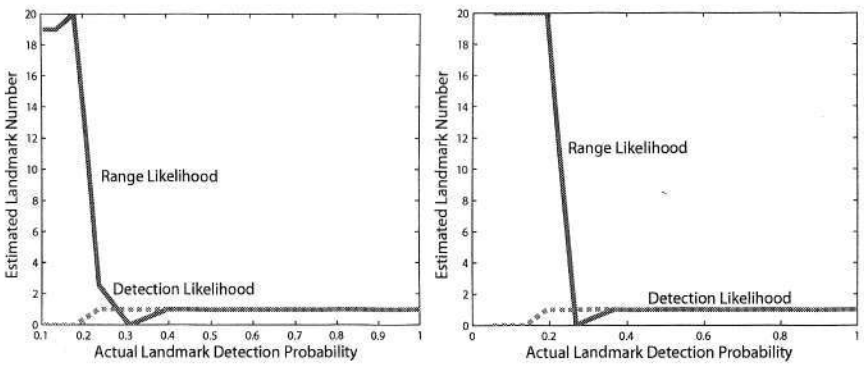

Figure 4.24: *Comparison of the continuous implementation of the detection-based framework with the classical range-based approach, for clutter rates of* $P_{fa} = 0.1$ *(left) and* $P_{fa}=0.05$ *(right). There is a single landmark present in the dataset.*

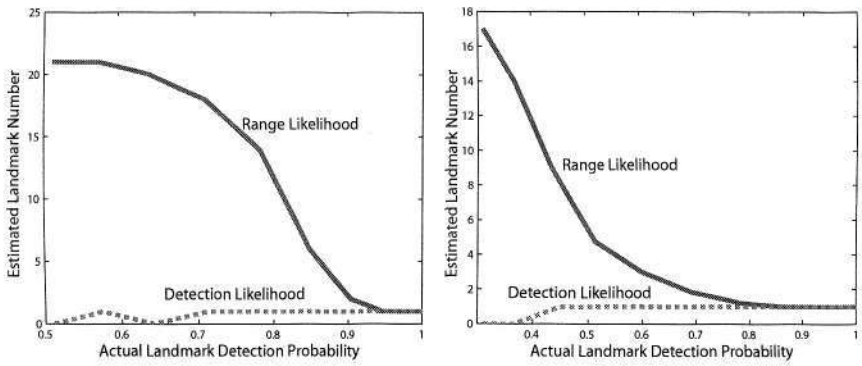

Figure 4.25: *Comparison of the continuous implementation of the detection-based framework with the classical range-based approach, for clutter rates of* P_{fa}=0.5 *(left) and* P_{fa}=0.3 *(right). There is a single landmark present in the dataset.*

4.8.2 Carpark Loop Dataset

The results from the continuous implementation of the proposed GBRM filter in the carpark environment are shown in this section. Figure 4.26 shows the posterior grid map estimate compared against the standard range-likelihood approaches. As was the case for the discrete implementations, a notable reduction the number of cells which are falsely estimated as occupied, and an increased mapping accuracy. Error quantification is again illustrated through the proposed NASSE metric, and shown in figure 4.27. To synthesise different environments, the P_{fa} parameter is again set at low and high values. The results again indicate improved mapping accuracy when compared to range-likelihood approaches. The continuous filter demonstrates slight improvement over that of the discrete implementation as a result of recursively estimating the measurement likelihoods.

Figure 4.28 shows a comparison of the final estimation error for both filters as a function of the detector sliding window width. The OS detector parameters, W, K, set the upper limit on the expected environmental landmark density along a single power-range spectrum in the environment. As the estimate of the noise signal intensity is taken as the K^{th} ordered sample, with W=40 and K=30 and a range resolution of $25cm$ per range bin, allows for (30/4)m to comprise of empty space and (10/4)m (at most) to comprise of landmarks [90]. The OS detection routine is quite robust to changing window size, however increased error at excessively small or large window sizes is evident.

Again, the detection parameters are necessary to generate the measurement inputs for both the proposed filters as well as the standard range-likelihood approaches. Such parameters are required by any sensor which adopts such an adaptive detector, and as such are not parameters of the proposed detection-based filters. The proposed

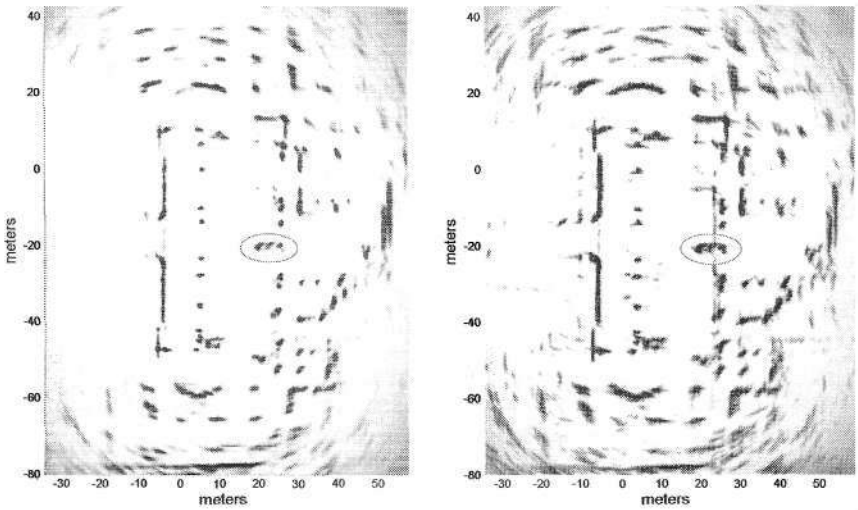

Figure 4.26: *The resulting occupancy maps produced by the proposed continuous GBRM filtering algorithm (left) and previous approaches with assumed likelihoods (right). Note the larger presence of falsely declared occupied cells using previous methods. Also highlighted is the only car present in the carpark during the time of the experiment.*

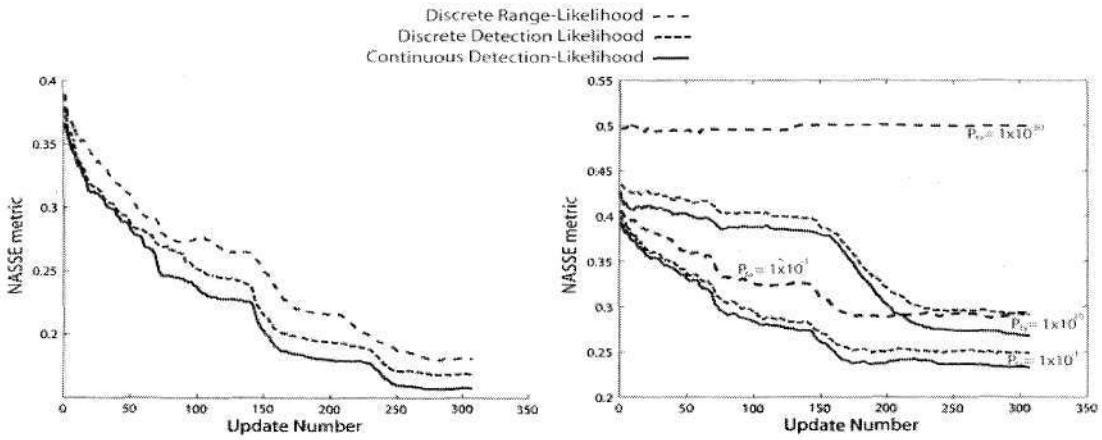

Figure 4.27: *Comparison of the NASSE metric between the estimated map from the continuous filter and that from the range-based filter. The result shows the monotonic reduction in the map error. For a given number of updates, the continuous approach displays superior mapping accuracy. The results from the discrete probabilistic implementation are also shown for comparison.*

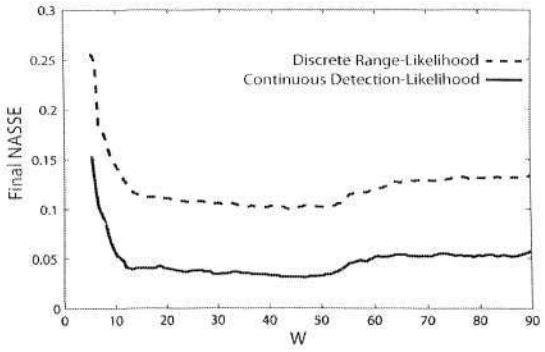

Figure 4.28: *Final posterior NASSE comparison with a varying detection sliding window width, W, P_{fa}=1×10^6 and $K = 0.75\times W$. For a given set of detector parameters, the proposed approach outperforms that of range-likelihood based methods, as the detection statistics are incorporated into the mapping algorithm.*

filters exploit the additional information available from a given set of detector parameter choices (as in section 4.4.2) and use it to estimate the measurement likelihoods required for solving the GBRM problem. The results shown here illustrate that given *any* set of detector parameters, the proposed detection-based filters return superior quality grid-based maps than that from filters which only exploit the range/bearing information.

4.8.3 Campus Loop Dataset

Solutions of the GBRM problem obtained from the proposed continuous filter for the campus loop dataset are presented in this section. The dataset comprises data recorded over the course of a $\sim 5Km$ loop within the university campus. Accurate quantification of the map building results is difficult for such a large scale run, due to the practical challenges of obtaining the ground truth, thus satellite imagery is provided as validation. Figure 4.29 shows the entire image and overlayed vehicle trajectory (red). Due to the size of the image and corresponding map, sample excerpts from the dataset (highlighted in dashed circles) are shown in the following segments.

Figure 4.30 shows the resulting map comparison from segment 1, where the dots are the local peaks of the posterior GB map estimate, with an occupancy probability greater that 0.6 (chosen arbitrarily). While accurate performance quantification is challenging in this environment, improvements can be seen in terms of increased detail and reduced false alarms in the proposed approach to that of the classical solution. Comparison of the mapping capability of the MMWR adopted in this section, and the

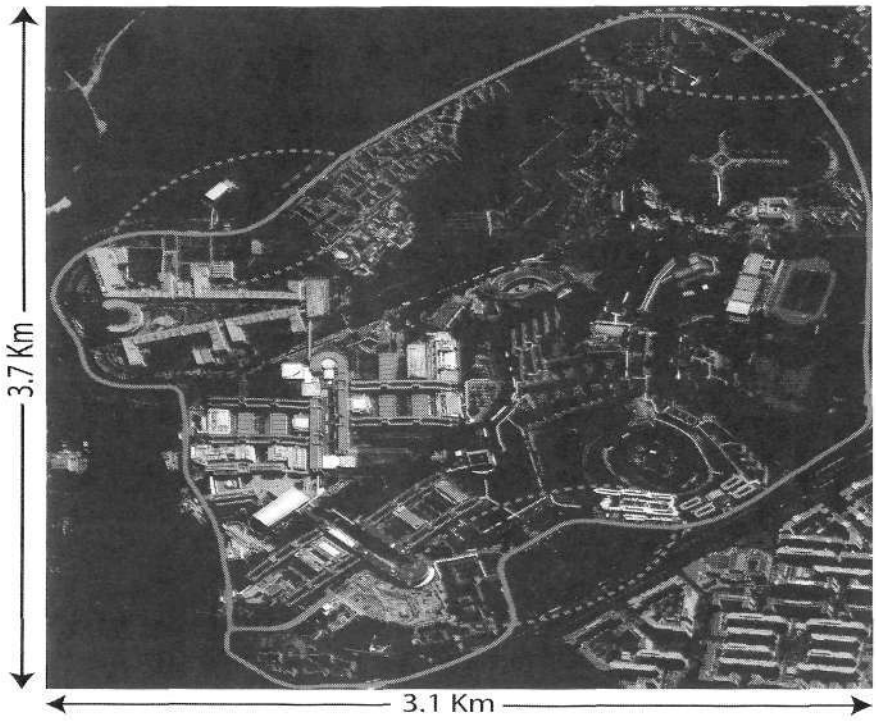

Figure 4.29: *A satellite image of the campus environment with superimposed vehicle trajectory in red. Slight mis-alignment between the path and the road is evident due to the slight off-normal plan-view image for some sections.*

commonly used laser range finder is illustrated in figure 4.31. Due to the multiple-landmark-per-bearing-angle detection capability of the radar sensor, far more detail is apparent in its map than that of the single-landmark-per-bearing-angle laser, thus highlighting an important merit of a MMWR as an outdoor exteroceptive sensor for use in mobile robotics.

An overview (with superimposed vehicle trajectory) of segments 2 and 3 are shown in figure 4.32, whereas figures 4.33 and 4.34 show the resulting map estimate comparisons. Again an improved map estimate is evident from the proposed method due to the recursive estimation of the detection likelihoods of the landmarks in the environment.

4.9 Conclusions

This chapter addressed the issues of measurement likelihoods for grid based autonomous navigation applications. It exposed a subtle assumption in the classical

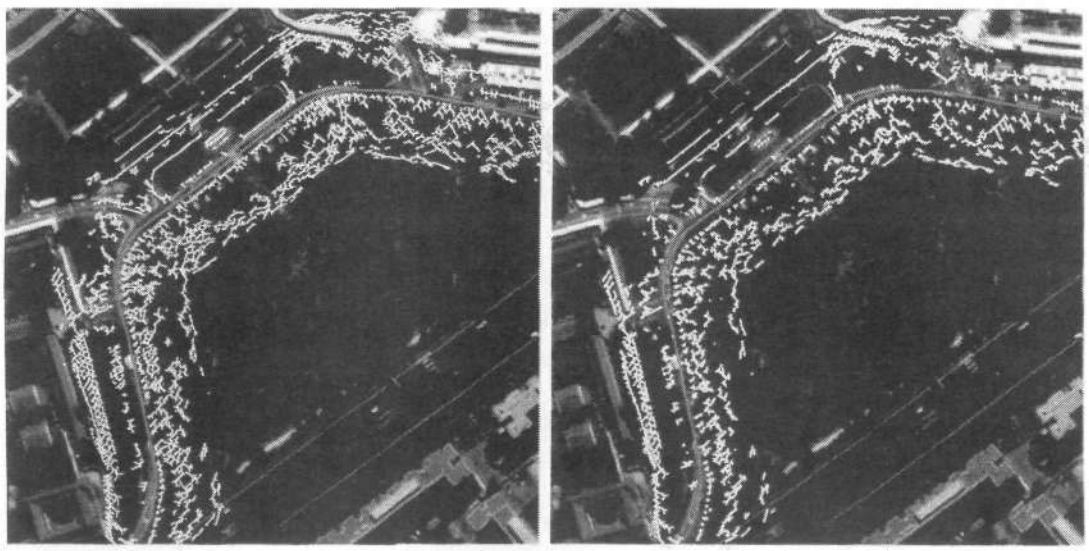

Figure 4.30: *Excerpt of the posterior estimated binary maps from the proposed continuous likelihood filter (left) and that using discrete range likelihoods (right). The proposed method displays improved mapping accuracy in terms of less missed landmarks and reduced false alarms.*

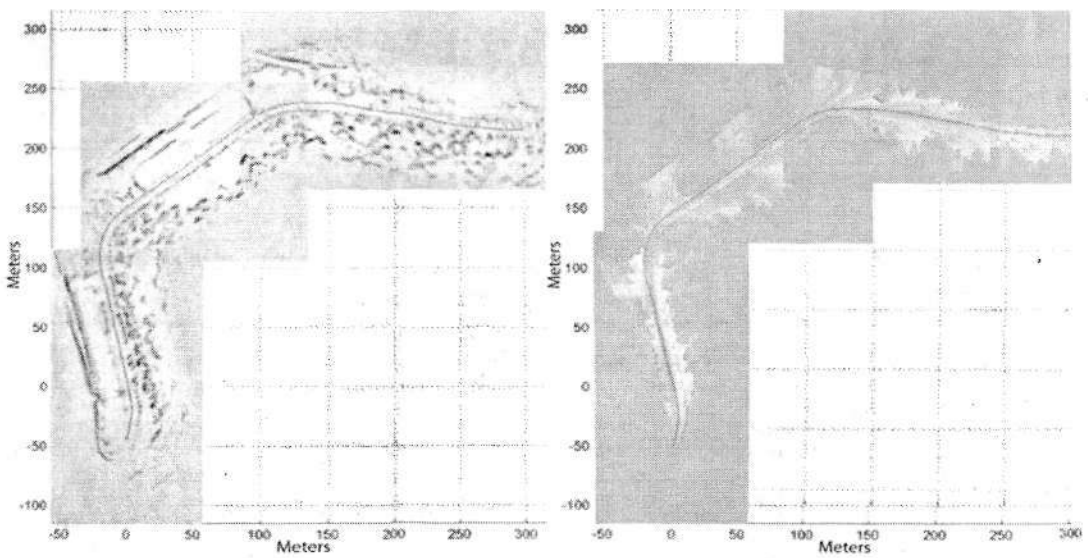

Figure 4.31: *The final posterior map estimates from a radar and laser sensor of the outdoor campus environment. Note the increased information content of the radar map, over that of the laser map, due to its ability to detection multiple landmarks at a single bearing angle.*

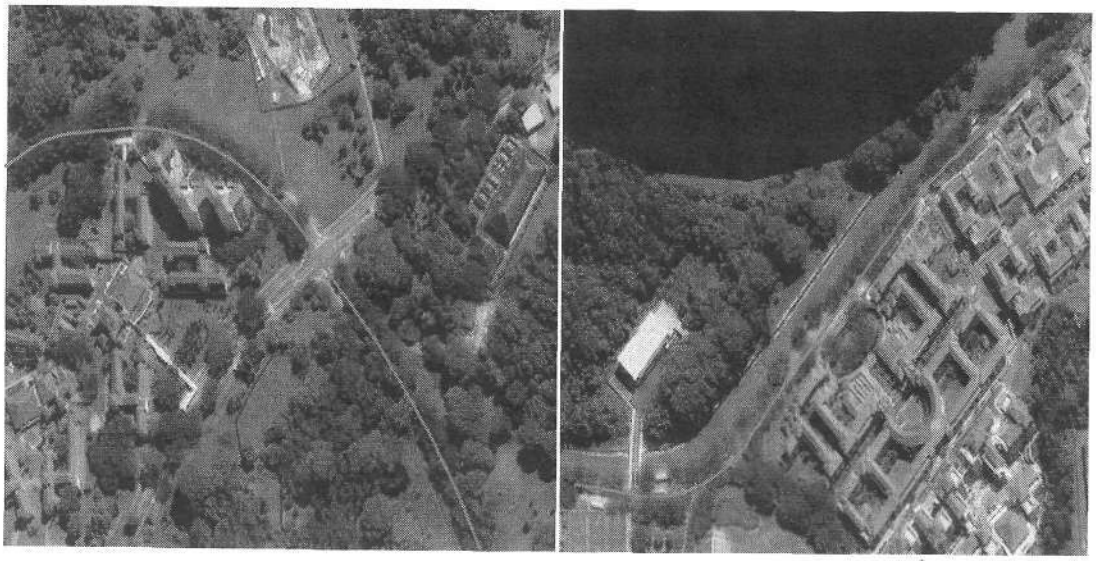

Figure 4.32: *Satellite image overviews of the campus segment on which the GBRM problem is solved and compared in subsequent figures 4.33 and 4.34.*

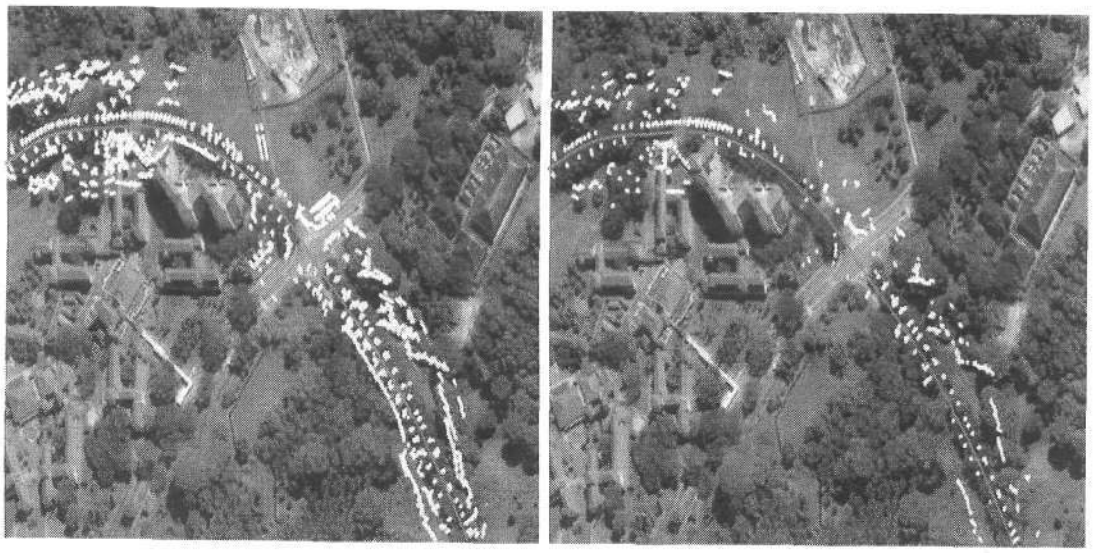

Figure 4.33: *Excerpt of the posterior estimated binary maps from the proposed continuous likelihood filter (left) and that using discrete range likelihoods (right).*

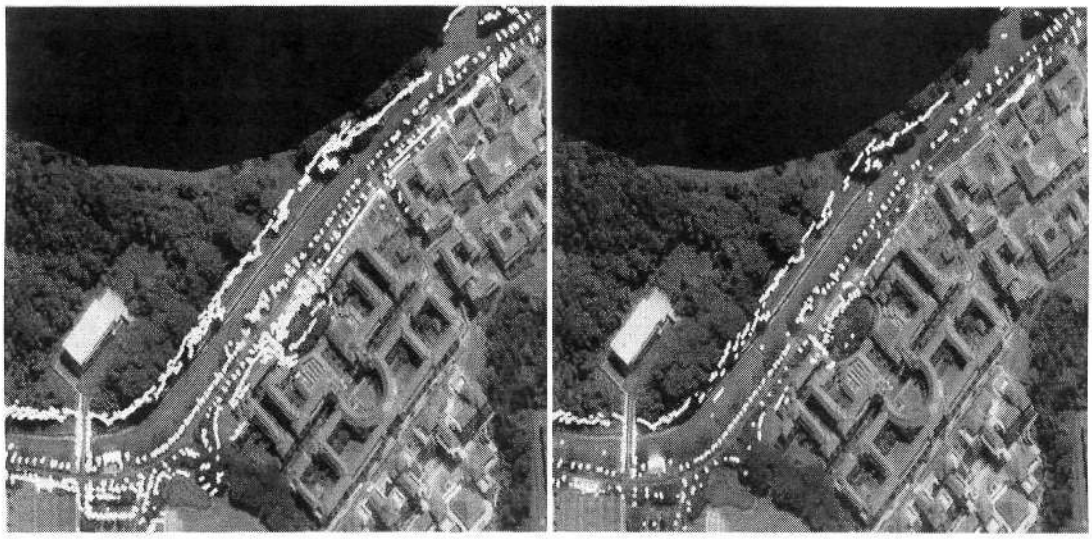

Figure 4.34: *Excerpt of the posterior estimated binary maps from the proposed continuous likelihood filter (left) and that using discrete range likelihoods (right).*

measurement likelihood and showed it to be in fact a state in-dependent measurement, if the commonly adopted range measurement likelihood is used. By reformulating the grid-based mapping problem with state dependent measurements, a theoretically consistent filter was derived. By examining the structure of the resulting measurement model and incorporating signal detection theory, it was shown that the occupancy random variable can be calculated in closed form without the need of heuristic models, as both the grid-based mapping problem and signal detection problem are closely related. Using a synthetic environment, improved grid based mapping results were demonstrated when the exact detection likelihoods were used to propagate the occupancy random variable, as opposed to implicitly assumed likelihoods as is the case for previous grid based mapping formulations, and thus verified the new detection-based mapping filter.

The chapter then expanded the proposed filter to incorporate the unavoidable measurement uncertainty. By incorporating statistical signal detection theory into the filter recursion, it was shown that the measurements required for the mapping problem are subject to large uncertainty. Discrete filter solutions were firstly outlined using both Bayesian and Evidential frameworks. A discrete Bayesian measurement, fails to encapsulate the inherent measurement uncertainty, which was then addressed by the proposed discrete Evidential solution. Experimental verification was achieved in an outdoor carpark environment using a manually constructed ground truth for error quantification.

The proposed probabilistic detection-based filter was then expanded to incorporate the detection measurement uncertainty by adopting continuous measurement likelihoods. A joint recursion was derived which jointly estimated the measurement likelihoods and the occupancy on the map. Due to the highly non-Gaussian noise of the detection measurement process, a particle solution was outlined. Using Markov transitions, the effects of occlusions and the appearance of new landmarks in the region are integrated into the algorithm. Particle representations allow for the propagation of the measurement likelihoods (derived through a non-linear function of the sensor received intensity) subject to non-Gaussian noise. Weights for these particles are obtained from the likelihood ratio used by the detector. The resulting set of posterior particles was then resampled and the recursion was established.

The performance of the mapping framework and newly proposed filters was demonstrated for a MMWR sensor which is typically used in an outdoor environment. The sensor gives access to unprocessed range data, allowing for custom landmark detectors to be developed. The framework then allows for the accurate assignment of map occupancy probabilities, irrespective of the hypothesis chosen by the detector. While results showed that the evidential approach was superior to filters which adopt a classical probabilistic range-based measurement likelihood, it was shown that the discrete probabilistic detection-based measurement likelihood filter produced a superior quality map in the controlled carpark environment. Despite its inability to accurately handle the inherent measurement uncertainty, the evidential approach was overly conservative in declaring occupied grid cells due to the inherent ambiguity (not randomness) in the measurement process, resulting in some missed landmarks. The proposed discrete detection-based filters were shown to significantly outperform standard range-based filters, especially in situations of high clutter or landmarks of low detection probabilities. This was as a consequence of incorporating the detection information directly into the filter which range-based methods disregard. The continuous recursion was shown to out-perform the other filters due to its recursive estimation of the true measurement likelihoods of the landmarks in the environment. Mapping results were also presented for as a subset of a 5km loop around the university campus, with satellite imagery being used for filter performance validation.

Chapter 5

Measurement Uncertainty in Feature Based Navigation

The previous chapter examined the grid based robotic mapping problem in which the mapping state space was discretised into a fixed number of cells and filtering occurred in the occupancy state space. This required special measurement likelihoods which were shown to have some pitfalls, the consequences of which where demonstrated. This chapter follows a similar theme, however in this chapter, the feature based (FB) framework is under examination. In FB approaches, the map state space is left in its original continuous form, and filtering occurs in the spatial state space, where the state of interest contains estimates of the feature locations (assuming the features exist).

This chapter shows that classical solutions of the FB-SLAM problem, fail to adequately address the problem in its entirety, specifically the problem of a *"variable number of dimensions"* [49]. In contrast, as shown in the previous chapter, the GBRM problem comprises a *fixed* number of dimensions since map tessellation is an *a priori* event. This chapter emphasises, for the first time, that optimal estimation of a feature-based map involves the joint estimation of both the *number* of features, as well as their corresponding locations, since in a feature-based map, the number of features is *a priori* unknown [49], [4]. This is in contrast to the previous chapter's grid based approaches, where the map (used in the measurement likelihood calculation) contains a *known* number of discrete cells.

Again, from examination of the measurement likelihood used for previous FB approaches, it is shown that a subtle assumption is made on the true number of features, and that the classical recursion fails to encapsulate this inherent uncertainty in feature number. This uncertainty is as a result of the detection and data association uncertainty induced by the sensor, as well as spurious measurements. As a result of this observation, the estimation theoretic for FBRM and FB-SLAM are re-derived from a finite-set-based perspective as opposed to a vector one as is the case for

classical FB recursions and implementations. Random finite set theory allows for uncertainty in the number of dimensions to be addressed in the filter recursion. This is not the case for previous vector based approaches. This chapter firstly outlines the problems of classical FB algorithms, showing how the measurement uncertainty is not fully addressed by the Bayesian recursion and consequently a new framework for FB autonomous navigation filters is proposed. A feature based mapping metric, which has been lacking in the robotics community, is also introduced for estimating feature map error. After firstly addressing the mapping only case, the finite-set-based formulation is extended to the full simultaneous localisation and mapping problem, where an alternative implementation of the Bayesian SLAM problem is presented and thoroughly analyzed with simulated and real experimental data.

5.1 Introduction

Feature-based mapping is popular for field robotic environments as through the use of robust data association algorithms, impressive localisation estimation accuracy can be acheived. Since an FB map has a variable number of dimensions, the FBRM (and consequently the FB-SLAM) problem requires the estimation of both the number of features and their states (typically in a 2D Euclidean space), since an *a priori* unknown map is completely unknown in both feature location *and* number. While this is not a new observation [49], [4] previous solutions proposed in the literature generally address the problem through independent filters which compromise the Bayesian optimality (in the sense of the ability of the algorithms to calculate the posterior on the map [100]) of the approaches. In most FBRM/FB-SLAM solutions, algorithms termed as 'feature initialisation' and 'feature management' coupled with data association techniques and extended Kalman filters are used to generate the posterior map estimate [43], [44], [26], [28], [50], [69], [12], [13]. Such independent approaches are necessary due to an oversight in the measurement likelihood, which fails to encapsulate the randomness in measurement number as a result of spurious measurements, missed detections as well as a fluctuating number of features within the sensor field of view.

In cluttered, outdoor or underwater environments there can be numerous spurious measurements and missed detections due to the vast diversity of landmarks present (as shown previously in section 3.5). Furthermore, if a feature representative approach is taken, this inherent landmark detection randomness can have detrimental effects on subsequent feature extraction algorithms [101] , [6], and result in numerous false/missed features. It is critical for data association algorithms not to use falsely declared features (or detections) in their hypothesis decision making process. In [44], M. Montemerlo *et. al* use algorithms from GBRM methods [39] to estimate the number of features in the map state. Such an approach has theoretical flaws as highlighted

in the previous chapter (section 4.2.2). Another method of feature management was introduced by D. Makarsov in [12] and used in [28] which outlined the 'Geometric feature track quality' measure of feature existence. This measure is inversely proportional to the innovation between a predicted feature and the measurements. Other techniques [13] simply use the number of successive associations over a fixed set of measurement frames which requires both low clutter rates and successive correct association hypotheses. Based on an intuitive threshold, features are then either added or removed from the map state. These measures are effectively pre/post-processing of the map state estimate at each time step and fail to jointly consider the problem. The number of features in the map state at any given time then gives an estimate of the number of features in the map, as *every* element of the map state is assumed to be a valid feature[1].

The latest emerging multi-target tracking algorithms [102], [103] represent the states and measurement as finite sets. Random finite sets (RFSs) are then used to model uncertainty in both the number of states/measurements as well as their individual values. An RFS-based measurement model, for example, allows for the inclusion of spurious measurements directly into the measurement equation, which then comprises the union of the set of detected measurements and the set of spurious measurements. The finite-set-valued state, at any instance, comprises the union of the predicted targets set and the set of new targets that may appear in the surveillance region. In [102], the mathematics are established for a Bayesian filtering formulation of the multi-target tracking problem, where the number of targets and their corresponding states can then be jointly estimated.

This chapter firstly approaches the FBRM problem from a theoretically optimal perspective where a finite-set-valued map and finite-set-valued measurement are used [102]. Vector based measurement likelihoods fail to encapsulate the uncertainty in measurement number at each time instant, a set-based likelihood is therefore introduced. Since the number of features in the FOV and their positions are variables and the order in which the features are listed has no physical significance, it is natural to represent the map as a *finite set*. In classical approaches, the number of features in the map is estimated sub-optimally through scoring routines [12], or occupancy grid mapping algorithms [44] which are both used in conjunction with data association techniques. In this work, feature initialisation/termination and data association algorithms are not required as the set based recursion incorporates the entire system uncertainty including detection/association as well as the measurement noise. The resulting filter, using an extended Kalman Gaussian mixture implementation, jointly propagates the estimate of the number of features and their states. The approach is then extended to the full Bayesian SLAM problem which uses a random finite

[1]Note this is an essential requirement due to the measurement equation formulation (see section 5.2.1)

set-valued joint vehicle-map state and recursively propagates the optimal likelihood on feature number, feature location and vehicle location. Both simulated and actual datasets are used to analyse the proposed algorithms. The new FB formulation and implementation are shown to have superior feature-based mapping performance, particularly in situations of high clutter and large data association ambiguity.

5.2 FBRM Estimation Theoretic Problem Formulation

The FBRM estimation theoretic problem requires the recursive evaluation of the posterior, $p_{k|k}(M_k|Z^k, X^k)$, through the Bayes recursion,

$$p_{k|k}(M_k|Z^k, X^k) = \frac{g(Z_k|M_k, X_k)p_{k|k-1}(M_k|Z^{k-1}, X^k)}{\int g(Z_k|M_k, X_k)p_{k|k-1}(M_k|Z^{k-1}, X^k)dM_k}. \tag{5.1}$$

The formulation in the previous chapter (section 4.2), concerned the case of an estimated GB map, $M_k = [m^1_{(x,y)}, \ldots, m^{\mathfrak{q}(k)}_{(x,y)}]$, in which the number of elements (grid cells) in the map vector, M_k, within the FOV at each instant, $q(k)$, is known. In this chapter however, the true map, M, shall be assumed to consist of a collection of points in a continuous $\mathbb{R}^2$ state space $m_1, \ldots, m_{\mathfrak{q}}$, indicating the location of the (constant) unknown number of, $\mathfrak{q}$, features in the map (FBRM). At each instant, M_k, then contains location estimates of the estimated $\mathfrak{q}(k) < \mathfrak{q}$ number of features that have passed through the sensors field of view. Thus, the number of dimensions in the state estimation process is a variable, $\mathfrak{q}(k)$, [49], [4], whereas the GBRM problem has a fixed number of dimensions, which was highlighted for the first time in this thesis. The theoretical consequences of this observation has not been addressed by the autonomous navigation community, and is the focus of this chapter.

In the most general case, to maintain the Bayesian representation of eqn.(5.1), assume at time $k-1$, a set of N weighted particles $\left\{w^{(i)}_{k-1}, M^{(i)}_{k-1})\right\}^N_{i=1}$ representing the prior $p_{k-1|k-1}(M_{k-1}|Z^{k-1}, X^{k-1})$ is available, i.e.

$$p_{k-1|k-1}(M_{k-1}|Z^{k-1}, X^{k-1}) \approx \sum_{i=1}^{N} w^{(i)}_{k-1}\delta_{M^{(i)}_{k-1}}(M_{k-1}).$$

The particle FBRM filter proceeds to approximate the posterior $p_{k|k}(M_k|Z^k, X^k)$ at time k by a new set of weighted particles $\left\{w^{(i)}_k, M^{(i)}_k)\right\}^N_{i=1}$ as follows:

The Sequential Monte Carlo (SMC) FBRM Filter Implementation

At time $k \geq 1$,

Step 1: *Sampling Step*

- For $i = 1, \ldots, N$, sample $\widetilde{M}_k^{(i)} \sim q_k(\cdot|M_{k-1}^{(i)}, X_{k-1}, Z_k)$ and set

$$\widetilde{w}_k^{(i)} = \frac{g(Z_k|\widetilde{M}_k^{(i)}, X_k) p_{k|k-1}(\widetilde{M}_k^{(i)}|M_{k-1}^{(i)}, Z^{k-1}, X^k)}{q_k(\widetilde{M}_k^{(i)}|M_{k-1}^{(i)}, X_{k-1}, Z_k)} w_{k-1}^{(i)}. \tag{5.2}$$

- Normalise weights: $\sum_{i=1}^{N} \widetilde{w}_k^{(i)} = 1$.

Step 2: *Resampling Step*

- Resample $\left\{\widetilde{w}_k^{(i)}, \widetilde{M}_k^{(i)}\right\}_{i=1}^{N}$ to get $\left\{w_k^{(i)}, M_k^{(i)}\right\}_{i=1}^{N}$.

To extract the posterior estimate of the features spatial state, MAP or EAP methods can be used. Using the EAP, a solution to the mapping problem can be obtained from the particle approximation of the posterior as follows. Given a particle approximation $\left\{w_k^{(i)}, M_k^{(i)}\right\}_{i=1}^{N}$ of $p_{k|k}(M_k|\cdot)$, the map state estimate $\hat{M}_k$ is given by,

$$\hat{M}_k \approx \sum_{i=1}^{N} M_k^{(i)} w_k^{(i)}.$$

The density $p_{k|k-1}(\widetilde{M}_k^{(i)}|M_{k-1}^{(i)}, Z^{k-1}, X^k)$ is the transition density of the map state which is typically static but can also model the dynamics of the map features in the case of a non-static environment. To ensure particle diversity, in the particle filter feature mapping algorithm the transition density is modeled by a static update corrupted by a zero mean Gaussian noise of 'small' variance, Σ_m. The measurement, Z_k is also assumed to be corrupted by normally distributed noise of variance Σ_Z. The measurement likelihood, $g(Z_k|\widetilde{M}_k^{(i)}, X_k)$, with a known vehicle trajectory, X^k, is therefore given by

$$g(Z_k|\widetilde{M}_k^{(i)}, X_k) = \frac{1}{\sqrt{2\pi\Sigma_Z}} \exp \frac{-(Z_k - \hat{Z}_k^{(i)})^2}{2\Sigma_Z}$$

with,

$$\hat{Z}_k^{(i)} = f(\widetilde{M}_k^{(i)}, X_k) + w_k$$

where $f(\cdot)$ is a linear function in this one-dimensional (range measurement only) scenario. The proposal function $q_k(\cdot)$ may simply be static (assuming a non-moving map) or a more intuitive proposal using information from the likely location of features, based on the measurement at time k. This framework is then theoretically correct for the propagation of a feature with a spatial state space using the range measurements provided by the sensor. Since the sensor returns measurements which are either linearly or non-linearly related to the spatial state space, the measurement likelihood $g(\cdot)$ can be calculated in closed form by invoking some distribution assumptions. In the previous algorithm, the normalisation of the particle weights infers an inherent indication that there is complete certainty of the features spatial state being at *one* of the particle locations. Therefore, this framework cannot handle sensor detection uncertainty (false alarms and missed detections), as every range reading is assumed to have originated from a valid feature. This problem is overcome through the use of the previously mentioned feature initialisation and management routines which are used in modern autonomous mapping algorithms. In practise, mapping algorithms commonly use an EKF approximation to solve the FBRM recursion of eqn.(5.1) [43] but for generality, a particle filter approach was presented here.

5.2.1 Probabilistic vector measurements

This section examines the commonly adopted range-bearing sensor model used in FB algorithms, highlighting some pitfalls in its ability to encapsulate the entire uncertainty present in the measurement[2]. In the general Bayesian formulation, from which most current FBRM (and subsequently both EKF and SMC FB-SLAM algorithms) are derived, the measurement is modeled as a vector,

$$Z_k = \boldsymbol{h}(m_1, \ldots, m_{\mathfrak{q}(k)}, X_k) + \boldsymbol{w}_k \tag{5.3}$$

where $\boldsymbol{h}(\cdot)$ is generally a non-linear function mapping the feature and vehicle locations into the relative range and bearing measurements. The Gaussian distributed random vector, $\boldsymbol{w}_k$, is used to model the additive measurement noise. The measurement likelihood $g(Z_k|m_1, \ldots, m_{\mathfrak{q}(k)}, X_k)$ in eqn.(5.1) is then treated as the likelihood of receiving a vector that contains $\mathfrak{q}(k)$ measurements, one from each of the $\mathfrak{q}(k)$ features $m_1, \ldots, m_{\mathfrak{q}(k)}$. From this measurement model and a vector-based state, an implicit assumption is made that the number of features present (but not necessarily their location) is known *a priori*. Moreover, it is assumed that each feature generates a detection, and the association between the features and measurements is known, as

[2]Recall from section 1.1.1, that in this thesis measurement uncertainty collectively refers to measurement noise, spurious measurements, detection and data association uncertainty, as well as sensor biasses.

the order of measurements is assumed to be the same as the order of the features in the map vector, i.e. z_1 is from feature m_1 etc.

It is obvious that in practise the q^{th} measurement does not necessarily correspond to the q^{th} feature, thus it is not known which feature generates which measurement. Furthermore, some features may not be detected by the sensor thereby generating no measurement, in addition to the sensor receiving a random number of spurious measurements (clutter) and/or measurements from new features. The classical measurement likelihood overlooks this uncertainty, and only models the ideal case of receiving a measurement from each of the features $m_1, \ldots, m_{\mathfrak{q}(k)}$. This has led robotics researchers to date, to add separates data association/feature management routines to the vector-based filtering framework.

While the presence of such measurement uncertainties are not new to the autonomous robotics community, this thesis for the first time explicitly highlights the theoretical drawbacks of current FB sensor models to sufficiently handle it. As a consequence of such inadequacies, a number remedies have been proposed. The collective task of estimating the true number of features, as well as addressing the measurement vs. feature vector ordering are usually addressed in data association algorithms [13], [14] [28], [12], [44], which deal with such measurement uncertainty by additional processing outside the Bayesian loop. Prior to the Bayesian update (5.1), data association techniques are used to determine the measurement-to-feature association [13], [14]. Note that data association considers detection uncertainty and clutter in the calculation of the likelihood of an association event. Measurements from new features are incorporated via separate feature initialization/termination techniques [28], [44].

In existing FBRM formulations, the Bayes filtering is only optimal for the individual hypothesised features if the decisions of the additional pre/post processing are correct. However, there is no concept of Bayes optimality for the map itself because the correct hypothesis is not known, and individual feature optimality does not imply joint optimality. The reason is that the measurement model of eqn.(5.3) can only result in the posterior pdf $p(m_1, \ldots, m_{\mathfrak{q}(k)}|Z^k, X_k)$ of the vector of features. This posterior pdf assumes that the number of features is $\mathfrak{q}(k)$ is known, and thus does not capture all relevant statistical information about the map.

5.2.2 Probabilistic set measurements

To contend with the realistic situation of missed detections and clutter, the measurement in this section is modeled as an RFS. An RFS can encapsulate uncertainty in both number and corresponding elements. Given the current vehicle state, X_k, and

the map M_k, the measurement consists of a set union,

$$Z_k = \bigcup_{m \in M_k} \Theta_k(m, X_k) \cup C_k(X_k) \tag{5.4}$$

where $\Theta_k(m, X_k)$ is the RFS of a measurement generated by a feature at m and $C_k(x_k)$ is the RFS of the spurious measurements at time k. Therefore Z_k consists of a random number measurements in $\mathbb{R}^{\mathfrak{n}_Z}$, where $\mathfrak{n}_Z$ is assumed 2 (range/bearing) in this work. Note that the number of detected measurement may differ from the number of features. It is also assumed that $\Theta_k(m, X_k)$, and $C_k(x_k)$ are independent RFSs.

The RFS of measurements generated by a feature at m is a Bernoulli RFS given by, $\Theta_k(m, X_k) = \emptyset$ with probability $1 - P_d(m, X_k)$ and $\Theta_k(m, X_k) = \{z\}$ with probability density $P_d(m, X_k)g(z|m, X_k)$. For a given robot pose X_k, $P_d(m, X_k)$ is the probability of the sensor detecting a feature at m, and conditioned on detection, $g(z|m, X_k)$, is the likelihood that a feature at m generates the measurement z. The RFS $C_k(X_k)$ of spurious measurements is modeled as a Poisson RFS, that is, the number of elements of $C_k(X_k)$ is Poisson distributed with mean $\lambda_c(X_k)$ while the clutter measurements themselves are uniformly i.i.d. in the sensor field of view. This assumption is also made in numerous data association articles [13], [12].

The RFS Z_k encapsulates all sensor characteristics such as measurement noise, sensor field of view (i.e. state-dependent probability of detection) and false alarms. The measurement likelihood that the sensor produces the measurement Z_k given the vehicle state X_k and map M_k at time k is then given by the convolution [102]:

$$g(Z_k|X_k, M_k) = \sum_{W \subseteq Z_k} \theta_k(W|M_k, X_k) c_k(Z_k - W) \tag{5.5}$$

with $\theta_k(\cdot|M_k, X_k)$ denoting the density of the RFS of observations generated from the features in the map M_k given the state of the vehicle, and $c_k(\cdot)$ denoting the density of the RFS C_k of false alarms. From eqn.(5.5) it can be seen that W represents the subset of measurements which are as a result of an environmental feature (i.e. not a false alarm), furthermore that the difference operation used in eqn.(5.5) is the set difference. The density of a random finite set requires more general mathematical constructs than that used for vectors (see for example [104]). $\theta_k(\cdot|M_k, X_k)$ describes the likelihood of receiving a measurement from the elements of the set-based map which incorporates detection uncertainty and measurement noises. $c_k(\cdot)$ models the spurious measurements of the sensor and is typically *a priori* assigned [13], [12]. Due to a limited sensor FOV, random distribution of features in the environment and vehicle motion, the true number of features in the map at any instant is a random number. Since the feature locations are also random, the map state, M_k is also modeled as an RFS, $M_k = \{m_1, \ldots, m_{\mathfrak{q}(k)}\}$ to encapsulate such joint uncertainty.

5.2.3 FBRM Error Metric

FB-SLAM algorithms and their mapping only counterpart, FBRM, both produce estimates of the locations of the features in the surrounding environment. However, the error in such an estimate is inadequately examined in the literature, with more work focussing on the localisation error. Since map estimation is critical to the algorithm, this section emphasises that consistent error analysis of the resulting map is also critical to algorithm performance. Previous methods of evaluating error, generally consider a subset of features only, analysing the consistency and convergence properties of the location estimate. While this is valid for individual features, it gives no information as to the joint multiple-feature map state as a whole. Furthermore, there is no cost metric for the case of falsely declared features, or missed feature declarations. Figures 5.1 and 5.2 for instance, show two sets of results from two Monte Carlo implementations of the benchmark NN-EKF FB-SLAM algorithm, with tentative feature lists to handle detection uncertainty and spurious measurements [13], [14] [28], [12], [44]. The true feature locations are indicated by circles, with feature estimates shown as crosses. The parameters for the presented implementation were: $0.5ms^{-1}$ and 0.5^o for velocity and steering control input noise respectively, $0.5ms^{-1}$ and 0.5^o for range and bearing measurement noise, and feature detection probability, P_d=0.95. SLAM jointly considers the mapping and localisation problems, however, evaluation of the mapping aspect, particulary of feature-based approaches, is poorly addressed in the autonomous navigation community. Both results indicate consistent localisation estimates, however the map estimates differ dramatically. This mapping error (differing feature location estimates and differing feature number estimates), is srarely quantified in FB-SLAM literature, and in this example is as a result of varying number of associations (as a result of detection and/or association uncertainty) for features which affects the feature management algorithms.

Consequently, due to the lack of an accurate metric, error evaluation for FB maps has received little attention, with the majority of focus being put on localisation estimation error. In environments with high spurious measurements, low landmark (and consequently, feature) detection probabilities, or multiple moving landmarks, the importance of accurate mapping (feature mapping in the case of the widely popular FB-SLAM), cannot be overlooked. Recent work in the tracking community however [105], has developed a consistent performance metric for evaluating such a joint multi-target estimation problem, as is the case in the FBRM and FB-SLAM problems. Briefly the feature map estimation error metric (which jointly considers errors in feature location estimate, and feature number estimate) is based on a p^{th}-order

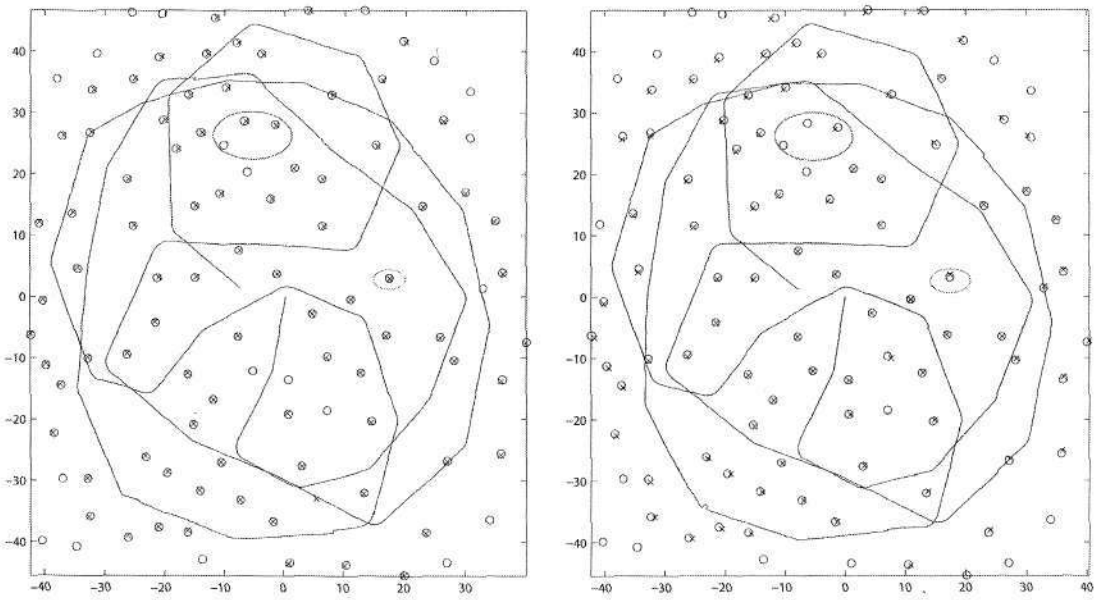

Figure 5.1: *This figure shows the estimated vehicle trajectory and corresponding feature based maps from two Monte Carlo runs of the standard nearest-neighbour EKF implementation of FB-SLAM. Note the differing maps produced by both runs, with both feature detections and location estimation errors.*

Wasserstein construction and is given by,

$$\bar{d}_p^{(c)}(\hat{M}_k, M) := \left(\frac{1}{|M|} \left(\min_{j \in \{1,\ldots,|M|\}} \sum_{i=1}^{|\hat{M}_k|} d^{(c)}(\hat{m}_i^k, m_j)^p + c^p(|M| - |\hat{M}_k|) \right) \right)^{1/p} \tag{5.6}$$

and,

$$d^{(c)}(\hat{m}_i^k, m_j) = \min(c, ||\hat{m}_i^k - m_j||) \tag{5.7}$$

is the minimum of the cut-off parameter, c, and the Euclidean distance between the estimated feature location, $\hat{m}_i^k$ and the true feature location m_j. As in [105], the common case of p being set at 2 is considered. The cut-off parameter, c, models a weighting between the cost of a cardinality estimate error to that of a feature location estimate error, and for this work is set at 10. While the choice of these metrics may affect the absolute value of the feature mapping error metric, the specific choice of these parameters is not critical to the work presented in this chapter, as all filter comparative results are obtained from a metric using the same parameter settings. In [105], it is proven that this is indeed a mathematically consistent metric. This metric is well suited to FB mapping evaluation as it includes joint costs for the error

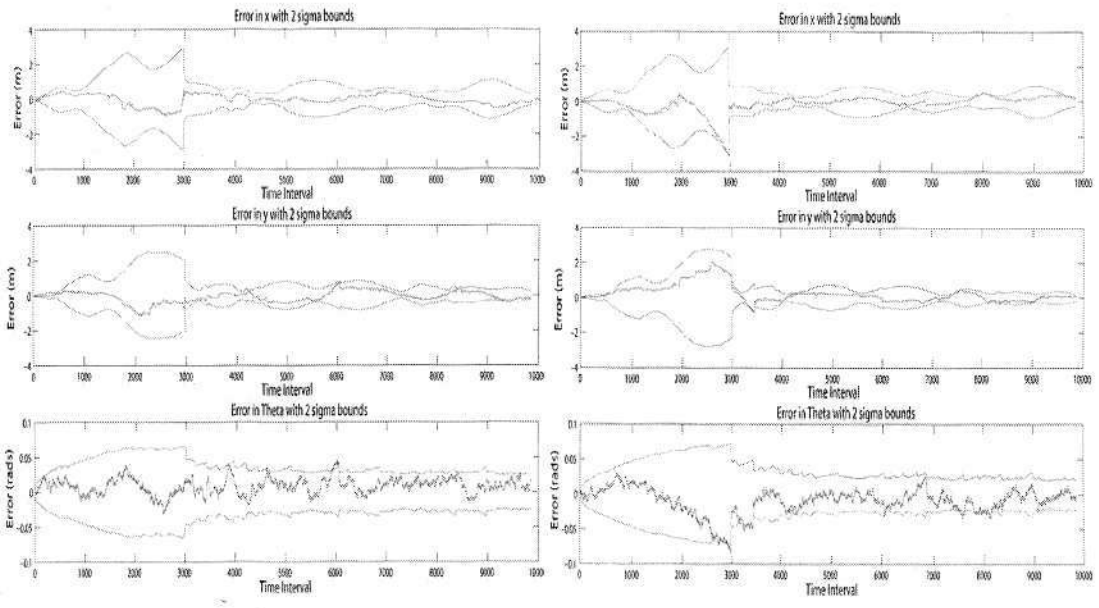

Figure 5.2: *The resulting vehicle pose error plots for the maps presented in figure 5.1. The metrics show consistent localisation estimates, but give no indication of map quality.*

in both the estimated number and the corresponding locations of the features. The metric is therefore applied in this chapter, for the first time, to evaluate FB mapping errors.

5.3 The PHD-FBRM Filter

The formulation presented here to solve the FBRM problem, accounts for the unknown number of features, data association uncertainty, detection uncertainty, and clutter. This can be achieved by treating the map M_k and the measurement Z_k as realisations of RFSs, as opposed to realisations of random variables within a state vector. For a FBRM approach, the set of features, M_k, being estimated at time k is a subset of the entire map, M, which has been observed by the robot. More precisely,

$$M_k = \{m_1, \ldots, m_{\mathfrak{q}}\} \cap FOV(X^k) \tag{5.8}$$

where $FOV(X^k)$ denotes the sensor field of view along the robot trajectory up to and including time k, and where $|M_k| = \mathfrak{q}(k)$, the number of features which have entered the sensor field of view. As the features are assumed static, M_k, then evolves in time

according to,

$$M_{k|k-1} = M_{k-1} \cup B_k(X_k) \tag{5.9}$$

which is the set union of the previous RFS of detected features and the RFS of the new features which enter the FOV at time k, $B_k(X_k)$, due to the motion of the robot. These sets are assumed both Poisson distributed and independent. Note that previous FBRM (and FB-SLAM) algorithms do not include the possibility of new features entering the sensor's field of view in the state transition equation.

Unlike the vector formulation for maps, the expected map cannot be used since such an operation is not defined for sets. Fortunately, there is an analogous notion to the 'expectation' of an RFS that can be borrowed from point process theory. This construct treats the random set as a random counting measure or a point process (a random finite set and a simple finite point process are equivalent [104]). The expectation of a point process is called the intensity measure and its density is the called the intensity function, also known as the probability hypothesis density (PHD) in the tracking literature [102]. For an RFS M_k, with probability distribution P, the intensity function is a non-negative function v_k, such that for each region S in the space of features,

$$\int_S v_k(m)dm = \int |M_k \cap S| \, P(dM_k). \tag{5.10}$$

Since, $|M_k \cap S| = \sum_{x \in X} \mathbf{1}_S(x)$, is the number of features, the integral of the intensity v over any region S gives the expected number of elements of M that are in S. Simply setting S to be the entire mapping region gives $\int v(x)dx$ which can be used as an estimate for the number of features in the map set. The (co-ordinates of the) peaks of the intensity are points (in the space of features) with the highest local concentration of the expected number of features and hence can be used to generate estimates for the spatial coordinates of the elements of M. The integral of the PHD gives the expected number of features and the peaks of the PHD function can be used as estimates of the positions of the features. An illustration of the intensity function for a simulated environment is shown later in figure 5.6.

The PHD filter recursion therefore propagates the intensity of the RFS state and uses the RFS measurement in the update stage. Since the intensity is the first order statistic of a random finite set, the PHD filter is analogous to the constant gain Kalman filter which propagates the first order statistic (the mean) of the vector-based state. However, the *intensity*, $v_k(m; X_k)$, can be used to estimate both the number of features in the map set, and their corresponding states (along with the uncertainty in the state estimate). Under the assumption of clutter measurement independence and the map set being a Poisson RFS, it can be shown that $v_k(m)$ can be recursively estimated through [102],

$$v_{k|k-1}(m|X_k) = v_{k-1}(m|X_{k-1}) + b_k(m|X_k) \tag{5.11}$$

$$v_k(m|X_k) = v_{k|k-1}(m|X_k)\Big[1 - P_d(m|X_k) + \sum_{z\in Z_k} \frac{P_d(m|X_k)g(z|m,X_k)}{c_k(z) + \int P_d(\zeta|X_k)g(z|\zeta,X_k)v_{k|k-1}(\zeta|X_k)d\zeta}\Big] \quad (5.12)$$

Also,

$c_k(\cdot)$ = intensity of the (state independent) clutter RFS C_k at time k.
$b_k(m|X_k)$ = intensity of the new feature RFS $B_k(X_k)$.

A block diagram of the proposed PHD-FBRM filter is depicted in figure 5.3.

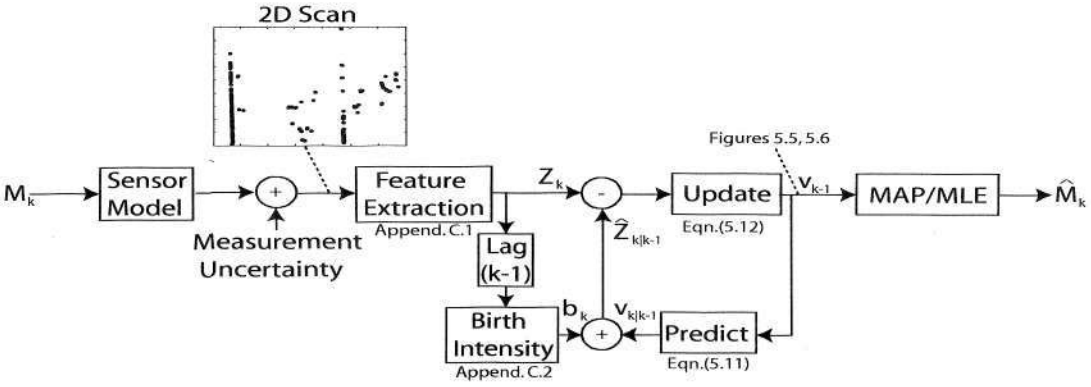

Figure 5.3: *An overview of the proposed PHD-FBRM filter, with associated equations indicated.*

As is similar to the Bayesian recursion in vector-based FBRM or SLAM, due to multiple integrals, closed form solutions in general unachievable and therefore some simplifying approximations are required. The following section briefly outlines a Gaussian mixture solution to the recursion.

5.3.1 Gaussian Mixture PHD-FBRM Filter Implementation

Let the predicted map intensity, $v_{k|k-1}$, be a Gaussian mixture of the form,

$$v_{k|k-1}(m|X_k) = \sum_{i=1}^{J_{k|k-1}} w_{k|k-1}^{(i)} \mathcal{N}\left(m; \mu_{k|k-1}^{(i)}, P_{k|k-1}^{(i)}\right) \quad (5.13)$$

which is a mixture of $J_{k|k-1}$ Gaussians, with $w_{k|k-1}^{(i)}$, $\mu_{k|k-1}^{(i)}$ and $P_{k|k-1}^{(i)}$ being their corresponding predicted weights, means and covariances. A static map implies $\mu_{k|k-1}^{(i)} =$

$\mu_{k-1}^{(i)}$, and since the robot location is known there is no process noise injected into the system during the time update so $P_{k|k-1}^{(i)} = P_{k-1}^{(i)}$. Let the new feature intensity, b_k, at time k also be Gaussian mixture of the form,

$$b_k(m|X_k) = \sum_{i=1}^{J_{b,k}} w_{b,k}^{(i)} \mathcal{N}\big(m; \mu_{b,k}^{(i)}, P_{b,k}^{(i)}\big) \tag{5.14}$$

where, $J_{b,k}$ defines the number of Gaussians in the new feature intensity at time k and $w_{b,k}^{(i)}$, $\mu_{b,k}^{(i)}$ and $P_{b,k}^{(i)}$ determine the shape of the new feature GM proposal density according to a chosen strategy. This is analogous to the proposal distribution in the particle filter and provides an initial estimate of the new features entering the map. The strategy in this work is outlined in the following section 5.3.2. As a static map is assumed in this work, and the vehicle motion is known, the predicted intensity $v_{k|k-1}$ is also a Gaussian mixture.

$$v_{k|k-1}(m|X_k) = \sum_{i=1}^{J_{k|k-1}+J_{b,k}} w_{k|k-1}^{(i)} \mathcal{N}\big(m; \mu_{k|k-1}^{(i)}, P_{k|k-1}^{(i)}\big)$$

which consists of the union of the time predicted previous map intensity, $M_{k|k-1}$, and the proposed new feature intensity according to eqn.(5.9). Since the measurement likelihood is also of Gaussian form, it can be seen from eqn.(5.12), that the posterior intensity, v_k is then also a Gaussian mixture given by,

$$v_k(m|X_k) = v_{k|k-1}(m|X_k)\Big[1 - P_d(m|X_k)) + \sum_{z\in Z_k} \sum_{i=1}^{J_{k|k-1}+J_{b,k}} v_{G,k}^{(i)}(z, m|X_k)\Big]. \tag{5.15}$$

The components of the above equation are given by,

$$v_{G,k}^{(i)}(z, m|X_k) = w_k^{(i)}(z|X_k)\mathcal{N}(m; \mu_{k|k}^{(i)}, P_{k|k}^{(i)})$$

$$w_k^{(i)}(z|X_k) = \frac{P_d(m|X_k) w_{k|k-1}^{(i)} \mathcal{N}^{(i)}(z, X_k)}{c_k(z) + \sum_{j=1}^{J_{k|k-1}+J_{b,k}} P_d(m|x_k) w_{k|k-1}^{(j)} \mathcal{N}^{(j)}(z, X_k)}$$

where, $\mathcal{N}^{(i)}(z, X_k) = \mathcal{N}\big(z; H_k\mu_{k|k-1}^{(i)}, S_k^{(i)}\big)$. The components are obtained from the standard EKF update equations,

$$\mu_{k|k}^{(i)} = \mu_{k|k-1}^{(i)} + K_k^{(i)}(z - H_k\mu_{k|k-1}^{(i)}) \tag{5.16}$$

$$P_{k|k}^{(i)} = [I - K_k^{(i)} \nabla H_k] P_{k|k-1}^{(i)} \tag{5.17}$$

$$K_k^{(i)} = P_{k|k-1}^{(i)} \nabla H_k^T [S_k^{(i)}]^{-1} \tag{5.18}$$

$$S_k^{(i)} = R_k + \nabla H_k P_{k|k-1}^{(i)} \nabla H_k^T \tag{5.19}$$

with ∇H_k being the Jacobian of the measurement equation with respect to the features estimated location. As stated previously, the clutter RFS, C_k, is assumed Poisson distributed [13], [12] in number and uniformly spaced over the mapping region. Therefore the clutter intensity is given by,

$$c_k(z) = \lambda_c V \mathcal{U}(z) \tag{5.20}$$

where λ_c is the average number of clutter returns per unit volume, V is the volume of the region and $\mathcal{U}(\cdot)$ denotes a uniform distribution.

5.3.2 The New Feature Proposal Strategy

The new feature proposal density is similar to the proposal function used in particle filters [44], [40], [106] and is used to give some *a priori* information to the filter about where features are likely to appear in the map. In SLAM, it is assumed that there is no *a priori* information about the map, thus the Gaussians of the mixture intensity, b_k, may be uniformly distributed in a non-informative manner about the space of features (analogous to the prior map used in occupancy grid algorithms). The sum $\sum_{i=1}^{N \times J_{b,k}} w_{b,k}^{(i)}$ then gives an estimate of the expected number of new features to appear at time k. This can be an *a priori* assigned as a constant or a function of the vehicle's control inputs.

However, in order for comparison with previous vector-based SLAM algorithms, in this work the feature birth proposal at time k is chosen to be the set of measurements at time $k-1$, Z_{k-1}. This maintains equality with previous approaches as the vector-based algorithms initially consider *all* extracted features to be potential new features (as there is no inclusion of clutter likelihoods in the recursion), and process them through the feature management methods described previously. This is outlined in more detail in Appendix C.

5.4 FBRM Experiments

This section compares the proposed finite-set-based FBRM framework to popular solutions from the literature using both simulated and real experimental data. Regardless of the choice of vehicle state representation, the vast majority of feature-based implementations adopt an EKF framework coupled with data association and

map management methods for propagating the feature map estimate [44], [12], [28], [6], [19], [13]. As emphasised throughout this chapter, such methods disregard the jointness of the feature-based map estimation problem and independently estimate the feature number and locations. The benchmark algorithm chosen for comparison purposes is therefore a nearest-neighbour EKF implementation, coupled with the 'log-odds' map management method [44]. This map-management approach 'propagates' the map dimensionality by assigning an intuitive log odds score to each associated or un-associated feature. As outlined in [44], the independent map management algorithms incorporated into vector-based recursions also require score values to be intuitively set. To this end, an associated feature receives a score of $+0.5$, while an unassociated feature (within the sensor field of view), receives a score of -0.2. A simple existence counting rule is therefore established. The probability of a feature existing can then be trivially recovered from the log-odds representation. For this analysis, a 95% χ^2 association confidence window is chosen. The following FBRM error metric results are obtained from eqn.(5.6), with parameters $c=5$ and $p=2$, with the effects of adjusting these parameters being discussed later.

As with the proposed framework, dimensionality estimates are extracted by comparison with a pre-defined threshold, ϵ. For all trials, all filters receive identical measurement sequences. The existence threshold is set at $\epsilon_N = N-0.4$ for $N \in [1, 2, 3, \ldots]$. Therefore, for previous approaches, $\epsilon_1 = 0.6$, with $\epsilon_2 = 1.6$, $\epsilon_3 = 2.6$, $\epsilon_4 = 3.6$ etc. being used for the proposed PHD solution, due to its ability to model multiple features by a single Gaussian.

5.4.1 Synthetic Data

The vehicle traverses a simulated environment as shown in figure 5.4. Over the entire trajectory, a total of 80 point features are observed, however at any given time only a subset are observed due to the limited sensor field of view (simulated as 15m maximum range and a 360^o field of view). The trials carried out here subject the system to varying amounts of measurement noise, varying clutter rates, varying feature detection probabilities and varying densities of dynamic features.

Measurement Noise and Clutter Rate Analysis

Increases in measurement noise (range/bearing), has the subsequent effect of increasing data association ambiguity and hence the difficulty of the FBRM problem. To highlight the merits of the proposed method, which avoids hard data association decisions as well as jointly estimating the map dimensionality, trials are carried out in which the measurements are subjected to increasing amounts of noise. The measurement noise covariance for each trial is set at $\mathrm{R} = \gamma[(0.25m)^2\ 0; 0\ (0.5^o)^2]$, where $\gamma \in [1, \ldots, 100]$. Figure 5.5 shows a comparison of the final FBRM error of the

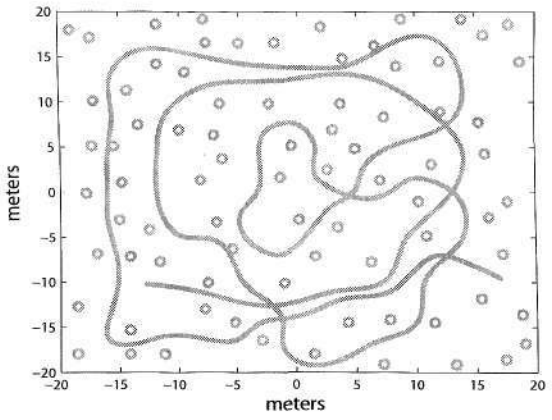

Figure 5.4: *An overview of the map and vehicle trajectory ground truth for the following FBRM filter analysis.*

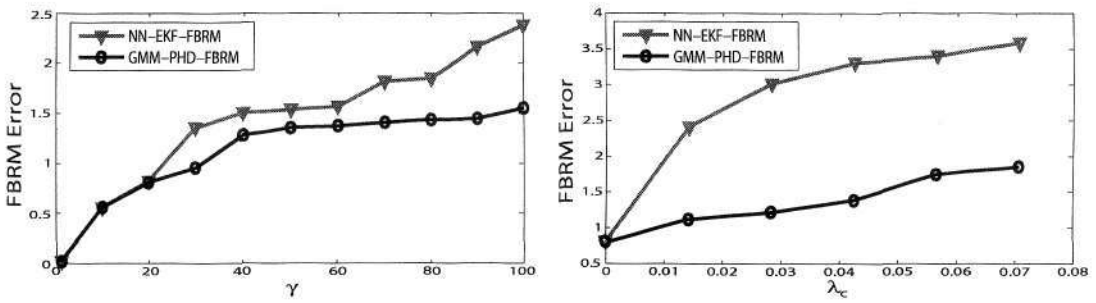

Figure 5.5: *Comparison of FB mapping error vs. measurement noise (left) and clutter rate (right) for the proposed filter and the classical EKF solution.*

posterior feature map estimate for each filter at differing amounts of noise inflation, γ.

Despite widespread acknowledgement that clutter is an important and common component of measurement uncertainty, a review of the literature exposes lack of proper filter analysis with respect to the spurious measurement rate. Data association literature, often completely neglects clutter rate analysis [14], [12], or adopts vague interpretations [13]. Any proposed FB navigation filter requires a thorough analysis of its ability to handle inevitable spurious measurements. Therefore, in this chapter, the clutter density is explicitly defined as the density of clutter measurements within the sensor field of view. Furthermore, clutter measurements are uniformly distributed in polar space, i.e. the sensor measurement space. Setting the measurement noise multiplier at a fixed value of $\gamma = 20$, which from figure 5.5 is seen to be the point just prior to significant deviation in filter performances, the map estimation error for

various clutter densities is analysed.

The right-hand plot in figure 5.5 depicts the map estimation error for clutter densities ranging from $\lambda_c = 0$ to $\lambda_c = 0.0707m^{-2}$, which correspond to a mean number of (Poisson distributed) clutter measurements of 0 to 50 per 360^o scan within a maximum range of $15m$. Given the commonly adopted map management methods, it is theoretically ambiguous how scoring regimes should be altered for a given clutter rate. The proposed framework however, directly incorporates clutter probabilities directly into the filter recursion of eqn.(5.12), thus no parameter adjustment/tuning is required.

The results demonstrate an increased robustness of the proposed framework to difficult situations of large measurement noise and high rate of spurious measurement. Increase data association breakdowns result in the continual deterioration of the EKF map estimate. In the case of closely lying features (and large measurement noise), the PHD approach may not be able to resolve the features, however it will represent the spatial density of both features by a singular Gaussian with a corresponding weight of 2 (or more). This is only theoretically possible using the RFS framework outlined in this chapter. A graphical example of such posterior map intensity is illustrated in figures 5.6 and 5.7.

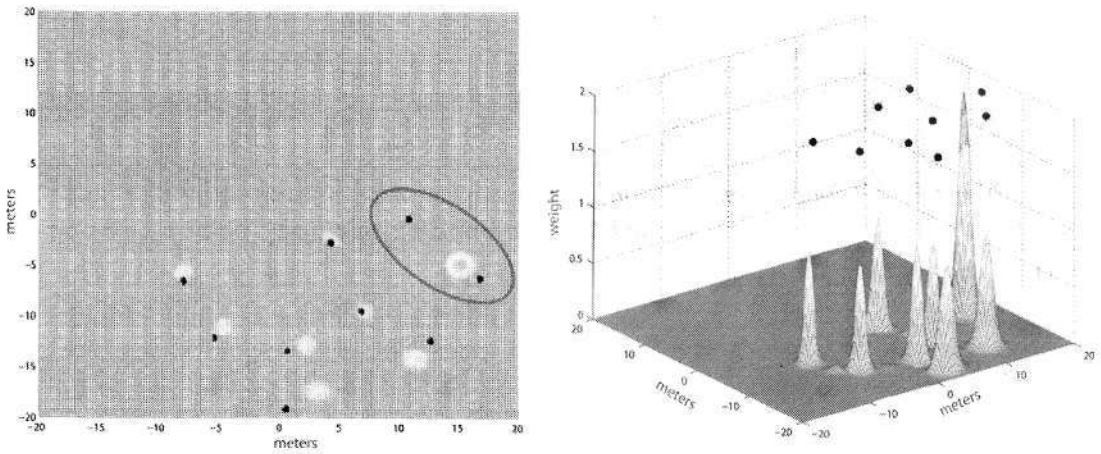

Figure 5.6: *Gaussian mixture representation of the intensity function, showing peaks at feature locations, with 2 features represented by a single peak with weight 2 as highlighted. Black dots show the true feature locations within sensor range.*

Dynamic Feature Density and Detection Probability Analysis

This section demonstrates algorithm robustness in the presence of dynamic features and varying feature detection / extraction probability. The measurement noise

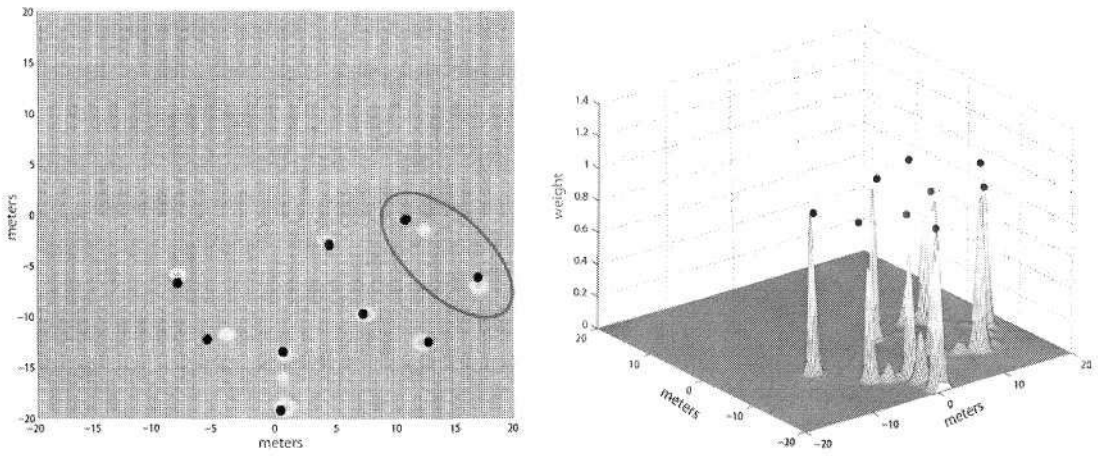

Figure 5.7: *Gaussian mixture representation of the intensity function, showing peaks at feature locations, with all features correctly resolved. The new Gaussians of the mixture have unity weights, with some smaller components also evident of small weight.*

multiplier is again fixed at $\gamma = 20$, with the clutter density set at $\lambda_c = 0.014m^{-2}$ (10 clutter measurements per scan). Dynamic features are uniformly distributed and evolve in time according to a Brownian motion model, $X_k = X_{k-1} + N_k$ with $N_k \sim \mathcal{N}(0, Q)$. The detection probability of a dynamic feature is set equal to that of a static feature ($P_d = 0.95$). Taking a map area to be $20m \times 20m$ (as in figure 5.4), the density of dynamic features is increased and the effects on the mapping accuracy examined.

For the detection trials, the feature detection probability is varied from 0.6 to 1. As is the case for the clutter trials of the previous section, classical vector-based approaches fail to theoretically incorporate detection uncertainty into the dimensionality estimation aspect of the FBRM algorithm. Figure 5.8 plots the posterior FBRM estimation error from both trials. In the case of interfering dynamic features, it is clear that the proposed method produces feature maps of increased accuracy compared to classical methods, however a reduced accuracy is evident for features of reduced detection probability.

As is evident from the update eqn.(5.12), given a single missed detection of feature j at time k, the updated weight becomes $(1-P_d)w_k^{(j)}$. Given two successive missed detections, the weight becomes $(1-P_d)(1-P_d)w_k^{(j)}$, which typically would be below the map dimensionality estimation threshold, ϵ. Consequently, given successive missed detections prior to exiting the sensor field of view, features may not be correctly declared resulting in an increased mapping error. This problem becomes more evident as P_d decreases. This is in contrast to scoring regimes which depend on the total

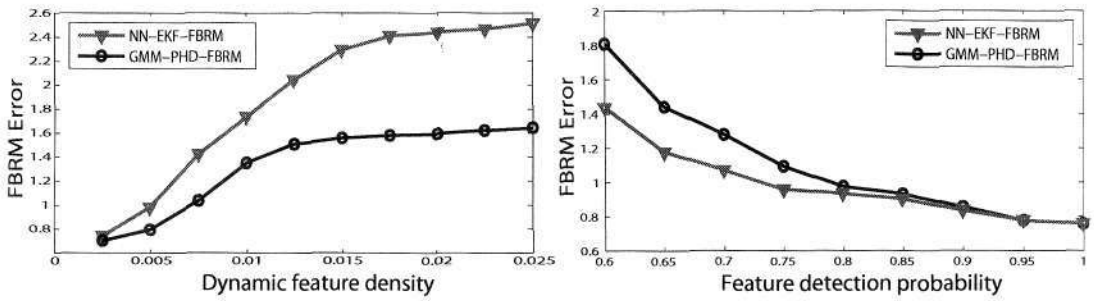

Figure 5.8: *Comparison of the map estimation error in the presence of increasing densities of moving features (left) and increasing feature detection probability (right).*

number of detections / missed detection of a given feature, as opposed to the *order* of the detection sequence.

Computational Complexity Analysis

At time k, given $\mathfrak{z}(k)$ measurements and $\mathfrak{q}(k)$ map states, the computational complexity of a direct implementation of a NN-EKF FBRM solution is $\mathcal{O}(\mathfrak{z}(k)\mathfrak{q}(k))$, due to conditional feature / measurement independencies and evaluation of the measurement-map state associations. According to update eqn.(5.12), the complexity of the proposed solution is also $\mathcal{O}(\mathfrak{z}(k)\mathfrak{q}(k))$. Absolute computational load is compared through side by side C++ implementations of varying map dimensionality, on an Intel(R) duo-core 1.73GHz processors with 2GB RAM. Figure 5.9 reports the average measurement update execution time, obtained through averaging 1000 Monte Carlo updates, for an increasing map dimensionality. The figure clearly illustrates the expected linear increase in computation load for both approaches, with the proposed method requiring more processing time than the simplistic NN-EKF solution, primarily due to the pruning and merging operations required for GMM implementations. Despite its increased load, real-time implementation is possible.

FBRM Error Metric Analysis

Figure 5.10 shows some simple generated input data, along with the resulting posterior feature map estimates. Manual observation exposes that, for the same set of measurements, a single false feature is declared with the NN-EKF approach coupled with increased feature localisation error when compared with the proposed method. As introduced previously in section 5.2.3, the c and p parameters in eqn.(5.6) determine the influence of both aspects of the estimation error which encapsulate the FBRM problem, that of localisation and dimensionality estimation error. Further insight into the effects of a given choice of parameters is shown in figure 5.11.

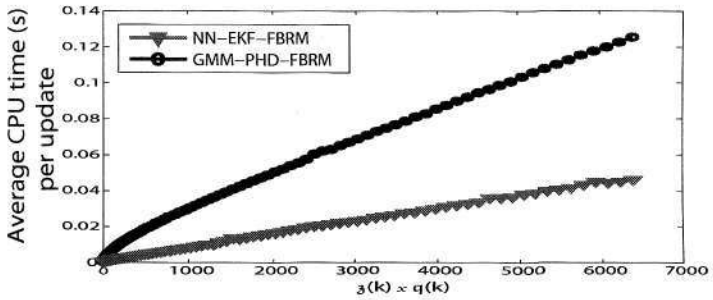

Figure 5.9: *Comparison of the computational complexity, demonstrating the linear increase in load with map dimensionality.*

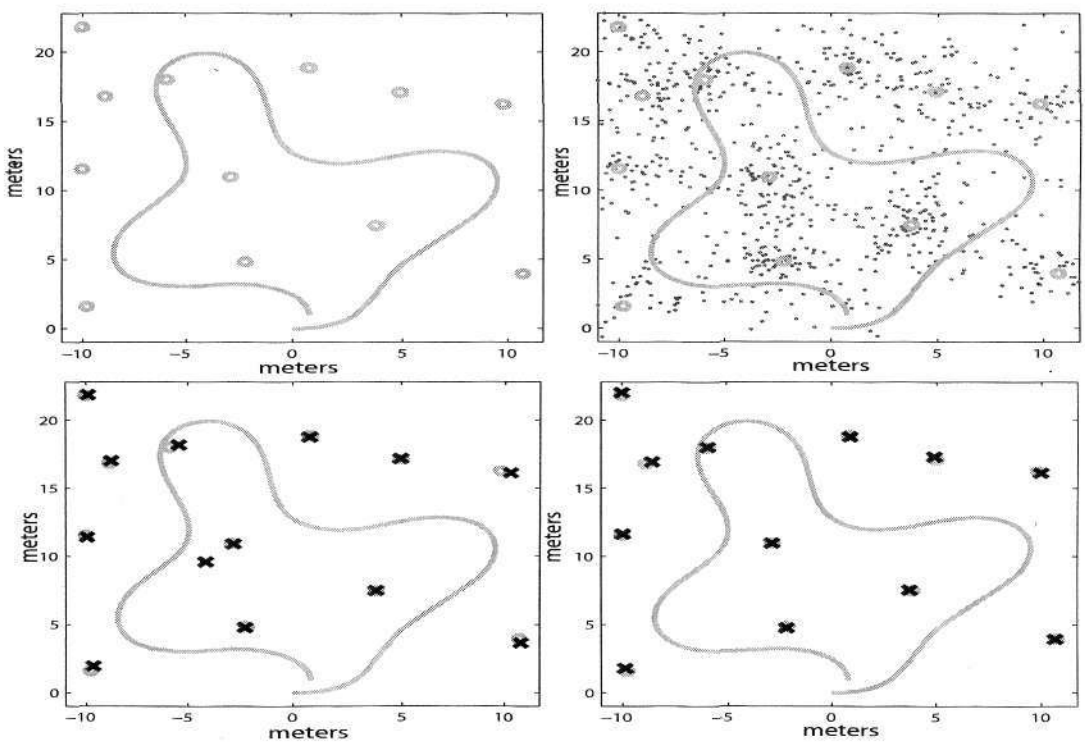

Figure 5.10: *A sample FBRM trial illustrating the ground truth (top-left) and raw measurement data (top-right), with the corresponding posterior FB map estimates from the classical NN-EKF-FBRM filter (bottom-left) and the proposed GMM-PHD-FBRM filter (bottom-right).*

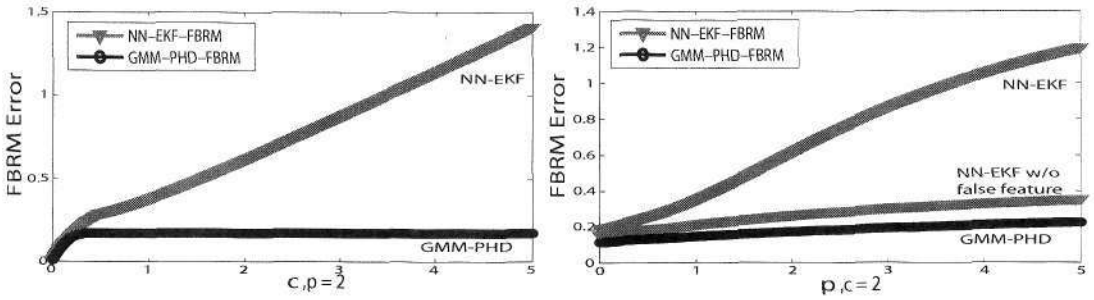

Figure 5.11: *FBRM error vs. c parameter, for a given value of p (left). The c parameter primarily determines the contribution of dimensionality errors to the total reported error. FBRM error vs. p parameter , for a given value of c (right). The p parameter primarily determines the contribution of localisation errors to the total reported error.*

As is evident from eqn.(5.6) and further illustrated in figure 5.11, an increasing c parameter results in an increasing overall error for the NN-EKF estimate. This is due to the contribution of the single false feature, which correspondingly has no effect on the error reported by the dimensionally correct GMM-PHD posterior estimate. The c parameter determines the maximum distance at which an estimate is classified as a poorly localised feature estimate, as opposed to a false feature declaration. For a given feature estimate-ground truth assignment, the p value influences the contribution of the localisation estimation error. The visually evident improved feature location estimates of figure 5.10 are evident in figure 5.11 by a lower total error reported for a given choice of p. To isolate the feature localisation estimation aspect, comparisons are also shown in which the false feature from the NN-EKF estimate, was both ignored and included.

5.4.2 Campus Dataset

This section applies the outlined algorithm to a portion of the outdoor campus dataset introduced in the previous chapter. A section of the university campus (shown in figure 5.12) is used to test the performance of the proposed algorithm with real data. Due to the common coverage fallacy of GPS sensors, the ground truth location for the experiment was obtained by manually matching successive laser scans. The 'true' vehicle control inputs were then derived and used to ensure the predicted vehicle location matched the ground truth location. In this testing ground, the trees and posts along the road side are used as the point features (figure 5.12) and were extracted from each laser scan using clustering techniques [6]. The goal therefore of the FBRM algorithms, is to estimate the number and location of the point features within the mapped region (over a path of approximately 300m). The 'geometric feature quality'

approach of estimating map dimensionality [28] is also compared in this section.

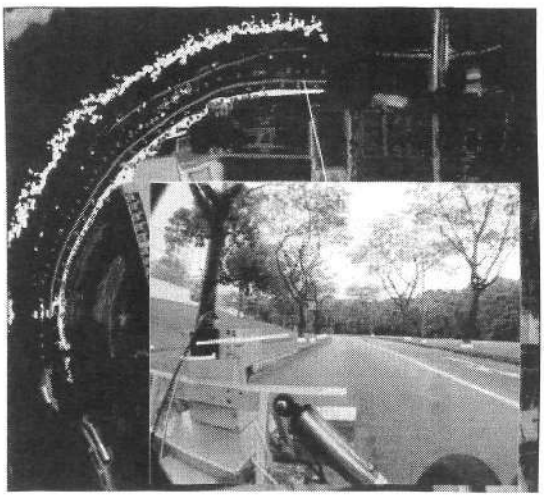

Figure 5.12: *An overview of the testing ground within the university campus. The path and raw laser measurements are superimposed on a portion of a satellite image of the campus. Also shown is a view from the vehicle showing the environment mainly consisting of trees, sign posts and lamp posts. The laser data is also projected into the image plane and plotted.*

Ground truth for this experiment requires knowledge at each time step as to how many features have passed through the surveillance region of the sensor, as well as their ground truth locations. This is a challenging task in a real outdoor environment. As the vehicle location is assumed known, laser scans were back projected from the known locations and superimposed on one another in order to highlight the point features in the scene. Furthermore, point features along the roadside are manually selected in the images at each time step and also plotted with respect to the laser sensor for data verification. Once the map ground truth is verified, the true number of features scanned at each time step can be trivially obtained. The number of extracted clusters per scan varied from zero to 21.

Figure 5.13 shows the estimated number of features in the map for each filter at each time step. The ground truth feature count is also plotted. Biasses in the map cardinality can be seen in the vector based approaches with the FQ method performing poorly due to non-uniform false alarms along the road bank and frequent data association failures. Whilst the PHD approach has some error in early scans it tracks the true number of features closely as the experiment continues. The corresponding maps produced can be seen in figure 5.14. The outlined PHD approach demonstrates an improved mapping quality in terms of less spurious features whilst maintaining accurate location state estimates. Low detection probability features still pose some problems to the algorithm however with some missed declarations being present. The

resulting map still compares well with the manually constructed ground truth, and possesses far fewer false declarations than the previous vector-based approaches.

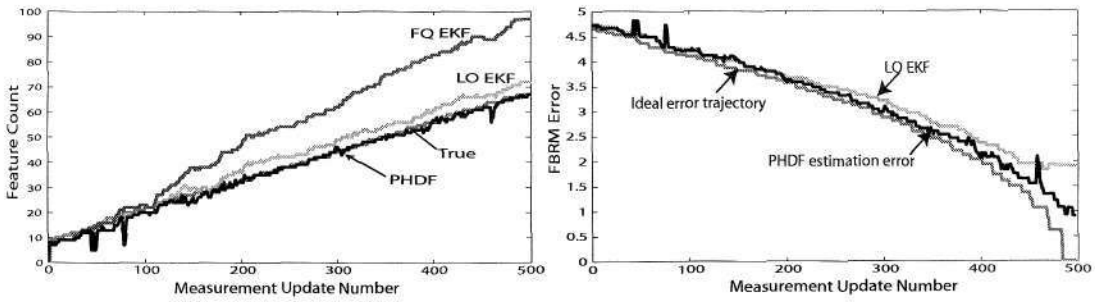

Figure 5.13: *The posterior estimate on the number of features present at each time step (left) and the temporal FBRM error metric (right). It can be seen that the presented set-based approach reports a reduced error in terms of the number of estimated features. Cardinality biasses are introduced to the vector based methods as the initialisation and termination routines rely on accurate data association decisions and can be prone to failure in environments of fluctuating detection probabilities and frequent spurious measurements.*

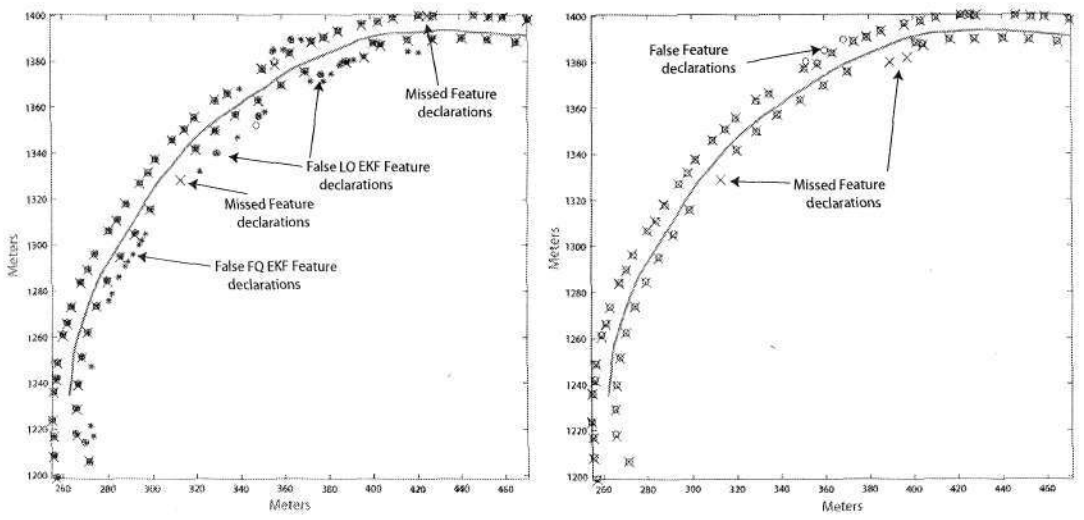

Figure 5.14: *The resulting map from the LO and FQ NN-EKF-FBRM filters as well as the posterior map estimate from the PHD-FBRM filter. The left hand figure shows the resulting map from the LO (circles) and FQ (stars) NN-EKF-FBRM filters. PHD-FBRM estimates (circles) can be seen in the right hand figure. Both figures plot the true feature locations (crosses).*

While accurate verification of the outlined FBRM solution is challenging in practise (as is the case for any real world state estimation problem), the experiment shown here demonstrates the mapping ability of the proposed set-based FBRM framework in a real outdoor environment in the presence of data association uncertainty and spurious measurements. The following section expands the set-based theoretic to the full SLAM problem.

5.5 An RFS Formulation for Bayesian SLAM

This section extends the previous RFS FBRM framework, to the full FB-SLAM problem, where the vehicle trajectory, X^k, must be jointly estimated with the number of features and their corresponding locations. A PHD recursion is again derived and a GM implementation for the full Bayesian SLAM problem introduced. The aim is to recursively propagate the density,

$$p_{k|k}(X^k, M_k|Z^k, u^{k-1}, X_0). \tag{5.21}$$

From an optimal Bayesian perspective, the posterior probability density should capture all relevant statistical information about the vehicle state and the map. Again, from Bayes rule,

$$p_{k|k}(X^k, M|Z^k, u^{k-1}, X_0) = \frac{g(Z_k|M_k, X_k)p_{k|k-1}(X^k, M_k|Z^{k-1}, u^{k-1}, X_0)}{\int\int g(Z_k|M_k, X_k)p_{k|k-1}(X^k, M|Z^{k-1}, u^{k-1}, X_0)dX_k dM_k} \tag{5.22}$$

where,

$$p_{k|k-1}(X^k, M_k|Z^{k-1}, u^{k-1}, X_0) = \int f(X_k|X_{k-1}, u_{k-1})p(X^{k-1}, M_k|Z^{k-1}, u^{k-2}, X_0)dX_{k-1}.$$

The motion of the vehicle is modeled as a first order Markov process with transition density $f(X_k|X_{k-1}, u_{k-1})$. In the general Bayesian formulation of SLAM [50], eqn.(5.21) is treated as being the joint probability density of a random vector containing the map state estimates, m, concatenated with the vehicle state, X_k. In this section, following from the FBRM formulation of section 5.2.2, and using the same reasoning, let the map, M_k and measurement, Z_k be modeled as RFSs. The unknown vehicle trajectory however, remains in its vector form as there is no uncertainty in number, since a single (known number) vehicle is assumed. Furthermore, the order of states in the vehicle trajectory, X^k, is significant as it describes the path traversed.

Therefore the vehicle state is not modeled as an RFS. The following section outlines the PHD recursion for the joint SLAM problem, where again, a first order approximation of an RFS which contains a joint estimate on the map and vehicle trajectory is adopted.

5.5.1 The PHD-SLAM Filter

The PHD-SLAM filter is an extension of the PHD-FBRM filter, with the addition of uncertainty in the vehicle trajectory. The first order approximation of an RFS (the intensity, v) was introduced previously in section 5.3 [102]. This approach considered only the intensity of the map RFS whereas SLAM requires the joint estimation of both the set of features and the vehicle state. Following a similar approach to previous SLAM implementations [21], [28], [44], a joint vehicle-map state is used in this filter.

Expanding on the formulation of section 5.3, let ζ_k denote a map state, m, concatenated with one of N hypothesised vehicle trajectories, $X^{k,(n)}$. Conditioning the trajectories of each individual map state, m, on the history of vehicle poses introduces a conditional independence between feature measurements allowing the joint states, ζ_k to be independently propagated through the PHD SLAM framework [29]. Each augmented map state evolves in time according to the transition $f(\zeta_k|\zeta_{k-1}, u_{k-1})$ where,

$$f_k(\zeta_k|\zeta_{k-1}, u_{k-1}) = f(X_k|X_{k-1}, u_{k-1})\delta(m_k - m_{k-1})$$

assuming, as per common practise, static features, and $f(X_k|X_{k-1}, u_{k-1})$ is the vehicle state transition density. If the map element is detected by the sensor, a measurement z is generated with likelihood $P_d(\zeta_k)g(z|\zeta_k)$. Let the vehicle state be sampled by N particles, to produce $N \times |M_k|$ augmented states, ζ_k. Exploiting Campbell's theorem [107]:

Theorem:. *If $\mathbb{L}$ denotes the space of features (map elements) and $\mathbb{K}$ denotes the space of vehicle states, Campbell's theorem implies that the intensity of the point process on $\mathbb{L} \times \mathbb{K}$ formed by the Cartesian product of a point process on $\mathbb{L}$, with intensity $\tilde{v}$, and a point process on the mark space (a vehicle pose particle) $\mathbb{K}$, is given by*

$$v(X_k, m) = p(X_k|m)\tilde{v}(m) \tag{5.23}$$

where $p(\cdot|m)$ is the mark distribution given a point m of the original point process on $\mathbb{L}$.

Moreover, if the point process on $\mathbb{L}$ (the set of features) is Poisson, then the product point process on $\mathbb{L} \times \mathbb{K}$ is also Poisson [107]. Since the RFS of the map can be assumed Poisson, (section 5.3), this implies that the RFS of the joint vehicle

and map state is also Poisson. Therefore, when conditioned on a vehicle trajectory, the derivation for the PHD-FBRM filter can be incorporated in this work to include the joint vehicle-map augmented state. Given a set of augmented features, ζ_k, joint estimates of the number of features, their locations as well as the vehicle state can then be obtained. The PHD-SLAM recursion can therefore be written as,

$$\begin{aligned} v_{k|k-1}(\zeta_k) &= \int f(\zeta_k|\zeta_{k-1}, u_{k-1}) v_{k-1}(\zeta_{k-1}) d\zeta_{k-1} + b_k \\ &= \int f(\zeta_k|X_{k-1}, m_k, u_{k-1}) v_{k-1}(X_{k-1}, m_k) dX_{k-1} + b_k \end{aligned}$$

$$v_k(\zeta_k) = \left[1 - P_d(\zeta_k) + \sum_{z \in Z_k} \frac{\Lambda(z|\zeta_k)}{c_k(z) + \int \Lambda(z|\xi) v_{k|k-1}(\xi) d\xi}\right] v_{k|k-1}(\zeta_k) \quad (5.24)$$

where at time k,

b_k	=	intensity of the new feature RFS B_k,
$\Lambda(z\|\zeta_k)$	=	$p_D(\zeta_k) g(z\|\zeta_k)$,
$g(z\|\zeta_k)$	=	likelihood of z, given the joint state ζ_k,
$P_d(\zeta_k)$	=	probability of detection/extraction of the feature in ζ_k ,given the pose in ζ_k,
c_k	=	intensity of the clutter RFS C_k.

In [103], Gaussian noise assumptions were used to obtain closed form solutions for the target tracking PHD filter. Similarly for the PHD-SLAM filter, Gaussian mixture (GM) techniques can be applied to solve the PHD-SLAM joint intensity recursion of eqn.(5.24). It is also possible to use a particle-based approach [108], however, for mildly non-linear problems the Gaussian mixture approach is much more efficient. The following section therefore presents a GM implementation of the PHD-SLAM filter.

5.5.2 GM-PHD SLAM Implementation

Let the joint intensity, $v_{k-1}(\zeta_{k-1})$, at time $k-1$ be a Gaussian mixture of the form,

$$v_{k-1}(\zeta_{k-1}) = \sum_{i=1}^{N \times J_{k-1}} w_{k-1}^{(i)} \mathcal{N}\left(\zeta; \mu_{k-1}^{(i)}, P_{k-1}^{(i)}\right) \quad (5.25)$$

composed of $N \times J_{k-1}$ Gaussians, with $w_{k-1}^{(i)}$, $\mu_{k-1}^{(i)}$ and $P_{k-1}^{(i)}$ being their corresponding weights, means and covariances respectively. Note that the weight, $w_{k-1}^{(i)}$ is a weight on *both* a particular feature state, m, and a particular vehicle pose $x_{k-1}^{(n)}$, i.e. on the joint state $\zeta_{k-1}^{(i)}$.

Again, let the new feature intensity at time k also be a Gaussian mixture of the form,

$$b_k = \sum_{i=1}^{N \times J_{b,k}} w_{b,k}^{(i)} \mathcal{N}\left(\zeta; \mu_{b,k}^{(i)}, P_{b,k}^{(i)}\right) \tag{5.26}$$

where $w_{b,k}^{(i)}$, $\mu_{b,k}^{(i)}$ and $P_{b,k}^{(i)}$ determine the shape of the new feature GM proposal density according to a chosen strategy. Each new feature density component, $\mathcal{N}(m; \cdot)$ is concatenated with each predicted vehicle pose particle, $x_k^{(n)}$ to form the $N \times J_{b,k}$ components of the GM new feature intensity. Therefore, the predicted intensity, $v_{k|k-1}(\zeta_k)$ is also a Gaussian mixture given by,

$$v_{k|k-1}(\zeta_k) = \sum_{i=1}^{J_{k|k-1}} w_{k|k-1}^{(i)} \mathcal{N}\left(\zeta; \mu_{k|k-1}^{(i)}, P_{k|k-1}^{(i)}\right) \tag{5.27}$$

where, $J_{k|k-1} = N(J_{b,k} + J_{k-1})$ and,

$$\left.\begin{array}{l} w_{k|k-1}^{(i)} = w_{k-1}^{(i)} \\ \mu_{k|k-1}^{(i)} = \zeta_{k|k-1}^{(i)} \\ P_{k|k-1}^{(i)} = P_{k-1}^{(i)} \end{array}\right\} \text{for i} \in \{1, \ldots, N \times J_{k-1}\}$$

$$\left.\begin{array}{l} w_{k|k-1}^{(i)} = w_{b,k}^{(i)} \\ \mu_{k|k-1}^{(i)} = \mu_{b,k}^{(i)} \\ P_{k|k-1}^{(i)} = P_{b,k}^{(i)} \end{array}\right\} \text{for i} \in \{N \times J_{k-1} + 1, \ldots, N \times J_{b,k}\}.$$

Assuming a Gaussian measurement likelihood, $g(z|\zeta_k)$, it can be seen from eqn.(5.24), that the joint posterior intensity, $v_k(\zeta_k)$, is consequently a Gaussian mixture given by,

$$v_k(\zeta_k) = v_{k|k-1}(\zeta_k)\left[1 - P_d(\zeta_k) + \sum_{z \in Z_k} \sum_{i=1}^{J_{k|k-1}} v_{G,k}^{(i)}(z|\zeta_k)\right] \tag{5.28}$$

where,

$$v_{G,k}^{(i)}(z|\zeta_k) = w_k^{(i)} \mathcal{N}(\zeta; \mu_{k|k}^{(i)}, P_{k|k}^{(i)})$$

$$w_k^{(i)} = \frac{P_d(\zeta_k) w_{k|k-1}^{(i)} \mathcal{N}^{(i)}(z, \zeta_k)}{c_k(z) + \sum_{j=1}^{J_{k|k-1}} P_d(\zeta_k) w_{k|k-1}^{(j)} \mathcal{N}^{(j)}(z, \zeta_k)}$$

with, $\mathcal{N}^{(i)}(z, \zeta_k) = \mathcal{N}\left(z; H_k \mu_{k|k-1}^{(i)}, S_k^{(i)}\right)$. The components are obtained from the standard EKF update equations,

$$\mu_{k|k}^{(i)} = \mu_{k|k-1}^{(i)} + K_k^{(i)}(z - H_k \mu_{k|k-1}^{(i)}) \tag{5.29}$$

$$P_{k|k}^{(i)} = [I - K_k^{(i)} \nabla H_k] P_{k|k-1}^{(i)} \tag{5.30}$$

$$K_k^{(i)} = P_{k|k-1}^{(i)} \nabla H_k^T [S_k^{(i)}]^{-1} \tag{5.31}$$

$$S_k^{(i)} = R_k + \nabla H_k P_{k|k-1}^{(i)} \nabla H_k^T \tag{5.32}$$

with ∇H_k being the Jacobian of the measurement equation with respect to the features estimated location. As stated previously, the clutter RFS, C_k, is assumed Poisson distributed [13] [12] in number and uniformly spaced over the sensor surveillance region. Therefore the clutter intensity is given by,

$$c_k(z) = \lambda_c V \mathcal{U}(z) \tag{5.33}$$

where λ_c is the average number of clutter returns per unit volume, V is the volume of the region and $\mathcal{U}(\cdot)$ denotes a uniform distribution.

5.6 FB-SLAM Experiments

This section analyses the proposed set based SLAM formulation and GM implementation on simulated and real experimental data. Accurate filter performance is demonstrated for vehicle localisation estimates, as are improved feature mapping capabilities, especially at high rates of environmental clutter, and large data association uncertainty.

5.6.1 Synthetic Data

This section analyses the performance of the proposed feature-based GM-PHD SLAM filter in a simulated environment. The dataset is the same as used in section 5.4.1 of this chapter with added control noise components. The vehicle is assumed to be subject to Gaussian speed control noise of standard deviation $0.5m/s$, and steering control noise of standard deviation 3^o. The measurement noise parameters are set as

before. Clutter rates are varied as for the previous FBRM simulations of section 5.4.1 and root mean square localisation estimation (RMSE) errors as well as the FBRM error metric are analysed. Results from NN-EKF [28], [6] (single-hypothesis data association) and FastSLAM [66] (multiple-hypothesis data association), with feature management algorithms, are compared to those from the proposed PHD-SLAM filter (no data association hypothesis). Results show the RMSE error at each time instant over the course of the trials at various clutter densities. For both the FastSLAM and proposed PHD-SLAM implementations, 100 particles are used to sample the estimated vehicle trajectory.

The first set of results were obtained using a smaller measurement noise to reduce data association uncertainty and having no spurious measurements. The range and bearing measurement noise standard deviation was set respectively at $0.25m$ and 0.5^o. Figures 5.15 and 5.16 shows a comparison of the RMSE over the estimated vehicle trajectory for each approach, as well as the mapping accuracy of each algorithm. At low clutter rate and reduced data association ambiguity for vector based approaches, all methods perform consistently and maintain low RMSE throughout the path.

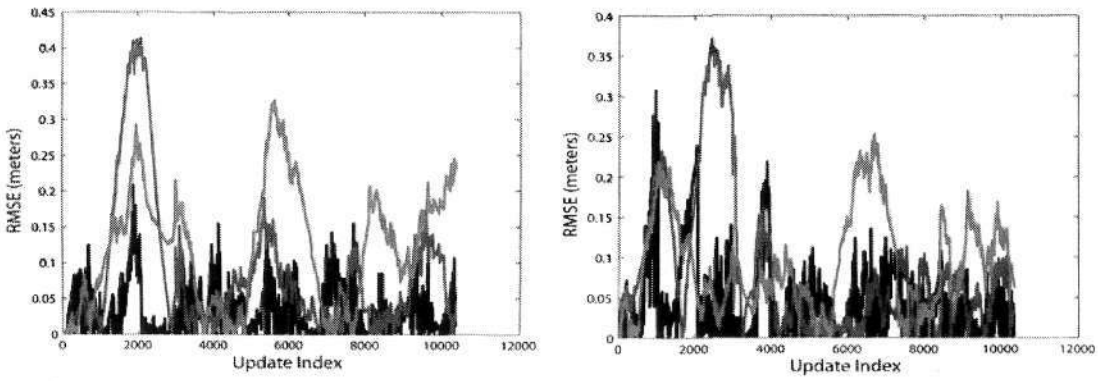

Figure 5.15: *x and y RMSE plots for NN-EKF (blue), FastSLAM (red), and the proposed PHD-SLAM filter (black). The results indicate consistent vehicle localisation estimates by all three approaches at low measurement noise.*

To increase the difficulty of the data association problem, whose accurate solution is critical to vector-based approaches, the measurement noise is inflated as before (section 5.4.1) to $1.75m$ and 3.5^o. The spurious measurements are kept at zero and the experiment is re-run for all three filters. Figures 5.17 and 5.18 again show the resulting RMSE plots as well as the mapping error for each approach. As expected, the error in the EKF increases with respect to FastSLAM. The proposed method performs similarly to FastSLAM, which both maintain reduced location errors through avoiding irreversible data association decisions.

The results presented in figures 5.19, 5.20 and figures 5.21, 5.22 illustrate the filter

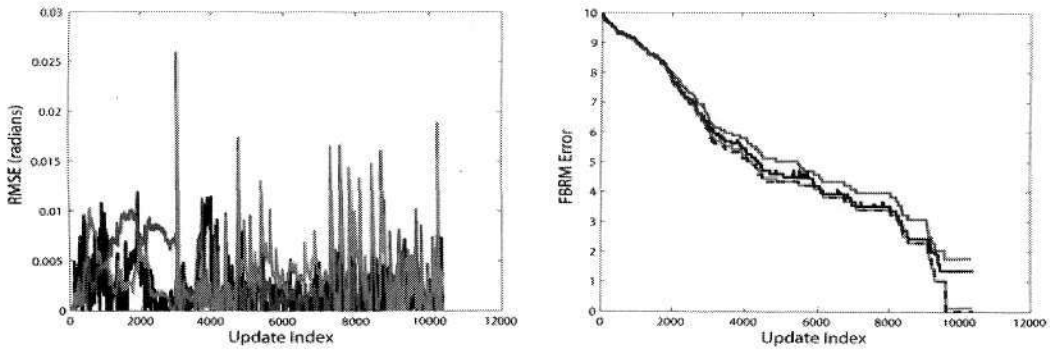

Figure 5.16: *α and map error NN-EKF (blue), FastSLAM (red), and the proposed PHD-SLAM filter (black). At low measurement noise, in this example FastSLAM produced the most accurate FB map according to the metric. As before, the ideal map metric at each time instant is shown (dashed black).*

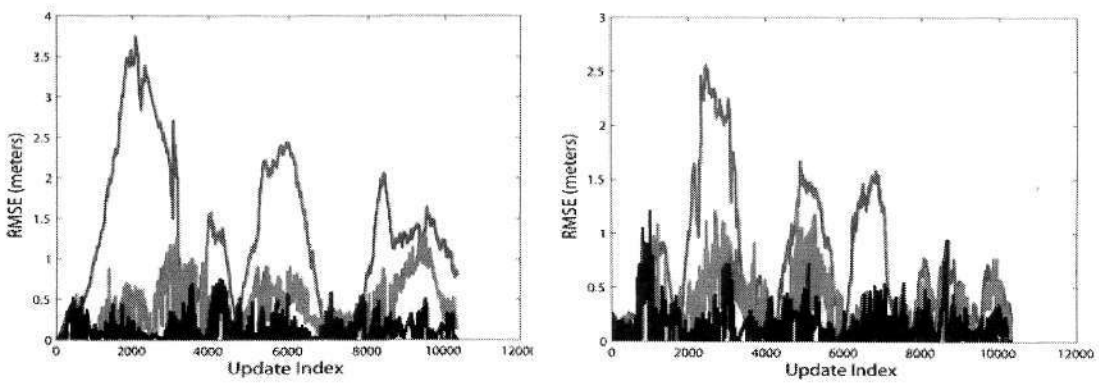

Figure 5.17: *x and y RMSE plots for NN-EKF (blue), FastSLAM (red), and the proposed PHD-SLAM filter (black). EKF error increases as expected, with FastSLAM and the proposed PHD-SLAM filter having reduced localisation errors.*

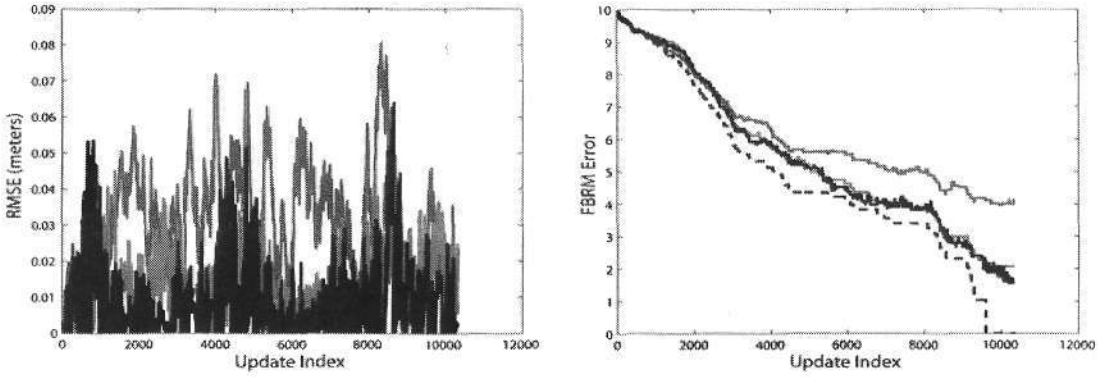

Figure 5.18: *α and map error NN-EKF (blue), FastSLAM (red), and the proposed PHD-SLAM filter (black). FastSLAM and PHD-SLAM again out perform EKF-SLAM. The mapping results shows theh superiority of the proposed method in the presence of data association ambiguity.*

performances when the clutter rate is set at $6.37 \times 10^{-3}/m^2$ and $12.74 \times 10^{-3}/m^2$ respectively. As the clutter rate increases, coupled with the large measurement noise, vector based methods fail to accurately solve the data association problem, as well as consistently estimate the feature based map. The results indicate that the proposed set-based SLAM recursion, is more robust to high clutter both in terms of maintaining low vehicle estimations errors, as well as an improved estimate of the feature map. As expected, as the localisation error increases, the resulting feature mapping error also increases.

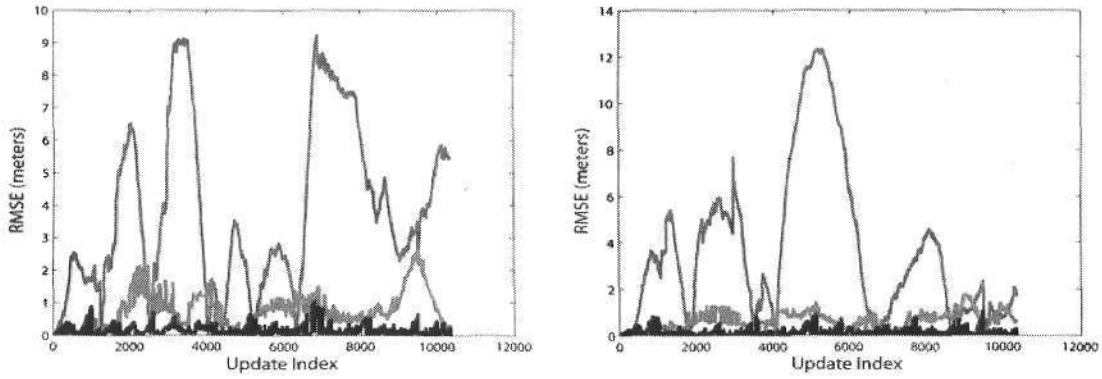

Figure 5.19: *x and y RMSE plots for NN-EKF (blue), FastSLAM (red), and the proposed PHD-SLAM filter (black). As the clutter rate increases ($\lambda_c = 1$), the proposed filter begins to out-perform the EKF and FastSLAM vector-based solutions.*

The RMSE localisation results as well as the corresponding FB mapping results

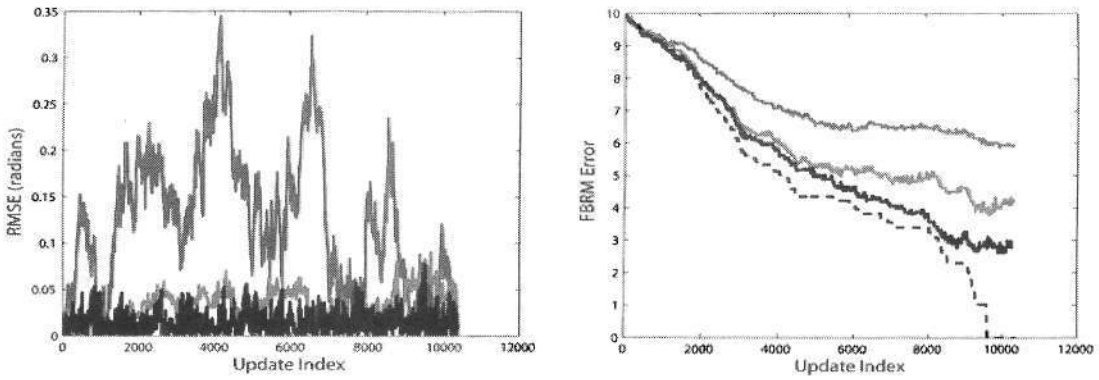

Figure 5.20: *α and map error NN-EKF (blue), FastSLAM (red), and the proposed PHD-SLAM filter (black), at λ_c=1. FastSLAM and PHD-SLAM again out perform EKF-SLAM. The mapping results show slight superiority of the proposed method in the presence of data association ambiguity.*

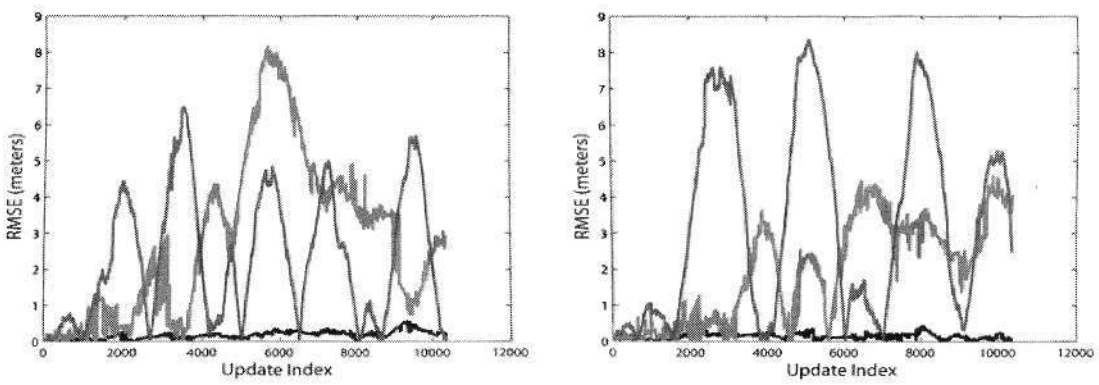

Figure 5.21: *As the clutter rate increases ($\lambda_c = 2$), increased localisation error becomes evident in the FastSLAM result whereas the proposed method maintains a low localisation estimate error.*

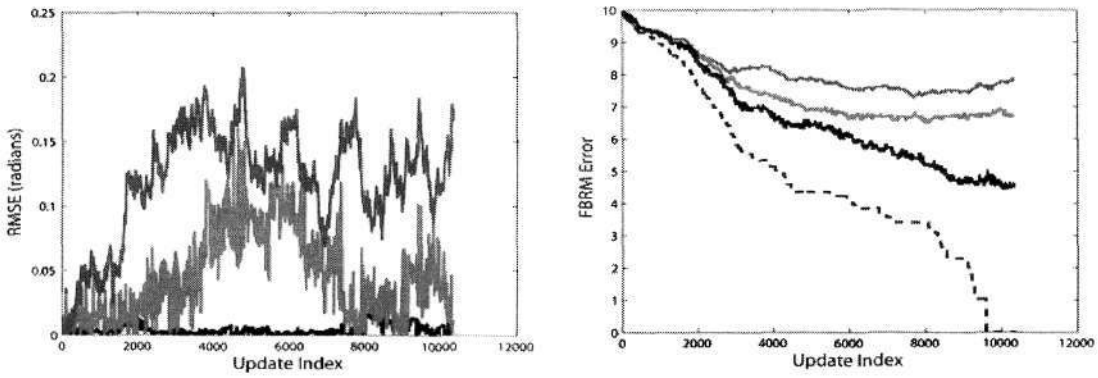

Figure 5.22: *α and map error NN-EKF (blue), FastSLAM (red), and the proposed PHD-SLAM filter (black), at $\lambda_c = 2$. At high clutter rates, the mapping performance of all three approaches deteriorates, however the proposed method maintains a low joint mapping error according to the metric.*

presented, clearly highlight the improvements of the proposed finite-set-based SLAM framework over traditional vector-based approaches. The formulation includes the entire measurement uncertainty into the filter recursion and consequently alleviates the need of map management and data association parameters and algorithms. By augmenting each map state with a vehicle trajectory sample, a conditional independence can be introduced, allowing for trajectories to be jointly estimated with the finite-set based map. Comparisons of the estimated vehicle trajectory and final map for the latter trial for each approach are shown in figures 5.23 and 5.24.

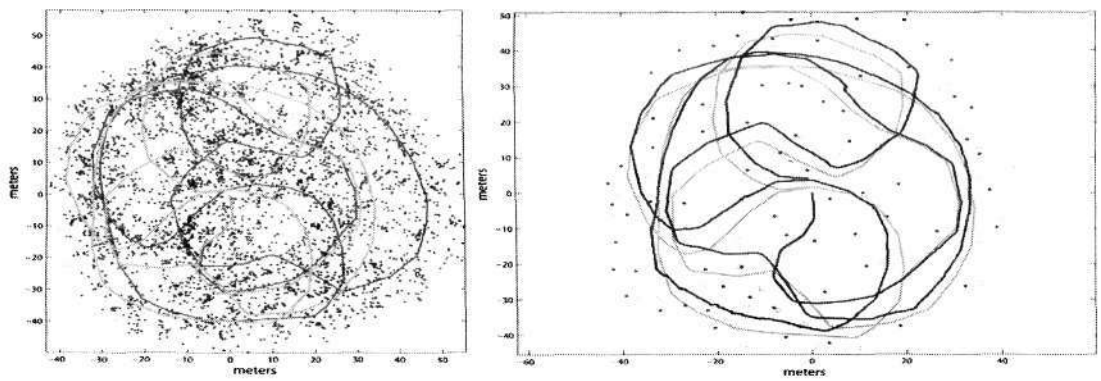

Figure 5.23: *This figure shows the raw data with clutter rate of $12.74 \times 10^{-3}/m^2$ and the corresponding posterior joint estimate from the NN-EKF filter.*

Improved map estimates for the proposed method can be achieved by lowering the feature presence decision threshold of 0.7. Figure 5.25 shows the posterior for

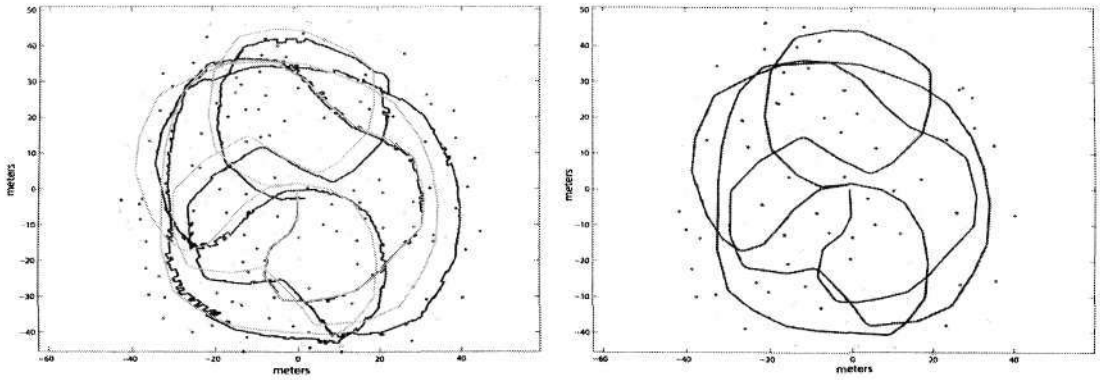

Figure 5.24: *This figure shows the joint posterior estimates given the raw data shown previously in figure 5.23. The improved localisation and map estimates of the proposed method are evident.*

feature presence thresholds of 0.3 and 0.1 respectively. Given the high clutter rate of the measurements, the proposed method still reports very few false features in the map.

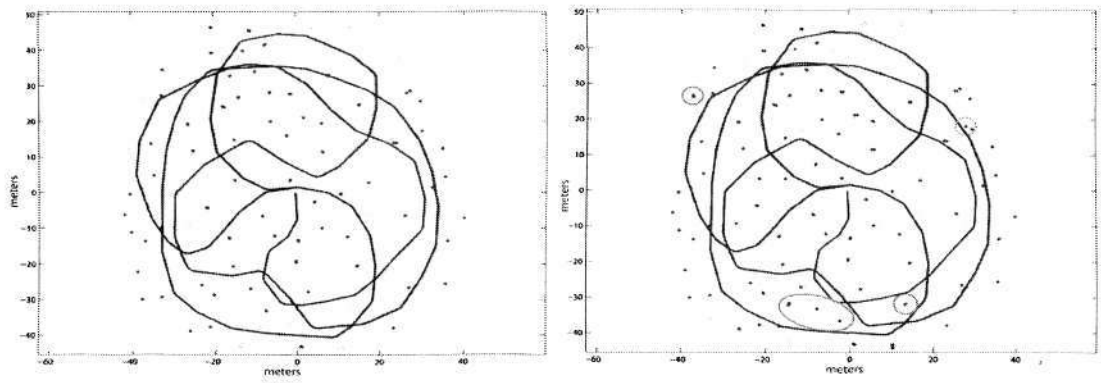

Figure 5.25: *The joint vehicle and map posterior estimates from the proposed set-based framework with feature presence thresholds of* 0.3 *and* 0.1. *Highlighted are added detected features as well as a singular false feature.*

While improved comparative results may be possible using more sophisticated data association routines such as MHT [12], MDA [13] or JCBB [14], the results shown in this section aim to prove the consistency and accuracy of the newly proposed set-based SLAM recursion and GM implementation. Given a classical vector-based approach, regardless of the data association method of choice, feature management parameters are further required to prune the number of features and cope with detection

uncertainty. The new filter however, integrates all the inherent measurement uncertainty (excluding sensor bias) into the filter recursion and therefore comprises the first optimal recursion of the FB-SLAM problem. Pre/post feature management and data association routines are not required, further reducing the number of intuitive parameters required, which is the case in classical vector-based Bayesian FB-SLAM implementations. The results therefore clearly verify the performance of the set-based estimation theoretic for the FB-SLAM, with the first-order PHD Gaussian mixture implementation displaying impressive results in situations of high clutter and closely spaced features.

5.6.2 Carpark Loop Dataset

This section analyses the proposed filter performance in the carpark environment. Noisy vehicle inputs as well as inaccuracies in the vehicle model contribute to an uncertain vehicle trajectory without incorporating absolute measurement information. Both a laser and imaging radar measurements are available, with the radar reporting more spurious detections than the laser sensor, as was presented previously in section 3.5, with increased measurement noise parameters. In this experiment, point features will be used although the filters can be readily expanded to incorporate other feature types such as lines and corners [12]. For the laser data, point feature extraction is performed as in [109]. However, for the radar data, with its reduced resolution compared to that of the laser, simple clustering and centroid extraction methods are used to generate the feature measurements, as outlined in Appendix C. With few spurious feature measurements and small measurement noise, vector based methods are expected to perform consistently using the laser sensor. In situations of higher clutter rates, and increased measurement noise however, as illustrated previously through simulation, the theoretical merits of the proposed finite-set-based filter are expected to produced improved results, both in vehicle localisation estimates and feature based map estimates. Results of the point feature extraction methods from both sensors are registered from the predicted vehicle trajectory in figure 5.26.

The ground truth vehicle trajectory is available from the manual matching of laser scans as before, however in practise it is difficult to obtain the 'true' number of point features, which is also required for full evaluation of an FB-SLAM algorithm. As emphasized previously, there is little work in the autonomous navigation community focussed on the evaluation of FB maps estimated from a given algorithm. Section 5.6.1 presented extensive simulated results which present a far more accurate performance metric compared to the commonly used range and bearing innovation or absolute estimation error of a subset of environmental features [72], [68], [28]. For the carpark dataset, the ground truth map was manually obtained as introduced previously in section 4.7. Using the same grid-based map, a hypothesised ground truth FB map

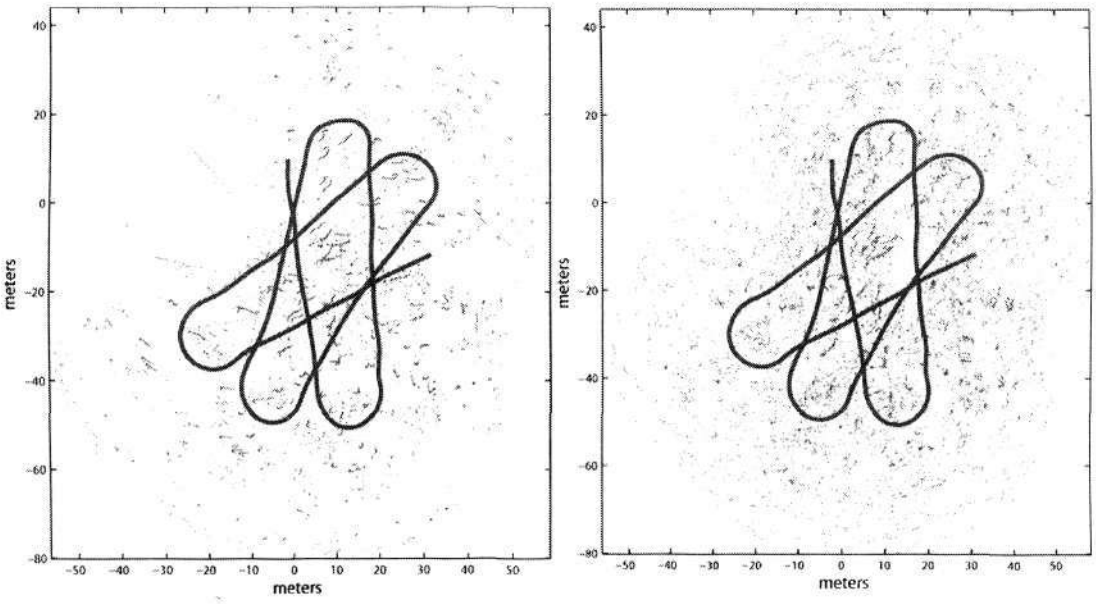

Figure 5.26: *Extract point feature measurements registered from the predicted vehicle path for both the laser (left) and imaging radar (right) sensors.*

can be extracted, allowing for FB mapping evaluation. Figure 5.27 shows the GB map from the previous chapter with superimposed ground truth vehicle trajectory as well as the extracted ground truth point feature map used for FB-SLAM algorithm evaluation.

The laser measurement data is first processed by the bench-mark full covariance NN-EKF FB-SLAM [6], maximum likelihood association Fast-SLAM [44] and the proposed PHD-SLAM filter. As both the FastSLAM and PHD-SLAM adopt particle based estimates of the vehicle pose, the RMSE of the pose estimate for all three filters is compared where, as per the simulation, both the FastSLAM and PHD-SLAM filters use 100 particles to sample the vehicle trajectories. Figures 5.28 and 5.29 show the results from the SLAM experiment in the carpark environment using the laser sensor for all three filters.

Figure 5.30 shows the standard method of proving filter consistency for feature based SLAM algorithms. While the localisation error with sigma bounds indicates filter consistency (in its vehicle location estimate only), the range innovation and covariance only indicates a consistent feature location estimate for that single feature in the map. There is no information as to the overall performance of the feature-based mapping component of the filter. The estimated vehicle trajectory and corresponding feature-based maps for all three filters are shown in figure 5.31. As laser measurements typically return accurate range and bearing measurements, coupled with the reduced

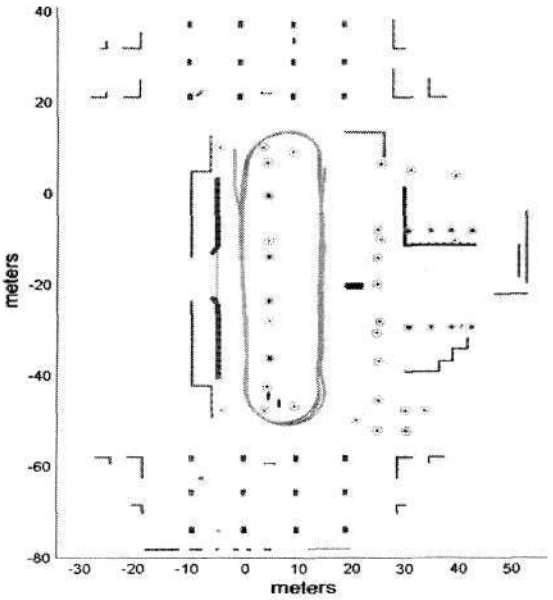

Figure 5.27: *Ground truth vehicle trajectory (green line) and point features (green circles) superimposed on the ground truth grid based map from the previous chapter, section 4.7.*

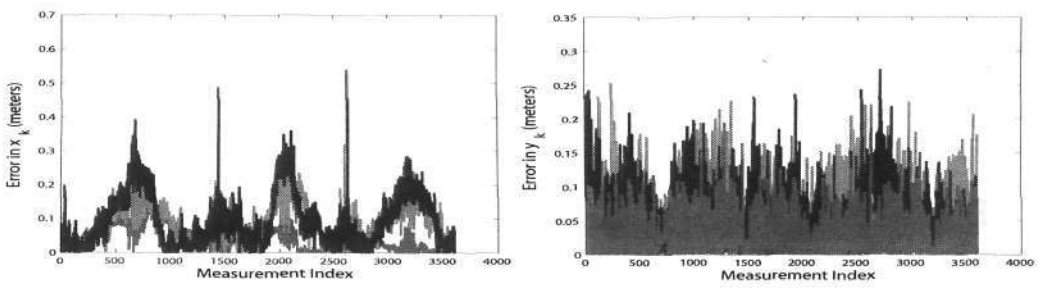

Figure 5.28: *Plots of RMSE vehicle position estimates for the EKF (blue), FastSLAM (red) and PHD-SLAM (black) filters.*

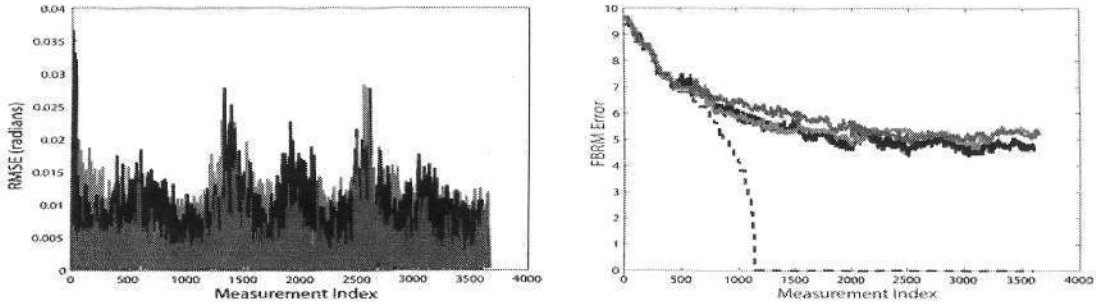

Figure 5.29: *Plots of the vehicle estimation error in θ, and the FB mapping error over the course of the vehicle trajectory. The results show similar feature mapping performance of all three filters using the reliable laser data.*

number of spurious feature detections, all three filters perform similarly. The result from the proposed approach mimics that of a FastSLAM algorithm due to its particle representation of the vehicle trajectory.

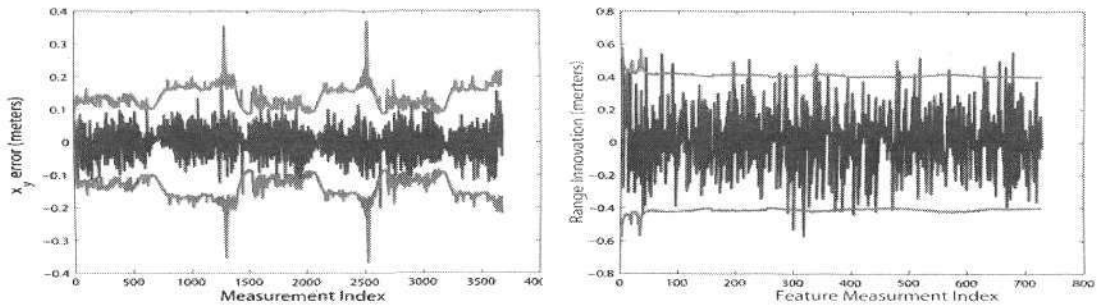

Figure 5.30: *Plots of the vehicle estimation error in y, and the range innovation of a feature in the map, using the laser sensor. Both plots show the 2 sigma uncertainty bounds (red), indicating filter consistency and unbiassed estimation error.*

When the radar sensor is used as the primary source of exteroceptive range/bearing feature measurements, there is an increase in the number of false alarms and missed feature detections. Due to an increased beamwidth and range quantisation (into $25cm$ discrete range bins), the effective measurement noise is also greater when compared to a laser sensor (as evident from figure 5.26). This has the coupled effect of increasing the data association ambiguity, and making the feature map management task (estimating the number of features) more difficult. In this more challenging situation, the merits of the proposed finite-set-based theoretic approach are expected to by highlighted. Figure 5.32 shows the SLAM results from the carpark environment using the radar sensor. In the presence of challenging measurement uncertainty, the proposed filter can be seen to outperform that of classical association-based approaches. While

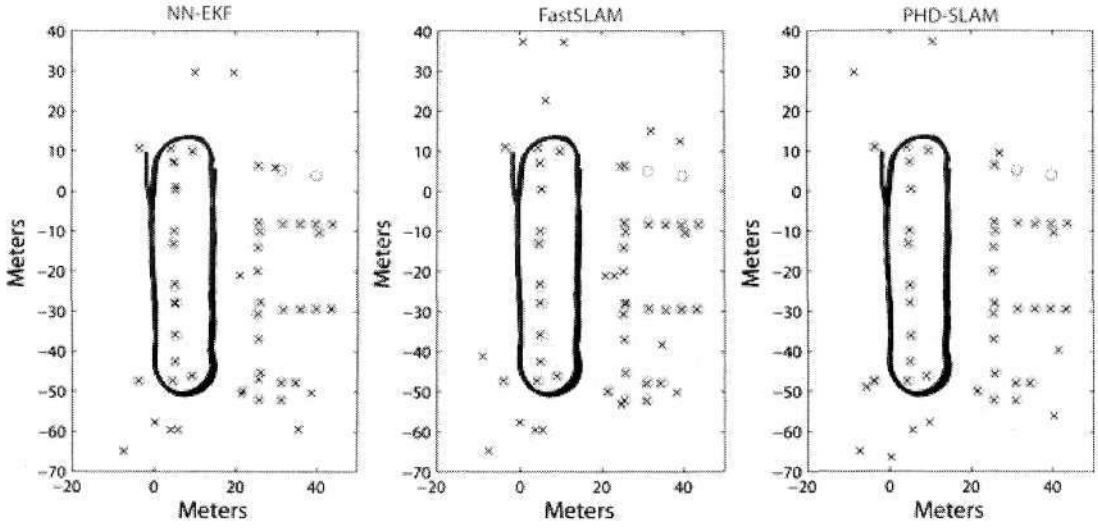

Figure 5.31: *The posterior estimated vehicle trajectory and corresponding feature maps for all three filters adopting the laser measurements. Comparable results for all approaches are evident under conditions of lower spurious measurements and low measurement uncertainty.*

the estimated vehicle trajectory closely tracks that of the ground truth, the posterior feature map estimate moderately compares with that of the ground truth. The effects of increased measurement noise and decreased feature detection probabilities are evident in the noisy location estimates. Some falsely declared point features are evident, with concrete pillars (at positions $y \leq -55$) being frequently modeled as point features, due to the beamwidth of the radar sensor.

5.7 Conclusions

This chapter addressed the treatment of measurement uncertainty in the popular feature-based autonomous navigation framework. Similar to the previous chapter, it was shown how, in particular, the detection uncertainty and spurious measurements are dealt with in a sub-optimal manner in most filter recursions outlined in the literature. Pre/post processing based on intuitive rules and heuristics are frequently adopted to handle spurious measurement through map management routines. This chapter however, outlined the theoretical reasons for the necessity of such methods, which until now, were independent of the Bayesian filtering loop and consequently compromised the optimality of the resulting posterior estimate. It was shown how the vector representation of the measurement equation does not theoretically facilitate practical measurement uncertainty such as spurious measurements, missed detections

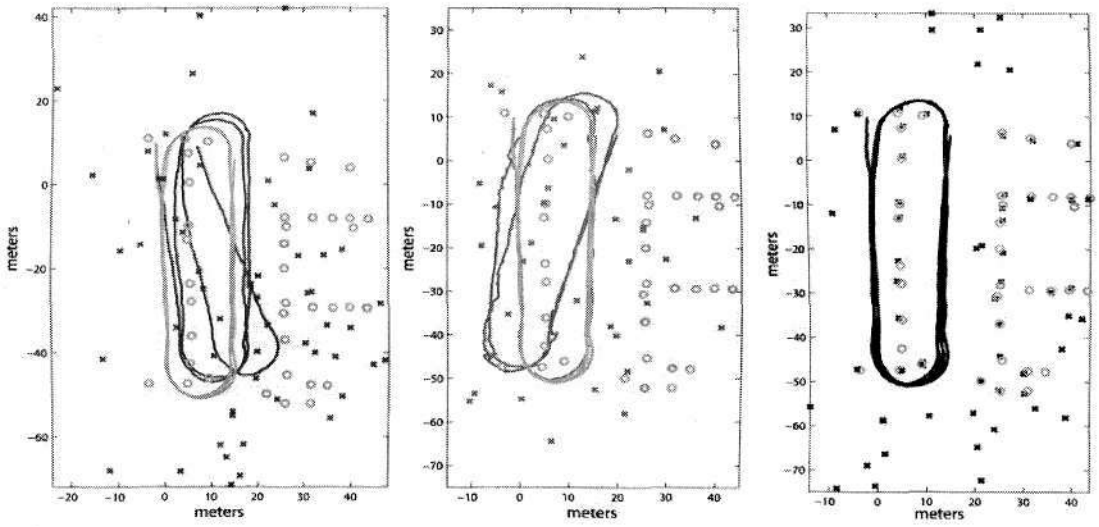

Figure 5.32: *The posterior estimated vehicle trajectory and corresponding feature maps for all three filters adopting the radar measurements. In the presence of large feature detection uncertainty, more frequent false alarms, and reduced measurement accuracy, the proposed method is seen to out-perform standard vector based approaches.*

as well as unknown data association. The resulting posterior then disregards the uncertainty of the dimension of the state estimation problem. Emphasis was also placed on the mapping aspect of a feature-based solution, and a suitable error metric from the multi-target tracking community, was introduced to quantify feature mapping errors. This is as a result of most feature-based literature, disregarding the estimation error of the mapping element of the SLAM algorithm, and only showing the consistent estimation errors of a single (or sub set) of map features. This gives no indication as to the error of the joint multi-feature estimation problem.

The chapter therefore outlined a set based theoretic approach to the FBRM problem, emphasising that a critical aspect requires recursive joint estimates of both the number of features in the map as well as their corresponding positional state. By using set-based models for the measurement and state, an optimal approach can be derived which encapsulates all the measurement and state uncertainty present in the system. Detection uncertainty, spurious measurements as well as data association uncertainty are all incorporated directly into the filter recursion. This is in contrast to previous sub-optimal FBRM approaches which require additional algorithms and pre/post processing to solve the data association problem prior to filter update, and to extract estimates of the number of features present in the map. These are necessary as such sources of uncertainty are not considered in the basic vector-based measurement

and subsequent filter recursion. Propagating the first statistic of the set (the probability hypothesis density) can be achieved in a Bayesian predictor/corrector context allowing for recursions to be developed. Due to direct implementation difficulties, Gaussian mixture models are assumed to represent the set intensities which are then propagated and updated through the PHD recursion. As both an estimate of the number of features and estimates of their corresponding states are represented by the PHD statistic, it can be used to jointly propagate both estimates.

The framework was then extended and an alternative formulation to the Bayesian SLAM problem, using random set theory, was proposed. By augmenting the feature state, with a history of vehicle poses, conditional independencies between the features and the vehicle state were introduced. The joint vehicle feature RFS was shown to maintain the necessary Poisson assumptions for application of the tracking based PHD recursion for the PHD-SLAM problem. A Gaussian mixture implementation of the PHD-SLAM filter was outlined assuming a Gaussian system with non-linear measurement and process models.

Extensive analysis of both the mapping and SLAM algorithms was performed in both simulated and real environments. Validation was performed in a simulated environment, showing the GM-PHD SLAM algorithm performing favorably in extremely high clutter environments, with few false feature declarations. Experiments using real data from a carpark and campus environment illustrated the effectiveness of the proposed FBRM algorithm, with added robustness to spurious measurements, data association uncertainty and missed detections. Experimental validation of the proposed PHD-SLAM filter was also demonstrated showing accurate vehicle location estimates whilst jointly estimating the number of features and their location states. Real experiments were performed using a laser and the noisier radar sensor, to highlight the increased robustness of the proposed framework. While classical vector based approaches performed similarly to the proposed filter using the laser sensor (less measurement uncertainty), significant SLAM estimate improvements were seen when the vehicle was navigating with the increased measurement uncertainty from the radar sensor. These experiments verify the performance of the proposed filter and validate the finite-set-based estimation theoretic, as an alternative and new solution to the feature-based SLAM problem.

Chapter 6

Conclusions and Recommendations

This chapter summarises the work presented in this thesis and discusses the contributions made to the field of autonomous navigation. Some research directions opened as a result of the contributions are then introduced.

6.1 Conclusions

Over the past number of years, autonomous guided vehicles have been the focus of considerable research throughout the military, automotive, aerospace and other industries. In any autonomous context, the ability of the mobile platform to incrementally construct an accurate representation of its surroundings, and to localise itself within such a representation, is of paramount importance. Errors in either the estimated location and/or the presence/absence of environmental landmarks can result in catastrophic mission failure, be it path planning, exploration or mapping, for the mobile platform. Chapters 1 and 2 highlighted the significance of these issues, in the context of the two main metric spatial estimation theoretics - grid based (GB) and feature based (FB) maps. The contrasting approaches were distinguished with respect to their estimation state space and corresponding measurement likelihoods, as opposed to simply their differing spatial representation as is commonly the case.

A prerequisite to any autonomous navigation using exteroceptive sensing capabilities is the reliable and accurate interpretation of the sensor data that is registered by the platform. To this end, Chapter 3 discussed the less widely researched, but no less important, hypothesis decision on landmark presence or absence in the sensor data. Mainly applicable to imaging range sensors, the chapter discussed common non-stochastic methods of landmark detection and introduced the constant false alarm rate detector (CFAR) for use in mobile robotics for the first time. It was shown how general navigation algorithms typically assume the landmarks are detected by a detector with such properties, whereas the actual detector may differ quite drastically.

Using a millimeter wave radar sensor, the stochastically founded CFAR detector was shown to exhibit superior detection capabilities in a semi-structured outdoor environment. The concept of various measurement types was also presented, highlighting the probabilistic significance of vector and set based measurements, recognising for the first time that grid based frameworks use vector-based measurements whereas those for feature based frameworks are set-based. The chapter expanded on the understanding of sensor measurements, and the significance of their theoretically accurate interpretation.

Following from the work of the previous chapter, Chapter 4 examined how the various measurements are used to create a probabilistic grid-based spatial representation of the environment. By using both positive (detections) and negative (non-detections) information, the GB was shown to validate the use of vector-based frameworks as the measurement and map (within sensor field of view) are of equal cardinality. However, the chapter highlighted that the commonly consider range measurement likelihoods provided measurements unrelated to the occupancy state of interest. Furthermore, by using such a likelihood, it was shown that the measurements were inherently regarded as being noise-free. As a result of this observation, the discrete GB estimation theoretic was reformulated with detection measurements as opposed to range measurements. Doing so allowed for a statistically accurate and state related recursion to be derived. The derivation also highlighted for the first time the correlation between the landmark detection problem, discussed in Chapter 3, and the widely adopted GB probabilistic mapping framework. Superior mapping capabilities were demonstrated using the discrete form of the proposed framework.

The re-formulation also exposed a further problem, being that the required likelihoods used for the detection-based GB recursion, are typically *a priori* unknown, and whose values can vary significantly in a given outdoor environment. The issue of online recursive likelihood estimation was then discussed, using the millimeter wave radar as the main sensor of choice. The inclusion of unknown likelihoods required the proposal of a continuous filtering framework where the likelihoods and occupancy random variables were jointly estimated. The proposed continuous GB filter was tested using real outdoor data and shown to display improved mapping capabilities.

Chapter 5 examined the FB framework, again focussing on the standard measurement interpretation and filtering framework adopted. FB frameworks typically only exploit positive (detections) sensor information and disregard the negative information. By further compressing the measurements into distinct features, the equal cardinality constraint for the measurement and map was shown to be violated. The chapter therefore proposed that the standard vector-based representations and resulting filtering frameworks, while valid for the GB problem, are not applicable to the FB mapping and FB-SLAM problems. The standard, and widely used, vector-based

measurement likelihood was also shown to have some pitfalls in its ability to encapsulate the entire uncertainty in the measurement, namely missed detections and spurious measurements. Vector-based measurement likelihoods lack that ability to model such events. Random finite set (RFS) representations for the measurement were introduced to overcome these subtle pitfalls. Furthermore, due to the random cardinality of the map state over time, the *joint* estimation of both the number of elements (features) and their corresponding locations is required, which has never before been recognised in the autonomous navigation community.

As a result of these observations, alternate formulations for the FB mapping and FB-SLAM frameworks were outlined from an RFS estimation theoretic perspective. The proposed methods theoretically included the entire autonomous system uncertainty (range/bearing measurement noise, control noise, detection and data association uncertainty as well as spurious measurements) directly into the filter recursion, thus providing an optimal formulation of the FB-SLAM and mapping problems for the first time. Exploiting the first order moment of the random set, which jointly incorporates cardinality and state uncertainty, recursions were outlined and implemented by Gaussian and sequential monte carlo methods. The proposed mapping and SLAM frameworks were shown to exhibit increased robustness to environments which produce a high number of spurious measurements. The concept of feature map estimation error was also emphasised in the chapter, which is typically overlooked in the FB robotics community, stressing that accurate map estimation is no less important than accurate localisation estimations, regardless of the map representation method that has been adopted.

In conclusion, the work of this thesis exposes subtle theoretical oversights in well-established autonomous navigation frameworks, specifically with respect to the interpretation of exteroceptive measurements registered by the platform. The contributions of the thesis comprise both the observations made and highlighted pitfalls of previous frameworks, as well as the proposed alternative formulations and implementations. It is argued that highlighting such issues provides a fresh insight into seemingly solved problems and will provide a basis for further advances towards the goal of fully autonomous systems.

6.2 Recommendations for Future Work

The work in this thesis exposed some theoretical pitfalls of previous frameworks and consequently opened up several issues that require further extensive investigation and analysis. Some sensor specific issues were raised, primarily for imaging sensors, which provide unprocessed signal intensity information requiring the development of algorithms which can exploit such increased information content. Numerous examples exist in the tracking community of such algorithms, whose applicability to real

world robotics problems need to be investigated. As research in unstructured domains, both outdoors and underwater, gains in popularity increased measurement data dimensionality may result in more accurate and robust performance, as the geometric environmental structure deteriorates. The theoretical significance of using multiple measurements/bearing angle in terms of entropy gain and computational load vs. error reduction are important research directions. The development of improved landmark detection algorithms may also significantly increase autonomous navigation capabilities, especially under the condition of unknown signal intensity distributions (as is commonly the case for real world deployments with imaging range sensors). From a theoretical perspective, due to such a daunting challenge, evidential likelihoods and continuous evidential filtering methods are likely to be the most appealing directions.

In terms of the grid-based mapping problem, the online estimation of measurement likelihoods can be incorporated into data association likelihoods to potentially improve performance in situations where features/landmarks have varying detection probabilities. Generally algorithms assume these values to be *a priori* known. Expanding the grid based framework to incorporate the localisation attributes of its feature-based counter part represent a significant research direction. It is argued that the optimal metric mapping solution would provide joint estimations on the landmarks (not their corresponding features) presence probability as well as its spatial uncertainty in a theoretically accurate manner. The primary difficulty is that grid based representations model landmarks of any shape of size, which from a tracking perspective represents 'extended targets', i.e. one landmark generating multiple measurements. General FB-SLAM and localistion methods require the assumption of one landmark having at most one detection, expanding this requirement would improve autonomous navigation capability significantly. Scan matching approaches, for instance, over come this problem by disregarding the propagation of the map elements (features or landmarks) spatial uncertainty. To this end, further development of the proposed set based theoretic may provide possibilities for such a framework. Recent work on the so called MemBer Filter, which propagates existence probabilities jointly with location uncertainty, possesses many attributes which would be of use to the autonomous navigation community. Incorporating the uncertainty of a moving platform for such frameworks is far from trivial but could potentially produce substantial performance improvements.

Author's Publications

Journal Papers

- J. Mullane, M.D. Adams, and W.S. Wijesoma, "Robotic Mapping Using Measurement Likelihood Filtering", *International Journal of Robotics Research.* 28(2):172-190, February 2009.
- J. Mullane, E. Jose, M.D. Adams, and W.S. Wijesoma, "Including Probabilistic Target Detection Attributes Into Map Representations",*International Journal of Robotics and Autonomous Systems*, 55(1):72-85, January 2007.
- J. Mullane, B.N. Vo, M.D. Adams and W.S. Wijesoma, "A Random Finite Set Theoretic Framework for Bayesian Feature-based Autonomous Robotics", *IEEE Transactions on Automatic Control.* Submitted.

Conference Papers

- J. Mullane, B.N. Vo, M.D. Adams and W.S. Wijesoma, "A Random Set Formulation for Bayesian SLAM", *in proceedings of the IEEE/RSJ International Conference on Intelligent Robots and Systems*, France, September, 2008.
- J. Mullane, B.N. Vo, M.D. Adams and W.S. Wijesoma, "A PHD Filtering Approach to Robotic Mapping", *proceedings of the 10th IEEE International Conference on Control, Automation, Robotics and Vision*, Hanoi, December, 2008. Accepted for publication.
- J. Mullane, M.D. Adams, and W.S. Wijesoma, "Outdoor Radar Mapping Using Measurement Likelihood Estimation", *in proceedings of the 6th International Conference on Field and Service Robotics*, France, July, 2007.
- J. Mullane, M.D. Adams, and W.S. Wijesoma, "Evidential versus Bayesian Estimation for Radar Map Building", *in proceedings of the 9th IEEE International*

Conference on Control, Automation, Robotics and Vision, Singapore December, 2006.

Book Chapters

- J. Mullane, M.D. Adams and W.S. Wijesoma, "Outdoor Radar Mapping Using Measurement Likelihood Estimation", in Springer Tracts in Advanced Robotics, pp.3-12, Springer Berlin / Heidelberg, June 2008.

Bibliography

[1] Defense Advanced Research Projects Agency. DARPA grand challenge. *http://www.darpa.mil/grandchallenge05/.*

[2] Defense Advanced Research Projects Agency. DARPA urban challenge. *http://www.darpa.mil/grandchallenge/.*

[3] S. Thrun. Robotic mapping: A survey. Technical Report CMU-CS-02-111, Carnegie Mellon University, Pittsburgh, Pennsylvania 15213, February 2002.

[4] H.F. Durrant-Whyte and T. Bailey. Simultaneous localization and mapping: Part I. *IEEE Robotics and Automation Magazine*, 13(2):99–110, June 2006.

[5] J.J. Leonard and H.F. Durrant-Whyte. Dynamic map building for an autonomous mobile robot. In *IEEE International Workshop on Intelligent Robots and Systems*, pages 89–96, Ibaraki, Japan, July 1990.

[6] J. Guivant, E. Nebot, and S. Baiker. Autonomous navigation and map building using laser range sensors in outdoor applications. *Journal of Robotic Systems*, 17(10):565–583, October 2000.

[7] A. Nuchter, H. Surmann, K. Lingermann, J. Hertzberg, and S. Thrun. 6d slam with an application in autonomous mine mapping. In *International Conference on Robotics and Automation (ICRA)*, New Orleans, USA, April 2004.

[8] R.M. Eustice, H. Singh, and J.J. Leonard. Exactly sparse delayed-state filters for view-based slam. *IEEE Transactions on Robotics*, 22(6):1100–1114, December 2006.

[9] S. Lacroix, A. Mallet, D. Bonnafous, G. Bauzil, S. Fleury, M. Herrb, and R. Chatila. Autonomous rover navigation on unknown terrains, functions and integration. *International Journal of Robotics Research*, 21(10):917–942, October 2002.

[10] L.D.L Perera, W.S. Wijesoma, and M.D. Adams. The estimation theoretic bias correction problem in map aided localisation. *International Journal of Robotics Research*, 25(7):645–667, July 2006.

[11] L.D.L Perera. *On the Issues of Localisation and Mapping in Outdoor Unstructured Environments for Mobile Robot Navigation.* PhD thesis, Department of Electrical and Electronic Engineering, Nanyang Technological University, Singapore, 2006.

[12] D. Makarsov and H.F. Durrant-Whyte. Mobile vehicle navigation in unknown environments: a multiple hypothesis approach. *IEE Proceedings of Contr. Theory Applict.*, vol. 142, July 1995.

[13] W.S. Wijesoma, L.D.L Perera, and M.D. Adams. Toward multidimensional assignment data association in robot localization and mapping. *IEEE Transactions on Robotics*, 22(2):350–365, April 2006.

[14] J. Niera and J.D. Tardos. Data association in stochastic mapping using the jointcompatibility test. *IEEE Transactions on Robotics and Automation*, 17(6):890–897, December 2001.

[15] S. Clark. *Autonomous Land Vehicle Navigation Using Millimetre Wave Radar.* PhD thesis, Australian Centre for Field Robotics, University of Sydney, 1999.

[16] S. Williams. *Efficient Solutions to Autonomous Mapping and Navigation Problems.* PhD thesis, Australian Centre for Field Robotics, University of Sydney, 2001.

[17] F. Tang, M.D. Adams, J. Ibanez-Guzman, and W.S. Wijesoma. Pose invariant, robust feature extraction from range data with a modified scale space approach. In *IEEE International Conference on Robotics and Automation (ICRA)*, New Orleans, USA, April 2004.

[18] S. Se, D. Lowe, and J. Little. Mobile robot localisation and mapping with uncertainty using scale-invariant visual landmarks. *International Journal of Robotics Research*, 21(8):735–758, August 2002.

[19] D. Ribas, P. Ridao, J.D. Tardos, and J. Niera. Underwater slam in a marina environment. In *IEEE/RSJ International Conference on Intelligent Robots and Systems (IROS)*, San Diego, CA, October 2007.

[20] A. Elfes. *Occupancy Grids: A Probabilistic Framework for Robot Perception and Navigation.* PhD thesis, Robotics Institute, Carnegie Mellon University, Pittsburgh, PA, May 1989.

[21] R. Smith, M. Self, and P. Cheeseman. A stochastic map for uncertain spatial relationships. In *The fourth international symposium of Robotics Research*, pages 467–474, 1987.

[22] D.F Dong, W.S. Wijesoma, and A.P. Shacklock. An efficient rao-blackwellized genetic algorithmic filter for slam. In *IEEE International Conference on Robotics and Automation*, pages 2427–2432, Rome, Italy, April 2007.

[23] M. Begum, G.K.I Mann, and R. Gosine. A fuzzy-evolutionary algoritm for simulataneous localisation and mapping of mobile robots. In *IEEE Congress on Evolutionary Computation*, pages 1975–1982, Vancouver, Canada, July 2006.

[24] J. Porta. Cuikslam: A kinematic-based approach to slam. In *IEEE International Conference on Robotics and Automation*, Barcelona, Spain, April 2005.

[25] J. Nieto, T. Bailey, and E. Nebot. Recursive scan-matching slam. *International Journal of Robotics and Autonmous Systems.*, 55(1):39–49, 2007.

[26] S. Clark and H.F. Durrant-Whyte. Autonomous land navigation using millimeter wave radar. In *IEEE International Conference on Robotics and Automation (ICRA)*, pages 3697–3702, Leuven,Belgium, May 1998.

[27] A. Foessel. *Scene Modeling from Motion-Free Radar Sensing.* PhD thesis, Robotics Institute, Carnegie Mellon University, Pittsburgh, PA, January 2002.

[28] G. Dissanayake, P. Newman, H.F. Durrant-Whyte, S. Clark, and M. Csorba. A solution to the simultaneous localization and map building (SLAM) problem. *IEEE Transactions on Robotic and Automation*, 17(3):229–241, June 2001.

[29] R. Murphy. Bayesian map learning in dynamic environments. In *Proc. Conf. Neural Inf. Process. Syst.*, pages 1015–1021, Colorado, 1999.

[30] J. Kim and S. Sukkarieh. Real-time implementation of airborne inertial-slam. *Internation Journal of Robotics and Autonmous Systtems*, 55(1):62–71, 2007.

[31] D. Borrmann, J. Elseberg, K. Lingemann, A. Nüchter, and J. Hertzberg. Globally consistent 3d mapping with scan matching. *International Journal of Robotics and Autonmous Systems.*, 56(2):130–142, 2008.

[32] A. Elfes. Using occupancy grids for mobile robot perception and navigation. *Computer*, 22(6):46–57, June 1989.

[33] A. Foessel, J. Bares, and W.R.L. Whittaker. Three-dimensional map building with MMW RADAR. In *Proceedings of the 3rd International Conference on Field and Service Robotics*, Helsinki, Finland, June 2001. Yleisjljenns - Painnoprssi.

[34] J.S Gutmann and K. Konolige. Incremental mapping of large cyclic environments. In *the Conference on Intelligent Robots and Applications (CIRA)*, Monterey, CA, 1999.

[35] D. Hähnel, W. Burgard, D. Fox, and S. Thrun. An efficient fastslam algorithm for generating maps of large-scale cyclic environments from raw laser range measurements. In *IEEE/RSJ International Conference on Intelligent Robots and Systems (IROS)*, pages 206–211, Las Vegas, Nevada, 2003.

[36] K. Konolige. Improved occupancy grids for map building. *Auton. Robots*, 4(4):351–367, 1997.

[37] H. Moravec and A.E. Elfes. High resolution maps from wide angle sonar. In *Proceedings of the 1985 IEEE International Conference on Robotics and Automation*, pages 116–121, March 1985.

[38] D. Pagac, E. Nebot, and H.F. Durrant-Whyte. An evidential approach for map building for autonomous vehicles. *IEEE Transactions on Robotics and Automation*, vol. 14(4), August 1998.

[39] S. Thrun. Learning occupancy grids with forward models. *Autonomous Robots*, 15(2):111–127, September 2003.

[40] G. Grisetti, C. Stachniss, and W. Burgard. Improved techniques for grid mapping with rao-blackwellized particle filters. *IEEE Transactions on Robotics*, 23(1):34–45, February 2007.

[41] S. Lacroix and G. Dudek. On the identification of sonar features. In *International Conference on Intelligent Robots and Systems (IROS)*, France, September 1997.

[42] M. Montemerlo and S. Thrun. Simultaneous localization and mapping with unknown data association using fastslam. In *IEEE Internationlal Conference on Robotics and Automation*, volume 1, pages 412–418, September 2003.

[43] M. Montemerlo, S. Thrun, D. Koller, and B. Wegbreit. Fastslam: A factored solution to the simultaneous localization and mapping problem. In *Eighteenth national conference on Artificial intelligence*, pages 593–598, Menlo Park, CA, USA, 2002. American Association for Artificial Intelligence.

[44] M. Montemerlo, S. Thrun, D. Koller, and B. Wegbreit. Fastslam 2.0: An improved particle filtering algorithm for simultaneous localization and mapping that provably converges. In *18th Int. Joint Conf. on Artificial Intelligence*, pages 1151–1156. Morgan-Kaufmann Publishers, 2003.

[45] S. Thrun, D. Haehnel, D. Ferguson, M. Montemerlo, R. Triebel, W. Burgard, C. Baker, Z. Omohundro, S. Thayer, and W. R. L. Whittaker. A system for volumetric robotic mapping of abandoned mines. In *Proceedings of the 2003 IEEE International Conference on Robotics and Automation (ICRA '03)*, volume 3, pages 4270 – 4275, May 2003.

[46] F. Lu and E. Milios. Robot pose estimation in unknown environments by matching 2D range scans. *Journal of Intelligent and Robotic Systems*, 18(3):249–275, 1997.

[47] M.C. Martin and H.P. Moravec. Robot evidence grids. Technical Report CMU-RI-TR-96-06, Carnegie Mellon University, Pittsburgh, Pennsylvania 15213, March 1996.

[48] T. Yang and V. Aitken. Evidential mapping for mobile robots with range sensors. *IEE Transactions on Instrumentation and Measurement*, 55(4):1422–1429, August 2006.

[49] S. Thrun. Particle filter in robotics. In *Uncertainty in AI (UAI)*, 2002.

[50] H.F. Durrant-Whyte and T. Bailey. Simultaneous localization and mapping: Part II. *IEEE Robotics and Automation Magazine*, 13(3):108–117, September 2006.

[51] J. Andrade-Cetto and A. Sanfeliu. Temporal landmark validation in cml. In *IEEE International Conference on Robotics and Automation (ICRA)*, volume 2, pages 1576–1581, September 2003.

[52] P. Newman, P. Cole, and K. Ho. Outdoor slam using visual appearance and laser ranging. In *IEEE Internationlal Conference on Robotics and Automation*, pages 1180–1187, May 2006.

[53] R.E. Kalman. A new approach to linear filtering and prediction problems. *Trans. of the ASME–Journal of Basic Engineering*, 82(D):35–45, 1960.

[54] T. Kirubarajan and Y. Bar-Shalom. *Multisensor-Multitarget Statistics in Data Fusion Handbook*. CRC Press,Boca Raton, 2001.

[55] Y. Bar-Shalom and T.E. Fortmann. *Tracking and Data Association.* Academic Press, 1988.

[56] P. Maybeck. *Stochastic Models, Estimation and Control*, volume 1. Academic Press, 1982.

[57] P. Moutarlier and R. Chatila. Stocastic multisensory data fusion for mobile robot location and environmental modeling. In *Fifth International Symposiam of Robotics Research*, pages 85–94, 1989.

[58] S.J. Julier and J.K. Uhlmann. A new extension of the kalman filter to nonlinear systems. In *Int. Symp. Aerospace/Defense Sensing, Simul. and Controls*, pages 35–45, Orlando, Florida, 1997.

[59] S. Clark and G. Dissanayake. Simultaneous localisation and map building using millimetre wave radar to extract natural features. In *IEEE International Conference on Robotics and Automation (ICRA)*, pages 1316–1321, Detroit,Michigan, May 1999.

[60] C.M. Smith, J.J. Leonard, A.A. Bennet, and C. Shaw. Feature based concurrent mapping and localisation. In *Proceedings of Oceans '97*, pages 90–102, October 1997.

[61] H.F. Durrant-Whyte, S. Majumder, M. de Battista, and S. Scheding. A bayesian algorithm for simultaneous localisation and map building. In *The Tenth International Symposium of Robotics Research (ISRR)*, Victoria, Australia, 2001.

[62] S. Majumder. *Sensor Fusion and Feature Based Navigation for Subsea Robots.* PhD thesis, The University of Sydney, August 2001.

[63] T. Bailey. *Mobile Robot Localisation and Mapping in Extensive Outdoor Environments.* PhD thesis, Australian Centre for Field Robotics, University of Sydney, 2002.

[64] P. Green. Reversible jump markov chain monte carlo computation and bayesian model determination. *Biometrica*, 82:711–732, 1995.

[65] M. Orton and W. Fitzgerald. Bayesian approach to tracking multiple targets using sensor arrays and particle filters. *IEEE Transactions on Signal Processing*, vol. 50(2):216–223, February 2002.

[66] M. Montemerlo. *FastSLAM: A Factored Solution to the Simultaneous Localization and Mapping Problem with Unknown Data Association.* PhD thesis, Robotics Institute, Carnegie Mellon University, Pittsburgh, PA, July 2003.

[67] D. Stoyan, W.S Kendall, and J. Mecke. *Stochastic Geometry and Its Applications*. John Wiley and Sons, Inc, New York, second edition, 1995.

[68] J. Nieto, J. Guivant, E. Nebot, and S. Thrun. Real time data association for fastslam. In *IEEE Internationlal Conference on Robotics and Automation*, volume 1, pages 412–418, September 2003.

[69] F.T. Ramos, J. Nieto, and H.F. Durrant-Whyte. Recognising and modelling landmarks to close loops in outdoor slam. In *International Conference on Robotics and Automation (ICRA)*, Rome, Italy, April 2007.

[70] K. Konolige, M. Agrawal, and J. Sola. Large-scale visual odometry for rough terrain. In *International Symposium on Research in Robotics (ISRR)*, Hiroshima, Japan, 2007.

[71] J.S Gutmann and D. Fox. An experimental comparison of localisation methods continued. In *International conference on Intelligent Robots and Systems (IROS)*, Lausanne, Switzerland, October 2002.

[72] I.T. Ruiz, S. de Raucourt, and Y. Petillot. Concurrent mapping and localization using sidescan sonar. *IEE Journal of Oceanin Engineering*, 29(2), April 2004.

[73] J. Tardos, J. Neira, P. Newman, and J. Leonard. Robust localization and mapping in indoor enviroments using sonar data. *International Journal of Robotics Research*, 21(4):311–330, April 2002.

[74] K.E Bekris, M. Glick, and L.E. Kavraki. Evaluation of algorithms for bearing-only slam. In *IEEE International Conference on Robotics and Automation (ICRA)*, Orlando,Floride, May 2006.

[75] E. Jose and M.D. Adams. An augmented state SLAM formulation for multiple line-of-sight features with millimetre wave radar. In *in Proceedings of the IEEE/RSJ International Conference on Intelligent Robots and Systems (IROS)*, Alberta, Canada, August 2005.

[76] F.R. Correa and J. Okamoto. Omnidirectional stereovision system for occupancy grid. In *12th IEEE International Conference on Advanced Robotics (ICAR)*, pages 628–634, July 2005.

[77] D. Murray and J.J. Little. Using real-time stereo vision for mobile robot navigation. *Autonomous Robots*, 8(2):161–171, 2000.

[78] SICK AG Division Auto Ident. LMS 200/LMS 211/LMS 220/LMS 221/LMS 291 laser measurement systems - technical description. Technical report, Available from: www.mysick.com/saqqara/get.aspx?id=IM0012759, December 2006.

[79] L. Angrisani, A. Baccigalupi, and R. S. Lo Moriello. Ultrasonic time-of-flight estimation through unscented kalman filter. *IEEE Transactions on Instrumentation and Measurement*, 55(4):1077–1084, August 2006.

[80] C.C. Wang, C. Thorpe, and S. Thrun. Online simultaneous localization and mapping with detection and tracking of moving objects: Theory and results from a ground vehicle in crowded urban areas. In *IEEE International Conference on Robotics and Automation*, May 2003.

[81] D. Langer. An integrated MMW RADAR system for outdoor navigation. In *IEEE International Conference on Robotics and Automation*, pages 417–422, Minneapolis, Minnesota, April 1996.

[82] G. Brooker. *Long-Range Imaging Radar for Autonomous Navigation.* PhD thesis, The University of Sydney, January 2005.

[83] E. Jose and M.D. Adams. Millimetre wave radar spectra simulation and interpretation for outdoor SLAM. In *International Conference on Robotics and Automation (ICRA)*, New Orleans, USA, April 2004.

[84] N.C. Currie and C.E. Brown. *Principles and Applications of MMW RADAR.* Artech House, Dedham, MA, 1987.

[85] G. Brooker, M. Bishop, and S. Scheding. Millimetre waves for robotics. In *Australian Conference for Robotics and Automation*, Sidney, Australia, November 2001.

[86] M. Chandran and P. Newman. Motion estimation from map quality with millimeter wave radar. In *IEEE/RSJ International Conference on Intelligent Robots and Systems (IROS)*, Beijing, China, October 2006.

[87] P.P. Gandhi and S.A. Kassam. Analysis of cfar processors in nonhomogeneous background. *IEEE Transactions on AES*, 4(24):427–445, July 1988.

[88] H. Rohling and R. Mende. OS CFAR performance in a 77 GHz radar sensor for car applications. In *CIE International Conference of Radar*, pages 109 – 114, October 1996.

[89] P.P. Gandhi and S.A. Kassam. Optimality of the cell averaging CFAR detector. In *IEEE Transactions on Information Theory*, volume 40, pages 1226–1228, July 1994.

[90] H. Rohling. Radar cfar thresholding in clutter and multiple target situations. In *IEEE Transactions, AES-19*, pages 608–621, 1983.

[91] S.M. Tonissen and Y. Bar-Shalom. Maximum likelihood track-before-detect with fluctuating target amplitude. *IEEE Transactions on Aerospace and Electronic Systems*, 34(3):796–809, July 1998.

[92] M.I. Skolnik. *Introduction to Radar Systems.* McGraw Hill, New York, 1982.

[93] H.L. Van Trees. *Detection, Estimation and Modulation Theory - Part I.* Willey, New York, 1968.

[94] H. Rohling. Some radar topics: Waveform design, range (cfar) and target recognition. In *NATO: Advances in Sensing with Security Applications*, Il Ciocco, Italy, July 2005.

[95] P.P. Gandhi and S.A. Kassam. Analysis of CFAR processors in nonhomogeneous background. *IEEE Transactions on AES*, 4(24):427–445, July 1988.

[96] R. L. Iman and W. J. Conover. *A Modern Approach to Statistics.* Wiley, 1983.

[97] G. Shafer. *A Mathematical Theory of Evidence.* Princeton University Press, New Jersey, 1976.

[98] Y. Rachlin, J.M. Dolan, and P. Khosla. Efficient mapping through exploitation of spatial dependencies. In *in Proceedings of the IEEE/RSJ International Conference on Intelligent Robots and Systems (IROS)*, Alberta, Canada, August 2005.

[99] J. Collins, M. Eaton, M. Masfield, and S. O' Sullivan. Developing a benchmarking framework for map building paradigms. In *in Proceedings of the 9th International Symposium on Artifical Life and Robotics*, Beppu, Japan, January 2004.

[100] M.S. Arulampalam, and N. Gordon S. Maskell, and T. Clapp. A tutorial on particle filters for online nonlinear/non-gaussian bayesian tracking. *IEEE Transactions on Signal Processing*, 50(2):174–188, February 2002.

[101] M.D. Adams, F. Tang, W.S. Wijesoma, and C. Sok. Convergent smoothing and segmentation of noisy range data in multiscale space. *IEEE Transactions on Robotics*, 24(3):746–753, June 2008.

[102] R. Mahler. Multi-target bayes filtering via first-order multi-target moments. *IEEE Transactions on AES*, 4(39):1152–1178, October 2003.

[103] B.N. Vo and W.K. Ma. The gaussian mixture probability hypothesis density filter. *IEEE Transactions on Signal Processing*, 54:4091–4104, November 2006.

[104] D. Stoyan, W.S Kendall, and J. Mecke. *Stochastic Geometry and Its Applications*. John Wiley and Sons, Inc, New York, second edition, 1995.

[105] D. Schuhmacher, B.T. Vo, and B.N. Vo. A consistent metric for performance evaluation of multi-object filters (to appear). *IEEE Transactions on Signal Processing*, 86:3447–3457, 2008.

[106] S. Grzonka, C. Plagemann, G. Grisetti, and W. Burgard. Look-ahead proposals for robust grid-based SLAM. In *Proceedings of the 6th International Conference on Field and Service Robotics*, Chamonix, France, 2007.

[107] J.F.C Kingman. *Poisson Processes (Oxford Studies in Probability)*. Oxford University Press, USA, January 1993.

[108] B. Vo, S. Singh, and A. Doucet. Sequential monte carlo methods for multitarget filtering with random finite sets. *IEEE Transactions on Aerospace and Electronic Systems*, 41(4):1224–1245, October 2005.

[109] J. Guivant. *Efficient Simultaneous Localisation and Mapping in Large Environments*. PhD thesis.

Appendix A

The Mobile Platform

This appendix presents the mobile platform used as the experimental test bed for this thesis.

A.1 The Platform

A robucar mobile robotic platform, available from robosoft (http://www.robosoft.fr/), fitted with autonomous sensing capabilities is shown in figure A.1.

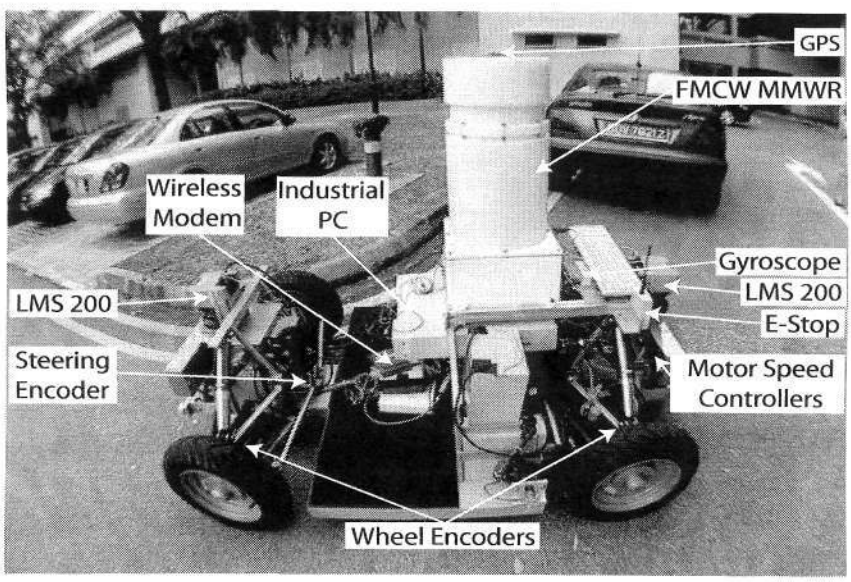

Figure A.1: *The Robucar experimental test bed.*

The industrial PC has a single motherboard (PIII 650MHz) with a National Instruments 7344/7334 Motion controller to manage all the low level controlling tasks such as the motion speed controllers, the brakes and the steering system actuator. Furthermore, it provides data acquisition capabilities for the 5 encoders. Also connected to the industrial PC (through ethernet, USB and serial connections) are the fibre-optic gyroscope (RS-232), 2xLMS 200 (USB), the GPS (RS-232) and the 77GHz FMCW MMWR (ethernet). The vehicle is remotely controlled over a wireless link.

A.2 Sensor Specifications

This section details the sensors used on-board the robucar testing platform during the course of this thesis. Figure A.2 shows the radar sensor adopted for the experimental verification of the proposed algorithms in this thesis. The system specifications of the sensor are shown in table A.1.

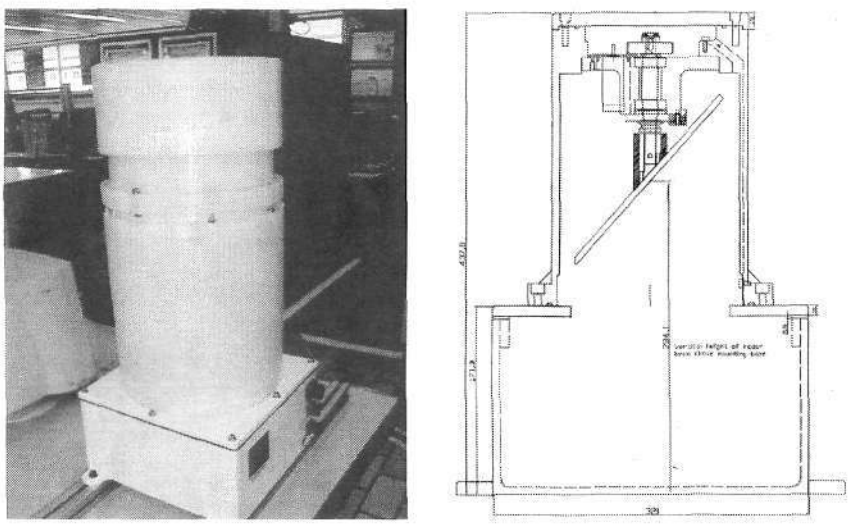

Figure A.2: *The 77GHz FMCW MMW Radar Sensor.*

The SICK LMS is shown in figure A.3. This sensor was used to verify the detection performance of the radar imaging sensor as this sensor displays very low false alarm probabilities in practise, however it can be prone to numerous missed detections as shown in the experimental sections of this thesis. The specification sheet for the sensor is shown in table A.2.

Table A.1: Specification of 77GHz FMCW MMW Radar.

Transmit Frequency	76 to 77 GHz
Chirp Bandwidth	600Mhz
Transmit Power	15dBm
Maximum Range	200 to 800m (configurable)
Range Accuracy	up to $\pm$ 0.03m
Beam Width	1.8^o
Scanner Resolution	0.09^o
Scanner Field of View	360^o
Scan Speed	2.5Hz (other speeds optional)
Travel in Elevation	$\pm$ 15^o
Elevation Resolution	0.02^o
Elevation scan rate	5^o/sec
Interfaces	Ethernet/CAN/RS 232
Supply Voltage	+24V nominal (18-36V)
Size	321x321x741 mm (Radar 321x321x171 mm + Optional 3D Raydome and Scanner 295 mmx570 mm)
Environmental	IP 66,NEMA-4X
Temperature	-20^o to +70°C

Figure A.3: *The SICK LMS 200 measurement unit.*

Table A.2: Specification of LMS 200.

Model	LMS 200
Range	Maximum 80m
Angular Resolution	$0.25^o/0.5^o/1^o$ (selectable)
Response Time	53ms/25ms/13ms
Measurement Resolution	10mm
System Error	Typ. ± 20 mm (mm-mode), range 1...8 m Typ. ± 4 cm (cm-mode), range 1...20 m
Statistical Error	Typ. ±5mm (at range ≤8m/≥10% reflectivity/≤ 5 klux)
Data Interface	RS 232/RS 422 (configurable)
Transfer Rate	9.6/19.2/38.4/500 kBd
Switching Outputs	3xPNP; typ. 24VDC; OUT A, OUT B max. 250mA, OUT C max. 100mA
Supply Voltage	24 V DC ±15% (max. 500mV ripple) current requirements maximum 1.8A (including output load)
Power Uptake	Approx. 20W (without upload)
Electrical Protection Class	Safety insulated, protection class 2
Interference Resistance	According to IEC 801, part 2-4; EN 50081-1/50082-2
Ambient Temperature	050°C (32°122°F) / -30°70°C (-22°158°F)
Enclosure Rating	IP 65
Weight	Approx. 4.5 kg
Dimensions	185 x 156 x 210mm (7.3 x 6.1 x 8.3in) with cables: 185 x 156 x 265 (7.3 x 6.1 x 10.4in)
Vibration Fatigue Limit	According to IEC 68 part 206, table 2c, frequency range 10...150Hz amplitude 0.35mm or 5g single impact IEC 68 part 2-27,table 2, 15 g/11ms permanent vibration IEC 68 part 2-29, 10 g/16ms, Shock absorbers are recommended for heavy vibration and impact demands (e.g. AGV applications)

Figure A.4 and table A.3 show the fibre-optic gyroscope and its specification sheet. This sensor is mounted over the rear axle of the vehicle and used to take a heading measurement reading.

Figure A.4: *The KVH DSP-5000 single-axis fibre optic gyroscope.*

Table A.3: Specification of KVH DSP-5000.

Model	KVH DSP-5000
Input Voltage	+5 VDC
Power Consumption	3 W
Weight	0.25kg
Size	112 x 99 x 43 mm
Connector Type	High density D-sub 29 pin (male)
Digital Output	Selectable: rate, incremental angle, angle & bit serial RS-232, 38400 baud or 3-wire high speed
Output Format	ASCII
Update Rate	100/sec
Operating Temperature	-40°C to + 75°C
Storing Temperature	-50°C to + 85°C
Shock	-90 G, 11 ms half-sine
MTBF	100,000 hours
Bias Instability vs. Time	1^o/h, 1σ
Bias Offset vs. Temp	10^o/h, 1σ
Angle Random Walk	$5^o/\mathrm{h}/\sqrt{Hz}$
Rotation Rate	$\pm 500^o$/sec
Instantaneous Bandwidth	100Hz
Scale Factor Linearity	500 ppm, 1σ
Scale Factor Stability	500 ppm, 1σ
Turn-on Time	1 sec

Figure A.5 shows incremental and absolute encoders used on the vehicle to measure velocity and steering angle. These measurements are used in the vehicle model to predict its location. The corresponding specifications are shown in tables A.4 and A.5.

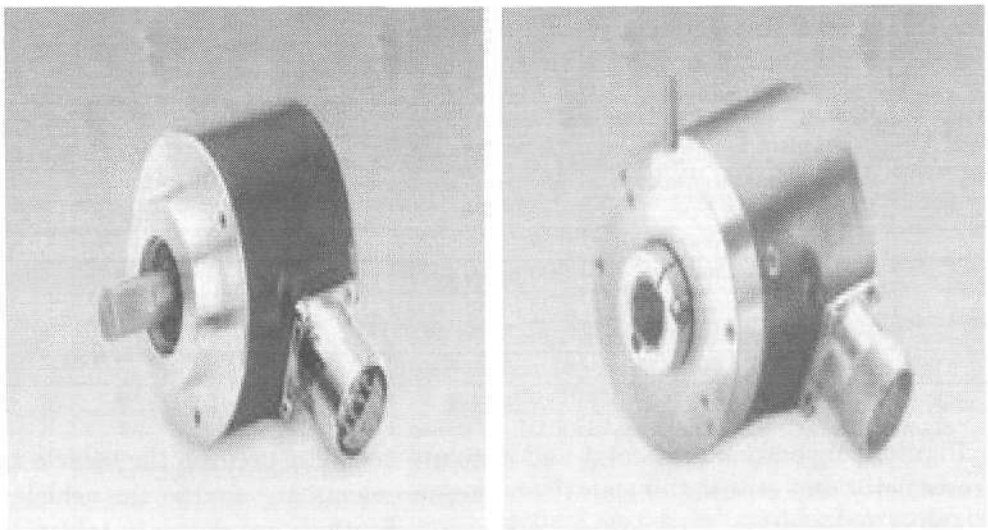

(a) G0355 Incremental Encoder (b) G0M2H SSI Absolute Encoder

Figure A.5: *Wheel (incremental) and steering (absolute) encoders.*

Table A.4: Specification of G0355 Incremental Encoder.

Model	G0355 Incremental Encoder
Supply Voltage	5 VDC ± 10%, 4.75...30 VDC
Reverse Polarity Protection	Yes (4.75...30 VDC)
Response Time	53ms/25ms/13ms
Consumption w/o load	≤30 mA (24 VDC) ≤60 mA (5 VDC)
Reference signal	Zero pulse, width 90°
Sensing Method	Optical
Output Frequency	≤300 Khz
Output Signals	A 90° B, N + inverted
Output Levels	Linedriver RS422 Push-pull short-circuit proof
Interference Immunity	DIN EN 61000-6-2
Emitted Interference	DIN EN 61000-6-4
Approval	UL Approval / E63076
Housing	58 mm
Shaft	12 mm
Protection DIN EN	IP 54 without shaft seal IP 65 with shaft seal
Operating Speed	≤10000 rpm
Starting Torque	≤20 N axial ≤40 N axial
Materials	Housing: aluminium Flange: aluminium
Operating Temp.	-25°C to + 100°C (5 VDC) -25°C to + 85°C (24 VDC)
Relative Humidity	95% non-condensing
Resistance	DIN EN 60068-2-6 Vibration 10g, 16-2000 Hz DIN EN 60068-2-27 Shock 200g, 6 ms
Weight approx.	250g
E-connection	Connector or cable

Table A.5: Specification of G0M2H SSI Absolute Encoder.

Model	G0M2H SSI Absolute Encoder
Supply Voltage	10...30 VDC
Reverse Polarity Protection	Yes
Consumption w/o load	$\leq$50 mA (24 VDC)
Initialising Time	$\leq$20 ms after power on
Interfaces	SSI Incremental A 90^o (optional)
Steps per turn	16384 / 14 bit
Number of turns	4096 / 12 bit
Incremental Output	2048 impulses A90^{o}B + inverted
Absolute Accuracy	$\pm$0.025^o
Sensing Method	Optical
Code	Gray or Binary
Code Sequence	CW/CCW coded by connection
Inputs	SSI clock Control signals UP/DOWN and zero
Output Levels	SSI data linedriver RS485 Diagnostic outputs push-pull
Interference Immunity	DIN EN 61000-6-2
Emitted Interference	DIN EN 61000-6-4
Diagnostic Functions	Self-diagnosis Code continuity check Multiturn sensing
Approval	UL Approval / E63076
Housing	55 mm
Shaft	10 mm
Protection DIN EN	IP 54
Operating Speed	$\leq$6000 rpm
Rotor moment of inertia	20gcm^2
Materials	Housing: aluminium Flange: aluminium
Operating Temp.	-25^{o}C to + 85^{o}C -40^{o}C to + 85^{o}C (optional)
Relative Humidity	95% non-condensing
Resistance	DIN EN 60068-2-6 Vibration 10g, 16-2000 Hz DIN EN 60068-2-27 Shock 200g, 6 ms
Weight approx.	400g
E-connection	Connector, 12 pins

Appendix B

CFAR Processors

This section outlines the derivation of other popular methods of statistical landmark detection for imaging sensors.

B.1 OS-CFAR with IID Exponential Noise

Throughout this thesis, the principle detection algorithm for the imaging sensor (section 3.4.2, section 4.4.2) is the OS-CFAR routine. Its mathematical derivation and proof of CFAR properties is outlined here. Assuming the noise signal has an IID exponential distribution of the form,

$$f(\psi) = \begin{cases} \frac{1}{\mu} e^{-\frac{\psi}{\mu}} & \text{if } \psi > 0 \\ 0 & \text{Otherwise} \end{cases}$$

where μ is unknown. The decision threshold is set as normal as

$$T = \tau Z$$

where, $Z = \hat{\psi}_{r,m_r=0}$ is an estimate of the average noise power μ and τ is a scaling factor to achieve a desired P_{fa} given by,

$$P_{fa} = E\{P[\psi_r > \tau Z | \mathcal{H}_0]\}$$

Here, ψ_r is the power at range bin r. In an ordered statistics CFAR, the test statistic , Z, is chosen as the k^{th} sample from the ordered samples within leading and lagging windows. Its pdf under null hypothesis must be evaluated. Firstly the cdf of Ψ_r can

be evaluated as,

$$F_\Psi(\psi) = \int_0^\psi f(\psi)d\psi$$

$$F_\Psi(\psi) = 1 - e\left(\frac{-\psi}{\mu}\right)$$

The pdf of the k^{th} value of the ordered statistic is then given by,

$$f_Z(z) = k\binom{2W}{k}(1 - F_\Psi(z))^{2W-k}(F_\Psi(z))^{k-1}f_\Psi(z)$$

In the case of IID exponentially distributed random variables we get,

$$\begin{aligned} f_Z(z) &= \frac{k}{\mu}\binom{2W}{k}(e^{-z/\mu})^{2W-k}(1 - e^{-z/\mu})^{k-1}e^{-z/\mu} \\ &= \frac{k}{\mu}\binom{2W}{k}(e^{-z/\mu})^{2W-k+1}(1 - e^{-z/\mu})^{k-1}. \end{aligned}$$

This then represents the pdf of the test statistic, Z. Then,

$$P_{fa} = \int_0^\infty P[\psi_r \geq \tau z|\mathcal{H}_0]f_Z(z)dz.$$

Since,

$$\begin{aligned} P[\psi_r \geq \tau z|\mathcal{H}_0] &= \int_{\tau z}^\infty f(\psi|\mathcal{H}_0)d\psi \\ &= e(-\tau z/\mu). \\ P_{fa} &= \int_0^\infty e(-\tau z/\mu)f_Z(z)dz \\ &= \frac{k}{\mu}\binom{2W}{k}\int_0^\infty e\{\frac{-\tau z}{\mu}\}(e^{-z/\mu})^{2W-k+1}(1 - e^{-z/\mu})^{k-1}dz. \end{aligned}$$

Using the substitution,

$$y = z/\mu$$

$$dy = dz/\mu$$

we get,

$$P_{fa} = k\binom{2W}{k}\int_0^\infty e^{-(\tau + 2W + 1 - k)y}(1 - e^{-y})^{k-1}dy$$

This can be evaluated by,

$$I_{k,M} = \int_0^\infty e^{-(M+1-k)y}(1-e^{-y})^{k-1}dy$$

Using integral by parts,

$$\begin{aligned} u &= (1-e^{-y})^{k-1} \\ du &= (k-1)(1-e^{-y})^{k-2}e^{-y} \\ dv &= \int_0^\infty e^{-(M+1-k)y}dy \\ v &= -\frac{e^{-(M+1-k)y}}{M+1-k}. \end{aligned}$$

Thus we get,

$$\begin{aligned} I_{k,M} &= -\left[\frac{(1-e^{-y})^{k-1}e^{-(M+1-k)y}}{M+1-k}\right]_0^\infty + \int_0^\infty \frac{e^{-(M+1-k)y}}{M+1-k}(k-1)(1-e^{-y})^{k-2}e^{-y}dy \\ I_{k,M} &= 0 + \frac{k-1}{M+1-k}\int_0^\infty e^{-(M+1-k)y}(1-e^{-y})^{k-2}e^{-y}dy \\ &= \frac{k-1}{M+1-k}\int_0^\infty e^{-(M+1-k+1)y}(1-e^{-y})^{k-2}e^{-y}dy \\ &= \frac{k-1}{M+1-k}I_{k-1,M} \end{aligned}$$

Now,

$$I_{k-1,M} = \frac{k-2}{M-k+2}I_{k-2,M}$$

thus,

$$\begin{aligned} I_{k,M} &= \left(\frac{k-1}{M-k+1}\right)\left(\frac{k-2}{M-k+2}\right)I_{k-2,M} \\ &= \left(\frac{k-1}{M-(k-1)}\right)\left(\frac{k-2}{M-(k-2)}\right)I_{k-2,M}. \end{aligned}$$

The end term,

$$\begin{aligned} I_{1,M} &= \int_0^\infty e^{-My} dy \\ &= \frac{1}{M}. \end{aligned}$$

Therefore we get,

$$\begin{aligned} I_{k,M} &= \left(\frac{(k-1)!}{(M-(k-1))!} \right) \frac{1}{M} \\ &= \frac{(k-1)!(M-k)!}{M!} \end{aligned}$$

and,

$$P_{fa} = k \binom{2W}{k} \frac{(k-1)!(\tau + 2W - k)!}{\tau + 2W!}.$$

Again the false alarm probability is independent of any unknowns, thus a scale factor, τ, can be set to achieve the desired constant rate of false alarm. Considering the detection probability,

$$P_d = \int_0^\infty P[\psi_r \geq \tau z | \mathcal{H}_1] f_Z(z) dz$$

$$P[\psi_r \geq \tau z | \mathcal{H}_1] = \int_{\tau z}^\infty f(\psi | \mathcal{H}_1) d\psi$$

Here, the distribution, $f(\psi|\mathcal{H}_1)$, under the alternate hypothesis is usually assumed *a priori* by an SNR fluctuation model derived from an RCS fluctuation model (usually Swerling).

B.2 Cell Averaging (CA) CFAR with IID Exponential Noise

Section 3.5 compared the CA-CFAR algorithm with that of the OS-CFAR approach. As such, this section outlines the mathematical derivation and proof of the CFAR property for the CA detector. A Cell-Averging (CA) CFAR detector is derived here under the situation of an exponentially distributed noise signal. The derivation in fact assumes Gaussian environment noise and clutter [92], however, after being passed through the mixer and square-law device (i.e. post-envelope), the distribution

becomes exponential of the form,

$$f(\psi) = \begin{cases} \frac{1}{\mu} e^{-\frac{\psi}{\mu}} & \text{if } \psi > 0 \\ 0 & \text{Otherwise} \end{cases}$$

where μ is unknown. Using CA-CFAR, the test statistic is the sample mean average,

$$\hat{\psi}_{r,m_r=0} = \frac{1}{2W} \sum_{i=r-W}^{r+W} \psi_i \quad \text{for} \quad i \neq r$$

and the likelihood ratio test is then,

$$\frac{\psi_r}{\frac{1}{2W} \sum_{j=r-W}^{r+W} \psi_j} \geq \tau$$

$$L(\psi_r) = \psi_r \geq \frac{\hat{\psi}_{r,m_r=0}}{2W} \tau$$

where τ is set to achieve a constant rate of false alarm. Since the threshold is itself a random variable, the probability of false alarm must be evaluated as,

$$P_{fa} = E\{P[\psi_r > \frac{\hat{\psi}_{r,m_r=0}}{2W} \tau | \mathcal{H}_0]\}$$

Under a Null hypothesis, if we let z denote the test statistic (or mean), $\hat{\psi}_{r,m_r=0}$, then z has a gamma distribution (sum of IID exponentials is a gamma distribution (shape a = 2W, scale b = $\frac{1}{\mu}$)) given by,

$$f_Z(z) = \frac{1}{\mu \Gamma(2W)} \left(\frac{z}{\mu}\right)^{2W-1} e^{\frac{-z}{\mu}}$$

where,

$$\Gamma(2W) = \int_0^\infty \xi^{2W-1} e^{-\xi} d\xi.$$

As $2W$ is as positive integer, z is an Erlang random variable with parameter $\frac{1}{\mu}$. The false alarm probability is then derived from,

$$P_{fa} = E\{z\} = \int_0^\infty z f(z) dz.$$

Given a Null hypothesis,

$$z = \frac{1}{\mu_r}\int_{\frac{z}{2W}\tau}^{\infty} e^{-\frac{\psi_r}{\mu_r}} d\psi_r$$

$$z = e\left\{-\frac{z}{\mu}\frac{\tau}{2W}\right\}$$

Therefore,

$$P_{fa} = \frac{1}{\mu\Gamma(2W)}\int_0^{\infty}\left(\frac{z}{\mu}\right)^{2W-1} e\left\{\frac{-z}{\mu}\left(1+\frac{\tau}{2W}\right)\right\} dz$$

Taking the temporary variable x,

$$x = \frac{z}{\mu}\left(1+\frac{\tau}{2W}\right)$$

$$dz = \mu\left(1+\frac{\tau}{2W}\right)^{-1} dx$$

therefore,

$$\begin{aligned} P_{fa} &= \frac{\mu}{\mu\Gamma(2W)\left(1+\frac{\tau}{2W}\right)}\int_0^{\infty} x^{2W-1}\left(1+\frac{\tau}{2W}\right)^{-2W+1} e^{-x}dx \\ &= \frac{\mu}{\mu\Gamma(2W)\left(1+\frac{\tau}{2W}\right)^{2W}}\Gamma(2W) \\ \Rightarrow P_{fa} &= \left(1+\frac{\tau}{2W}\right)^{-2W} \end{aligned}$$

Thus, given the window width, W and desired probability of false alarm, P_{fa}, the scale factor, τ, can be calculated,

$$\tau = 2W\left(P_{fa}^{-\frac{1}{2W}} - 1\right)$$

which is independent of the mean noise level, μ. Thus as the false alarm probability is independent of any unknowns (namely μ), it is by definition a CFAR detector. Note that there is no information as the to detection probability sicne there has been no inclusion of the distribution of, ψ, under landmark presence. Under situations of high landmark density, the CA-CFAR processor suffers numerous problems due to landmark masking and biassed noise estimates due to interfering signals from landmarks.

B.3 CA-CFAR with IID Gaussian Noise

Section 4.4.1 comments that in the case of Gaussian signal noises after internal processing, the CFAR property cannot be obtained for such signal distribution assumptions. This section outlines the mathematical proof of violation of the CFAR property for such a scenario. Assume noise of the form,

$$f(\psi_r) = \begin{cases} \frac{1}{\sqrt{2\pi\sigma^2}} e\left\{-\frac{(\psi_r-\mu)^2}{2\sigma^2}\right\} & \text{if } \psi_r > 0 \\ 0 & \text{Otherwise} \end{cases}$$

where μ and σ^2 are unknown. Using CA-CFAR, the test statistics become,

$$\hat{\mu}_r = \frac{1}{2W} \sum_{i=k-W}^{k+W} \psi_i \quad \text{for} \quad i \neq k$$

$$\hat{\sigma}_r^2 = \frac{1}{2W} \sum_{i=k-W}^{k+W} \left(\psi_i - \hat{\mu}_r\right)^2 \quad \text{for} \quad i \neq k$$

The mean of $2W$ identical Gaussian random variables $\sim\mathcal{N}(\mu, \sigma^2)$ is a Gaussian $\sim \mathcal{N}(\mu, \frac{\sigma^2}{2W})$ with pdf,

$$f_Z(z) = \sqrt{\frac{2W}{2\pi\sigma^2}} e\left\{\frac{-2W(\psi-\mu)^2}{2\sigma^2}\right\}$$

Thus, P_{fa} is evaluated as,

$$P_{fa} = \alpha\sqrt{\frac{2W}{2\pi\sigma^2}} \int_0^\infty e\left\{\frac{-2W(\psi-\mu)^2}{2\sigma^2}\right\} d\psi$$

where,

$$\alpha = Q\left(\frac{\tau - \hat{\mu}}{\hat{\sigma}}\right)$$
$$\Rightarrow P_{fa} = \alpha$$

Therefore the scale factor, τ, can be calculated as,

$$\tau = Q^{-1}(P_{fa})\hat{\sigma} + \hat{\mu}$$

Note that in the case of unknown Guassian distribution moments, the CFAR property is not maintained as the scale factor (and P_{fa}) is a function of the noise statistics,

i.e. it depends on unknowns μ and σ^2.

Appendix C

Point Feature Extraction for Imaging Radar and Birth Density Formation

This appendix details the point feature extraction module used for FBRM and FB-SLAM trials using the FMCW MMW radar sensor presented in appendix A, as well as the formation of the birth density required by the PHD recursion of chapter 5, as in eqn. The appendix comprises a section on the point feature extraction and also the birth intensity formation for the PHD recursion proposed in eqn.(5.14).

C.1 Clustering Operation

Given the raw power scan, range and bearing measurements to hypothesised point features in the scan are returned. Figure C.1 shows a sample raw polar power vs. range scan returned by the imaging radar in the carpark environment. Each range bin corresponds to $0.25m$. The columns correspond to a discrete bearing angle. The power magnitude in each bin is represented by a blue-red colour scale.

Figure C.2 the shows the sample imaging radar scan, which has been transformed into the Cartesian domain through,

$$Grid(x, y|x_f, y_f) = \frac{\psi_{(r,\theta)}}{2\pi|\Sigma|^{0.5}} \exp\left(\left(\begin{bmatrix} x \\ y \end{bmatrix} - \begin{bmatrix} x_f \\ y_f \end{bmatrix}\right)^T \Sigma^{-1} \left(\begin{bmatrix} x \\ y \end{bmatrix} - \begin{bmatrix} x_f \\ y_f \end{bmatrix}\right)\right) \quad \text{(C.1)}$$

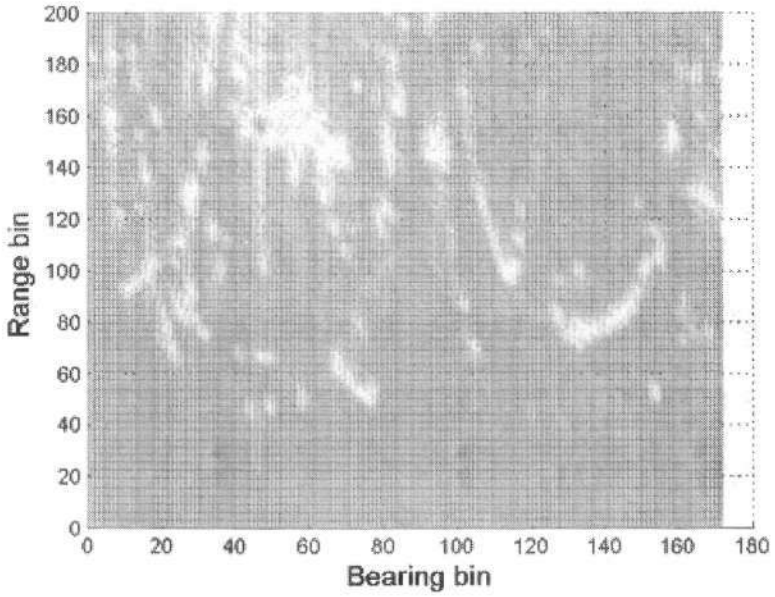

Figure C.1: *A raw power vs. range measurement from the imaging radar sensor in a carpark environment.*

where,

$$\begin{bmatrix} x_f \\ y_f \end{bmatrix} = \mathbf{H} \begin{bmatrix} r \\ \theta \end{bmatrix} \tag{C.2}$$

$$\Sigma = \nabla \mathbf{H}^T \mathbf{R} \nabla \mathbf{H} \tag{C.3}$$

with (r, θ) being the range and bearing to a given power cell of the raw polar scan, and $\psi_{(r,\theta)}$ being the measured power in that cell.

Due to the range imaging capability of the radar sensor, point like objects can be readily identified in the scan by observation. However, the received powers depend on landmark properties. The radar power profiles for sample point features in the environment are shown in figure C.3.

For this reason, detections are first registered by applying an adaptive OS-CFAR detector outlined in section 3.4. Simple clustering and centroid extraction then allows for point features to be readily extracted from the data. Using an intra-detection distance of 2m, clusters are formed as shown in figure C.4 bounded by black boxes. Point-like features are selected according to a cluster span distance threshold of 1m. The centroids of clusters hypothesised as point features are shown as black dots. Some missed feature detections and false alarms with this simplistic method of feature extraction are evident when compared with the ground truth shown in figure C.2.

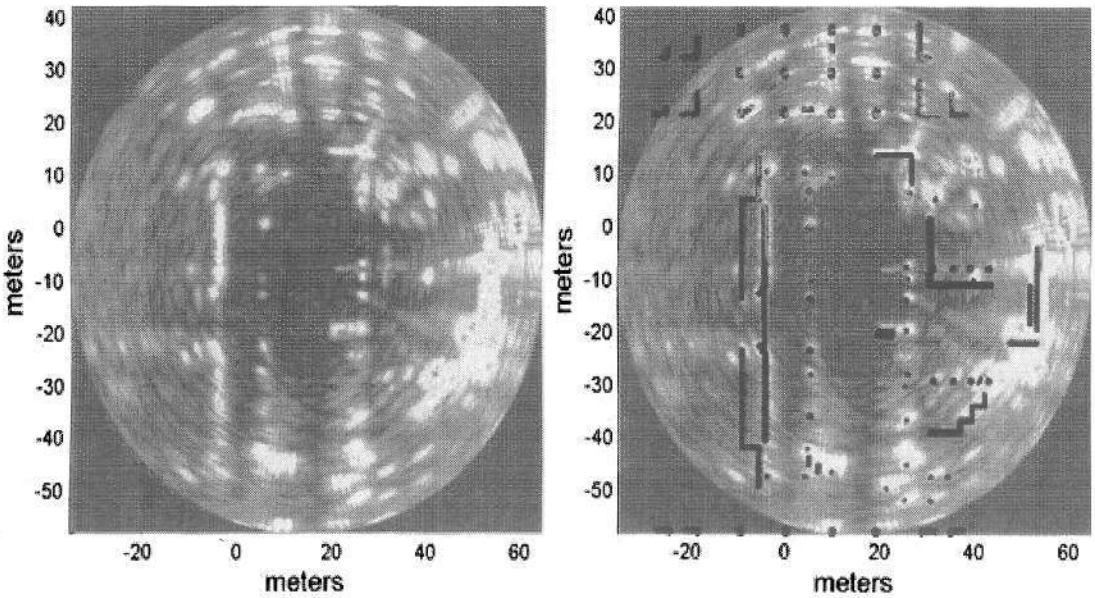

Figure C.2: *The raw polar radar scan rendered onto a 2D Cartesian grid. Also shown for comparison are the hypothesised map ground truth (black) and laser scan (red). The data shows good correlation with the ground truth map.*

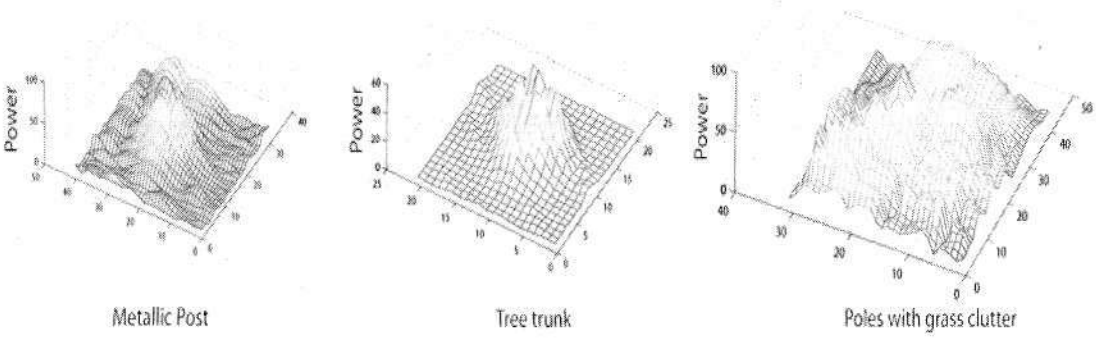

Figure C.3: *The power profile from point features. Note the differing power values as well as the difficulties in identifying point features when corrupted by clutter.*

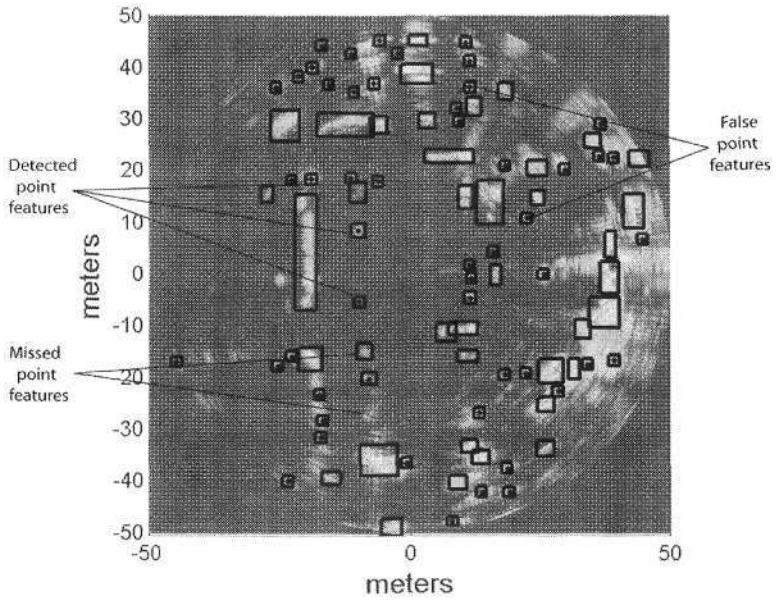

Figure C.4: *This figure highlights the clustered regions of the scan (black bounding boxes) as well as the hypothesised point features (black dots).*

C.2 Birth Density Formation

Following the clustering and extraction of the hypothesised point features in the scan, they form the birth density for the PHD-FBRM and PHD-SLAM recursions according to eqn.(5.14). As outlined in section 5.3.2, the birth density is an arbitrary proposal giving the filter an initial estimate as to where and how many features are likely to appear. In this regard, the birth proposal may simply be a non-informative uniform distribution (approximated by a Gaussian mixture). In this thesis however, the filter uses the measurement at time $k-1$ to initialise the birth density as follows:

- Consider at time $k-1$, that global cartesian co-ordinates of the clustered centroids outlined in the previous section are denoted $\{\mu_{c,1}, \ldots, \mu_{c,J_{b,k}}\}$ (k is used as these will form the birth density at the following time step k).

- At time k, the Gaussian mixture representation of the birth intensity function, $b_k(m|X_k) = \sum_{i=1}^{J_{b,k}} w_{b,k}^{(i)} \mathcal{N}(m; \mu_{b,k}^{(i)}, P_{b,k}^{(i)})$ is then formed where, for $i \in \{1, \ldots, J_{b,k}\}$:

  $\mu_{b,k}^{(i)} = \mu_{c,i}$

$P_{b,k}^{(i)} = \Delta_h \mathrm{R} \Delta_h^T$, where R is the measurement noise covariance and

$$\Delta_h = \begin{bmatrix} \cos(\gamma + \alpha_i) & -r_i * \sin(\gamma + \alpha_i) \\ \sin(\gamma + \alpha_i) & r_i * \cos(\gamma + \alpha_i) \end{bmatrix}.$$

γ is the vehicle heading, (r_i, α_i) are the range and bearing to the centroid cluster $\mu_{c,i}$ from the vehicle pose at time k, X_k.

For each measurement at time $k-1$, the filter puts a belief that a new feature will appear at each of the centroid locations. The covariance of that belief is obtained simply from the Jacobian of the measurement equation from an 'imaginary' measurement generated from each cluster location, $\mu_{c,1}$, and the measurement noise covariance R.

- As stated in section 5.3.2, the sum of the weights of the intensity function, gives the expected number of features. Strictly following this principle, the weight of each Gaussian in $b_k(m|X_k)$, $w_{b,k}^{(i)}$ should be equal to 1. However, this results in erroneous map cardinality estimates since not all measurements at time $k-1$ are from *new* features. In this case the PHD filter may assume that 2 features exist at locations from which the centroid $\mu_{c,i}$ is an existing feature in the map. Simulated trials concluded that a pessimistic birth density weight of 0.01 on each Gaussian, avoided the erroneous double feature estimates, and was sufficiently high to confirm new features with subsequent measurement updates.